Computer Simulation of Confined Liquid Crystal Dynamics

Richard Edward Webster

A thesis submitted in partial fulfilment of the requirements of
Sheffield Hallam University
for the degree of Doctor of Philosophy

November 2001

Abstract

Results are presented from a series of simulations undertaken to determine whether dynamic processes observed in device-scale liquid crystal cells confined between aligning substrates can be simulated in a molecular system using parallel molecular dynamics of the Gay-Berne model.

In a nematic cell, on removal of an aligning field, initial near-surface director relaxation can induce flow, termed 'backflow', in the liquid. This, in turn, can cause director rotation, termed 'orientational kickback', in the centre of the cell. Simulations are performed of the relaxation in nematic systems confined between substrates with a common alignment on removal of an aligning field. Results show that relaxation timescales of medium sized systems are accessible. Following this, simulations are performed of relaxation in hybrid aligned nematic systems, where each surface induces a different alignment. Flow patterns associated with director reorientation are observed. The damped oscillatory nature of the relaxation process suggests that the behaviour of these systems is dominated by orientational elastic forces and that the observed director motion and flow do not correspond to the macroscopic processes of backflow and kickback.

Chevron structures can occur in confined smectic cells which develop two domains of equal and opposite layer tilt on cooling. Layer tilting is thought to be caused by a need to reconcile a mismatch between bulk and surface smectic layer spacing. Here, simulations are performed of the formation of structures in confined smectic systems where layer tilt is induced by an imposed surface pretilt. Results show that bookshelf, chevron and tilted layer structures are observable in a confined Gay-Berne system. The formation and stability of the chevron structure are shown to be influenced by surface slip.

Acknowledgements

I would like to thank my supervisors Doug Cleaver and Chris Care for their support and guidance throughout the project and Nigel Mottram at the University of Strathclyde for helpful discussions. I would like to thank my colleagues in the Modelling Lab for helping me get off to a good start and the staff in the Materials Research Institute and the School of Science and Mathematics at Sheffield Hallam University for their help and support. I would also like to thank my family for their support throughout this project.

Funding for this project was provided by the Engineering and Physical Sciences Research Council Grant No. GR/M16023. Access to the Cray T3E at the Edinburgh Parallel Computing Centre was provided by the High Performance Computing Initiative: Consortium on Simulation and Statistical Mechanics of Complex Fluids.

Advanced Studies

The following is a chronological list of related work undertaken and meetings attended during the course of study:

- Liquid crystal simulation meeting, DERA Malvern, 19 October 1998
- British Liquid Crystal Society (BLCS) Winter Workshop, University of Hull, 20–22 December 1998
- Edinburgh Parallel Computing Centre (EPCC) Course: MPI Programming on the Cray T3D and T3E, University of Edinburgh, 26–27 January 1999
- BLCS Annual Conference, University of Durham, 29–31 March 1999
- Materials Research Institute Research Open Day, Sheffield Hallam University, 25 May 1999
- Level 3 Research Methods unit, SET Graduate School, Sheffield Hallam University, 1998–1999
- Level 3 Research Studies unit, SET Graduate School, Sheffield Hallam University, 1998–1999
- Collaborative Computational Project 5 (CCP5) Methods in Molecular Simulation Summer School, UMIST, 21–29 June 1999
- Presentation: *Computer simulation of switching in thin liquid crystal films*, Materials Research Institute Seminar, Sheffield Hallam University, 25 October 1999

- Poster presentation: *Computer simulation of switching in thin liquid crystal films*, CCP5 Annual Meeting: Molecular Simulation in the 21st Century, University of Surrey, 2–5 July 2000

- Poster presentation: *Computer simulation of switching in thin liquid crystal films*, Institute of Physics Complex Fluids Group meeting: Complex Fluids 2000, Sheffield Hallam University, 11–13 September 2000

- Poster presentation: *Computer simulation of switching in thin liquid crystal films*, Materials Research Institute Research Open Day, Sheffield Hallam University, 16 January 2001

- Poster presentation: *Computer simulation of confined liquid crystal dynamics*, BLCS Annual Conference 2001, St. John's College, University of Oxford, 19–21 March 2001

Contents

1 Introduction **1**

1.1 Overview 1

1.2 Aims 2

1.3 Summary of Thesis 3

1.4 Liquid Crystal Phases 5

1.4.1 Classification 5

1.4.2 Thermotropic Rod-Shaped Mesogens 6

1.4.3 Identification of Mesophases 8

1.5 Confined Liquid Crystals 10

1.5.1 Elastic Properties 10

1.5.2 Substrate Alignment 11

1.5.3 Field Alignment 14

1.5.4 Flow Phenomena 15

1.5.5 Relaxation Phenomena 17

1.5.6 Structures in Confined Smectic Phases 20

1.6 Display Applications 22

1.6.1 Twisted Nematic Displays 22

1.6.2 Ferroelectric Smectic Displays 23

2 Theoretical Models **26**

2.1 Continuum Theory of the Nematic State 26

2.1.1 Ericksen-Leslie Theory 26

2.1.2 Static Distortions Due to Fields 27

2.1.3 Relaxation of Field Aligned Systems 29

2.2 Theoretical Modelling of Chevron Structures 32

3 Computer Simulation **38**

3.1 Introduction 38

3.2 Methods 39

3.2.1 Classical Dynamics 39

3.2.2 Statistical Ensembles 40

3.2.3 Monte Carlo Methods 42

3.2.4 Molecular Dynamics 42

3.3 Models 44

3.3.1 Modelling the Atom 44

3.3.2 Multisite Molecular Models 46

3.3.3 Gay-Berne Single Site Model 48

3.4 Practical Aspects 60

3.5 Parallel Molecular Dynamics 64

3.5.1 Parallel Processing 64

3.5.2 Replicated-Data 65

3.5.3 Domain Decomposition 71

3.5.4 Comparison of RD and DD 73

3.6 Analysis 74

3.6.1 Strategies 74

3.6.2 System Parameters 75
3.6.3 Time Resolved Data 77

4 Simulation of Confined Liquid Crystals **78**

4.1 Introduction 78
4.1.1 Aims 78
4.1.2 Simulation Program 79
4.1.3 Surface Model 80
4.1.4 Initial Configurations 82
4.2 Confined Unaligned System 82
4.3 Relaxation from the Splay Fréedericksz
Geometry 86
4.3.1 Aligning Field Model 86
4.3.2 Analysis 88
4.4 Relaxation of a GB35 System 89
4.4.1 Surface Alignment 89
4.4.2 Field Alignment 91
4.4.3 Relaxation on Field Removal 95
4.5 Relaxation of a GB25 System 99
4.5.1 Alignment 99
4.5.2 Relaxation 105
4.6 Large Confined GB25 System 107
4.7 Summary 111

5 Relaxation of Hybrid Aligned Systems **114**

5.1 Hybrid Aligned Systems 114

5.2 Particle-Substrate System 115
5.3 Planar Upper Surface System 122
5.4 Tilted Upper Surface System 132
5.5 Summary 139

6 Chevron Formation and Stability **141**
6.1 Introduction 141
6.2 Simulation Details 143
6.3 Analysis 145
6.4 Quenching 147
6.4.1 Quenching on Smooth Surfaces 147
6.4.2 Quenching on Rough Surfaces 160
6.5 Formation 168
6.5.1 Introducing Rough Surfaces 168
6.6 Relaxation to Tilted Layer Structure 175
6.7 Fixed Particle Substrate System 179
6.8 Summary 185

7 Conclusions **189**
7.1 Introduction 189
7.2 Relaxation of Field Aligned Systems 189
7.3 Confined Smectic Systems 193
7.4 Summary 196

A Calculating Forces due to Continuum Surface Potentials **209**

Chapter 1

Introduction

1.1 Overview

Liquid crystalline phases are intermediate phases between the liquid and the crystal state. Molecules in a nematic phase possess long range orientational order but no long-range positional order. Molecules in a smectic phase also possess restricted positional order in the form of two-dimensional fluid-like layers.

Confinement by substrates can induce alignment of molecules in the surface regions, which, in turn, can align the bulk material. Bulk alignment can also be influenced by applied fields. Commercial display applications exploit the optical properties of liquid crystalline materials whose bulk alignment is influenced both by confining substrates and by applied fields.

Nematic display devices exploit switching between substrate-aligned and field-aligned bulk states. Relaxation on removal of the field induces flow in the liquid, which, in turn, affects the bulk orientation. These 'backflow' and 'orientational kickback' processes slow the relaxation, thus limiting the switching speed of the device.

Smectic displays exploit field induced switching of molecular orientations within each layer. An ideal device geometry is a so called bookshelf structure, where the plane of the layers is perpendicular to the confining substrates. However, such cells typically form a chevron structure, comprising two domains of equal and opposite layer tilt. This chevron structure reduces the contrast of the display.

Theoretical studies of switching in nematic cells predict backflow and kickback and demonstrate the role of induced flow in the relaxation behaviour. Theoretical models of chevron structures in confined smectic cells predict that the chevron structure is stabilised by non-slip boundary conditions at the surfaces.

Simulation methods can play a role in the development of theories and in the interpretation of experimental results. Theoretical treatments make a number of assumptions and approximations and do not account for molecular scale effects. Experimental studies can reveal the behaviour of a system, without possessing the time and spacial resolution to determine the exact mechanism responsible. Simulation can provide insight into the effects of molecular properties and molecular-scale phenomena on the properties of the bulk material.

The Gay-Berne intermolecular potential model has proved successful in simulating most of the main bulk liquid crystal phases. The use of supercomputers and parallel molecular dynamics simulation techniques allows long timescale simulations suitable for the study of the dynamics of medium sized confined Gay-Berne systems to be performed.

1.2 Aims

The aim of the work described in this thesis is to determine whether phenomena observed experimentally in device-scale liquid crystal cells can be simulated in a

molecular system using parallel molecular dynamics of the Gay-Berne model.

Firstly, simulations of nematic systems confined by aligning substrates are performed. The relaxation behaviour of these systems on removal of an applied aligning field is studied with the intention of observing the relaxation processes of backflow and orientational kickback.

Secondly, simulations of confined smectic systems are performed with the intention of investigating the effects of surface slip on the formation and stability of a chevron structure.

1.3 Summary of Thesis

The following gives an overview of the structure of this thesis.

Chapter 1 gives an introduction to the work and presents background information relevant to the systems studied. The classification of bulk liquid crystal phases is considered, along with background information on the mechanisms of substrate induced and field induced alignment of nematic liquid crystals. The characteristics of flow phenomena in nematic phases and the role of backflow and orientational kickback in the relaxation behaviour of field-aligned systems is presented. The structures observed in confined smectic systems are examined. A brief overview is given of the principles behind the operation of nematic and smectic display devices.

Chapter 2 reviews relevant theoretical models of confined nematic and smectic systems. Continuum theory treatments of field alignment and relaxation in nematic systems and the theoretical predictions of the relationship between induced flow and orientational kickback are considered. A review of theoretical models of the formation and stability of chevron structures in confined smectic systems and

the predictions of the influence of surface slip on stability is presented.

Chapter 3 reviews simulation techniques and models of liquid crystal molecules. A detailed description is given of the Gay-Berne intermolecular potential and a review is presented of relevant results from simulations of bulk and confined systems using this model. A description of parallel molecular dynamics techniques and simulation analysis methods is given.

Chapter 4 describes the development work done on an existing bulk Gay-Berne parallel molecular dynamics simulation program in order to introduce aligning surfaces. Results of simulations of the relaxation of field-aligned nematic systems demonstrating the accessibility of relaxation timescales are presented. Two parameterisations of the Gay-Berne model are considered.

Following on from this, Chapter 5 presents results of the relaxation on field removal in hybrid aligned nematic systems, where one surface promotes normal alignment and the other promotes either planar or tilted alignment. Flow patterns associated with the relaxation are observed.

Chapter 6 presents the results of simulations of the formation of structures in a confined smectic system. Bookshelf, chevron and tilted layer structures are observed. Surface slip is shown to influence the formation and stability of the chevron structure.

Chapter 7 summarises the main results of this thesis and presents conclusions and suggestions for future work. A bibliography is included.

1.4 Liquid Crystal Phases

1.4.1 Classification

Materials can be classified according to their structure on a molecular or *mesoscopic* scale [1]. Molecules in a crystal have short and long range positional and orientational order. Molecules in an isotropic liquid have no long range positional or orientational order. Molecules in a liquid crystalline phase, often termed a mesophase, have long range orientational order and either no or only restricted long range positional order.

Liquid crystal materials can be further classified according to what controls their phase behaviour. *Thermotropic* liquid crystals, used in display devices, have their phases controlled by temperature. *Lyotropic* liquid crystals, such as detergents, have their phases controlled by concentration in a solvent.

To form liquid crystalline phases, molecules must generally have anisotropic shape with some stiffness in the middle and some flexibility at the ends. Overall molecular shape is the main factor influencing the types of phase adopted, the two main shapes being rod-like and disk-like.

Rod shaped molecules are known as *calamitic mesogens* and form phases with a common molecular orientation and, in some cases, positional layering. Typically this type of molecule consists of two or more ring structures with hydrocarbon chains on each end. Fig.1.1 shows the molecular structure of 5CB, a room temperature thermotropic liquid crystal material. This is one of a number of liquid crystal materials referred to as nCB's where n is the number of carbon atoms in the tail section.

Disk shaped molecules form phases where the axes normal to the faces of

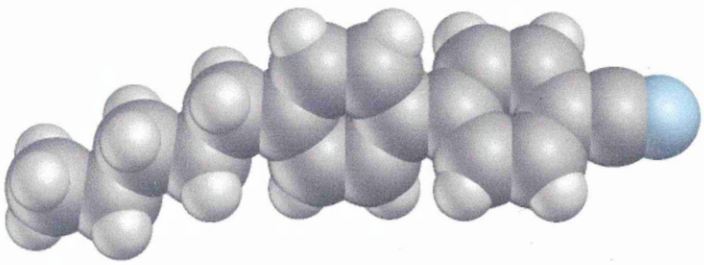

Figure 1.1: Typical calamitic mesogen 5CB.

the molecules are oriented around a common direction. Here, positional ordering typically involves molecules becoming stacked in columns.

Liquid crystalline phases can also be formed by polymers and biological mesogens such as the tobacco mosaic virus, but there are many rod shaped and disk shaped molecules which do not form such phases. No general theory exists which can predict with certainty whether a given molecule will form any particular liquid crystalline phases.

1.4.2 Thermotropic Rod-Shaped Mesogens

At a high enough temperature, all mesogens form an *isotropic* phase (Fig.1.2.a) where the molecules have no long-range orientational order. On cooling, the material can enter a *nematic* phase (Fig.1.2.b) where the long axes of the molecules orient around a common direction.

This average orientation is represented as a unit vector, $\mathbf{n}$, called the *director*. The director has no head or tail so that reversing the its sign does not change its meaning. The degree of alignment around the director is represented by a second rank *order parameter*

$$S = \frac{1}{2}\langle 3\cos^2\theta - 1\rangle, \tag{1.1}$$

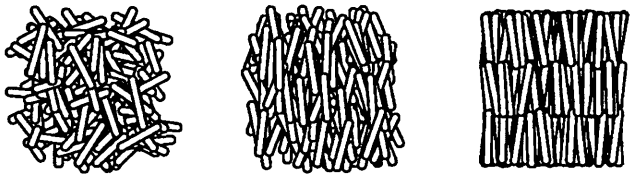

a b c

Figure 1.2: Molecular arrangements in mesophases: (a) isotropic, (b) nematic, (c) smectic-A.

where θ is the angle between each molecule and $\mathbf{n}$, and the angle brackets denote the average over all molecules. This gives $S = 1$ for perfect alignment and $S = 0$ for random (isotropic) distributions of orientations [1].

Further cooling can cause transitions through various *smectic* phases where there is also some positional ordering, in the form of two-dimensional fluid-like layers (Fig.1.2.c). Smectic phases are classified according to the arrangement of layers with each other and the arrangement of molecules within each layer.

In a smectic-A or S_A phase (Fig.1.3.a), the director is normal to the layers but molecules have no positional order within the plane of each layer. In a smectic-B or S_B phase (Fig.1.3.b), the director is normal to the layers and there is hexagonal packing of molecules within the plane of each layer. In a smectic-C or S_C phase (Fig.1.3.c), the director is tilted with respect to the layer normal and, thus, the layer spacing is less than that of the S_A for any given material.

The positional order orthogonal to the layers in a smectic phase can be described by a complex order parameter

$$\psi(\mathbf{r}) = \rho_1(\mathbf{r})e^{i\phi}, \tag{1.2}$$

where $\mathbf{r}$ is a position vector, ρ_1 is the translational order parameter which represents the amplitude of the smectic density wave and ϕ is a phase factor relating

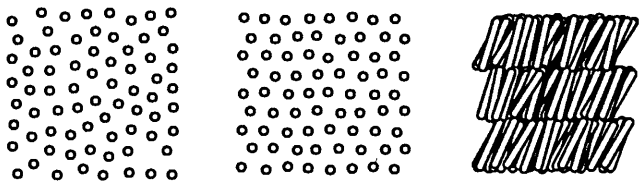

a b c

Figure 1.3: Arrangements of molecules within smectic layers: (a) smectic-A, (b) smectic-B, (c) smectic-C.

the position of the smectic layers to the origin of the coordinate system used [1].

There are many further variants of the smectic phase, each defined by the positional order within each layer, the relationship between the tilt and packing of molecules within each layer, and any correlations between the packing arrangements in adjacent layers. The classification of liquid crystal phases, although well established, is still a developing area.

1.4.3 Identification of Mesophases

Optical Microscopy

Optical microscopy is the main technique used to identify liquid crystalline phases [2]. An isotropic material has a single index of refraction n. For linearly polarised light passing through an anisotropic material, the index of refraction is different for light with different polarisations. For a nematic phase, the index of refraction is $n_{\|}$ for light polarised parallel to the director and $n_{\perp}$ for light polarised perpendicular to the director. The difference, $\Delta n = n_{\|} - n_{\perp}$, is the optical anisotropy or *birefringence* of the material.

This property is exploited in phase characterisation by placing a temperature controlled sample, lit from below, between crossed-polarisers under a microscope.

With an isotropic phase, no light passes through the upper polariser and the sample appears dark. In the nematic phase, if the director is parallel or perpendicular to the polarisation of the light, the light travels according to a single index of refraction and the sample again appears dark. If, however, the director is at an angle to the polarisation of the light, the components of the light parallel and perpendicular to the director experience different indices of refraction and a phase difference is introduced between them. As a result, the light which emerges from the sample becomes elliptically polarised and, therefore, some of it is transmitted by the upper polariser.

Although locally the molecules align around the director, the director can change across the sample, creating a defect structure which is often peculiar to the phase present. Under crossed polarisers, this can create characteristic patterns of light and dark which give more information about the type of phase. Patterns of colours can also be seen in such samples due to birefringence being a function of wavelength.

Differential Scanning Calorimetry

Not all phase transitions lead to changes in the optical properties of liquid crystalline materials, and not all changes in optical properties are caused by phase changes. For this reason, optical microscopy is often used with the complimentary technique of differential scanning calorimetry or DSC. DSC can reveal the occurrence of phase transitions but cannot be used to characterise the types of phase present.

DSC instruments measure the energy absorbed by a sample as it is heated or released as it is cooled [2]. Typically, a DSC instrument consists of two pans, one

containing the sample and one empty, each with its own heater. The difference in energy needed to keep the pans at the same temperature as that temperature is slowly raised or lowered is recorded. This is sensitive to phase changes because, for example, if the sample melts, more energy will be needed to keep the sample at the same temperature as the empty pan due to the latent heat of the transition.

X-ray Diffraction

X-ray diffraction can be used to study some liquid crystal phases as it can reveal periodic features in the structure of materials at a molecular scale [2]. This can be used to obtain structural information about smectic phases if the sample is a mono-domain which can be aligned with the x-ray beam. The presence of long range positional order in smectics gives strong, sharp diffraction peaks unlike an isotropic liquid or a nematic phase which gives a weak, diffuse pattern. If the incident beam is parallel to the planes of the layers in a smectic phase then the angle between the un-scattered beam and the smallest angle reflection is related to the layer spacing. If the incident beam is normal to the layers in a hexatic S_B phase then the diffraction pattern becomes a hexagonally arranged set of points.

1.5 Confined Liquid Crystals

1.5.1 Elastic Properties

Unlike isotropic liquids, liquid crystals can transmit torques. The orientational elastic properties of the bulk material are specified by 3 elastic or *Frank* constants, k_{11}, k_{22} and k_{33}, corresponding to the restoring forces opposing splay, twist and bend director distortions respectively [1]. The splay distortion has non-zero di-

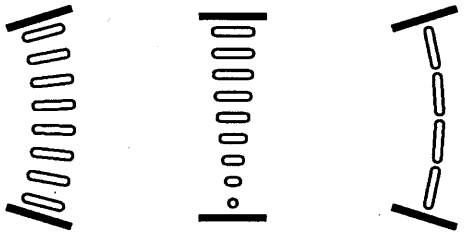

a b c

Figure 1.4: Distortions of the nematic director: (a) Splay, (b) Twist, (c) Bend.

vergence

$$\nabla \cdot \mathbf{n} \neq 0, \tag{1.3}$$

the twist distortion has curl parallel to the director

$$(\nabla \times \mathbf{n}) \parallel \mathbf{n}, \tag{1.4}$$

and the bend distortion has curl perpendicular to the director

$$(\nabla \times \mathbf{n}) \perp \mathbf{n} \tag{1.5}$$

as shown in Fig. 1.4.

1.5.2 Substrate Alignment

Liquid crystals in contact with a substrate can experience positional and orientational ordering referred to as *anchoring* [3]. *Strong anchoring* usually refers to a situation where the imposed orientation or positioning of molecules does not change in response to bulk director distortions or applied fields.

The uniform bulk density of a nematic phase can be perturbed in the surface region due to a layer of molecules forming at the surface. A second, less well defined layer can then form above the first and so on inducing a degree of positional

order on the nematic in the form of stratification near the surface to around 100Å. This can be determined using surface forces apparatus or SFA measurements [4]. Here, the liquid film is confined between two cylinders aligned at right angles in a bulk reservoir and the surface separation is measured by optical techniques. The surfaces are assumed to be flat on a molecular scale. The film thickness is varied by applying a stress normal to the surfaces. Plots of stress as a function of separation show a damped oscillatory curve which is attributed to stratification.

Molecules in the surface monolayer can develop orientational and positional ordering through physisorption. This has been shown by scanning tunnelling microscopy or STM which can determine positions and orientations of individual molecules on a substrate [5].

This technique exploits quantum tunnelling whereby penetration of a potential barrier by an electron wavefunction occurs due to the finite probability of an electron being found at the other side of a potential barrier. An atomistic metal tip is moved across a substrate at a height of around 1nm. A current passes from the substrate to the tip as electrons tunnel across the small gap. Images are created by measuring changes in the current or the height required to maintain a constant current as the tip is moved over the surface. Layered substrate structures are the most easily prepared for STM studies and the method is limited to smectic phases as nematic phases are not ordered enough to produce images.

STM studies of 8CB, 10CB and 12CB adsorbed on graphite by Smith *et al.* [6, 7] and McMaster *et al.* [8] found molecules in registry with the graphite structure. The surface molecules had a smectic layer arrangement across the substrate similar to the bulk layers but more highly ordered, with the structure of a two-dimensional molecular crystal rather than a liquid crystal. Hara *et al.* [9] used STM to study

8CB on molybdenum disulphide. Images revealed a periodic pattern of four rows of molecules. The periodicities of the structure correlated with the lattice of the underlying substrate rather than with the bulk structure which demonstrates that molecule-substrate interactions can impose structure on the adsorbed layers.

Alignment of the director near the surface can impose alignment on the bulk. Surface alignments can be planar, normal to the surface or tilted, and azimuthal anchoring can create an easy-axis for the director in the plane of the surface. For nematics, the anchoring energy has number of minima corresponding to the anchoring directions or easy-axes. A single minimum leads to monostable anchoring in one direction, many minima give multistable anchoring, and degenerate anchoring has no minima and no preferential alignment. Different anchorings are obtainable from different surface treatments which can increase or decrease alignment and order in the surface region.

If a surface is coated with a polymer which is then rubbed mechanically, the director tends to align in the rubbing direction giving planar alignment with azimuthal anchoring, although there is usually a small pre-tilt of a few degrees at the surface. Deposition of silicon monoxide can give anchoring with alignments tilted from the plane of the surface and surfactant coatings can produce alignments normal to the surface [10].

Most liquid crystal devices depend on azimuthal anchoring produced by rubbed polymer surfaces but the exact mechanism of alignment is unclear. A macroscopic scale mechanism thought to cause alignment is the influence on the director field of grooves in the polymer surface caused by the rubbing. To minimise elastic energy due to director distortion, the director lies along rather than across the grooves, as shown in Fig.1.5.

a b

Figure 1.5: Surface director alignment due to grooves produced by rubbing. Elastic energy is lower for a director lying along the grooves (a) than across the grooves (b).

Experimental evidence also suggests that the alignment process is taking place at the molecular scale where molecule-substrate and molecule-molecule interactions combine to give alignment. Cheng and Boyd [11] used polarised microscopy to study alignment on photolithographic gratings etched onto a substrate. They found that grooves are neither necessary nor always sufficient to produce alignment. Toney *et al.* [12] used grazing incidence x-ray scattering to study rubbed polymer films and showed that the rubbing causes near-surface alignment of the polymer molecules. The authors suggested this was due either to friction causing the local temperature at the surface to become high enough that the chains reoriented on rubbing or to the yield stress of the polymer being less at the surface than in the bulk.

1.5.3 Field Alignment

Just as liquid crystals possess optical anisotropy, they also possess diamagnetic and dielectric anisotropy [1]. Typical liquid crystal molecules have two aromatic rings. A ring experiencing a magnetic field H normal to the plane of the ring has a higher energy than one experiencing a field in the plane of the ring. This is caused by expulsion of the field lines due to currents which build up inside the ring in the first case but not the second. The effect on an isolated molecule is negligible,

but a bulk sample can be aligned by the field. The diamagnetic anisotropy of a nematic material is expressed as

$$\chi_a = \chi_{||} - \chi_{\perp}, \tag{1.6}$$

where $\chi_{||}$ and $\chi_{\perp}$ are the magnetic susceptibility parallel and perpendicular to the director respectively. Most liquid crystal molecules possess positive diamagnetic anisotropy and will align parallel to the field.

In a confined geometry, where the equilibrium director throughout the cell is determined by planar or normal surface alignment, an applied field has no effect on director alignment until the field strength reaches a critical value H_c. Above this, the system exhibits a continuous transition to a state where a component of the director aligns with the field except for regions near the surface. This is known as the *Fréedericksz* effect.

Different field directions and surface alignments lead to geometries corresponding to splay, twist and bend distortions of the director as shown in Fig 1.6. Combined with theory linking critical field strengths with elastic constants outlined in Section 2.1.2 this allows the elastic constants to be measured experimentally [1]. Typically, changes in the director orientation are detected by placing the sample between crossed polarisers, illuminating it with monochromatic light and observing the transmitted light. Generally, for nematics, $k_{33} > k_{11} > k_{22}$ with $k_{33}/k_{11} \approx$ 1.2–2. The elastic constants vary strongly with temperature but the ratio k_{33}/k_{11} is nearly independent of temperature.

1.5.4 Flow Phenomena

Director orientation and fluid flow in nematic liquids are strongly coupled [10]. The flow behaviour of a nematic can be characterised by five viscosity coefficients.

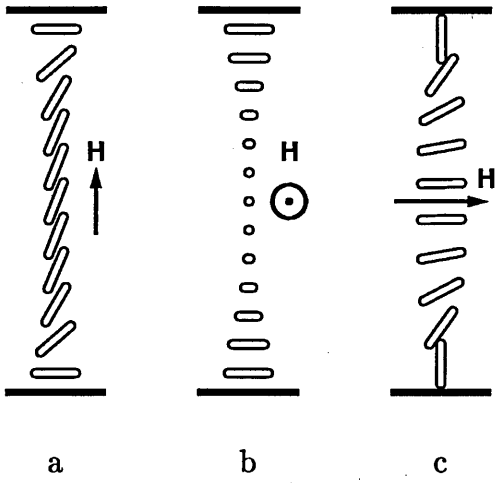

Figure 1.6: Fréedericksz geometries: (a) Splay, (b) Twist, (c) Bend.

Three of these, called the *Miesowicz* viscosity coefficients η_1, η_2 and η_3, define the behaviour for cases where the director is parallel to the flow, where the director is parallel to the flow velocity gradient and where the director is orthogonal to both the flow and velocity gradient, respectively. These geometries are shown in Fig. 1.7. For the first two of these, a viscous torque causes the director to rotate, leading, in turn, to an induced flow. The two remaining coefficients characterise the torque associated with a rotation of the director and the contribution to the torque due to shear.

The coefficients cannot be measured directly, but certain linear combinations of them can [13]. Techniques include adaptations of classical fluid analysis techniques such as measuring pressure-driven laminar flow through a capillary. Rotational viscosities can be determined by measuring the torque on a sample as it is rotated at a constant rate in a stationary aligning magnetic field. Alternatively, if the elastic constants of the material are known, light scattering can be used to determine the viscosity coefficients; local fluctuations in the director scatter light in ways which depend on the elastic and viscous material properties and the

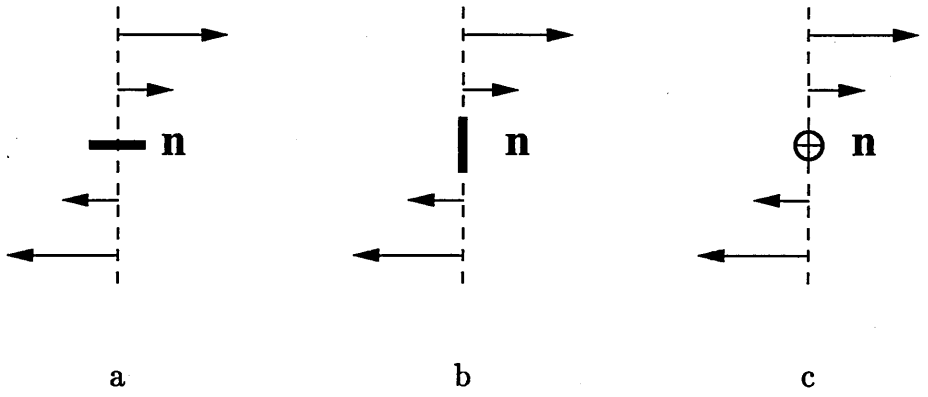

Figure 1.7: Flow geometries for measuring the Miesowicz viscosities of a nematic liquid crystal: (a) Director parallel to flow, (b) Director parallel to flow velocity gradient, (c) Director orthogonal to flow and velocity gradient.

relative orientations of the incident beam and the director.

The complete set of coefficients has only been measured for a few liquid crystalline materials. For rod-shaped nematic liquid crystals, the viscosity corresponding to flows parallel to the director (Fig. 1.7.a) is lower than that corresponding to flows perpendicular to the director (Fig. 1.7.b).

1.5.5 Relaxation Phenomena

When an aligning field is removed from a nematic system with competing surface and field alignments the director relaxes back to its equilibrium orientation. This relaxation process is affected by the coupling between director orientation and flow. This effect is greatest for the splay Fréedericksz transition geometry shown in Fig. 1.6.a and does not occur for the twist case of Fig. 1.6.b.

On removal of the field, the initial reorientation of the director in the surface regions induces a flow, termed *backflow*, in the liquid. The liquid is stationary at the surfaces and in the centre of the cell and the flow occurs at $\frac{1}{4}d$ and in the opposite direction at $\frac{3}{4}d$ where d is the distance between the surfaces. This

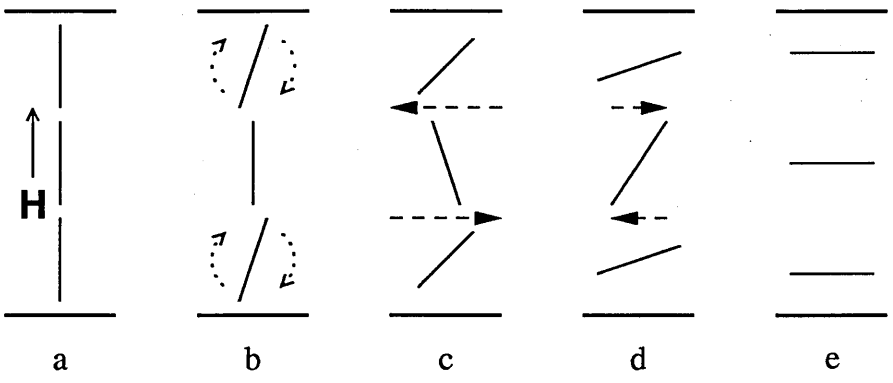

Figure 1.8: Backflow and kickback on relaxation from the splay Fréedericksz geometry: (a) Field aligned system. (b) On field removal, the director in the surface regions reorients. (c) Director reorientation near the surfaces induces 'backflow' which causes 'kickback' of the director in the centre. (d) Flow reverses and the director in the centre rotates. (e) System relaxes to equilibrium orientation.

backflow in turn causes a rotation of the director, termed *orientational kickback*, in the centre of the cell. The flow then reverses and the director finally relaxes to its equilibrium surface-aligned state. This is illustrated in Fig. 1.8. The characteristics of the relaxation are affected by the initial director profile, the elastic constants and viscosity coefficients of the material, and the cell dimensions.

The influence on director orientation of induced flow can be observed as an 'optical bounce' in the transmittance of a cell when an aligning field is removed [10]. The transmittance falls, then rises before falling to its equilibrium value.

Pieranski *et al.* [14] used optical birefringence techniques to measure the transition rates for field on and field off cases in a splay geometry cell. For weak fields, $H < 2.5H_c$, similar transition rates were observed. As the field strength was increased, the field off rates became progressively larger than the field on rates. For $H \approx 4H_c$, the field off transition rates were double the field on values. This difference is attributed to induced backflow in the field off case.

Fukazawa *et al.* [15] studied relaxation from the splay configuration of a Fréedericksz

cell using a spectroellipsometry technique. This approach exploits the fact that a linearly polarised beam becomes elliptically polarised after reflection from a planar surface. Measurements of the polarisation state of the beam can, therefore, be compared with a model of the process to reveal material properties. In [15], measurements were made on a nematic 5CB in a cell with rubbed polymer surfaces (for alignment) and a surface separation of 6.35μm. The bulk behaviour was determined by measuring the transmitted beam and a reflected beam was used to study a thin layer of molecules near the surface. For strong fields, the surface and bulk rise times were similar. However, while the relaxation times of the interface molecules showed fast reorientation of around 3ms, the bulk showed a much longer relaxation time of around 100ms.

Optical techniques which measure the waveguiding modes of a liquid crystal can also be used to study orientation in thin films [16]. Here, the liquid is placed between a transparent substrate and a cladding layer. The index of refraction of the substrate is made less than that of the liquid, which in turn is less than that of the cladding. At high angles of incidence, therefore, the light is able to 'leak' from the surfaces. Fully guided modes have no leaks, half-leaky guided modes leak from the substrate and full-leaky guided modes leak from both surfaces. For liquid crystal studies, a plane parallel, monochromatic, linearly polarised beam is used. Typically, a prism is used as the cladding layer and results are obtained by monitoring the angle dependent reflectivity and the polarisation of the beam directed through the prism at the cladding-liquid boundary. Different modes and surface coatings can be used to determine the director orientation in different regions of the liquid. The measured data is fitted to a model of the optics of the cell to reveal the director profile.

Mitsuishi *et al.* [17] used a time-resolved optical waveguide technique to study director reorientation in the splay configuration of 7–8μm 5CB cells with rubbed polymer aligning surfaces. The technique, which can resolve the director profile in 3-dimensions, showed that reorientation occurs in a plane defined by the rubbing direction and the field direction. For the field on case, the transition time was around 4ms and for the field off case the relaxation time was around 250ms.

1.5.6 Structures in Confined Smectic Phases

If a confined nematic system with director alignment parallel to the surfaces is cooled into a smectic phase, the geometry of the resultant structure has a layer normal parallel to the surface, leading to the *bookshelf* arrangement as shown in Fig. 1.9.a. This has been determined even in a cell with a high surface pre-tilt [18]. Director profiles were measured using optical mode techniques. On cooling a nematic with a surface pre-tilt angle of $\approx 29°$ into the S_A phase, a bookshelf structure formed across the cell. The director splay was localised in regions near the surface and the pre-tilt reduced to $\approx 24°$

However, an alternative structure can also form, which was first determined by Rieker *et al.* [19]. X-ray scattering data obtained from a $\approx 3\mu$m cell showed a single peak in the Bragg reflection corresponding to a bookshelf structure for the S_A phase. On cooling into a S_C phase, two sharp peaks were found, indicating two distinct and opposite tilt angles in the cell. This was attributed to the formation of a *chevron* structure as shown in Fig. 1.9.b. The layer tilt increased as the temperature decreased. Various rubbed and surfactant-coated surfaces were used and the tilt was found to be independent of the surface treatment. A tilted layer structure, shown in Fig. 1.9.c, was also observed in some cases.

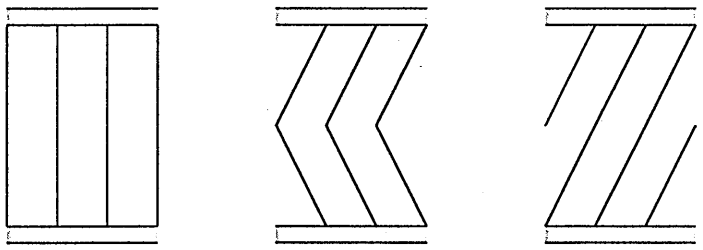

Figure 1.9: Structures which can occur in a confined smectic system: (a) bookshelf, (b) chevron, (c) tilted layer.

The mechanism proposed for the layer tilt relies on the smectic positional order being frozen at the surfaces in the S_A phase. With a S_C phase in the bulk, the reduced spacing of the bulk layers creates a mismatch between the bulk and surface layer spacing, which is resolved by a tilting of the bulk layers.

The presence of the chevron structure in a S_C cell was confirmed by Elston and Sambles [20] using optical waveguide techniques. The layer shrinkage mechanism of chevron formation is supported by evidence of positional anchoring of smectic layers in a sheared planar-aligned S_A cell obtained by Cagnon and Durand [21]. Piezoelectric transducers cemented to each surface allowed measurement of shear stress transmitted through the sample as a continuous shear strain was applied normal to the layers. The stress showed viscoelastic relaxation with superimposed oscillations whose period corresponded to the smectic layer spacing. This was attributed to the periodic melting and recrystallisation of the layers near to the surface forced by the strong positional anchoring of layers at the surface.

Chevron structures have also been observed in S_A cells by other x-ray diffraction studies. Srajer *et al.* [22] cooled 5–20μm cells through the S_A phase into the S_C phase in order to study S_C chevron structures but found that the chevron

structure occurred whilst the cell was still in the S_A phase. Morse and Gleeson [23] found a chevron structure occurring on cooling a 50μm cell from the nematic phase into the S_A phase. As the temperature was lowered, the tilt angle increased to a maximum of 8.5°.

1.6 Display Applications

1.6.1 Twisted Nematic Displays

Twisted nematic (TN) displays use Fréedericksz switching to control light transmission through a cell. These are found in watches and calculators and make up 99% of commercial liquid crystal displays. The are cheap and reliable, but backflow and kickback effects limit switching speeds to around 10ms.

Fig. 1.10 shows the light and dark state of a TN cell. Clear rubbed polymer aligning surfaces are aligned at 90° to each other. This creates a 90° twist in the director running across the cell. Polarisers are mounted on the top and bottom of the cell, lined up with the rubbing directions.

In the light state (Fig. 1.10.a), with no field applied, as the light passes down through the cell, its polarisation is rotated by the twist in the director, allowing it to pass through the lower polariser. In the dark state (Fig. 1.10.b), an electric field is applied normal to the surfaces, aligning the bulk director along the field. This disrupts the twist, allowing the light to pass through the cell with its unmodified polarisation. The transmission of light is therefore blocked by the lower polariser. By combining this cell with reflectors or a light source, a segment of a display can be made to appear light or dark.

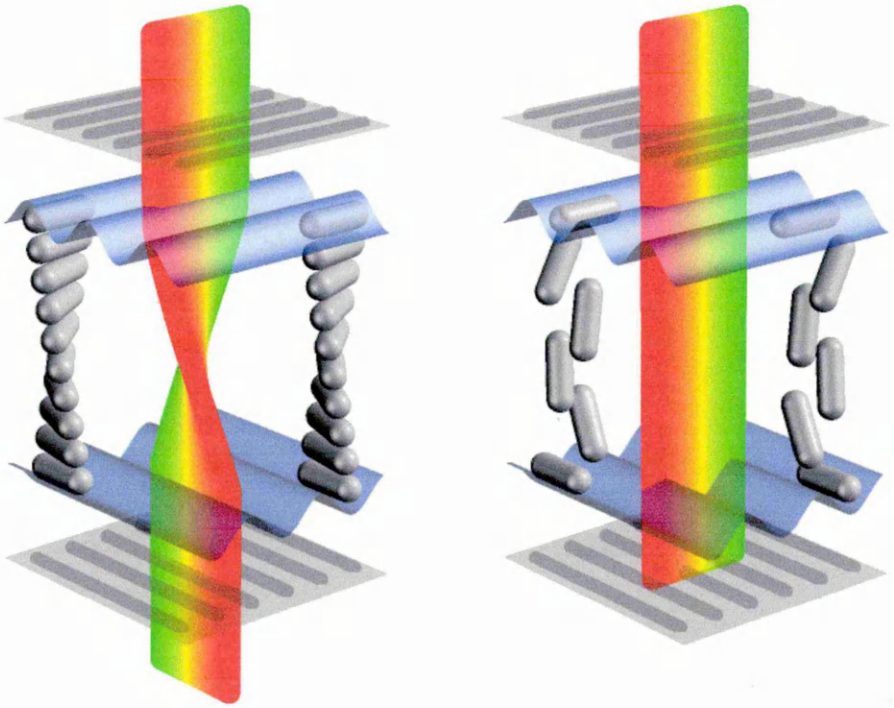

a b

Figure 1.10: Operation of a twisted nematic display: (a) Light state: with no field, the director twist rotates the polarisation of the light allowing it to pass through the lower polariser. (b) Dark state: with an aligning field applied normal to the surfaces, the twist is disrupted and light transmission is blocked.

1.6.2 Ferroelectric Smectic Displays

In the S_A phase there is equal probability of molecules assuming any orientation about their long axes. Hence, the transverse components of dipole moments are averaged out and there is no net polarisation in the plane of the layers. In a ferroelectric S_C phase the molecules are tilted and their rotation about their long axes is biased. This allows the existence of a permanent dipole moment in the plane of the layers, perpendicular to the long molecular axes, and so each layer is spontaneously polarised.

A given tilt angle θ defines a cone of possible director orientations. The po-

sition of the director on this cone defines the tilt direction. The polarisation is perpendicular to the tilt direction as shown in Fig 1.11.a. The bulk ferroelectric S_C phase has a twist about the layer normal such that the tilt direction and the polarisation rotate from one layer to the next. This means that in a bulk sample there is still no net polarisation.

Clark and Lagerwall [24] discovered that the twist of the director can be suppressed by confinement in a thin cell, thus producing a macroscopic polarisation. This phenomena is exploited in surface-stabilised ferroelectric liquid crystal displays. Switching of the cell is possible because the polarisation vector and the director are coupled. An applied electric field can control the polarisation, and can therefore control the tilt direction. Reversing the field direction reverses the tilt.

A typical device uses rubbed polymer coatings for alignment. The cell is placed between linear crossed polarisers with one polariser parallel to one of the two possible directions of the director. A field is applied normal to the surfaces. Reversing the field causes switching of the director as shown in Fig. 1.11.b. Ferroelectric devices have faster switching speeds than twisted nematic devices, typically around $50\mu s$, as switching does not involve bulk movement, but the chevron structure which forms in the cell reduces the contrast of the display.

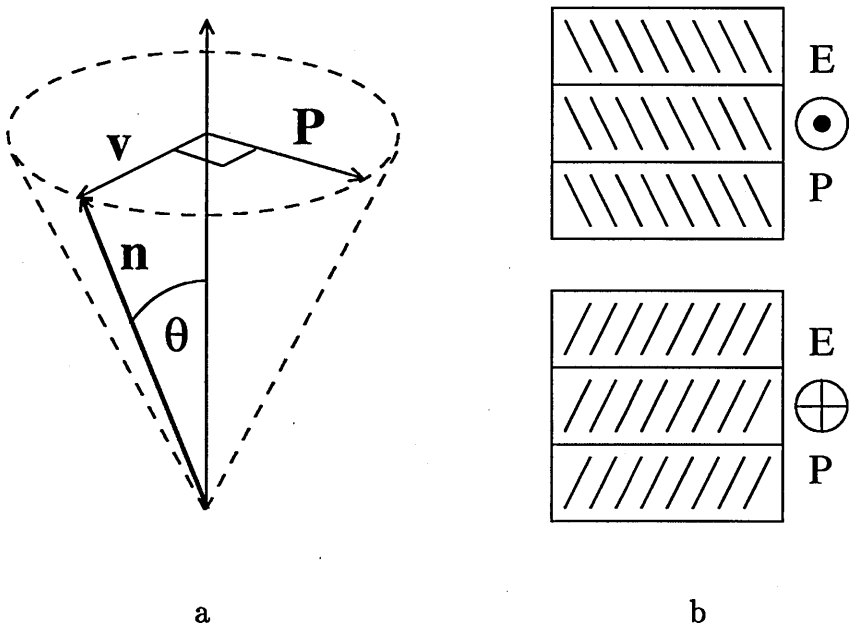

Figure 1.11: Operation of a ferroelectric smectic-C display: (a) Ferroelectric smectic-C phases exhibit spontaneous polarisation **P**. The layer tilt angle θ defines a cone of possible tilt directions for the director **n**. Tilt direction vector **v** and polarisation vector **P** are perpendicular. (b) An applied field **E** controls polarisation and hence director tilt direction. Reversing the field reverses the tilt direction.

Chapter 2

Theoretical Models

2.1 Continuum Theory of the Nematic State

2.1.1 Ericksen-Leslie Theory

The most widely used theory describing the mechanical behaviour of the nematic state is due to Ericksen and Leslie who formulated the general conservation laws and constitutive equations [10]. The assumptions are made that the fluid is incompressible and at constant temperature. The forces responsible for elastic distortions and viscous flow are assumed to be small compared with the intermolecular forces creating local order. Thus, the nematic order parameter is assumed to be constant and is, therefore, ignored.

The main equations take the form of a pair of coupled partial differential equations:

$$\rho \dot{v}_i = f_i + t_{ji,j}, \tag{2.1}$$

$$\rho_1 \ddot{n}_i = G_i + g_i + \pi_{ji,j}, \tag{2.2}$$

where v_i is the linear velocity and $\mathbf{n}$ is a unit vector defining the local director.

For the velocity equation, ρ is the density of the fluid, f_i is the body force per unit volume and t_{ji} is the stress tensor. Unlike a normal fluid, the stress tensor is asymmetric, and includes the influence of the director. It can be split into a static part containing the orientational elastic constants and a hydrodynamic part containing the viscosity coefficients.

For the director equation, ρ_1 is a material constant having dimensions of moment of inertia per unit volume, G_i is the external director body force, g_i is the intrinsic director body force and π_{ji} is the director surface stress. The external director body force G_i accounts for the influence on the director of external fields. The intrinsic director body force g_i can be split into a static part concerning forces due to distortions and a dynamic part concerning forces due to director and fluid motion. When $\mathbf{n} = (0, 0, 0)$ the equations reduce to the equations of hydrodynamics of a normal fluid.

Other key equations give the free energy per unit volume for distortions,

$$F = \frac{1}{2}k_{11}(\nabla \cdot \mathbf{n})^2 + \frac{1}{2}k_{22}(\mathbf{n} \cdot \nabla \times \mathbf{n})^2 + \frac{1}{2}k_{33}(\mathbf{n} \times \nabla \times \mathbf{n})^2 \tag{2.3}$$

and the equation of equilibrium for static distortions,

$$\left(\frac{\partial F}{\partial n_{i,j}}\right)_{,j} - \frac{\partial F}{\partial n_i} + G_i + \gamma n_i = 0 \tag{2.4}$$

where γ is an arbitrary constant.

2.1.2 Static Distortions Due to Fields

The external director body force G_i due to an applied magnetic field $\mathbf{H}$ is given by,

$$G_i = \chi_a H_j n_j H_i \tag{2.5}$$

where χ_a is the diamagnetic anisotropy. For a nematic confined in the z direction by surfaces leading to planar alignment, with a common easy axis (1,0,0), the equilibrium director alignment is $\mathbf{n} = (1, 0, 0)$ throughout the cell.

If θ is the tilt angle of the director $\mathbf{n}$ with respect to the lower surface and the separation between the surfaces is d, when a field is applied perpendicular to the surfaces the system is can be described by, $\theta(0) = 0$, $\theta(d) = 0$, $\mathbf{H} = (0, 0, H)$, $\mathbf{G} = (0, 0, \chi_a H^2 \sin\theta)$ and $\mathbf{n} = (\cos\theta, 0, \sin\theta)$. Due to the assumed director alignment near the surfaces, the maximum distortion $\theta_{\max}$ occurs at $d/2$.

Using Eqn.2.3, the free energy equation for this geometry can be substituted into Eqn.2.4 and, by considering only very small distortions, it can be shown that deformation occurs only above a certain critical field strength H_c where

$$H_c = \frac{\pi}{d}\sqrt{\frac{k_{11}}{\chi_a}}. \tag{2.6}$$

It is this expression which allows experimental determination of the splay elastic constant k_{11} by identification of the critical field associated with a Fréedericksz transition. Other geometries yield equivalent expressions involving the twist and bend elastic constants but such critical field expressions are only valid if the zero-field director is parallel or normal to the surface and strong anchoring is present such that the director at the surface is unaffected by the field.

At the critical field H_c, the distortion is small. As the field strength increases, an increasingly large region in the centre of the cell aligns with the field, creating small regions near the surfaces where the director changes from the field-aligned to the surface-aligned orientation, as shown in Fig.2.1.a. De Gennes [1] introduced a magnetic coherence length ξ, shown in Fig.2.1.b, which defines the size of this

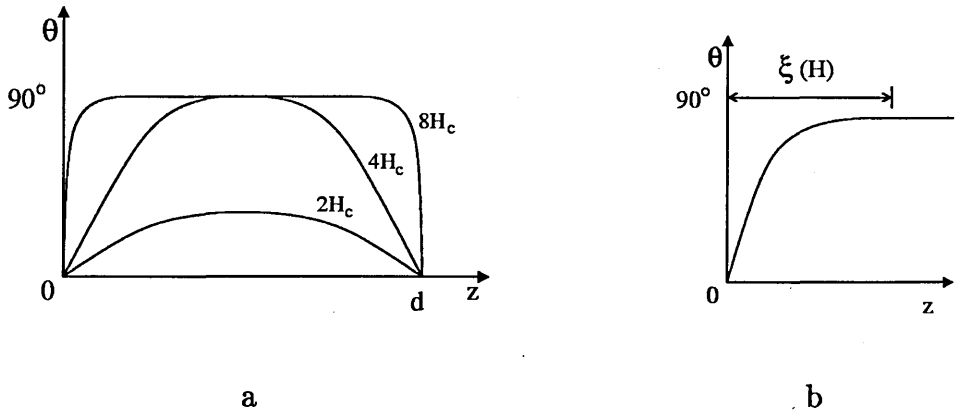

a b

Figure 2.1: Director tilt due to a magnetic field applied normal to planar aligning surfaces of separation d: (a) Typical director profiles for various field strengths H relative to the critical field H_c. (b) Magnetic coherence length ξ defining the size of the transition region.

region. For the splay case,

$$\xi(H) = \frac{1}{H}\sqrt{\left(\frac{k_{11}}{\chi_a}\right)}. \tag{2.7}$$

For a typical cell, a magnetic field of 10^4G produces a transition region of around a micron [10].

2.1.3 Relaxation of Field Aligned Systems

Solutions to the Ericksen-Leslie equations confirm the effects of backflow and kickback on the relaxation behaviour of field-aligned cells.

There is no general solution to the equations Eq. 2.1 and Eq. 2.2 which describe the dynamics of a nematic liquid, but solutions can be obtained in certain cases, if a number of approximations are made. Generally, the assumptions are made that the moment of inertia constant ρ_1 is small for most situations and that the timescale of the establishment of the initial velocity is small compared to the timescale of the overall relaxation, and therefore inertial effects can be neglected.

This reduces Eq. 2.2 to $G_i + g_i + \pi_{ji,j} = 0$. An unrealistic characteristic which can arise from solutions using this approximation is an effectively infinite velocity at the instant that the aligning field is removed. Systems are generally considered to be two-dimensional, and for distortions involving more than one elastic constant, the one-constant approximation $k_{11} = k_{22} = k_{33} = k$ is often used.

Brochard, Pieranski and Guyon [14, 25] performed combined theoretical and experimental studies of small distortions in nematic cells due to changes in magnetic field strengths around the critical value H_c. Splay, twist and bend geometries were studied, experimental measurements being made using polarised microscopy to observe distortions. The experimental results agreed with predictions of Ericksen-Leslie theory and so validated its use for the study of very small director distortions. To simplify the equations, the cell was assumed to have ideal boundary conditions of infinitely strong anchoring and either planar or normal director alignment at the surfaces.

An extension of the Ericksen-Leslie equations for small distortions was used by van Doorn [26] to examine the switching behaviour of a twisted nematic cell. Director orientation at the surfaces was assumed to be parallel to the surfaces and flow was only allowed parallel to the surfaces. By considering the system as a strongly damped oscillator and using typical material parameters, two time constants characterising the behaviour of the director on removal of the field were estimated. The first, representing the time needed for the initial director acceleration to take place, was estimated at around 10^{-6}s. The second, representing the time needed for the elastic energy to relax to zero, was estimated at around 1s. Due to the large difference, the assumption was made that the velocity pattern must have been established almost instantaneously, thus justifying neglecting

inertial effects.

Numerical solutions were obtained for the director motion and flow and from these the optical transmission of the cell was calculated. The solution showed the 'optical bounce' which is observed experimentally in twisted nematic cells. This was attributed to a tipping over of the director in the middle of the cell and also a temporary reversal of the twist in some regions. The calculations were repeated without the fluid motion and no bounce was found, demonstrating the role of fluid flow in director reorientation. The calculated relaxation time was around 0.25s with flow and around 0.015s without flow.

A numerical study of the Ericksen-Leslie equations for a twisted nematic cell was by also performed by Berreman [27]. Constant boundary conditions of planar surface director and zero flow at the surfaces were made. The cell was discretised by division into planes of points with each plane parallel to the surfaces. Again, when the field was removed, a reverse twist and director tilt occurred, which did not occur when flow effects were neglected in the calculations

One of the most widely used techniques for obtaining numerical solutions of Ericksen-Leslie equations was developed by Clark and Leslie [28] and used to study relaxation in a system with planar alignment at the surfaces and a field applied normal to the surfaces.

The method uses an approximate analysis which removes non-linearities in the coupled partial differential equations by replacing variables with constants. During the numerical solution, these constants are periodically replaced with their correct instantaneous values. This reduces the computational effort required to obtain numerical solutions and also means that the method is not limited to the study of small distortions.

In Ref. [28], a solution with infinite initial distortion, where the initial director was taken to be normal to the surface except at the surface, showed backflow and kickback throughout the cell, but strongest in the centre. A solution for a more realistic distortion, where the director angle changed throughout the cell, found that kickback only occurred in the centre of the cell. The predictions given by the solutions do not reveal anything new but confirm results for backflow and orientational kickback as reported by previous workers and confirm the role of induced flow in director reorientation.

The behaviour of the cell at small times was found to be sensitive to the initial distortion profile. The authors used this to justify their approximate analysis scheme on the grounds that it is more important to start with the correct initial distortion than to treat non-linearities in the equations more rigorously.

An illustration of the type of director and flow behaviour predicted by Ericksen-Leslie theory for the case of relaxation on field removal in a splay geometry cell is shown in Fig. 2.2.

2.2 Theoretical Modelling of Chevron Structures

Unlike a nematic phase, in which splay, twist and bend distortions cause the director to vary continuously throughout the liquid, smectic layers expel bend and twist distortions. This suggests that smectic layers submitted to bending stresses either resist until a critical stress induces a transition towards a nematic state or dislocations occur. The *smectic penetration depth* λ is a measure of how far into the smectic phase the bend nematic deformation persists [1] and is a key parameter in theories of stability of the chevron structure in thin cells.

There are two main approaches to the theoretical modelling of the formation

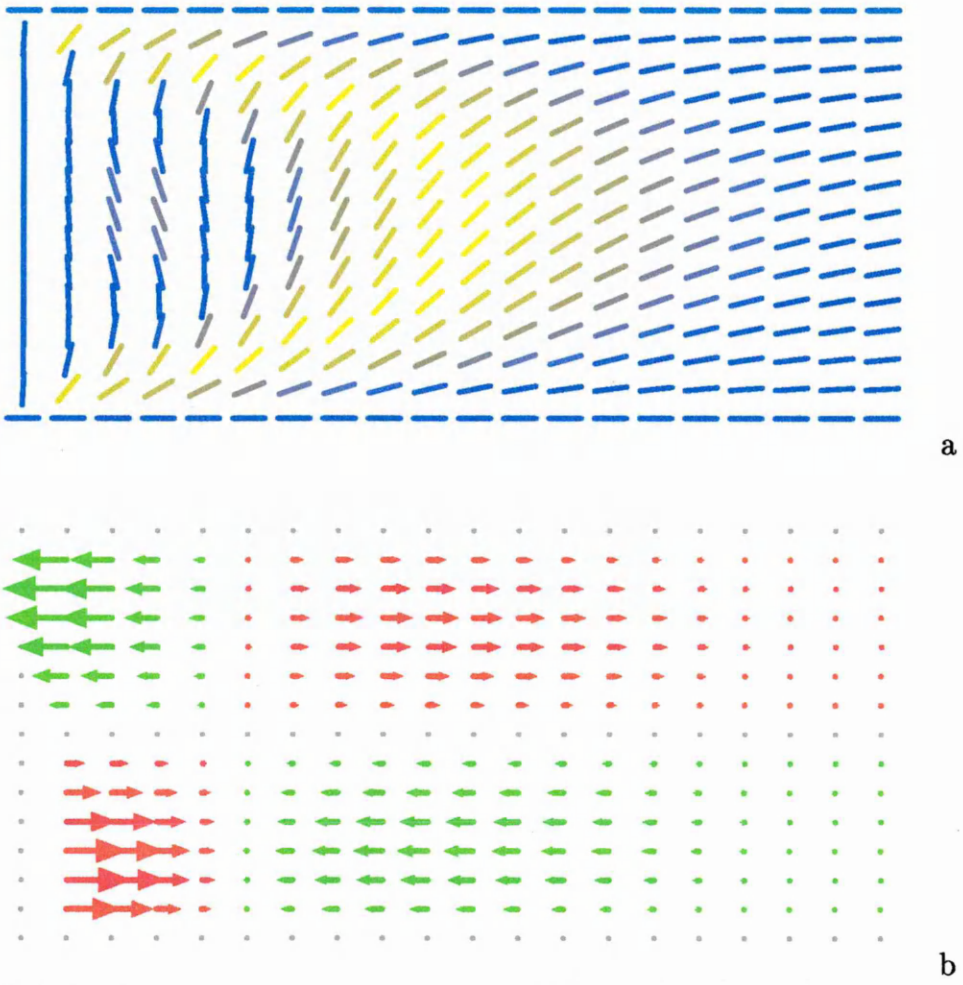

Figure 2.2: Illustration of backflow and kickback in a splay geometry cell on field removal. Successive profiles run from left to right. Directors (a) are coloured blue for $\theta = 0°$, through yellow at $\theta = 45°$ and back to blue at $\theta = 90°$. Velocities (b) are coloured red for $v > 0$ and green for $v < 0$. The initial near-surface director reorientation induces large magnitude flow which rotates the director in the centre of the cell. The flow then reverses and the director relaxes to its equilibrium orientation.

and stability of chevron structures. The first is to extend the expression for the free energy associated with distortions of the director (Eq. 2.3) to include terms involving the distortions of smectic layers due to a chevron structure.

The second is based on an extension of the Landau-de Gennes model for the nematic-isotropic phase transition. Landau-de Gennes theory was developed by de Gennes and is based on the Landau theory of temperature controlled phase transitions. It takes the form of a power series expansion of the free energy in terms of the nematic order parameter S. This is extended to model smectic systems by expressing the free energy in terms of the smectic order parameter ψ, described in Section 1.4.2, which takes account of the degree of layering and the position of the layers relative to a fixed point.

An analytical model for the S_A chevron structure was developed by Limat and Prost [29]. Strong anchoring and different surface and bulk layer spacing were assumed. An expression was constructed for the strain on a bookshelf structure as a function of the difference between the surface and the bulk layer spacing. Then an expression for the free energy density in terms of this strain and the layer tilt angle θ was derived.

Solutions showed that above a critical strain, the chevron structure was the most stable. This is because in the bookshelf structure, as the bulk layers shrink, the strong anchoring maintains the surface spacing throughout the cell, putting the whole bookshelf structure in tension. For the chevron structure, the elastic energy is localised in regions of thickness λ/θ at the surfaces and $2\lambda/\theta$ at the tip. The model also gives a critical cell thickness, dependent on λ, below which the chevron structure does not appear and is replaced by a tilted layer structure.

A model of S_C chevron profiles was developed by de Meyere *et al.* [30] based

on an expression for the Frank elastic energy with extra terms for the energy of layer bending and the variation in the cone angle (and, thus, the variation in the layer spacing). For a one dimensional case where the only variables were the layer tilt and cone angle this gave a small tip region of around 4% of the layer spacing.

Kralj and Sluckin [31] used Landau-de Gennes theory to develop a model of the S_A chevron structure, based on a free energy expression in the form of a power series in the nematic and complex smectic order parameters. It indicated that a chevron structure can exist if the smectic penetration depth λ is less than the cell thickness. The key variables were the strain, the smectic penetration depth and a surface extrapolation depth describing the influence of surface anchoring on the director profile and including a slip or non-slip constraint at the surface. From an initial bookshelf structure, a chevron structure was formed for a non-slip constraint whereas if surface slip was allowed, a tilted layer structure formed. The model predicted that the free energy of the tilted layer structure is always lower than that of the chevron structure. The authors argued, however, that since surface slip is necessary for tilted layers to form, surface anchoring can create an energy barrier between the chevron and tilted layer structures.

A subsequent Landau-de Gennes model of a S_C chevron by Vaupotič *et al.* [32] assumed a constant smectic order parameter due to local smectic elastic distortions being too weak to cause significant variation in the positional order parameter. Below a critical temperature a chevron structure was predicted to form, with a tip width of 10^{-3} of the cell thickness.

Ul Islam *et al.* [33] investigated the formation of S_C chevron and tilted layer structures on cooling from a S_A bookshelf structure. Their model used a Landau expression for the free energy in terms of the smectic cone angle and an assump-

tion was made that the chevron tip could be treated as a localised bend in the continuous director with zero cone angle, i.e. the tip was treated as an internal surface.

A term was included to model the energy associated with surface layer slip, based on the experimental results of Cagnon and Durand [21] for sheared S_A cells. The periodic smectic layer positional anchoring energy was described by a term $E = E^{max} \sin^2(\pi\Delta/d_s)$ with layer displacement Δ, layer spacing d_s and E^{max} taken from [21].

Near the S_A–S_C transition, for small cone angles the bookshelf was found to be the only stable structure. For larger cone angles the lowest energy structure was the chevron for zero displacement, but a tilted layer structure if displacement were allowed. The periodic variation in positional anchoring energy proved sufficient to create a local minimum which trapped the chevron structure and so prevented the formation of the tilted layer structure by layer slip.

Following on from this, and using a similar model, Mottram and Elston [34] studied the shearing of S_C chevron structures. This model assumed the director to lie in a plane perpendicular to the surfaces and the formation of S_A layers at the tip. This made the model equally applicable to the formation of S_A chevrons. The cone and layer tilt angles were assumed to be coupled and to vary with the temperature of the system. Strong surface anchoring and zero cone angles at the surfaces were assumed and shear was modelled through its effect on the cone angle.

For a temperature where the chevron had the lowest energy structure for zero shear, as the system was sheared, the chevron continuously deformed into a tilted layer structure via an asymmetric chevron as shown in Fig. 2.3.

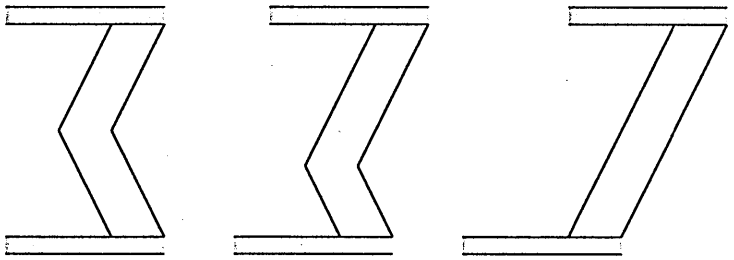

Figure 2.3: Formation of a tilted layer structure by shearing a chevron structure.

The lower the temperature, the larger the energy difference between the higher energy chevron and lower energy tilted layer structure. As a result, for low temperatures, the system was predicted either to exert a shear force on the surface or, if the layers were free to move across the surface, to form a tilted layer structure.

Chapter 3

Computer Simulation

3.1 Introduction

Simulation of liquid crystals can be compared with a simple input–process–output model of computation. The input is generally the model of a molecule which defines its interactions with other molecules or the model of a small volume which defines its interaction with surrounding volumes. The process is the simulation method used to generate, from the model, samples representative of a bulk system or to evolve a bulk system through time. The output is generally the bulk properties of the system revealed by analysis of the samples.

Models are typically not meant to be fully realistic representations of particular molecules but are considered to be theoretical approximations of true molecules. These are designed either to recreate the important features found in real systems or to explore purely theoretical features not found in real systems. Simulating theoretical molecules deliberately missing some features of real molecules can reveal which features are important in producing bulk behaviour. Analysis of simulation data to calculate bulk material properties corresponds to using experimental tech-

niques to study real liquids. This gives simulation a role in both the development of theories and the interpretation of experiments and provides a link between theory and experiment.

If the goal of a theory is to link molecular properties with bulk material properties, a system of the theoretical molecules can be simulated and the bulk properties measured to test the theory. Experiments often reveal information about the behaviour of a system, without having the spatial or time resolution to determine the exact mechanism responsible. A simulation which records the positions of individual molecules can offer insight into possible mechanisms and suggest further experiments to confirm this.

3.2 Methods

3.2.1 Classical Dynamics

For models in which the motion of electrons has been averaged out, an assumption can be made that the classical description of the system is adequate [35]. The Hamiltonian $\mathcal{H}$ of the system can be expressed as a function of nuclear variables giving the sum of kinetic $\mathcal{K}$ and potential $\mathcal{U}$ energy functions of theses variables.

For a system of N molecules, let $\mathbf{q}$ be the set of particle coordinates $\mathbf{q}_i$ where $1 \leq i \leq N$ and let $\mathbf{p}$ be the corresponding momenta $\mathbf{p}_i$. This gives,

$$\mathcal{H}(\mathbf{q}, \mathbf{p}) = \mathcal{K}(\mathbf{p}) + \mathcal{U}(\mathbf{q})$$

An equation of motion which describes the entire time evolution of the system can now be constructed [36].

Statistical mechanics provides the means by which to measure the thermodynamic properties of the system. Taking a statistical perspective of the system's

evolution allows consideration of simulation methods other than the classical dynamics approach.

3.2.2 Statistical Ensembles

Measuring System Properties

The thermodynamic state of a system is defined by a small set of parameters such as its pressure and temperature. If the state is well defined, all other thermodynamic properties can be derived from the known parameters. In an experiment, some of these parameters are controlled, to set the conditions for the experiment, and others are measured. The properties of the system which are controlled define the statistical mechanical ensemble in which the experiment is being carried out.

In a system of atoms, the instantaneous positions and momenta can be considered to be a point in the phase space defined by all possible positions and momenta for those atoms. The instantaneous value of some system property, such as energy, is a function of the positions and momenta, so the system property is a function of the location in phase space of the system. To conduct a simulated experiment, the assumption is made that the experimentally observable property in a real system corresponds to the time average of this property over a long time. In a real system, phase space is taken to be continuous and averages are found through phase space integrals. In a computer simulation, positions and momenta are stored to finite precision so phase space is discrete and averages can only be found by summing over points.

Although a real system evolves through time, the averaging process means that measuring one system over a long time is equivalent to taking an instantaneous measurement of a large number of systems, so long as the points are obtained

by sampling the regions of phase space corresponding to the correct ensemble. A generalised simulation method would be able to generate sample points from the phase space of the system and take a weighted average of the properties of interest, each weight being derived from the probability that the sample point belongs to the required ensemble. The convention is to name ensembles using the properties which are held constant, such as total energy E, number of atoms N, temperature T, volume V or pressure P. Common ensembles are the micro canonical constant-NVE ensemble, the canonical constant-NVT ensemble and the isothermal-isobaric constant-NPT ensemble.

Sampling Phase Space

One way of generating samples for a system would be to choose random atomic positions and momenta. However, this would lead to overlaps in almost all cases, and therefore the probability of generating representative samples from the required ensemble would be close to zero. A more efficient approach is to take a starting point in phase space, and to generate from this another point by making some change to the system. This can be used to create a sequence of points, evolving the system through phase space rather than through time.

An ideal method would produce an ergodic system which visited all possible points. During a simulation, in practice it is only possible to sample a limited set of points, so these must be representative of the whole. Unrepresentative samples can be generated if the system is prevented, by a barrier, from exploring some region of phase space or travels around a closed circuit containing only a small number of points. There is no sure way of preventing this, but standard checks for such behaviour include comparing simulations started from different points and

running some simulations for longer to check for barriers.

The method used to generate points does not have to be physically realistic and can be deterministic or stochastic or a combination of both, as long as certain conditions are met:

- The probability of a point belonging to the required ensemble should not change as phase space is explored,
- It should produce a series of points whose probability tends toward this stationary value if not at that value initially,
- The system should be 'effectively ergodic'.

3.2.3 Monte Carlo Methods

Monte Carlo (MC) simulation methods sample phase space by making random changes to a system. Typically, the changes are small, such as randomly displacing an atom. Each new system is then accepted or rejected using a criterion based on the probability that it belongs to the required ensemble. The method can determine the static properties of a system at a given state point but not the dynamic behaviour. The set of systems generated is a representative sample characteristic of the state point rather than a sequence giving evolution of a single system over time.

3.2.4 Molecular Dynamics

Molecular dynamics (MD) solves Newton's equation of motion for a system of molecules. The assumption is made that translational and rotational motion can

be considered separately. Typically, an integrator of the type adopted by Verlet is used to advance the system by a small timestep δt [35].

In a typical Verlet scheme, first the molecular positions and orientations are used to calculate the forces $\mathbf{F}$ responsible for translational and rotational motion given by

$$\mathbf{F} = -\nabla U \tag{3.1}$$

where U is the intermolecular potential. The accelerations are then calculated and used to update the translational and angular velocities and hence the positions and orientations.

Two common variants of the scheme are the Verlet leapfrog algorithm and the velocity Verlet algorithm. The Verlet leapfrog algorithm stores the velocities out of step with the positions, on each step advancing the velocities from $t - \frac{1}{2}\delta t$ to $t + \frac{1}{2}\delta t$. The velocity Verlet algorithm stores positions and velocities on the same timestep and minimises roundoff error.

Although not as accurate in the short term as more traditional numerical integration methods such as the Runge-Kutta method, such algorithms have proved to be more stable in the long term and so are more suitable to molecular dynamics where a system is advanced over many timesteps.

In its simplest form the molecular dynamics method conserves energy and thus samples the NVE ensemble. With modifications to the equations of motion, other ensembles can be generated. A simple method of generating samples from the constant temperature NVT ensemble is velocity rescaling. To achieve an average required temperature T, the translational and angular velocities are scaled on each step by a factor $\sqrt{T/T_m}$, where T_m is the measured temperature in the simulation.

3.3 Models

3.3.1 Modelling the Atom

A first-principles approach is the *ab initio* method which attempts to model the full quantum-mechanical detail of a system of electrons and nuclei, solving the Schrödinger equation for the electrons [37]. Determination of the interaction energy by this method is computationally intensive and is limited to molecular scale studies such as adsorption of a molecule on a surface.

Typically, when studying bulk properties of a system, an idealised interaction potential is used which models the van der Waals forces of attraction and repulsion between atoms. This usually has the characteristics of a long-range weakly attractive tail, a negative well and a strongly repulsive region at short range. For the long-range attractive forces, the energy of interaction behaves as some inverse power of the separation r. For the short-range repulsive forces, the energy increases exponentially with decreasing r.

The potential energy of a system involves terms depending on the positions of single atoms, interactions between pairs, interactions between triples and so on. The pairwise contributions are the most significant, but the three body potentials are also known to be important at liquid densities. Calculating the three body and higher terms would take up most of the time in a simulation so, to avoid this, the assumption is often made that the average effect of the higher terms can be implicitly included in the pair-wise interactions. This makes the two body term an 'effective' pair-potential representing the effect of all interactions in the system.

A common model of the potential between two atoms is the Lennard-Jones 12-6 pair potential shown in Fig.3.1. The exponential repulsive term is replaced

by a computationally more efficient r^{-12} term giving

$$U(r) = 4\epsilon\left[\left(\frac{\sigma}{r}\right)^{12} - \left(\frac{\sigma}{r}\right)^{6}\right]. \tag{3.2}$$

It is parameterised to model a particular atom through the range constant σ and well-depth constant ϵ. The range constant sets the 'size' of the atom such that two atoms can be said to touch when the separation between their centres equals σ. The well-depth constant ϵ sets the minimum of the potential well.

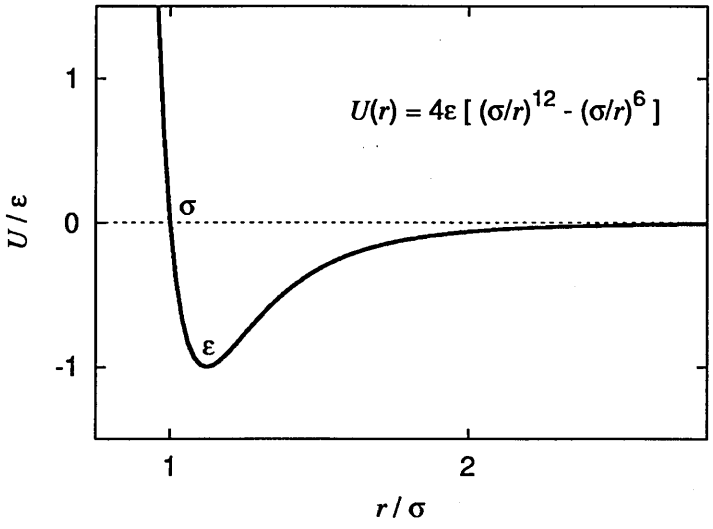

Figure 3.1: Lennard-Jones 12-6 effective pair potential.

The interaction between a Lennard-Jones 12-6 atom and a generic continuum surface can be modelled by taking the half-space integral $\int_{z_0}^{\infty}\int_{-\infty}^{\infty}\int_{-\infty}^{\infty} U/\sigma^3\, dx\, dy\, dz$, of the atom-atom potential, where the wall is at z_0 and parallel to the xy plane. This gives an atom-surface potential of the form

$$U_s(z) = \frac{2}{3}\pi\epsilon\left[\frac{2}{15}\left(\frac{\sigma}{z-z_0}\right)^{9} - \left(\frac{\sigma}{z-z_0}\right)^{3}\right]. \tag{3.3}$$

3.3.2 Multisite Molecular Models

The motive for using atomistic representations of molecules in the simulation of liquid crystals is the fact that stiffness of the core and flexibility of the tail are known to play a role in bulk phase behaviour. Modelling molecules at an atomistic scale involves including intramolecular potential terms as well as intermolecular terms [38]. Typically, bond stretching, bending and torsional potential terms are included in the model of the molecule. Hydrogen atoms are often not included explicitly but accounted for in a united-atom model of the atom to which they attach.

The two main techniques applied to atomistic models are molecular mechanics and molecular dynamics [39]. Molecular mechanics techniques perform conformational searches on individual molecules by repeatedly adjusting molecular coordinates to find the lowest energy structures. In MD simulations, a small timestep is needed, as the intramolecular motions are fast compared with the motion of molecule as a whole. Accessible timescales are typically long enough for the assessment of phase stability but restrict the study of larger scale phenomena such as bulk phase transitions. Studies are generally limited to a few hundred molecules so that small system size effects can have a large influence on the bulk behaviour.

Molecular models can also be used to generate accurate information on interactions between molecules, which can then be used to fit the parameters of simpler, more computationally efficient models.

Energy minimisation and MD simulations of united-atom models of 8CB monolayers on graphite substrates have found registration between molecules and the underlying graphite lattice consistent with STM studies [40, 41]. MD simulations of 8CB on graphite [42] have also shown that a planar probe which restricts out

of plane motion of the molecules can stabilise the structure of the monolayer, suggesting the presence of the tip in STM studies could influence the surface order.

McBride *et al.* [43] performed a bulk MD simulation of united-atom models of the liquid crystal 5.5-BBCO. In a system of 125 molecules in the isotropic phase, a nematic phase formed as the system was cooled.

Binger and Hanna [44] used MD and molecular mechanics to study alignment of 5CB and 8CB molecules on various crystalline polymeric substrates and on graphite. Each substrate was modelled by atoms fixed in position so that the crystalline polymer structures effectively corrugated the surface at a molecular level. For the polymer substrates, alignment was observed along the corrugations. The order induced in the molecules nearest the surface was close to crystalline, as found in STM studies of 8CB on graphite. Substrates which produced effectively deeper corrugations gave rise to the highest surface order. However, the graphite substrate did not show any preferential alignment, in disagreement with STM studies and results in [40, 41, 42].

The same authors also studied the use of atomistic molecular models with pseudopotentials to represent the surface, in order to reduce the computational effort required when studying the influence of a generic corrugated surface [45]. The surface model was a Lennard-Jones half-space 9-3 type potential in which either the range or the well-depth was modulated across the surface by a term $1+\cos(2\pi x/\lambda)$, where x is the x-coordinate of an atom, λ is the wavelength of the corrugation and the surface is parallel to the xy-plane. The well-depth-modulated case represented a smooth surface with periodic potential wells, whereas the range-modulated case incorporated steric corrugations due to surface topography. The parameters of the surface potential were fitted to an atomistic representation of a

crystalline polymer surface.

An amplitude term $E/2$ was included in the well-depth modulation. For a united atom model of 8CB, with $E = 0$, no preferential alignment was observed. An amplitude of $E = 1$ produced preferential alignment parallel to the corrugations. Values $E = 2$ and $E = 3$ produced strong alignment where molecules rarely moved from their preferred orientations.

The range-modulated results produced a lesser degree of alignment. This was thought to be due to the range-modulated potential producing effectively shallower corrugations than the well-depth-modulated potential.

3.3.3 Gay-Berne Single Site Model

An approach often adopted to make a mesogenic model which is more computationally efficient is to introduce anisotropy into a single-site model. Such an intermolecular potential was proposed by Corner [46] in the form,

$$U = \epsilon f\left(\frac{r}{\sigma}\right), \tag{3.4}$$

where f is some function of the distance between the molecular centres r. Unlike a model of an atom, where the well-depth parameter ϵ and the range parameter σ are constants, here they are both functions of the orientations of the two molecules and the intermolecular vector.

Berne and Pechukas [47] derived forms for ϵ and σ by evaluating the overlap of two approximately ellipsoidal Gaussian distributions representing electron clouds. These were used by Kushick and Berne with the function f in the form of a Lennard-Jones 12-6 potential and σ set to give a length to width ratio of 3 [48]. No stable nematic phase was found, and subsequent analysis showed that the model contains unrealistic features. In a model using four Lennard-Jones atoms

in a line, spaced to give length to width ratio of 3, the side-by-side well depth is about five times greater than the end-to-end well depth. In the Kushick and Berne model, however, the end-to-end and side-by-side orientations have equal potential well depths and also the well width varies with orientation.

To remedy these shortcomings, Gay and Berne introduced a shifted form for the function f and an anisotropic well-depth function [49]. For two particles i and j with centres defined by particle position vectors $\mathbf{r}_i$ and $\mathbf{r}_j$ and orientations defined by unit vectors $\mathbf{u}_i$ and $\mathbf{u}_j$, the Gay-Berne intermolecular potential is given by

$$U(\mathbf{r},\mathbf{u}_i,\mathbf{u}_j) = 4\epsilon(\mathbf{r},\mathbf{u}_i,\mathbf{u}_j)\left[\left(\frac{\sigma_0}{r-\sigma(\hat{\mathbf{r}},\mathbf{u}_i,\mathbf{u}_j)+\sigma_0}\right)^{12} - \left(\frac{\sigma_0}{r-\sigma(\hat{\mathbf{r}},\mathbf{u}_i,\mathbf{u}_j)+\sigma_0}\right)^{6}\right], \tag{3.5}$$

where $\mathbf{r} = \mathbf{r}_i$ - $\mathbf{r}_j$, $r = |\mathbf{r}|$ and $\hat{\mathbf{r}} = \mathbf{r}/r$. The well-depth anisotropy function ϵ is given by

$$\epsilon(\mathbf{r},\mathbf{u}_i,\mathbf{u}_j) = \epsilon_0\epsilon_1^{\nu}\epsilon_2^{\mu} \tag{3.6}$$

where

$$\epsilon_1(\mathbf{u}_i,\mathbf{u}_j) = \left[1-\chi^2(\mathbf{u}_i.\mathbf{u}_j)^2\right]^{-\frac{1}{2}} \tag{3.7}$$

and

$$\epsilon_2(\mathbf{r},\mathbf{u}_i,\mathbf{u}_j) = 1 - \frac{1}{2}\chi'\left[\frac{(\hat{\mathbf{r}}.\mathbf{u}_i+\hat{\mathbf{r}}.\mathbf{u}_j)^2}{1+\chi'(\mathbf{u}_i.\mathbf{u}_j)} + \frac{(\hat{\mathbf{r}}.\mathbf{u}_i-\hat{\mathbf{r}}.\mathbf{u}_j)^2}{1-\chi'(\mathbf{u}_i.\mathbf{u}_j)}\right]. \tag{3.8}$$

The well-depth anisotropy is controlled by parameter χ' given by

$$\chi' = \frac{\kappa'^{\frac{1}{\mu}}-1}{\kappa'^{\frac{1}{\mu}}+1}, \tag{3.9}$$

where $\kappa' = \epsilon_{ss}/\epsilon_{ee}$ and represents the the ratio of side-by-side and end-to-end well depths. The shape function σ is given by

$$\sigma(\hat{\mathbf{r}},\mathbf{u}_i,\mathbf{u}_j) = \sigma_0\left[1-\frac{1}{2}\chi\left[\frac{(\hat{\mathbf{r}}.\mathbf{u}_i+\hat{\mathbf{r}}.\mathbf{u}_j)^2}{1+\chi(\mathbf{u}_i.\mathbf{u}_j)} + \frac{(\hat{\mathbf{r}}.\mathbf{u}_i-\hat{\mathbf{r}}.\mathbf{u}_j)^2}{1-\chi(\mathbf{u}_i.\mathbf{u}_j)}\right]\right]^{-\frac{1}{2}} \tag{3.10}$$

and the shape anisotropy is controlled by the parameter χ given by

$$\chi = \frac{\kappa^2 - 1}{\kappa^2 + 1} \tag{3.11}$$

where $\kappa = \sigma_{ee}/\sigma_{ss}$ and represents the ratio of the end-to-end and side-by-side range parameters.

The constants ϵ_0 and σ_0 correspond to the constants ϵ and σ in the Lennard-Jones 12-6 model; if the anisotropy parameters are set to $\chi = \chi' = 1$ the Gay-Berne model reduces to the Lennard-Jones model. The constants ν and μ can be adjusted to 'fit' the desired well characteristics. Values of $\nu = 1$ and $\mu = 2$ produce a function equivalent to the four-site Lennard-Jones model, with $\kappa = 3$ and $\kappa' = 5$. The potential for two parallel particles with this parameterisation is shown in Fig. 3.2.a.

Different configurations show deviation of the shape function from a true ellipsoid as the particles effectively change shape as a function of relative orientation. Fig. 3.2.b shows the potential as a function of separation for the side-side, end-end, cross and T configurations. With $\kappa = 3$, the side-side and end-end configurations give $\sigma = \sigma_0$ and $\sigma = 3\sigma_0$ respectively but the T configuration gives $\sigma = \sqrt{5}\sigma_0$ rather than the $\sigma = 2\sigma_0$ as would be the case for a constant shape.

The Gay-Berne model has proved successful in simulating most of the main bulk liquid crystal phases. Adams *et al.* [50] performed MD simulations of a 256 particle system with the original Gay-Berne GB35 parameters $\kappa = 3$, $\kappa' = 5$, $\nu = 1$ and $\mu = 2$, and found isotropic and nematic phases. Luckhurst *et al.* [51] performed similar simulations but with the parameters $\nu = 2$ and $\mu = 1$, which has the effect of deepening the side-side well-depth, and was expected to stabilise mesophases. The system was slowly cooled and exhibited isotropic, nematic, S_A, S_B and crystal phases. For the smectic phases, the layer normal aligned along

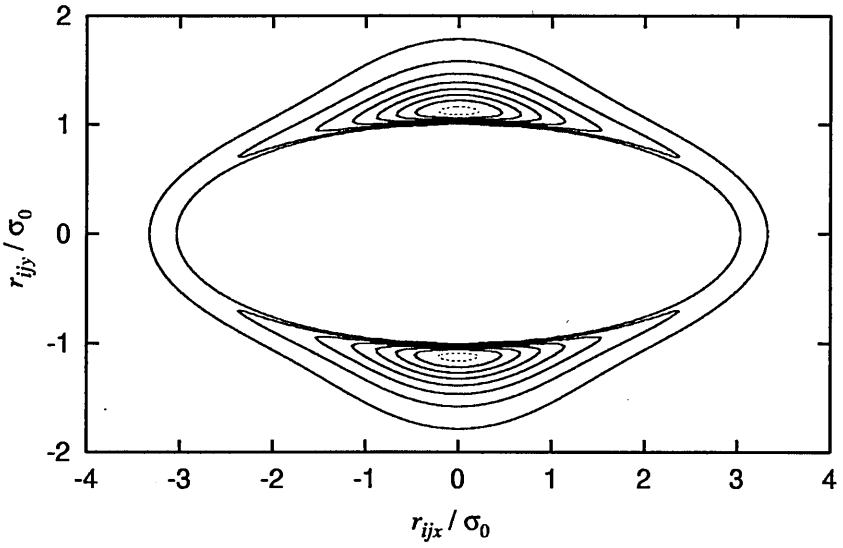

a

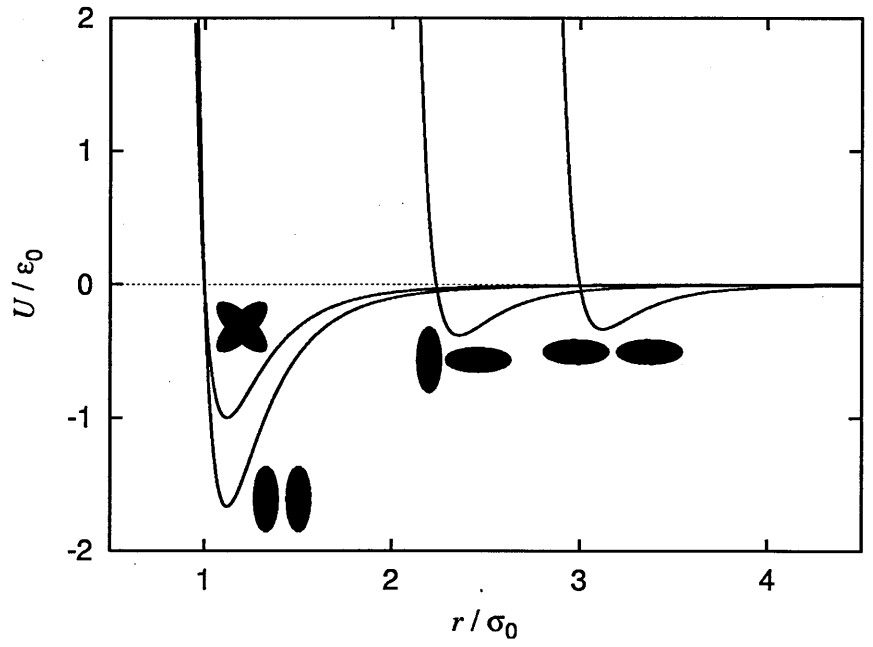

b

Figure 3.2: Gay-Berne intermolecular potential with $\nu = 1$, $\mu = 2$, $\kappa = 3$, and $\kappa' = 5$: (a) Illustration of well-depth contours for parallel particles. (b) Potential for side-side, end-end, cross and T configurations.

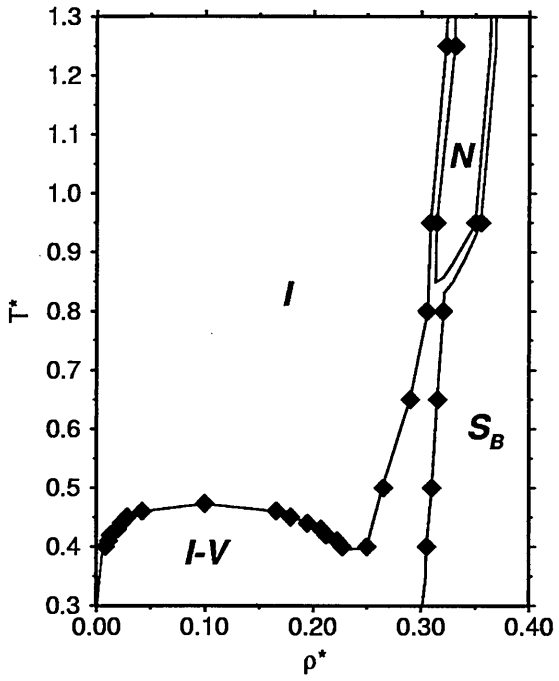

Figure 3.3: Temperature-density phase diagram of the Gay-Berne model with $\kappa = 3$, $\kappa' = 5$, $\nu = 1$ and $\mu = 2$ [54].

main diagonal of the cubic simulation box. The layer spacing was $\approx 2.6\sigma_0$.

A series of studies of the GB35 model by de Miguel *et al.* [52, 53, 54] used MC and MD simulations to examine liquid-vapour coexistence, nematic-isotropic transition and vapour, isotropic, nematic and S_B phases. Combining these results allowed the phase diagram for the GB35 model to be plotted. This is shown in Fig. 3.3. In addition, MD simulations on a GB35 model with no attractive part produced a nematic phase which remained nematic even at high densities. The authors suggest that, for this elongation, the formation of the S_B phase is controlled more by attractive forces than by shape.

Chalam *et al.* [55] further enhanced the GB35 phase diagram, defining more clearly the nematic and S_B regions, and also investigated system size effects on

phase transitions. Simulations of systems of size 256, 500 and 864 particles revealed that reducing the system size lowers the density at which the nematic-isotropic transition occurs.

Berardi *et al.* [56] performed MC simulations using the parameters $\kappa = 3$, $\kappa' = 5$, $\nu = 3$ and $\mu = 1$. This parameterisation enhances the side-side and end-end interactions and destabilises the T configuration. Isotropic, nematic and S_B phases were produced but compared to the $\nu = 1$, $\mu = 2$ parameterisation, the nematic phase was more stable, occurring at higher temperatures.

The effect of system size on the GB35 nematic-isotropic transition was further studied by de Miguel [57]. MD simulations on systems of size 256, 500 and 864 showed that the transition shifts to higher densities and weakens as N increases. The measured density (or volume) change at the transition was found to be $\approx 2.0\%$ whereas a typical experimentally observed density change is $\approx 0.5\%$.

An attempt to 'fit' the GB potential to a real molecule was made by Luckhurst and Simmonds [58]. Here, the parameterisation was derived from a multi-site model of *p*-terphenyl as an example of a typical mesogen. This gave values of $\nu = 0.74$, $\mu = 0.8$, $\kappa = 4.4$ and $\kappa' = 39.6$. Even though this value of κ' is almost 8 times larger than the 'standard' value, the results obtained were similar to those of previous bulk simulations. MD simulations on a system of 256 particles produced isotropic, nematic and S_A phases. The structure of the isotropic and nematic phases was dominated by short range repulsive forces. The stability of S_A phase was critically dependant, however, on the anisotropy in the attractive forces.

Hashim *et al.* [59] studied the S_B phase of the GB35 model using NPT Monte Carlo simulations where the simulation box dimensions were allowed to vary so that the periodicity imposed on the system by the periodic boundary conditions

was able to become commensurate with the periodicity of the layer structure which formed within the box. The planes of the layers and the layer normal aligned with the sides of the box. The orientational order parameter S was 0.9 and the layer spacing d_s, measured from period of the density wave parallel to the director, was $\approx 2.6\sigma_0$ The layer spacing was found to vary with temperature from $d_s \approx 2.64\sigma_0$ at T=0.6 to $d_s \approx 2.57\sigma_0$ at T=0.4. This was due to increased interdigitation.

The effects on bulk phase transitions of varying κ' with constant $\kappa = 3$ was studied by de Miguel *et al.* [60]. Using NVT MD, various systems with values of $1 \leq \kappa' \leq 25$ were compressed systems at a range of temperatures. The authors found that smectic order occurred at lower densities as κ' was increased, and that as κ' was decreased, the nematic phase became increasingly stable at lower temperatures.

The same authors also studied [61] the effects of varying κ with constant $\kappa' = 5$. Using bulk MD and MC with $3 \leq \kappa \leq 4$, it was found that, the liquid-vapour critical point moved to lower temperatures when κ was increased, and the isotropic-nematic transition moved to lower density and pressure at a given temperature. There was also a growth of a stable S_A range with $\kappa > 3.0$, but varying κ did not dramatically vary the lowest temperature at which the nematic phase was stable. For $\kappa > 3$ no S_B-crystal transition was identified and the authors suggested that for this parameterisation, the S_B and crystal are indistinguishable.

Bates and Luckhurst [62] used NPT MC to study a large system of 16,000 particles with a realistic parameterisation of $\kappa = 4.4$, $\kappa' = 20$, $\nu = 1$ and $\mu = 1$, based on that used in [58]. Nematic and S_A phases were observed. The layer spacing d_s was found by maximising the positional order parameter with respect to d_s, the positional order being calculated using the method described in Section 3.6.2.

Only a small change was found over a large temperature range. At T=1.45, at the nematic-S_A transition, $d_s \approx 3.9\sigma_0$. At T=1.3, $d_s \approx 3.85\sigma_0$.

Although no S_C phase has been observed by varying the parameters of the Gay-Berne model, S_C phases can be formed by the addition of quadrupole terms. Neal and Parker [63] performed MD simulations of Gay-Berne particles with longitudinal linear quadrupoles and observed S_A, S_B, S_C and crystal phases. The maximum tilt in the S_C phase was 17.2° which is comparable with experimental measurements.

Estimates have been made of the splay k_{11}, twist k_{22} and bend k_{33} elastic constants of the GB35 model in the nematic phase. Stelzer *et al.* [64] used NPT MD to study a 405 particle system at various temperatures and densities. Elastic constants were estimated by considering their role in the orientational distribution function and the pair orientational correlation function. At a density $\rho = 0.33$ and temperature T=1.0, values of $k_{11} \approx 2.7$, $k_{22} \approx 2.5$ and $k_{33} \approx 3.1$ were obtained.

Allen *et al.* [65] used MD with an 8000 particle system to estimate the elastic constants by relating them to orientational fluctuations. This required a fixed director so the equations of motion were rewritten to constrain the director to a fixed orientation. At $\rho = 0.33$ and T=1.0, values of $k_{11} \approx 0.7$, $k_{22} \approx 0.72$ and $k_{33} \approx 2.43$ were calculated. The authors suggested that the reason for the difference between these values and the equivalent values in [64] was the effect on macroscopic behaviour of the small system size in [64].

Estimates have also been made for the viscosity coefficients for the GB35 nematic. Smondyrev *et al.* [66] performed NVT MD on a 256 particle system over a range of temperatures. Values for the Miesowicz viscosity coefficients η_1, η_2 and η_3 and a rotational viscosity γ_1 were calculated from correlation functions

of the director. For this, the director needed to be stationary during the run. An applied field was used to stabilise the director. At $\rho = 0.345$ and T=1.25, values of $\eta_1 \approx 2.5$, $\eta_2 \approx 12$, $\eta_3 \approx 3.1$ and $\gamma_1 \approx 10$ were calculated.

Cozzini *et al.* [67] performed MD simulations on a 500 particle system. To avoid possible effects on the bulk behaviour of constraining the director, an intrinsic frame was defined, which moved along with the director at each timestep. At $\rho = 0.345$ and T=1.25, values of $\eta_1 \approx 0.2$, $\eta_2 \approx 14.3$, $\eta_3 \approx 3.3$ and $\gamma_1 \approx 5.6$ were calculated. The authors attributed the differences between these values and the equivalent values in [66] to the smaller system size and shorter run lengths used in [66].

Both of these studies, nevertheless, showed the expected characteristics of a nematic: the coefficient corresponding to a director parallel to the flow velocity gradient, η_2, is significantly greater than that corresponding to a director parallel to the flow, η_1.

The Gay-Berne potential was extended by Cleaver *et al.* to account for interactions between uniaxial or biaxial particles with different shapes, such as rod-disk interactions [68]. Such generalised Gay-Berne potentials have been used in hybrid models of liquid crystal molecules, where the flexible sections of the molecule are modelled on an atomistic level, but the rigid sections are represented by Gay-Berne particles. These models allow simulations of larger system sizes than purely atomistic molecular models enabling studies such as the relationship between bulk phase changes and conformational changes.

Wilson [69] used MD to study a hybrid model of a liquid crystal dimer comprising two mesogenic Gay-Berne units, linked by a Lennard-Jones united-atom model of flexible alkyl chain. In a 512 molecule system, isotropic, and S_A phases

were observed.

McBride and Wilson [70] performed MD simulations with a hybrid model of a liquid crystal molecule consisting of a Gay-Berne core with a flexible alkyl chain of united-atom Lennard-Jones units on each end. Isotropic, nematic and S_B phases were formed, with large conformational changes accompanying phase transitions.

Chalam *et al.* [55] performed MD simulations of the GB35 model confined between surfaces promoting alignment normal to the surfaces. The particle-surface potential did not account for the shape of the particle and was separable into a translational part, based on a 9-3 atom-surface potential, and an orientational part, which scaled the potential based on the angle between the particle long axis and the surface normal. The authors found that in a system of 800 particles with a surface separation of $30\sigma_0$, confinement shifted the isotropic-nematic transition to higher temperatures and lower densities, thus stabilising the nematic phase.

Zhang *et al.* [71] studied the effects on the GB35 nematic model of substrate alignment. The substrate was modelled by a modified 9-3 continuum wall, where the range and well-depth parameters were functions of the angle between the particle long axis and the surface normal, chosen to represent the interaction between a Gay-Berne ellipsoid and a sphere. The effect of a rubbed-surface was modelled by the addition of an azimuthal alignment term which deepened the well-depth as the angle between the particle long axis and a surface easy-axis vector reduced. This rubbed surface term was only applied to particles less than $1.5\sigma_0$ from the surfaces, thus creating a discontinuity in the surface potential. Using MC simulations, the authors found a pre-tilt of the adsorbed monolayer of $\approx 20°$ relative to the surface. This was reduced if the intermolecular interactions for the surface particles were weakened. This suggests that the pre-tilt mechanism

involves both particle-surface and particle-particle interactions, and their relative strengths. The surface pre-tilt imposed a similar tilt on the bulk director, but in regions of around $1\sigma_0$ between the surface monolayers and the bulk, the tilt increased to around 40–50°.

A continuum wall with some surface structure was used by Stelzer *et al.* [72] to study surface induced ordering of GB35 nematics in an NVT MD simulation with 810 particles. Surface structure was created by sinusoidally modulating the surface height in the x and in the y directions. In a system of 810 particles with a surface separation $\approx 33\sigma_0$, the authors reported finding S_C layering of particles in contact with the surface and strong director distortions close to the surface. However, certain factors raise doubts about the details of the results. A 12-6 form was used for the surface potential rather than a 9-3 form, and the position and orientation terms were separable, making the minimum of the potential independent of the orientation. The initial configuration was taken from a bulk system with full periodic boundaries. The surfaces were instantaneously imposed on this bulk system, which was then equilibrated for only a short time.

A system confined by smooth continuum surfaces was studied by Wall and Cleaver [73]. A small system of 256 GB35 particles with a surface separation of $13\sigma_0$ and number density $\rho = 0.3$ was simulated using NVT MD. A non-separable surface-particle potential was used, representing a half-space integral of a Gay-Berne model with one particle reduced to a sphere. The form was derived by analogy with the half-space integral of the Lennard Jones 12-6 potential, giving

$$U_{sp} = \alpha\epsilon_{sp}\left[\frac{9}{10(1-\chi^2)^\nu}\right]^{\frac{1}{2}}\left[\frac{2}{15}\left(\frac{\sigma_0}{z+\sigma_0-\sigma_{sp}}\right)^9 - \left(\frac{\sigma_0}{z+\sigma_0-\sigma_{sp}}\right)^3\right], \quad (3.12)$$

with shape parameter

$$\sigma_{sp} = \sigma_0\left[\frac{1}{1-\chi\cos^2\theta}\right]^{\frac{1}{2}}, \quad (3.13)$$

and well-depth function

$$\epsilon_{sp} = \epsilon_0(1 - \chi' \cos^2\theta)^\mu, \tag{3.14}$$

where α is a surface-particle coupling strength parameter and θ is the angle with the surface normal. Two values of α were used, weak coupling with $\alpha = \sqrt{10(1-\chi^2)^\nu/9}$ and moderate coupling with $\alpha = 4\sqrt{10(1-\chi^2)^\nu/9}$.

For both coupling strengths, a tilted layer formed at each surface. Layer tilt and density were only weakly affected by temperature as the system was cooled from isotropic to nematic. On further cooling, smectic layers formed in the bulk and the tilt of the surface layers changed. This change was greater in the weak coupling system, where the surface layers became almost planar, and less in the moderate coupling system, where some tilt remained. The authors suggested that this was due to positional order in the bulk inducing the tilt transition of the surface regions.

Palermo *et al.* [74] studied adsorption of the GB35 model on a graphite substrate. One surface represented the graphite lattice, the other a 'lid' on the system, comprising a portion of a bulk GB35 simulation in which particle positions and orientations had been frozen. The graphite surface model took the form of a sum of two contributions. The first was due to two layers of spherical carbon atoms modelled using the generalised Gay-Berne model from [68]. The second was a Fourier series based potential to model the remaining graphite layers. Systems where the lid gave planar alignment and where the lid gave normal alignment were studied. In both of these cases the authors found that the structure of the first two layers was not affected by the orientation of the bulk, and saw a discontinuous change in anchoring, from planar to normal, in going from the first to the second adsorbed layer on the graphite surface.

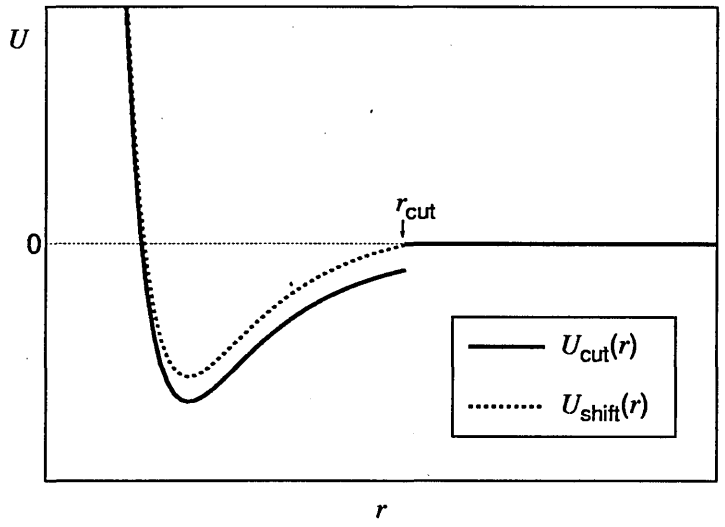

Figure 3.4: Cut and shifted potentials: Cutoff at r_{cut} produces a discontinuity which is corrected by shifting the potential by its value at r_{cut}.

The potential now becomes

$$U_{\text{shift}}(r) = \begin{cases} U(r) - U(r_{\text{cut}}), & r < r_{\text{cut}} \\ 0, & r \geq r_{\text{cut}} \end{cases} .$$

Periodic Boundary Conditions

If the small number of particles in a simulation were enclosed on all sides by surfaces, the effects on the system would make measurement of bulk properties difficult. Periodic boundary conditions enable a finite number of particles to model an effectively infinite system. However, in a system with periodic positional ordering, the period of the internal structure will be influenced by the periodicity imposed by the boundary conditions. To reduce the effects of periodicity on the system, potential cutoffs are used together with a *minimum image convention* in which each particle interacts only with the nearest of the periodic images of each other particle. Fig. 3.5 shows a system confined by surfaces in one direction with periodic boundaries in the other directions.

Latham and Cleaver [75] used the generalised Gay-Berne potential to study a confined bidisperse mixture of equal numbers of $\kappa = 3$ and $\kappa = 3.5$ particles. The surface potential was similar to that used by Wall and Cleaver [73], with the well-depth term extended to model azimuthal alignment as observed experimentally on rubbed polymer surfaces. The form of the surface potential is described in detail in Section 4.1.3. As in Ref. [73], tilted surface layers were seen. The concentration profile between the surfaces varied with temperature, with longer particles migrating to the central region on cooling. At lower temperatures, the surface alignment switched from tilted to planar.

3.4 Practical Aspects

Cut and Shifted Potentials

To find all forces acting in a system of particles, interactions between each particle and all other particles have to be considered. Intermolecular potentials typically approach zero within a few molecular lengths, therefore interactions between particles at large separations are negligible. This can be exploited by only considering, for each particle, interactions with surrounding particles located within a cutoff radius r_{cut}. This gives for the potential $U(r)$,

$$U_{\text{cut}}(r) = \begin{cases} U(r), & r < r_{\text{cut}} \\ 0, & r \geq r_{\text{cut}} \end{cases} .$$

This creates a discontinuity in the potential at r_{cut} which can be corrected by shifting the potential so that it is zero at the cutoff distance, as shown in Fig.3.4.

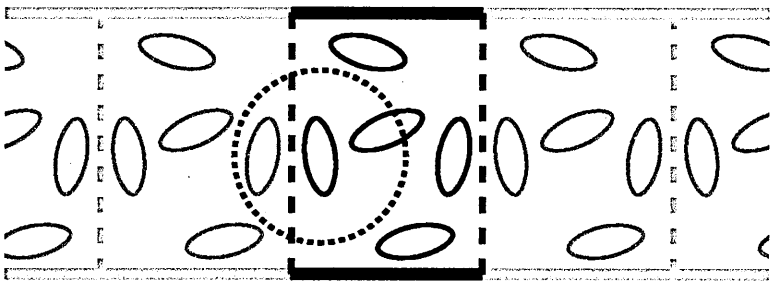

Figure 3.5: Periodic boundaries and minimum image convention: Periodic boundaries tile the box in space and each particle interacts only with other particles or their images within a cutoff radius.

Neighbour Lists

Both in MD and MC methods, the positions of particles tend to change by only a small amount on each step. When a cutoff radius is used, for each particle, the subset of particles in the system which need to be considered for interactions will often be the same for consecutive steps. This can be exploited to reduce the time needed to identify which pairs of particles need to be considered: the list of interacting sites can be stored and reused.

In the Verlet neighbour list method, for each particle, a list is constructed of neighbouring particles within a radius slightly larger than the cutoff radius. The difference in size between the cutoff and the neighbour list radii is to allow for movement of particles in and out of the cutoff radius between updates of the neighbour list. For a large number of particles, the need to store a list for each particle requires large amounts of memory. In this case a cell index method is used. The volume of the simulation box is divided into cells of side greater than the cutoff distance. Lists are made of the particles in each cell. For each particle, to identify candidates for interaction calculations, only particles in the same and neighbouring cells need be examined.

Lists can be updated at fixed intervals, large intervals being more efficient, but there is a risk of ignoring particles which may have moved together suddenly. A better method is to store the displacement of all particles in the system since the lists were last constructed. Once the largest displacement is large enough for the current lists to be invalid, the lists are reconstructed automatically.

Reduced Units

Simulations involving one type of molecule are often carried out in reduced units, where the fundamental units of system parameters such as energy and length are defined in terms of the molecular parameters. Table 3.1 lists some reduced thermodynamic variables for a system of Lennard-Jones atoms which are defined by well-depth ϵ, size σ and mass m. This can prevent duplicate simulation of equivalent systems. For example, if the density ρ for a system was changed, then at some future time the range parameter σ was changed, this could effectively recreate the original system; despite the apparently different densities, the reduced density would be the same in both cases. Computational efficiency can be improved by setting $\sigma = \epsilon = m = 1$ and so removing these parameters from the calculations where possible.

density	ρ^*	$=$	$\rho\sigma^3$
temperature	T^*	$=$	$k_{\mathrm{B}}T/\epsilon$
energy	E^*	$=$	E/ϵ
pressure	P^*	$=$	$P\sigma^3/\epsilon$
time	t^*	$=$	$t\sqrt{\epsilon/(m\sigma^2)}$

Table 3.1: Reduced units.

3.5 Parallel Molecular Dynamics

3.5.1 Parallel Processing

The aim of parallel processing is to increase the work that can be done in a given time by dividing it amongst a number of processing *nodes* which run simultaneously, each working on a different part of the problem. Typically, a parallel algorithm will involve a repeating two-step cycle of a processing step, where each node works on its part of the problem, followed by a communication step, where each node receives updated information necessary for its next processing step. This leads to two important factors which affect the efficiency of the algorithm: *load balancing* and *communication.*

The aim of load balancing is equal division of work amongst the nodes, as if one node takes more time than the others on its processing step, then all other nodes will be idle while they wait for that node to finish.

For maximum speed, the communication must be minimised, but this is not always easy. As the number of nodes increases, more work is done simultaneously but each node can be forced to communicate with more of the other nodes, so reducing the overall speed of the program. For parts of the algorithm, having each node independently calculate the same result can give an overall better performance, despite the duplication of effort, because of the reduced need for communication. Generally, only the parts of the algorithm which take the most time should be parallelised. Typically, to avoid the complications of multiple nodes trying to read from or write to the same file, one node is assigned all input/output tasks.

For a molecular dynamics algorithm, most of the time taken is spent first

calculating the forces on each particle and then integrating the equations of motion to obtain the new positions. Other parts of the algorithm take a relatively short time to complete, so the force calculations and the move calculations are the parts of the method which need to be parallelised.

There are two well established approaches to distributing an MD method across a set of nodes, *replicated data* and *domain decomposition*, each exploiting different characteristics of a system of particles.

3.5.2 Replicated-Data

Particle-Particle Interactions

In the replicated data or RD method, each node maintains a copy of the whole system of particles. In MD, forces arise from interactions between particles and these interactions are divided amongst the nodes. This can be done because the forces are assumed to be pair-wise additive. During the calculation phase, each node calculates the subset of forces in the system which arise from its allocated interactions. This is followed by a communication phase where the partial totals are summed so that each node has a complete set of forces in the system.

Load balancing is achieved by using a Brode Ahlrichs version of the Verlet neighbour list method. For a system of N particles, the total number of interactions that need to be considered is $N(N-1)/2$. In a system of N_{nodes} nodes, each node is given a number i_{node} from 0 to $N_{\text{nodes}}-1$. Each node is allocated a subset of particles i by stepping through the particle indices using N_{nodes} as a step size, and its node number as a start index as follows:

for $i = 1 + i_{\text{node}}$ to N step N_{nodes}

    allocate particle i to node i_{node}

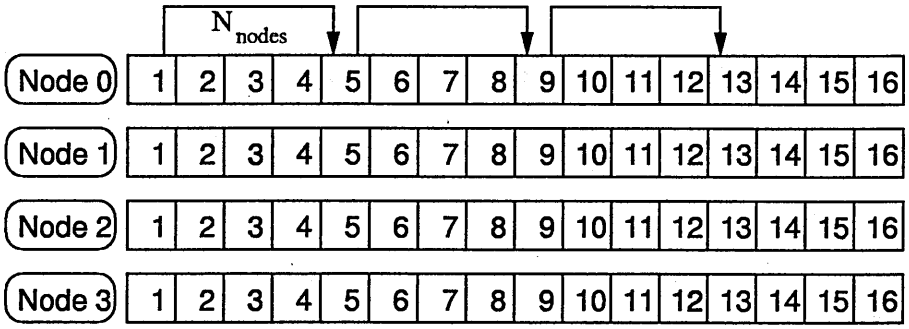

Figure 3.6: Replicated data algorithm: Allocation of particles to nodes for a system of 4 nodes and 16 particles. Each node steps through the particle indices using the number of nodes as a step size and its node number as an offset for the start position.

This is illustrated in Fig.3.6. For each particle i allocated to a node, that node considers its interactions with particles j given by

for $j = i + 1$ to $i + N_{\text{offset}}$

if $j < N$

allocate interaction (i, j)

else

allocate interaction $(i, j - N)$

where,

$$N_{\text{offset}} = \begin{cases} n & \text{if } N \text{ is odd} \\ n & \text{if } N \text{ is even and } i \leq n \\ n-1 & \text{if } N \text{ is even and } i > n \end{cases}$$

and

$$n = \text{floor}(N/2)$$

The following table shows the distribution using this method of the 28 interactions (i, j) in a system of 8 particles and and 4 nodes, each node taking 7 interactions.

node 0, $i = 1$	1,2	1,3	1,4	1,5
node 1, $i = 2$	2,3	2,4	2,5	2,6
node 2, $i = 3$	3,4	3,5	3,6	3,7
node 3, $i = 4$	4,5	4,6	4,7	4,8
node 0, $i = 5$	5,6	5,7	5,8	
node 1, $i = 6$	6,7	6,8	6,1	
node 2, $i = 7$	7,8	7,1	7,2	
node 3, $i = 8$	8,1	8,2	8,3	

Each node constructs its own Verlet neighbour list for each particle i allocated to it. For each particle i, the list contains the particles j from the corresponding interaction list which fall within the neighbour list radius.

Particle-Surface Interactions

Again, assuming interactions are pair-wise additive means that the force on a particle due to its interaction with the surface can be added to that already calculated for the bulk interactions. The same method used to initially allocate particles to nodes for the particle-particle interactions can be used to distribute the particle-surface interactions across the nodes. This gives on each node i_{node},

for $i = 1 + i_{\text{node}}$ to N step N_{nodes}

find force on particle i due to surface interaction

add force to total for particle i

Communication

Once each node has found its allocated subset of forces in the system, the nodes need to communicate to give each node a copy of all forces in the system. Even with good load balancing, no two nodes will take exactly the same time, so this communication needs to be synchronised.

Most parallel environments provide a simple way to coordinate this communication using a *global sum* operation. This is designed to find the sum of a set of vectors, each node having one vector, and give each node a copy of the final vector sum. To find the total forces in the system and give each node a copy, a global sum operation is carried out on the arrays containing the partial forces. A global sum is a *barrier* operation, which means that each node waits until all nodes have reached that point in the program, and this provides the global synchronisation.

Move Calculations

Once each node has a complete copy of the forces in the system, these can be used to update the particle positions and orientations. To distribute the work amongst the nodes, the same method initially used to allocate particles to nodes for the force calculations is implemented. First, on each node, the positions of particles not to be changed by that node are set to zero. Then, each node i_{node} updates the positions of its allocated particles using,

for $i = 1 + i_{\text{node}}$ to N step N_{nodes}

    move particle i

A global sum operation is then called on the arrays containing the positions. Since for a given particle i, on all the nodes except one, each position i is set to

zero, the sum operation just combines the updated positions into one full set of new positions, as shown in Fig. 3.7. The same procedure is used to update the orientations.

node 0		node 1		node 2		node 3		sum
p_1		0		0		0		p_1
0		p_2		0		0		p_2
0		0		p_3		0		p_3
0	+	0	+	0	+	p_4	=	p_4
p_5		0		0		0		p_5
0		p_6		0		0		p_6
0		0		p_7		0		p_7
0		0		0		p_8		p_8

Figure 3.7: Global sum operation used to combine work distributed across the nodes. Each node finds a particle property p for a subset of particles i and sets the value for other particles to zero. The results are combined by taking the vector sum across the nodes.

Replicated Data Characteristics

Each step in a RD MD algorithm can be summarised as four stages: force, communicate, move, communicate, as shown in Fig.3.8. As each step requires two global communication operations, communication is the main factor limiting the efficiency of the algorithm. Increasing the number of nodes to speed up the calculations also increases the amount of communication needed for all nodes to share information. With large numbers of nodes, this communication becomes the dominant part of the algorithm making the overall speed of the method communica-

tions bound. As the number of particles in the system increases, the amount of information each node needs to communicate increases, again reducing efficiency. As each node stores the whole system plus a neighbour list for each particle, the size of the system can also be limited by the memory available on each node rather than total amount of memory of all nodes combined.

The main technique of parallelisation in the RD MD method is to step through arrays using offsets for the start position. This is a simple technique and is easily adapted from the serial case. Thus, the RD method is simple and easy to develop, but limited to small system sizes and small numbers of nodes.

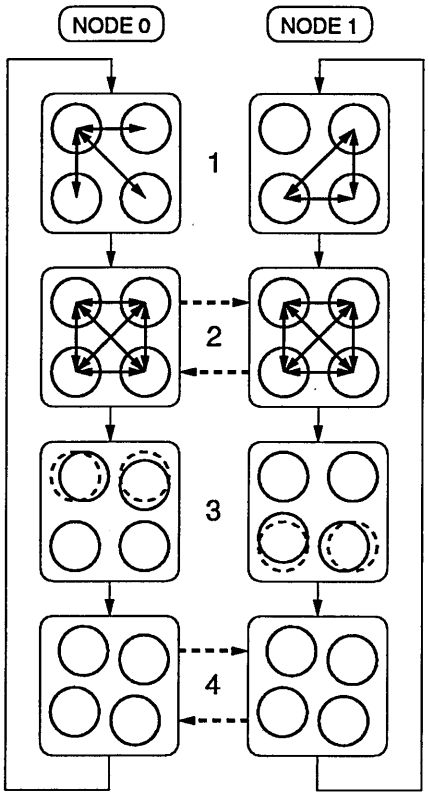

Figure 3.8: Replicated data algorithm: (1) Each node finds a subset of forces in the system. (2) Nodes communicate so each has total forces in system. (3) Each node moves a subset of particles. (4) Nodes communicate so each has updated system.

3.5.3 Domain Decomposition

Force and Move Calculations

In the domain decomposition (DD) method, the volume of the simulation box is divided into domains and each node is allocated one domain (Fig.3.9.a). Each node stores its allocated domain and, on each timestep, finds the forces on all particles within that domain. Since the particles, rather than the interactions, are spread amongst the nodes, a cell index method is used to store information on local interactions in the system.

The force calculations are the same as for the serial case, except for particles near domain boundaries. To find the force on a particle close to a boundary, a node requires the positions of particles in neighbouring domains (Fig.3.9.b), whilst taking account of periodic boundary conditions on the system as a whole. To allow this, each node also stores the positions and orientations of particles within a *halo region*, defined as the region containing particles near the boundaries in neighbouring domains, to a depth equal to the cut-off distance for the interaction potential (Fig.3.9.c). Once a node has found the forces on each of its particles, the move calculations are the same as for the serial case. Nodes use the halo region to determine the forces, but move only the particles within their own domain.

Communication

There are two stages to the communication step in the DD molecular dynamics algorithm. After each node has updated the positions of its particles, some may have moved into or out of the halo regions of neighbouring domains and some may have moved from one domain into another. Therefore, nodes must communicate to update each other's halo regions and to exchange responsibilities for particles

which have crossed domain boundaries.

For the halo regions, each node first makes a list of its particles which need to be in the halo regions of neighbouring nodes. The following sequence of messages is used on all nodes to pass the lists:

- send list to $+x$ neighbour, receive list from $-x$ neighbour
- send list to $-x$ neighbour, receive list from $+x$ neighbour
- send list to $+y$ neighbour, receive list from $-y$ neighbour
- send list to $-y$ neighbour, receive list from $+y$ neighbour
- send list to $+z$ neighbour, receive list from $-z$ neighbour
- send list to $-z$ neighbour, receive list from $+z$ neighbour

This sequence reduces communication as it avoids the need for a node to explicity pass information to nodes responsible for diagonally adjacent domains.

To exchange particles, each node makes a list of particles it has lost through each boundary. Again, the above communication sequence is used. Each node sends the list of particles it has lost through a boundary and receives a list of particles which have entered its domain through the opposite boundary. When the sequence is complete, each node updates the list of particles for which it is responsible.

Characteristics of DD

Good load balancing is achieved in DD of homogeneous systems because each domain has the same volume and so approximately the same number of particles. Each node requires only enough memory to store information about its allocated

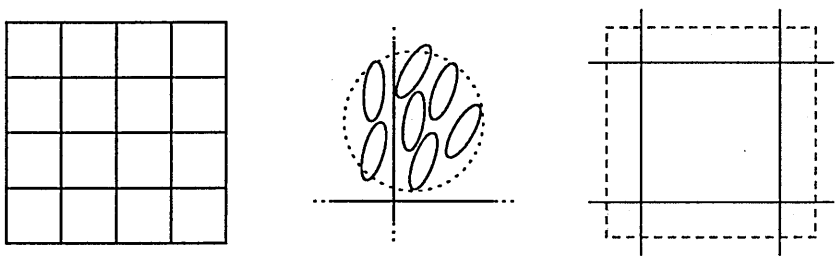

Figure 3.9: Domain decomposition: (a) System is divided into domains of equal volume and each node maintains one domain. (b) Each node needs the position of particles near the boundaries of neighbouring domains. (c) The halo region for a domain contains particles which are referenced but not moved.

domain. This means that the method is not memory limited for large systems, provided that the number of nodes is increased accordingly. The communication step only involves local communication between each node and nodes responsible for neighbouring domains. This means that the method does not become communications bound as the number of nodes is increased. However, program development using this method is difficult and error prone due to the complexity of the communication steps and the 'particle accounting' which the nodes must perform.

3.5.4 Comparison of RD and DD

Wilson *et al.* [76] studied the use of RD and DD methods for MD simulations of Gay-Berne particles on a Cray T3D. The authors found that for small system sizes of around $N < 10^3$ and 8 or less nodes, the RD method was faster. The DD method gave poor load balancing on a small system of $N = 256$ due to the differences in the number of particles in each domain. For medium size systems of $10^3 < N < 10^4$ on 16 and 32 nodes, the two methods were equally efficient. For

large systems of $N > 10^4$, DD gave a speed up which increased linearly with the number of nodes whereas RD gave no speed up with the number of nodes, as it became communications bound. The load balancing of the DD method improved with increasing system size due to the difference in the number of particles in each domain becoming smaller.

3.6 Analysis

3.6.1 Strategies

Statistics for system properties which are computationally expensive to calculate are typically accumulated during the run, especially if the parameter needs to be calculated at every step as part of the simulation algorithm. Less computationally expensive analysis is typically performed after a simulation run, using data describing the state of the system saved throughout the run.

In a Gay-Berne MD simulation, the state of the system at one timestep can be saved in a configuration file, containing the positions, orientations, translational velocities and angular velocities of each particle. In MD simulations, the state of the system changes only slightly over one timestep and so each new configuration reveals little new information when compared to that from the previous step. For this reason, configuration files are saved at intervals, typically of around 1000 steps. This also reduces the storage requirements.

In a confined system, to resolve the variation of a system property between the confining surfaces, the simulation box is divided into a number of thin regions, or 'slices', parallel to the plane of the surfaces. The property of interest is calculated independently for each slice.

3.6.2 System Parameters

Orientational Order

To calculate the orientational order parameter for a system of particles with orientation vectors $\mathbf{u}$, $S = \frac{1}{2}\langle 3\cos^2(\mathbf{u}\cdot\mathbf{n}) - 1\rangle$, defined in Section 1.4.2, the director $\mathbf{n}$ must be known. The director can be found by maximising S with respect to rotations of $\mathbf{n}$. In a system of N particles this can be reduced to diagonalising the ordering matrix

$$Q_{ab} = \frac{1}{2N}\sum_i (3u_{ai}u_{bi} - \delta_{ab}), \tag{3.15}$$

where δ is the Kronecker delta function. The largest eigenvalue corresponds to S and the associated normalised eigenvector gives $\mathbf{n}$ [77].

For a single configuration, S and $\mathbf{n}$ can be found from the Q-matrix formed by averaging over all particles in the configuration. For a run averaged value of S, the Q-matrix can be accumulated over the run. However, if the true S remains constant but the director varies throughout the run, then the order calculated from the run averaged Q-matrix will be lower than the true value. This can be avoided by first finding S and $\mathbf{n}$ for individual configurations or small blocks throughout the run. The run averaged mean and error for S can then be calculated from the individual values. The run averaged director can be determined by constructing a new Q-matrix from the individual directors throughout the run.

Positional Order

In distorted smectic phases the scalar positional order parameter S_k can be more significant than the scalar orientational order parameter S. This parameter corresponds to the amplitude of the smectic layer density wave in the complex order

parameter described in Section 1.4. In a simulation this can be calculated as

$$S_k(\mathbf{k}) = \left\langle \frac{1}{N} \left\{ \left(\sum_{i=1}^{N} \cos(\mathbf{k} \cdot \mathbf{r}_i) \right)^2 + \left(\sum_{i=1}^{N} \sin(\mathbf{k} \cdot \mathbf{r}_i) \right)^2 \right\}^{\frac{1}{2}} \right\rangle \tag{3.16}$$

where $\mathbf{k}$ is a reciprocal lattice vector and $\mathbf{r}_i$ is the position vector of particle i. For a smectic system with the layer normal parallel to the x-axis, $\mathbf{k} = (2\pi/d_s, 0, 0)$, where d_s is the layer spacing.

To use this method, both the director and the layer spacing need to be known. The director can be found along with the orientational order parameter as described in Section 3.6.2. The positional order can then be found, along with the layer spacing, by maximising, with respect to the layer spacing, the positional order in the direction of the director. A simple method of achieving this is to is to calculate S_k for a range of layer spacings and to select the largest S_k value found.

Density of a Confined System

In a simulation with fully periodic boundary conditions, the number density can be found by using the simulation box dimensions to calculate the volume of the system. In system with a confining substrate potential, the exact location of the surface, and hence the exact volume of the system, is not well defined. In this work, the density of a confined system is taken as that which would be given in a fully periodic system with the same simulation box dimensions.

To show the influence of confinement on the density profile, the normalised density is usually shown. This is the ratio of the measured density in a slice to the overall density of the system.

3.6.3 Time Resolved Data

Time-resolved profiles can be produced by calculating block averages over small block sizes. The block size is limited by the space-resolution required. The greater the number of slices the larger the block size needed to accumulate sufficient data in each slice.

If fine space-resolution is not required then parameters can be calculated for each configuration and a parameter can be tracked continuously using a moving average method. Exponential smoothing is a computationally convenient moving average method often used in times series analysis [78]. Each value in a series is given as a weighted average of itself and all previous values, with the weights decaying exponentially as values move into the past. Calculating the current smoothed value requires storage of only the current raw value and the previous smoothed value. It has a simple implementation whereby, for each data point x_i in a series, the smoothed value $\bar{x}_i$ is given by

$$\bar{x}_i = wx_i + (1 - w)\bar{x}_{i-1}, \tag{3.17}$$

where $\bar{x}_0 = x_0$. The level of smoothing is controlled by the parameter w and values of $w < 0.1$ are typically used for data with large variations. The initial raw value x_0 can have a large arbitrary effect on the first few smoothed values because it is taken as the average up to that point. This effect can be reduced by initiating the smoothing at a time point before the time of interest.

Chapter 4

Simulation of Confined Liquid Crystals

4.1 Introduction

4.1.1 Aims

The results presented in this chapter are from a series of simulations of confined and field-aligned Gay-Berne systems. The aim of these was to determine relaxation timescales of such systems and to determine whether the relaxation processes of backflow and orientational kickback could be observed within the timescales accessible.

Due to the limitations of system size, the simulation of a device-scale twisted nematic cell was not possible in this work. The system chosen for study was the simpler case of relaxation from the splay Fréedericksz geometry, as this shows the greatest induced flow of the three cases of relaxation in a field-aligned confined film.

4.1.2 Simulation Program

As part of the EPSRC funded High Performance Computing Initiative consortium 'Simulation and Statistical Mechanics of Complex Fluids', time was provided on the Cray T3E-900 at the Edinburgh Parallel Computing Centre (EPCC) in the University of Edinburgh and access was given to consortium simulation programs GBMESO and GBMEGA.

These are FORTRAN parallel MD programs designed to simulate large bulk systems of Gay-Berne particles with no confining surfaces. GBMESO uses a RD algorithm whereas GBMEGA uses DD and is designed for larger system sizes. For large systems, $N > 10^4$ particles, GBMEGA is the more efficient but for smaller system sizes of around $10^3 < N < 10^4$ particles the two programs give similar parallel speedups [76]. Since some development would be needed to introduce confining surfaces and the aim was to study smaller system sizes, the simpler replicated data GBMESO program was chosen.

The program is divided into two main sections: a platform-independent calculation section and a 'harness' which provides platform-specific and parallel functions. The force routine of the calculation section of the program was extended to include forces on particles due to particle-surface interactions. An example of the method used in this work to implement particle-surface potential models in an MD simulation is given in Appendix A.

Some development work was also done on the parallel processing sections of the program. Originally, the harness for the Cray used the PVM (Parallel Virtual Machine) library and was effectively a low-level implementation of the high-level parallel routines, such as the global sum operation, needed by the calculation routines. Development of the PVM library at the EPCC had been frozen and

work had switched to the more current MPI (Message Passing Interface) library. The MPI standard provides a library of high-level parallel procedures which can be used without knowledge of their low level implementation. On the advice of EPCC support, a new MPI harness was developed which gave a speedup of around 10-15%.

GBMESO originally used a 'leapfrog' version of the Verlet algorithm for integrating the equations of motion. This had proved stable for systems of 8000 particles but, on preliminary runs of a small 256 particle system, this gave poor energy conservation leading to the system becoming unstable after around 2×10^6 timesteps. The leapfrog version of the Verlet integrator was replaced by a more recently developed 'velocity Verlet' algorithm, which minimises roundoff errors [79], and this produced the desired long-term stability.

GBMESO uses simple velocity-scaling to control the temperature in the constant-NVT ensemble. Intermolecular potentials are cut and shifted at the cutoff distance. In all the simulations performed in this work, the Gay-Berne parameters σ_0, ϵ_0, m and the moment of inertia I are set $\sigma_0 = \epsilon_0 = m = I = 1$.

4.1.3 Surface Model

The surface potential used was that from Wall and Cleaver [73], with modifications, suggested by Latham and Cleaver [80] and later used by the same authors to study confined binary mixtures [75], to model the aligning influence of rubbed surfaces by creating an easy-axis in the plane of the surfaces. The modification is to the well-depth function, giving

$$\epsilon_{sp} = \epsilon_0 \left[(1 - \chi' \cos^2 \psi)^\mu + \chi'' \cos^2 \phi (1 - \cos^2 \theta) \right]. \tag{4.1}$$

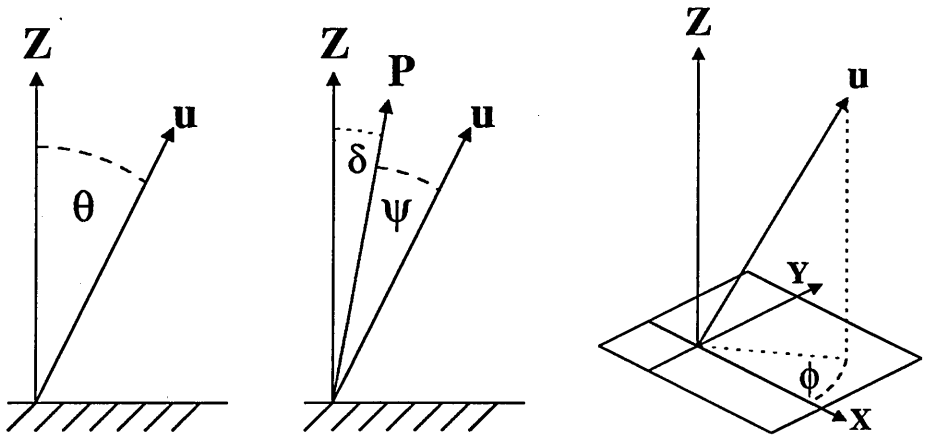

Figure 4.1: Particle-surface model angles. (a) Angle θ with surface normal $\mathbf{Z}$. (b) Angle ψ with tilted normal $\mathbf{P}$ at tilt δ. (c) Azimuthal angle ϕ with surface easy-axis $\mathbf{X}$.

Here, θ is the angle between the particle long axis and the surface normal $\mathbf{Z} = (0, 0, 1)$, as shown in Fig.4.1.a. The first term is a surface pre-tilt term, where ψ is the angle between the particle long axis and a tilted surface normal $\mathbf{P}$, tilted from the true normal by an angle δ in the azimuthal alignment direction, as shown in Fig.4.1.b. This is used to influence the sign of the tilt angle when measured relative to the surface normal, and can be used to coordinate the tilt angles on opposite surfaces.

The second term creates the azimuthal alignment, where χ'' is the azimuthal alignment strength, ϕ is the azimuthal angle between the surface easy-axis $\mathbf{X} = (1, 0, 0)$ and the particle long axis projected onto the plane of the surface, as shown in Fig.4.1.c. Here, the $\cos^2 \phi$ part deepens the well-depth in the aligning direction and the $(1 - \cos^2 \theta)$ part reduces the aligning influence as the particle tilts up away from the surface.

4.1.4 Initial Configurations

In an MD simulation, any initial particle overlaps in the system will lead to very large forces on particles, which, in turn, will produce a large movement on one timestep, leading to another large overlap.

A typical method employed to avoid this is to create an initial configuration by choosing random particle positions and orientations in a very low density, high temperature system, where overlaps can be avoided. MD is then used to slowly compress the system to the required density and then to slowly cool to the required temperature. In the large nematic and smectic systems studied in this work, this process would take more time than the simulation runs themselves.

A compromise solution was developed using a Monte-Carlo type packing algorithm which created a nematic system at the required density, with no large overlaps. The temperature of this packed configuration was then set to a temperature higher than that required by choosing random initial velocities from the Maxwell-Boltzmann distribution, generated using the Numerical Recipes pseudo-random number generator ran3 [81]. This configuration was used as the initial configuration for GBMESO and then cooled slowly to the required temperature.

4.2 Confined Unaligned System

To validate the confined Gay-Berne code, a preliminary series of simulations was performed to reproduce some of the published results obtained by Wall and Cleaver [73] for a small confined system of 256 particles. The results were obtained by slowly cooling the system in steps of 0.1 from a temperature T=2.5 in the isotropic phase, through the nematic phase, to T=0.5 in the smectic phase.

The system had a number density of $\rho = 0.3$ with the surfaces on the z ends of the simulation box at a separation of $13\sigma_0$. The same particle-surface potential as in Ref. [73] was used with an anchoring strength parameter $\alpha = \sqrt{10(1-\chi^2)^\nu/9}$ corresponding to weak anchoring. Intermolecular potential parameters were $\nu = 1$, $\mu = 2$, $\kappa = 3$ and $\kappa' = 5$, and the simulation timestep was $\delta t = 0.0015$. No potential cut-off was used for the particle-surface interactions but unlike the original work in Ref. [73], a cut-off of $3.8\sigma_0$ was used for particle-particle interactions together with a neighbour list radius of $4\sigma_0$. This cutoff is smaller than the typical cutoff of $4\sigma_0$ for Gay-Berne particles with $\kappa = 3$ because of the small dimensions of the box in the x and y directions.

The initial configuration was a face-centred cubic packing of particle centres in a cube with all orientations along the main diagonal. Initial velocities were randomly chosen to give T=2.5 and the box was gradually resized to the required dimensions over 500,000 steps. At each temperature, 500,000 equilibration steps were performed followed by 200,000 production steps. The start configuration for each temperature was taken from the final configuration at the previous temperature. Simulations were performed on 16 nodes and 500,000 steps took around 55 minutes.

Snapshots of the system at T=1.5, T=1.0 and T=0.7, corresponding to isotropic, nematic and smectic-B phases respectively, are shown in Fig. 4.2. The particle-surface potential contained no azimuthal alignment but the smectic layers aligned with the sides of the simulation box. This was due to an interplay between the periodicity of the smectic layers and the fixed periodic boundary conditions in the x and y directions.

The corresponding orientational order parameter profiles between the surfaces

a b c

Figure 4.2: Configuration snapshots of the 256 particle system confined in the z direction viewed along the y-axis with the z-axis vertical: (a) Isotropic T=1.5. (b) Nematic T=1.0. (c) Smectic-B T=0.7.

are shown in Fig. 4.3. For the nematic phase at T=1.0, the high order in the surface layers produced a ∪ shaped profile. For the S_B phase at T=0.7, the high order in the bulk does not extend into the surface region, which has similar order to that found in the nematic case. The corresponding normalised density profiles are shown in Fig. 4.4. As in Ref. [73], these show, at each surface, a well-defined surface layer and a low density trough caused by the excluded volume of the surface molecules.

In the original work in Ref. [73], two cooling runs were performed, one with weak surface anchoring $\alpha = \sqrt{10(1-\chi^2)^\nu/9}$ and one with moderate surface anchoring $\alpha = 4\sqrt{10(1-\chi^2)^\nu/9}$. The weak anchoring system produced lower order at the surfaces, leading to an ∩ shaped order profile in the nematic phase, and formed a bookshelf structure in the smectic phase. The moderate anchoring system produced higher order at the surfaces, leading to a ∪ shaped order profile in the nematic phase, and formed a tilted layer structure in the smectic phase. This difference in behaviour was attributed to the different surface anchoring strengths.

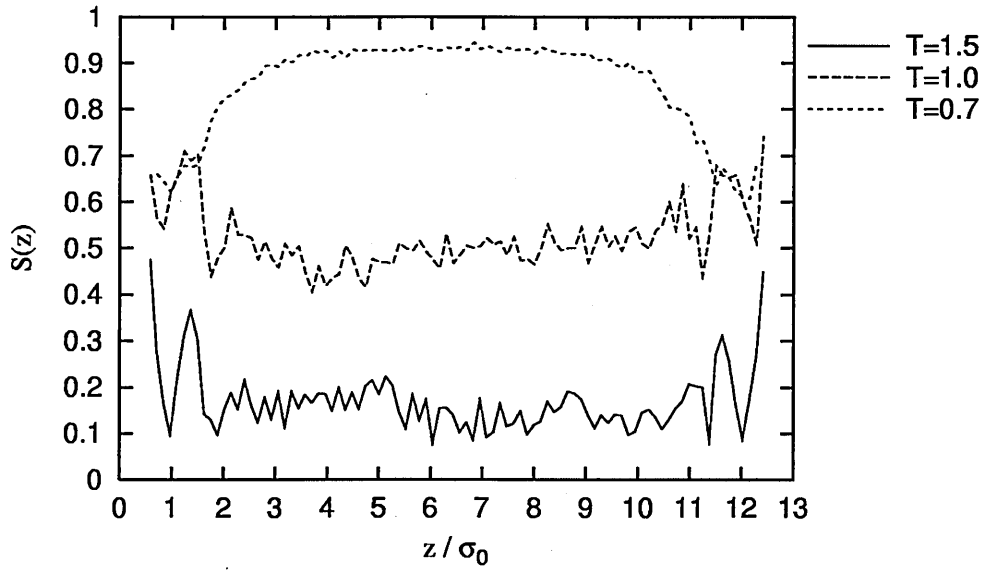

Figure 4.3: Orientational order profiles for the confined 256 particle system.

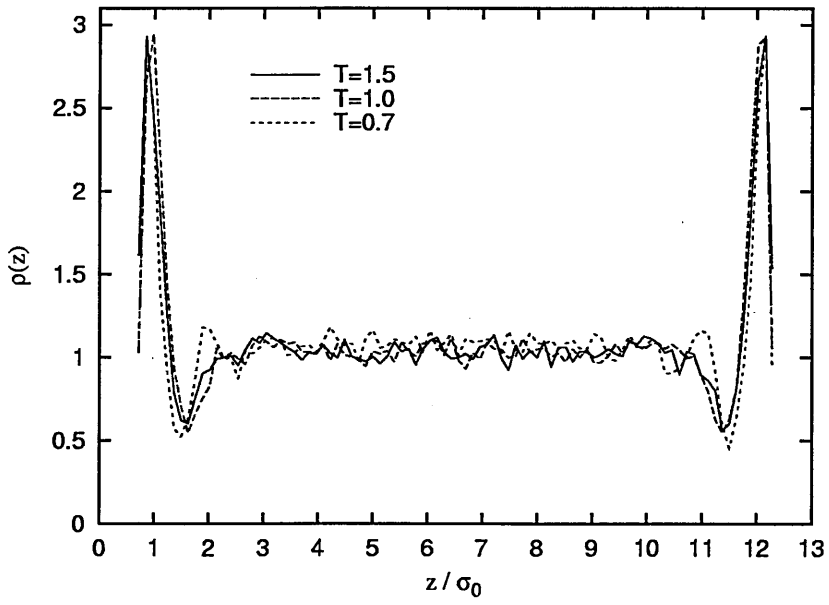

Figure 4.4: Normalised density profiles for the confined 256 particle system.

However, the results for the weak anchoring system simulated here, shown in Fig. 4.2 and Fig. 4.3, correspond to the moderate anchoring system in Ref. [73]. This suggests that the difference in the overall behaviour of two systems in Ref. [73] could be due inherent bias in the particular configurations used, rather than due directly to the influence of the surface anchoring strengths.

4.3 Relaxation from the Splay Fréedericksz Geometry

4.3.1 Aligning Field Model

The energy density associated with the interaction between the director $\mathbf{n}$ and a magnetic field $\mathbf{H}$ is given by

$$U_{\mathrm{M}} = -\frac{1}{2}\chi_a(\mathbf{n}\cdot\mathbf{H})^2, \tag{4.2}$$

where χ_a is the diamagnetic anisotropy of the bulk material [1].

In an MD simulation, the field must be applied to each particle individually, rather than to the bulk as a whole. The relationship between the anisotropy of the bulk material χ_a and the anisotropy of an individual molecule χ_a^{mol} is given by $\chi_a = S\rho\chi_a^{\mathrm{mol}}$, where S is the orientational order parameter and ρ is the number density.

In this work, the aim of the applied field was just to create the initial alignment of the system in order to observe relaxation processes, rather than to model in detail the alignment process itself. Therefore an assumption was made that the continuum description of the material holds down the molecular scale and so a constant order $S = 1$ exists at all points.

In this case, from Eq. 4.2, for an individual particle in a splay Fréedericksz geometry system, with the surfaces in the xy-plane and the field applied normal to the surfaces, the energy is given by

$$U_{\mathrm{M}} = -\frac{1}{2}\frac{\chi_a}{\rho}H^2 u_z^2, \tag{4.3}$$

where H is the field strength and u_z is the z-component of the particle orientation vector $\mathbf{u}$.

Solving the critical field expression Eqn. 2.6 for χ_a and substituting into Eqn. 4.3 gives

$$U_{\mathrm{M}} = -\frac{1}{2}\frac{H^2}{H_c^2}\frac{k_{11}}{\rho}\left(\frac{\pi}{d}\right)^2 u_z^2, \tag{4.4}$$

where d is the surface separation. Substituting $h^2 = H^2/H_c^2$ gives

$$U_{\mathrm{M}} = -\frac{1}{2}h^2\frac{k_{11}}{\rho}\left(\frac{\pi}{d}\right)^2 u_z^2, \tag{4.5}$$

which allows the field strength to be expressed relative to the continuum theory prediction for the critical field strength so that $h^2 = 1$ defines the critical field.

The magnetic coherence length in the splay geometry, $\xi(H) = H^{-1}\sqrt{k_{11}/\chi_a}$, defines the size of transition region near the surface where the director changes from its surface-aligned direction to its field-aligned direction. This can be used to give some idea of the real value of the field strength required to align the bulk region in the Gay-Berne system studied in this work.

In a typical nematic cell, a magnetic field of around 10^4G produces a transition region of around 1μm [10]. A typical value of the Gay-Berne model σ_0 parameter for an nCB molecule would be 0.5nm. A large simulation with a surface separation of $60\sigma_0$ and transition regions at each surface of around $20\sigma_0$ could be said to correspond to an experimental transition region of around 10nm. Since the magnetic coherence length is inversely proportional to the field strength, a very

general assumption can be made that the field needed to create a 10nm transition region would be around 10^6G. This would be difficult to achieve in experimental conditions and would be likely to enhance the order parameter in the bulk and reduce it in the surface regions, thus invalidating the assumptions of continuum theory. This does, however, illustrate that the alignment processes observed in the simulations in this work may not correspond to the processes which are observed in a real cell.

4.3.2 Analysis

To create static system profiles showing the variation in a parameter across the simulation box between the surfaces, the box was divided into 100 slices parallel to the surfaces, and a block-averaged parameter was calculated for each slice.

To calculate the orientational order parameter and the director in each slice using the method described in Section 3.6.2, the ordering matrix was diagonalised using the Numerical Recipes Jacobi diagonalisation routine which produces normalised eigenvectors and the associated eigenvalues [81].

In a 3-dimensional planar aligned system, the director profile can be described by a tilt angle, measured relative to the plane of the surfaces, and an azimuthal twist angle, measured relative to the alignment direction in the plane of the surfaces. However, when the bulk region is aligned by an applied field normal to the surfaces, the twist angle is no longer defined. For this reason, in the following sections, the full director profile is shown by plotting the individual components (n_x, n_y, n_z) of the director $\mathbf{n}$.

Changing the sign of the director does not change its meaning. When creating a profile of the director throughout the simulation box by dividing the box into

slices, the sign of the director in each slice is dictated by the signs of the individual particle orientation vectors in that slice. This can lead to apparent discontinuities in the profile, caused by the arbitrary sign of the director in each slice. Forcing one component of the director to have a fixed sign throughout the profile does not necessarily solve this problem in the case of the splay Fréedericksz transition, as each component of the director might need to change sign in some part of the profile. The method used here to create a continuous director profile was to choose a sign for the director in the first slice of the profile, then for each subsequent slice i, to choose the sign of the director which maximised $\mathbf{n}_i \cdot \mathbf{n}_{i-1}$.

For time-resolved plots of the tilt angle and the velocity profile during relaxation, the box was divided into 15 slices and a value in each slice was calculated for each saved configuration. The tilt angle was taken from the director. The velocity was calculated as $(\sum v_x)/N_s$, where v_x was the x component of the translational velocity of each particle in the slice and N_s was the number of particles in the slice. The values were then smoothed using the exponential smoothing method described in Section 3.6.3 with a smoothing parameter $w = 0.02$. The smoothing was started 240,000 timesteps before the field was removed.

4.4 Relaxation of a GB35 System

4.4.1 Surface Alignment

A system of 3008 GB35 particles was created with the method described in Section 4.1.4, at a temperature T=1.0. This was then cooled in steps of 0.01 until strong nematic ordering was observed at T=0.95. At each intermediate step the system was equilibrated for 240,000 timesteps. The timestep was $\delta t = 0.0015$

Figure 4.5: Snapshot of the surface-aligned GB35 system: Lower surface on left, upper surface on right.

and 240,000 timesteps on 32 nodes took around 315 minutes. The surface separation was $L_z = 50$ and the remaining dimensions were set $L_x = L_y$ to give a number density of $\rho = 0.325$. Configurations were saved every 2000 steps for analysis. Based on results obtained using this aligning surface model in Ref. [80], the surface parameters used were $\chi'' = 0.2$, $\delta = 5°$ and $\alpha = 2\sqrt{10(1-\chi^2)^\nu/9}$. The T=0.95 system was equilibrated in the NVT ensemble for 960,000 timesteps. A snapshot of the equilibrated system is shown in Fig. 4.5. Static profiles were compiled, block averaged over 240,000 timesteps.

As with previous simulations performed with the GB35 particle using the particle-sphere shape function for the surface model, the surface layer was tilted. The director profile in Fig. 4.6 shows that the system divided into 3 regions. Near to both substrates, the director orientation was dominated by the tilt at the surface. This tilt reduced slightly in the central third of the box. This suggests that the overall effect of the presence of the surfaces was to induce some planar alignment in the bulk region, even though the surface alignment itself was tilted. The tilt profile also reveals discontinuities at the surfaces, which suggests a three-layer surfaces structure, each layer having a different tilt. The n_y component of the director shows that there was no equivalent twist discontinuity at the surfaces,

however, the lower surface is not aligned along the x-axis but at around 17 °.

The orientational order profile in Fig. 4.7 shows a strong nematic in the bulk with increased order in the surface layers. The normalised density in Fig. 4.8 shows the enhanced density of the surface layer.

Fig. 4.9 shows the reduced density, orientational order and director n_z components in regions near both surfaces of size $5\sigma_0$, each region divided into 40 slices. The order was generally enhanced in the high density surface layer and reduced in the low density trough. The greater resolution of these plots shows that the tilt profile was not discontinuous in the surface region, rather that it changed radpidly from its lowest value around the low density trough to its highest value around the high density surface layer. However, the details of the density, order and director profiles in these surface regions do not relate to each other in an obvious way. The mechanisms responsible for the surface structure are likely to have included particle-surface interactions, particle-particle interactions and packing constraints. In this work, the surfaces take the role of boundary conditions on the system, so no attempt was made to analyse the detailed mechanism responsible for the structures seen in the surface regions.

4.4.2 Field Alignment

Although estimates of the elastic constants of the GB35 particle have been made [64, 65] the exact value of the splay elastic constant k_{11} is not known. Using the fact that $h^2 = 1$ corresponds to the critical field strength in Eqn. 4.5, an estimate of k_{11} could be made by increasing the overall value of $h^2 k_{11}$ and identifying the point at which distortion of the bulk director occurs. However, at the critical field strength there is only a small percentage change in the tilt angle at the centre of

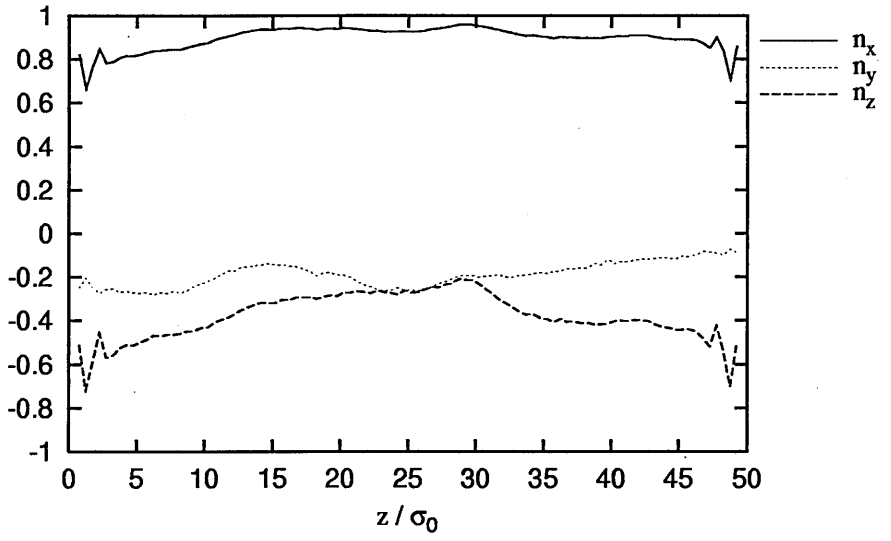

Figure 4.6: Field off director profile of the GB35 system.

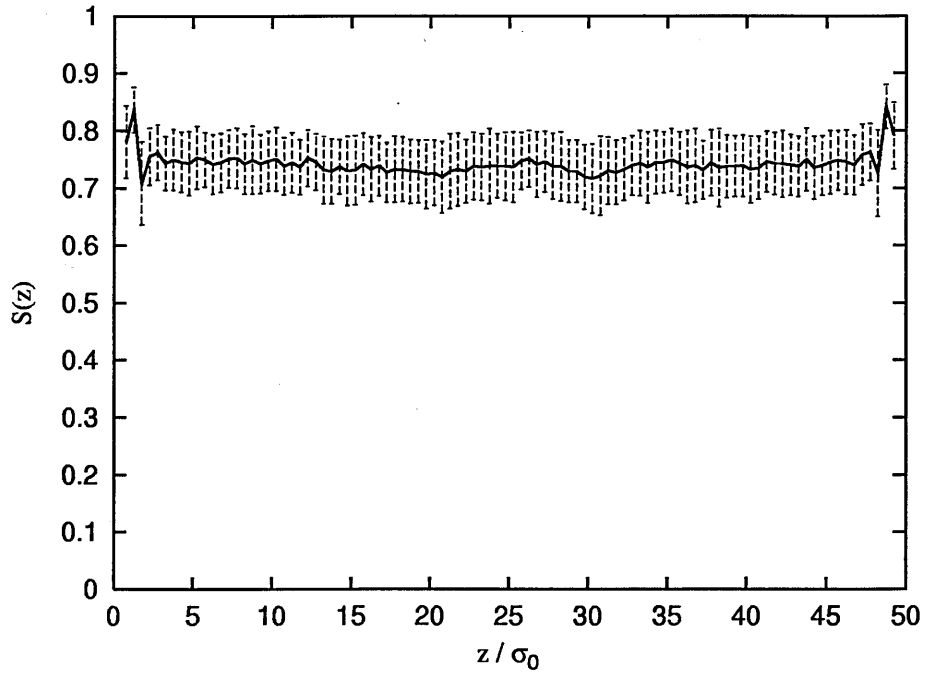

Figure 4.7: Field off orientational order profile of the GB35 system.

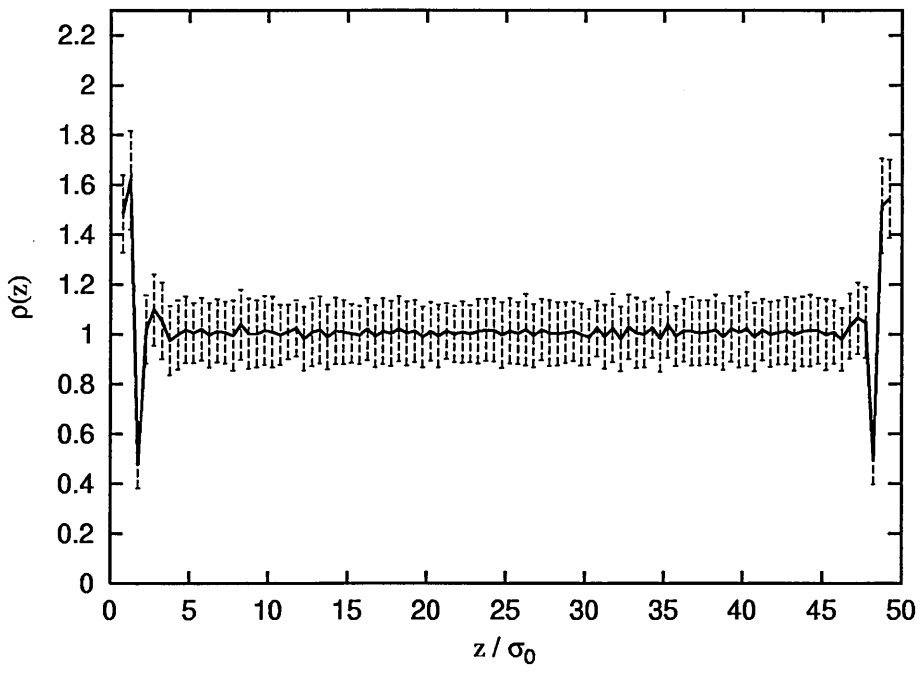

Figure 4.8: Field off normalised density profile of the GB35 system.

the cell. Due to the natural variation of the director in the centre of the simulation box, this would be difficult to identify without very long runlengths to average out the variations. Also, the critical field equation is only valid for a system with initial planar alignment throughout. For these reasons, no attempt was made to measure the elastic constant by the critical field method, and for the following simulations, a value of $h^2 k_{11}/\rho$ was used to represent the field strength.

To create a field-aligned system, a field was applied to the surface-aligned system, with increasing values of $h^2 k_{11}/\rho$ of 1,2,4 and 8. On each increase, the system was equilibrated for 240,000 timesteps, but no significant change in the director was observed. A value $h^2 k_{11}/\rho = 16$ produced significant distortion. This system was equilibrated for 480,000 timesteps. A snapshot of the field-aligned system is shown in Fig. 4.10.

The director profile in Fig. 4.11 reveals that the bulk region had not become

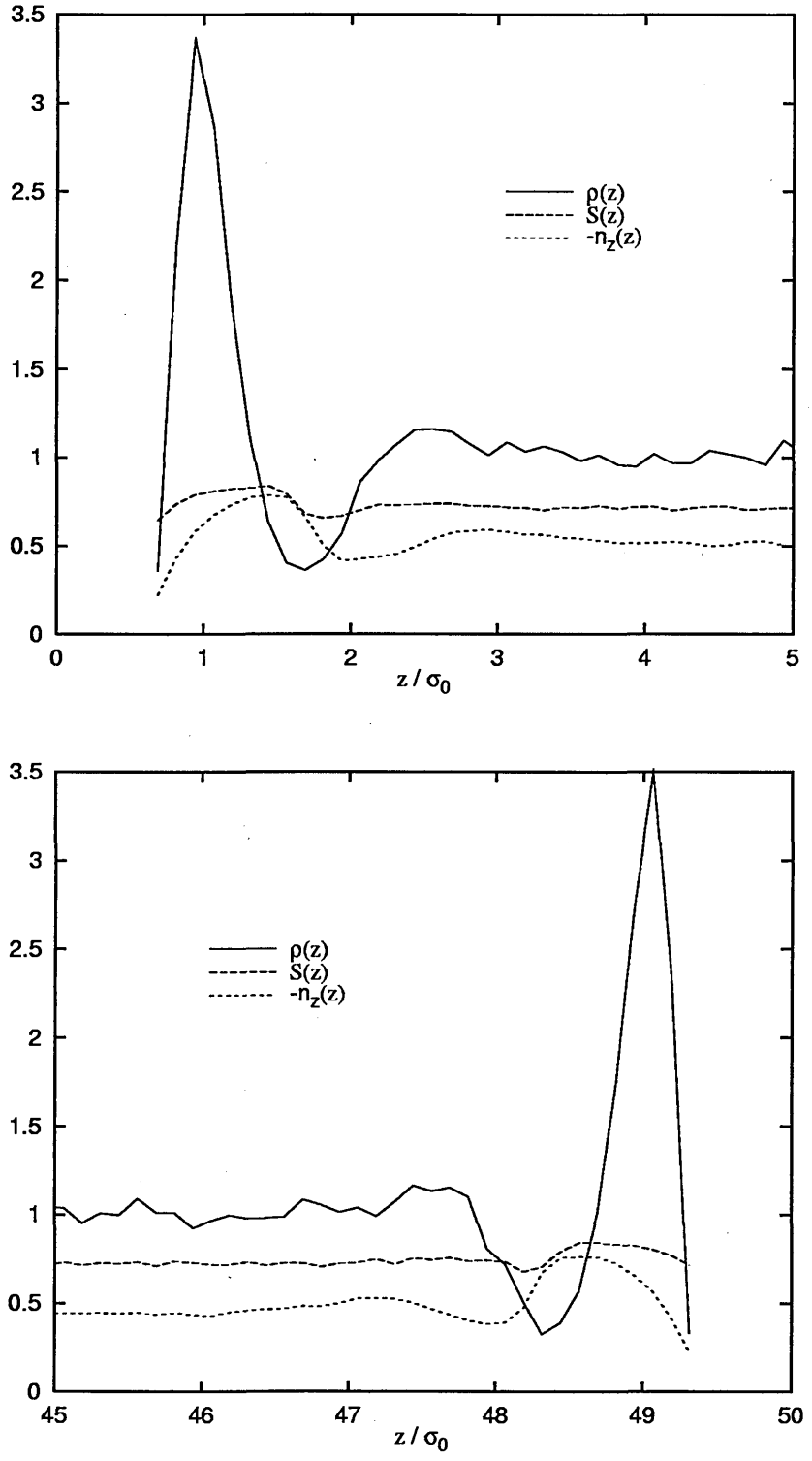

Figure 4.9: Surface region profiles of the GB35 system.

Figure 4.10: Snapshot of the field-aligned GB35 system: Lower surface on left, upper surface on right.

saturated as there was a smooth tilt profile between the surfaces. In contrast to the field-off system, the lower surface was aligned along the easy-axis and the upper surface was slightly twisted. A comparison of the order profiles for the field-off and field-on systems in Fig. 4.12 shows that even with the smooth distortion profile, the order had been reduced in the splay regions near the surface.

The fact that the bulk was not saturated is consistent with the value $h^2 k_{11}/\rho = 16$ corresponding to a field strength of around 3 to 4 times the critical value. If the critical field equation were valid for this system, this would give an estimate for k_{11} of between 0.325 and 0.578. This is comparable with the values $k_{11} \approx 0.7$ in [65] and $k_{11} \approx 2.7$ in [64] for the state point $\rho = 0.33$ and T=1.0.

4.4.3 Relaxation on Field Removal

Controlling the temperature in the NVT ensemble can have undesirable effects on a velocity profile in a simulation [82]. Flow in some region creates an effectively higher temperature in the system as a whole. The temperature control method tries to cool the whole system, thus reducing the flow and cooling the system below the desired temperature in other regions. To avoid these possible effects, relaxation

on removal of the field was performed in the NVE ensemble. Configurations were saved every 2000 timesteps for analysis. The box was divided into 15 slices, identified by an index i where $i = 1$ was at the lower surface.

The relaxation of the tilt angle θ measured relative to the surfaces is shown in Fig. 4.13. The timescale is shown in units of 10^6 timesteps with the field removed at $t = 0$. Due to the symmetry of the director profile, the tilt angles for the lower half of the box only are shown. Unlike an experimental cell, where the surface regions reorient initially whilst the bulk regions remain in the field-aligned state, here all regions of the box relaxed together.

The corresponding time-resolved x-velocity is shown in Fig. 4.14 for the surface regions and alternate bulk regions. Each slice is plotted with an offset of 0.05 so the lower surface corresponds to the lowest line on the plot. On the initial relaxation, the lower surface regions showed a short lived positive velocity, the upper surface regions showed a negative velocity. No flow occurred at 1/4 and 3/4 of the surface separation, as would be expected in the backflow mechanism of relaxation from the splay Fréedericksz geometry.

This behaviour could be explained by the two reorientation regions at the surfaces being sufficiently large to effectively touch in the centre of the box. This would allow translational movement of particles between the reorientation region and the surfaces, but any movement of the bulk particles due to reorientation of these regions would cancel out. Another contributing factor is the inherent tilt of the surface layers would have meant that the angle through which the near surface director had to rotate on removal of the field was not as large as it would have been for a true planar aligned system.

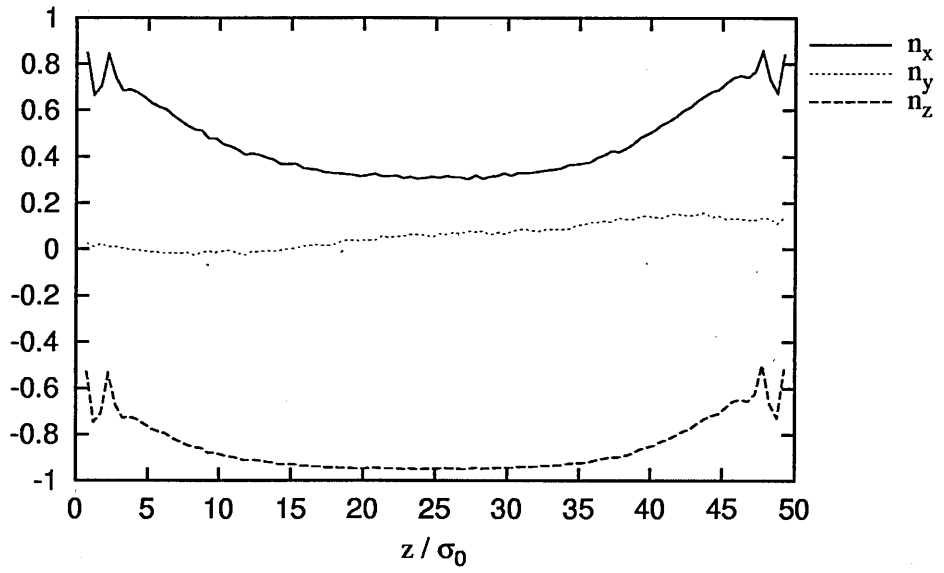

Figure 4.11: Field on director profile of the GB35 system.

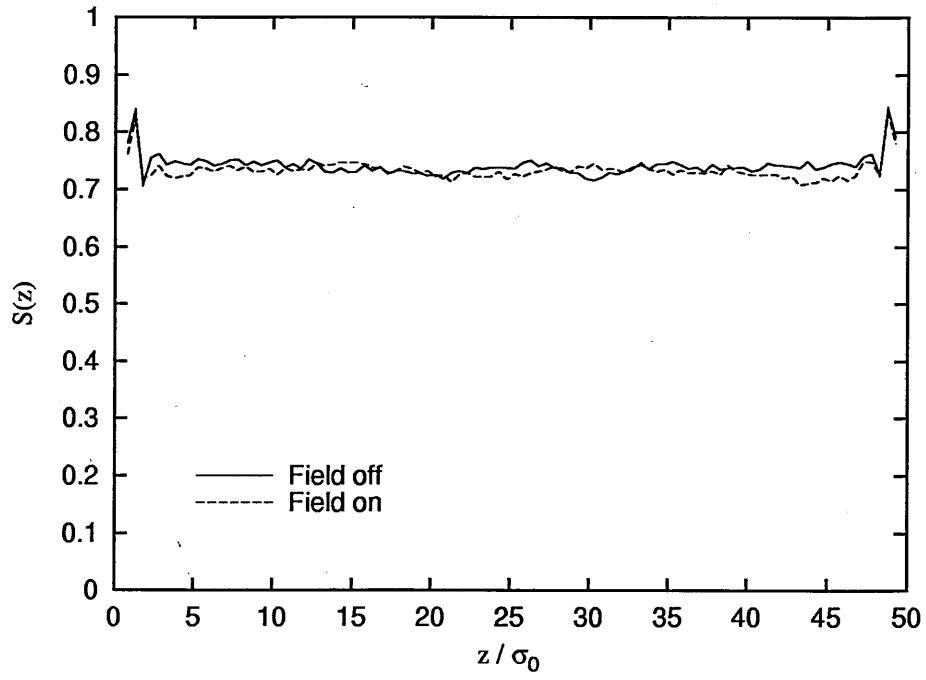

Figure 4.12: Comparison of orientational order profiles of the field off and field on GB35 system.

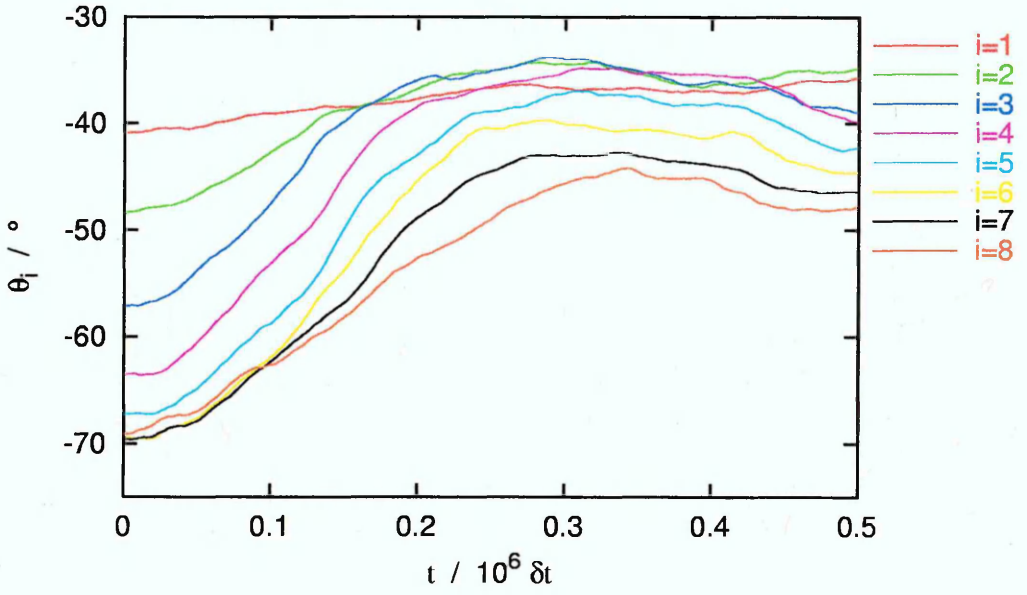

Figure 4.13: Director tilt angle on relaxation of the field-aligned GB35 system. The simulation box is divided into 15 slices with index i, where $i = 1$ is the lower surface.

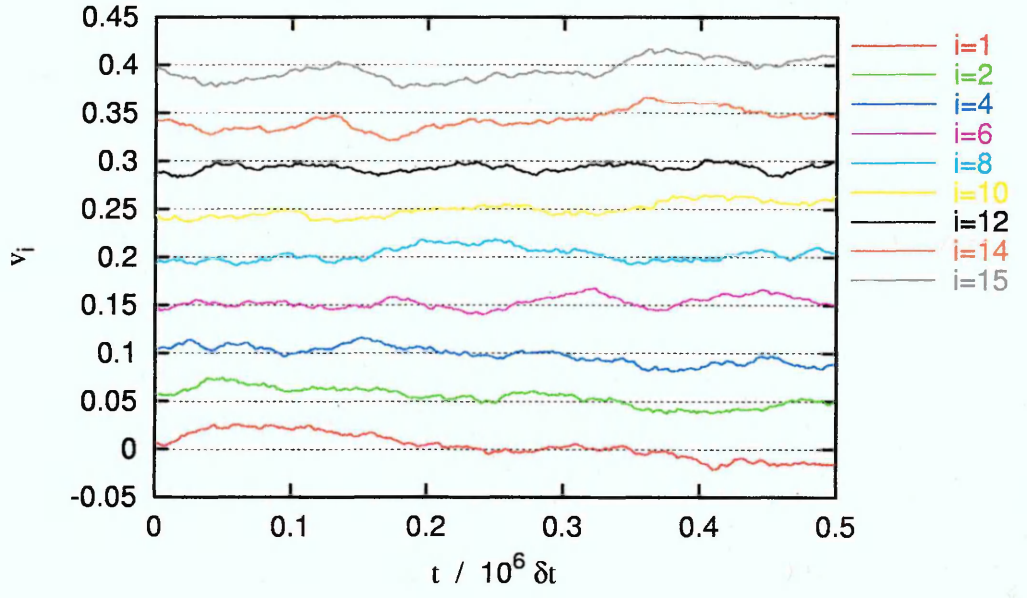

Figure 4.14: Velocity on relaxation of the field-aligned GB35 system. The simulation box is divided into 15 slices with index i, where $i = 1$ is the lower surface and the lowest line on the plot. Each slice is plotted with a 0.05 offset from the previous slice.

4.5 Relaxation of a GB25 System

4.5.1 Alignment

In order to increase the degree of reorientation near the surfaces, a relaxation run on a planar aligned system was performed. Planar alignment at the surfaces can be achieved through a change in the bulk Gay-Berne potential parameters to $\nu = 2$, $\mu = 1$, $\kappa = 2$, and $\kappa' = 5$. The main difference between the GB35 system and this GB25 system is the shortened length-to-width ratio of 2. This parameterisation was known to produce a planar aligned nematic system at $\rho = 0.415$ and T = 0.53 [83].

A system of 3008 particles was created at a temperature T=0.56 using the method described in Section 4.1.4 and then cooled in steps of 0.01 to T=0.53, equilibrating for 240,000 timesteps at each step. Each run took around 270 minutes on 32 nodes. The surface separation was $L_z = 45\sigma_0$ and the L_x and L_y sides of the box were set equal to each other. The surface parameters were the same as those for the GB35 system except that there was no surface pretilt term ($\delta = 0$). The simulation timestep was δt= 0.0015, with the potential cutoff and neighbourlist radii being $3\sigma_0$ and $3.3\sigma_0$ respectively. Configurations were saved every 1000 steps and the static profiles were block averaged over 240,000 steps.

A snapshot of the equilibrated surface-aligned system is shown in Fig. 4.15. The director profile in Fig. 4.16 shows near planar alignment throughout the system. The order and normalised density profiles (Fig. 4.17, Fig. 4.18) show stratification near the surfaces, which was not seen in the tilted surface GB35 system.

Using the same field alignment method as was adopted when simulating the

Figure 4.15: Snapshot of the surface-aligned GB25 system: Lower surface on left, upper surface on right.

GB35 system, three field strengths were identified, which were termed weak, medium and strong, based on their effect on the profile data.

The director profile for the weak field $h^2k_{11}/\rho = 8$ is shown in Fig. 4.19. Here, the system developed a smooth tilt profile with no saturation of the bulk. The director profile for the medium field $h^2k_{11}/\rho = 12$ is shown in Fig. 4.21 and indicates that the system developed a small saturated bulk region in the centre. A snapshot of this system is shown in Fig. 4.20. The director profile for the strong field $h^2k_{11}/\rho = 16$ is shown in Fig. 4.22. This system developed the type of tilt profile assumed necessary for the observation of backflow and kickback effects. This included a transition region of around $15\sigma_0$ at each surface and a saturated bulk region of around $15\sigma_0$.

However, a comparison of the order parameter profiles of these systems, shown in Fig. 4.23, reveals that the director distortions just described had a large effect on the order near the surfaces. The weak field created a large reduction in order in the lower surface region. The medium field reduced the order near both surfaces. The strong field caused a further reduction in order at the lower surface, and a significant breakdown of orientational order at the upper surface.

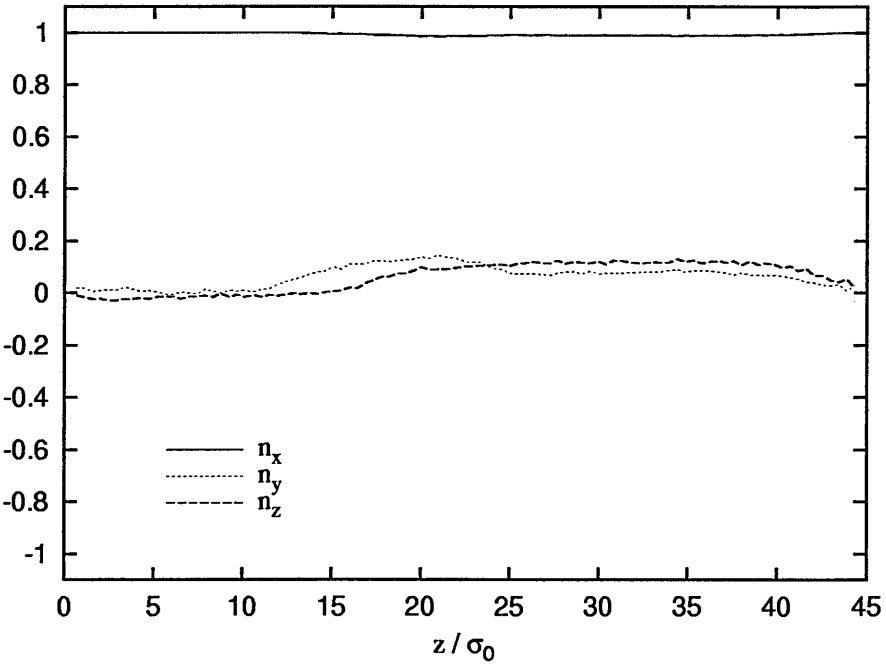

Figure 4.16: Field off director profile of the GB25 system.

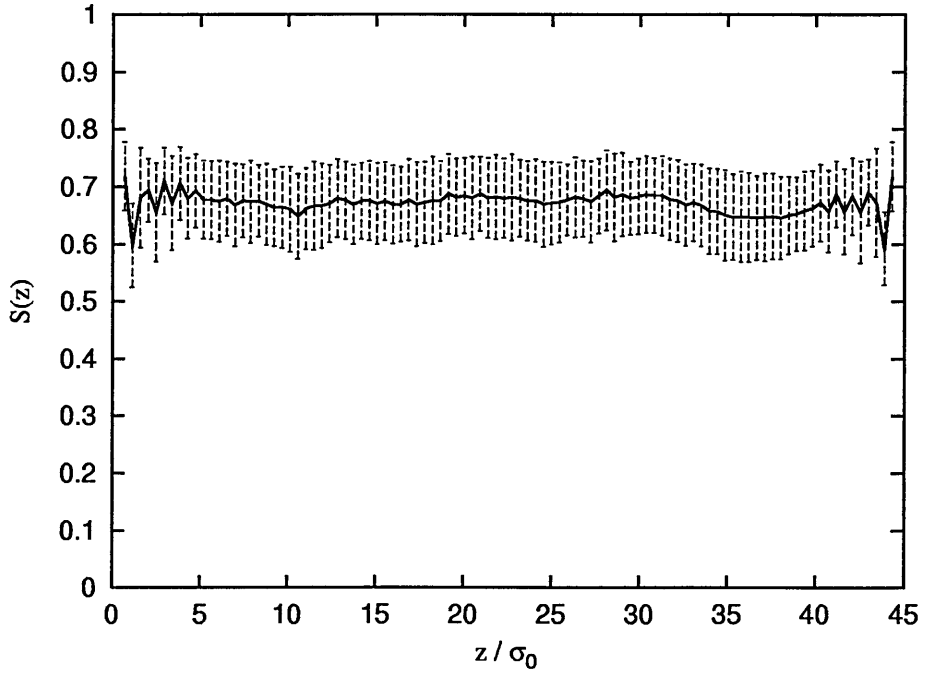

Figure 4.17: Field off orientational order profile of the GB25 system.

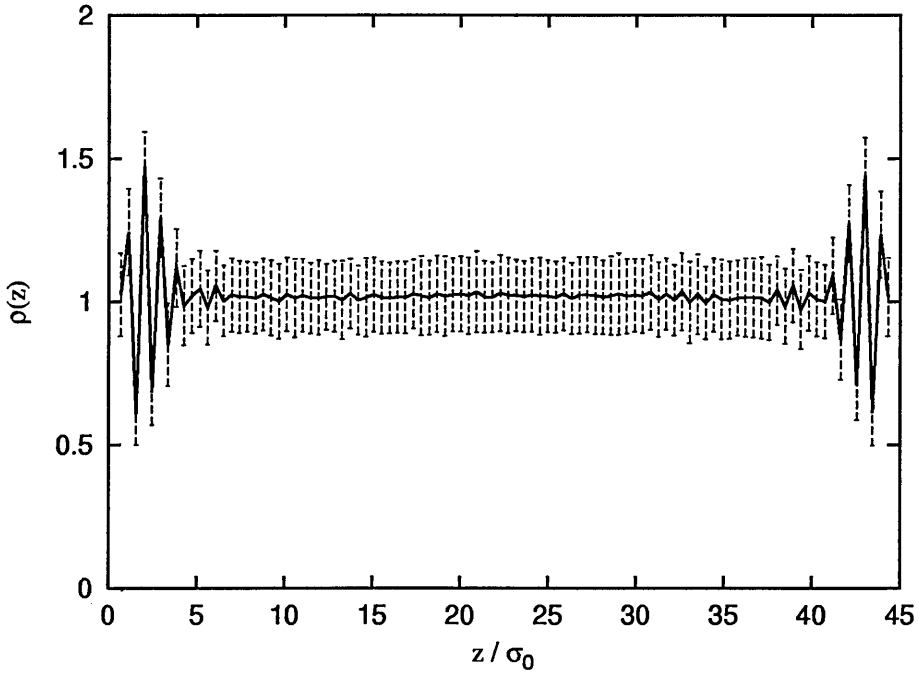

Figure 4.18: Field off normalised density profile of the GB25 system.

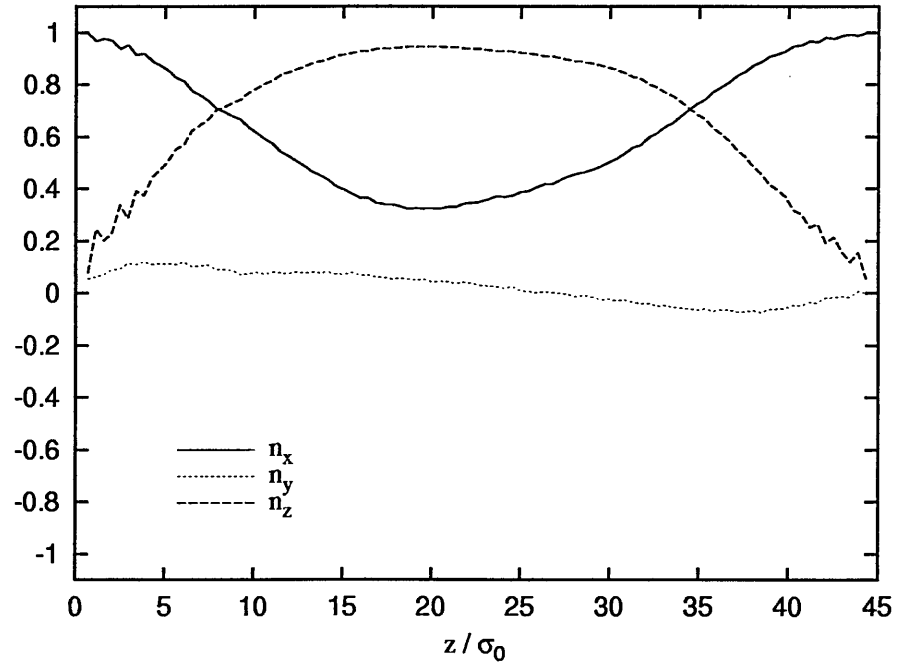

Figure 4.19: Weak field director profile of the GB25 system.

Figure 4.20: Snapshot of the medium field aligned GB25 system: Lower surface on left, upper surface on right.

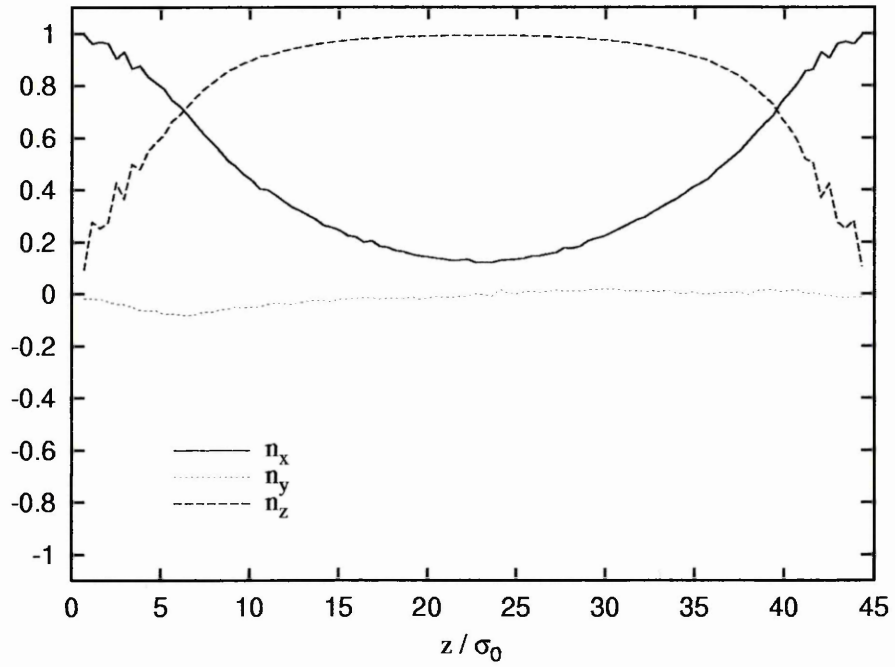

Figure 4.21: Medium field director profile of the GB25 system.

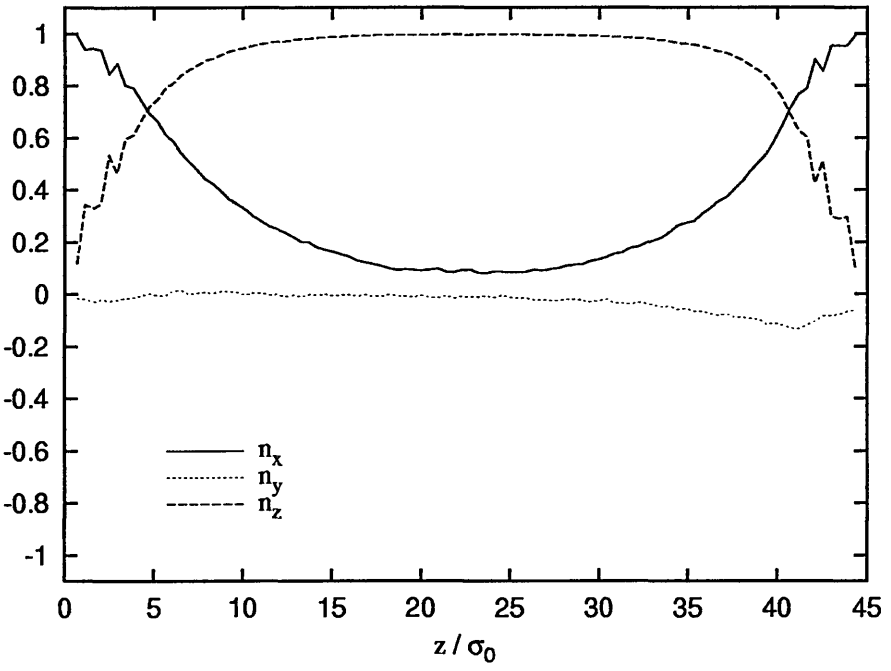

Figure 4.22: Strong field director profile of the GB25 system.

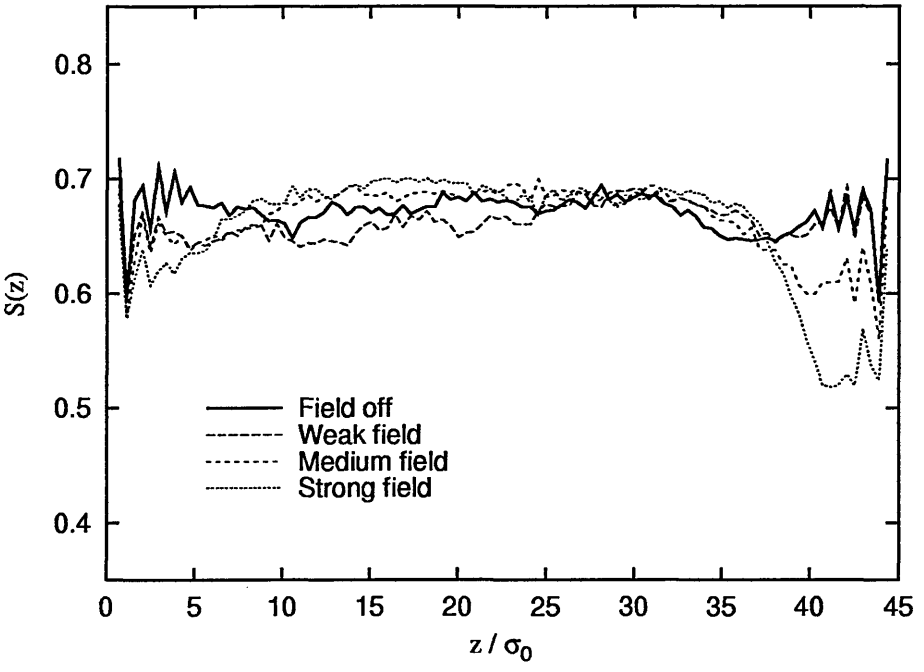

Figure 4.23: Orientational order profiles of the weak, medium and strong field-aligned GB25 systems.

4.5.2 Relaxation

As a compromise between the desired director profile and the effect of the distortion on the order parameter, a relaxation run was performed on the medium field GB25 system. The relaxation of tilt angles in Fig. 4.24 shows that, as with the GB35 relaxation, all regions within the box relaxed together. The flow on relaxation, presented in Fig. 4.25, shows no resolvable pattern.

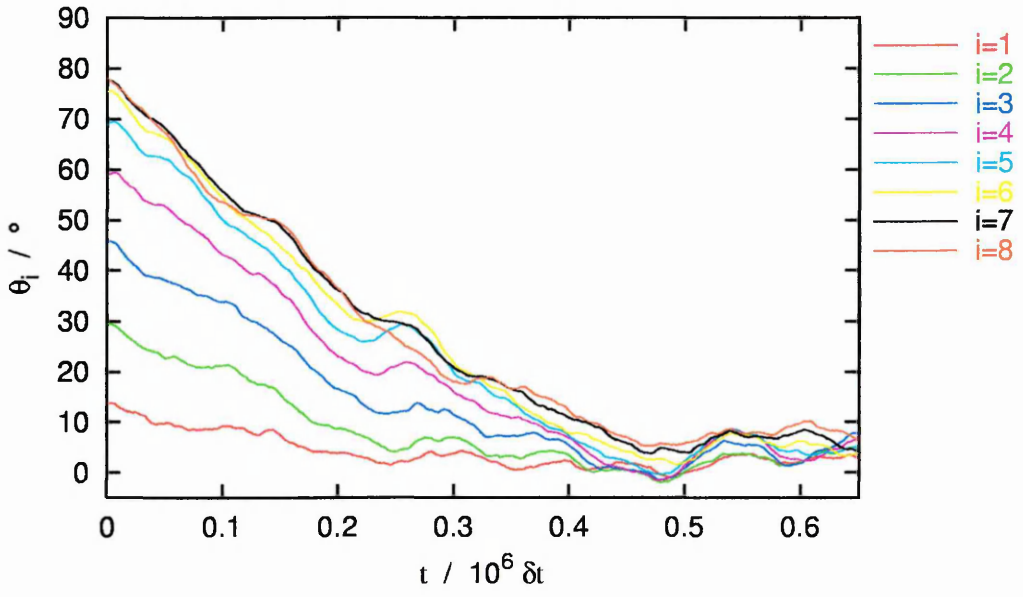

Figure 4.24: Director tilt angle on relaxation of the medium field-aligned GB25 system. The simulation box is divided into 15 slices with index i, where $i = 1$ is the lower surface.

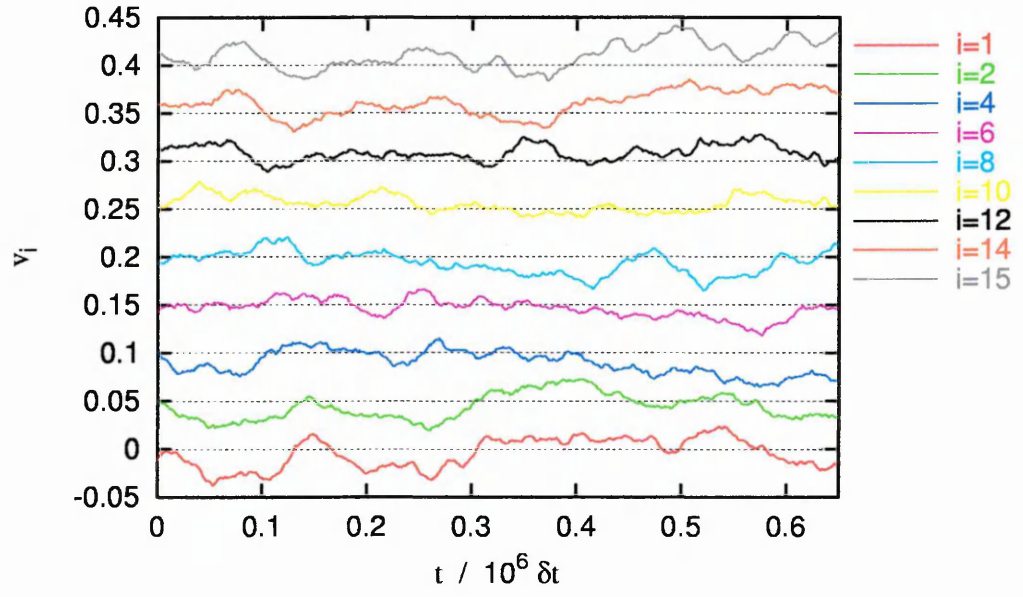

Figure 4.25: Velocity on relaxation of the medium field-aligned GB25 system. The simulation box is divided into 15 slices with index i, where $i = 1$ is the lower surface and the lowest line on the plot. Each slice is plotted with a 0.05 offset from the previous slice.

4.6 Large Confined GB25 System

In order to increase the size of the saturated bulk region without reducing the size, and hence the order, of the transition regions, a large GB25 system of 5120 particles was created, with a surface separation of $L_z = 80\sigma_0$. However, a satisfactory field alignment of this system could not be achieved.

A field of $h^2 k_{11}/\rho = 8$ produced large reductions in the order parameter in the transition regions and in the central region, without saturating the bulk orientation, as shown in Fig. 4.26 and Fig. 4.27. There was also a large, long timescale drift in the twist of the director in the central region. This was assumed to be due to the large surface separation reducing the direct influence of the surface alignment on the central bulk region, creating an arrangement which, unlike the smaller GB25 system, was not aligned in the xz plane.

At a field strength $h^2 k_{11}/\rho = 14$, strong enough to saturate the bulk region, the order broke down in the lower surface region, producing a discontinuous director profile as shown in Fig. 4.28 and Fig. 4.29.

In order to achieve uniform alignment of the centre of the film in the easy-axis plane, a field tilted in the x-direction of the form $\mathbf{H} = (H/2, 0, H)$, was used. Again, this produced large variations in order through the box and, as the field strength was increased to $\mathbf{H} = (6, 0, 12)$, the planar surface region extended into the bulk region, thus effectively reducing the surface separation, as shown in Fig. 4.30 and Fig. 4.31.

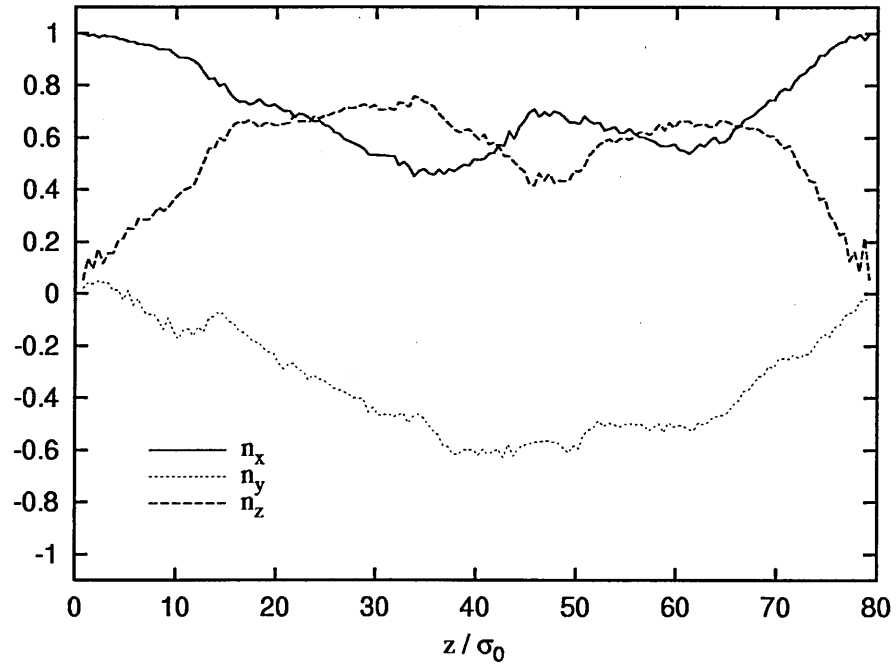

Figure 4.26: Director profile of the large GB25 system with unsaturated field-aligned bulk region.

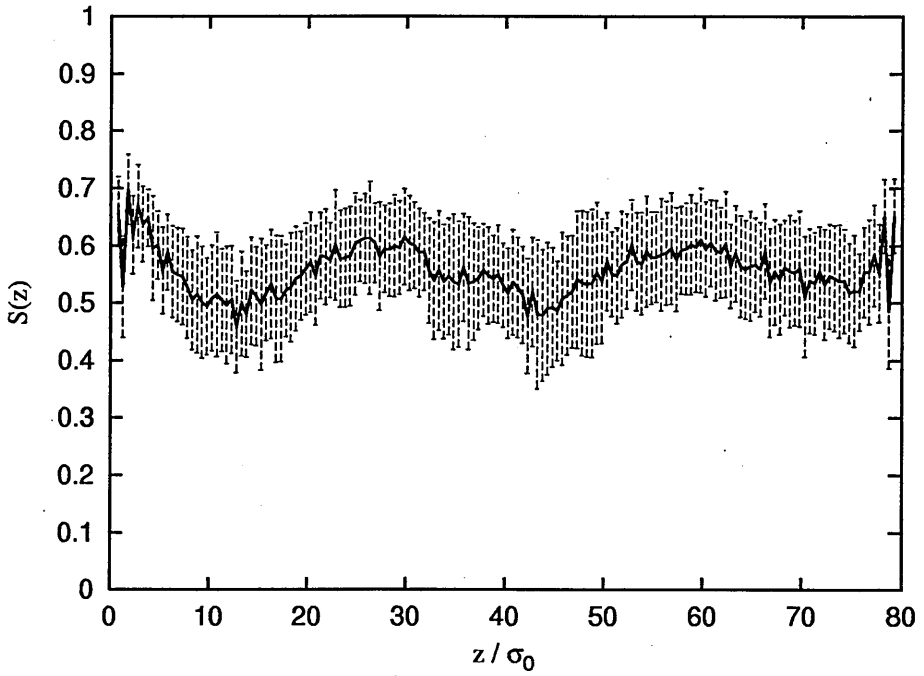

Figure 4.27: Orientational order profile of the large GB25 system with unsaturated field-aligned bulk region.

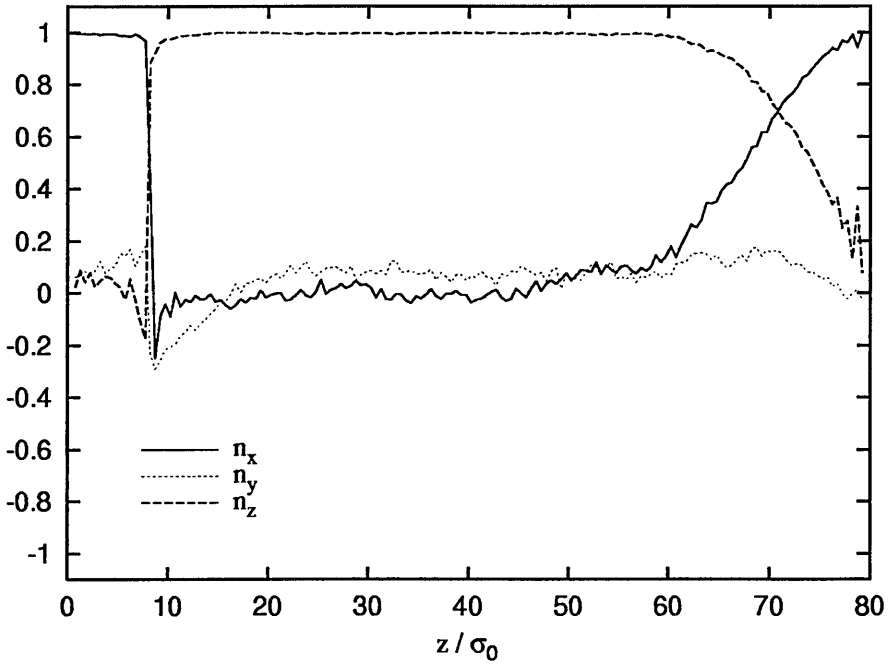

Figure 4.28: Director profile of the large GB25 system with saturated field-aligned bulk region.

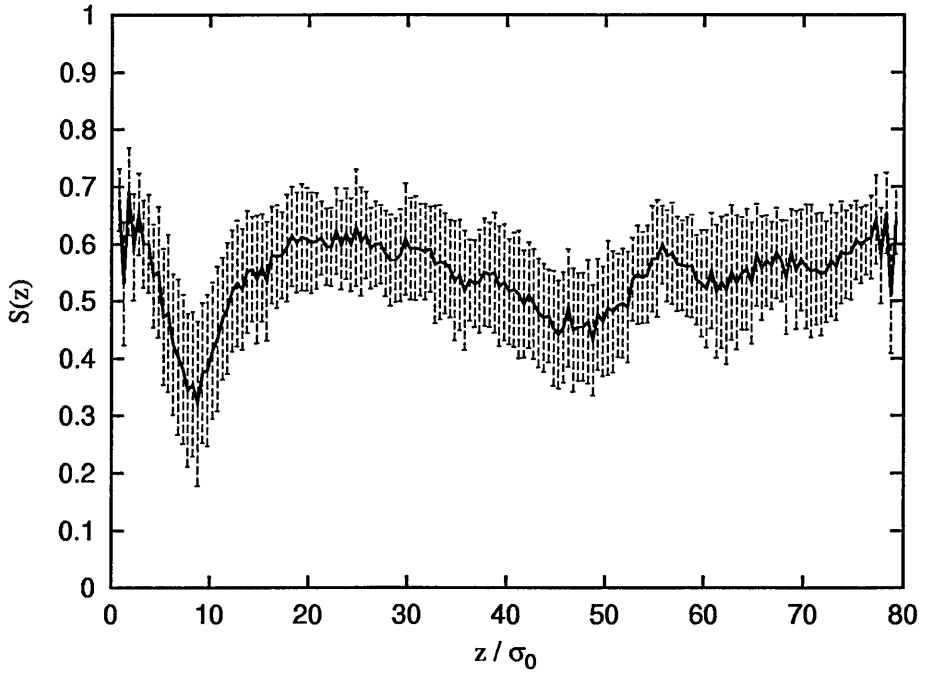

Figure 4.29: Orientational order profile of the large GB25 system with saturated field-aligned bulk region.

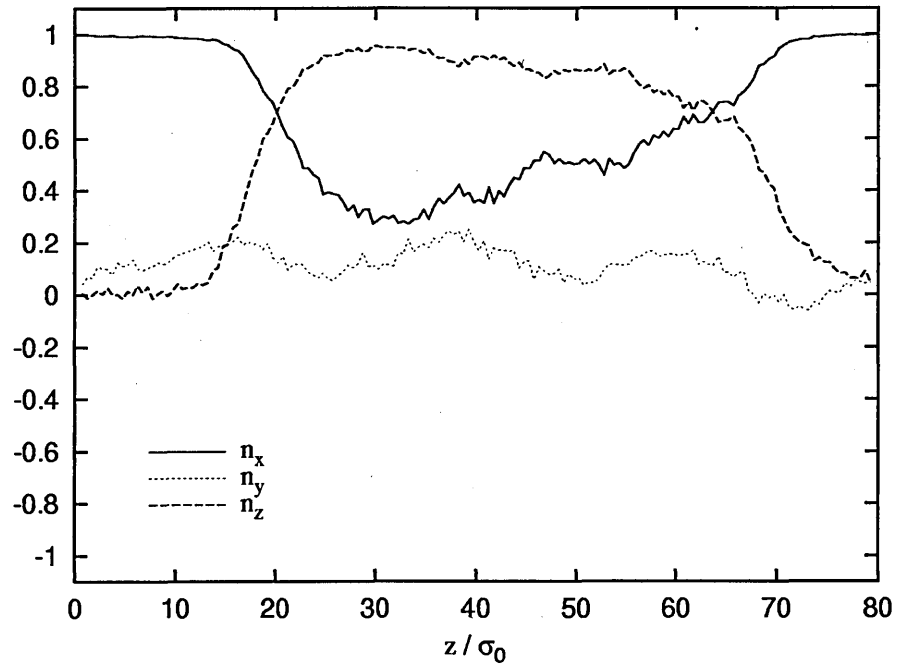

Figure 4.30: Director profile of the large GB25 system with tilted applied field.

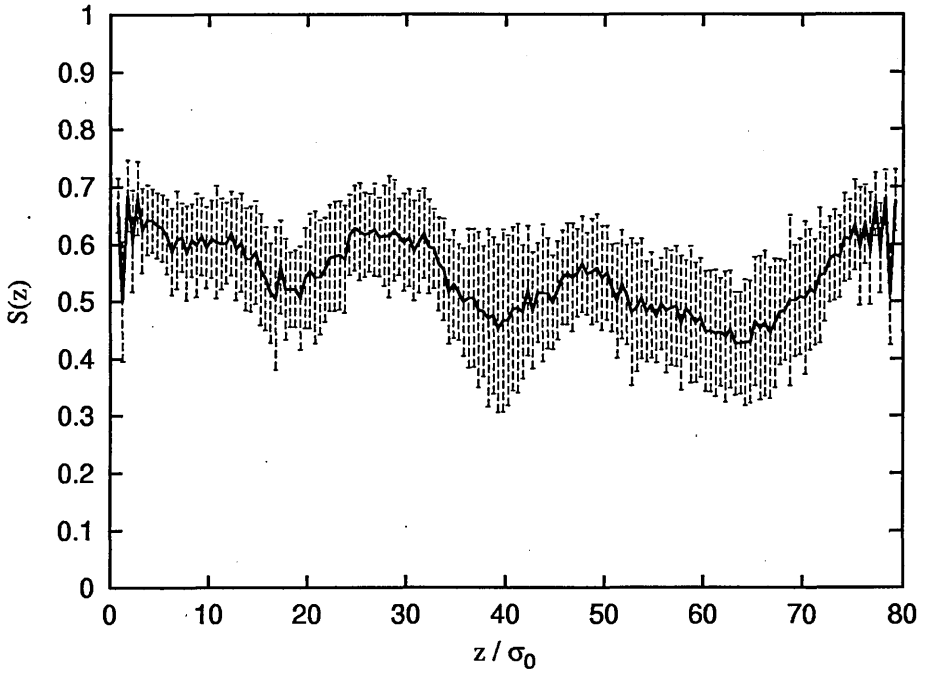

Figure 4.31: Orientational order profile of the large GB25 system with tilted applied field.

4.7 Summary

The results presented in this chapter show that relaxation of field-aligned systems confined between tilted and planar aligning substrates has been simulated using molecular dynamics of the Gay-Berne particle.

An examination of the region near the tilted surface layers suggests a complicated relationship between density, director and orientational order profiles. The relaxation results demonstrate that relaxation timescales of systems of around 3000 Gay-Berne particles are accessible. However, the relaxation did not involve any significant backflow or orientational kickback processes.

Taking a typical value of the Gay-Berne model σ_0 parameter for an nCB molecule of 0.5nm gives an estimate of the size of cell which these simulations represent of around 30nm. Estimating a real value for the timescale of the relaxation is more difficult.

The reduced timestep δt used in this work is defined as $\delta t = \delta t_{\text{real}}\sqrt{\epsilon_0/(m\sigma_0^2)}$, where δt_{real} is the real timestep in seconds, and m is the mass of a particle. Values of m and σ_0 corresponding to a typical mesogen can be readily identified, but choosing an equivalent typical value for ϵ_0 is more difficult as the overall characteristics of the Gay-Berne potential needed to simulate nematic phases, controlled by the parameters κ', μ and ν, does not necessarily correspond to the overall characteristics of the interaction between molecules. This was illustrated in a study by Luckhurst and Simmonds [58] who fitted the Gay-Berne model to a typical mesogen producing values of $\nu = 0.74$, $\mu = 0.8$, $\kappa = 4.4$ and $\kappa' = 39.6$ as opposed to the more common values of $\nu = 1$, $\mu = 2$, $\kappa = 3$ and $\kappa' = 5$.

Estimates have been made for ϵ_0 in real units for some parameterisations of the Gay-Berne model by relating the temperature of the isotropic-nematic tran-

sition of the Gay-Berne fluid and that for a real material through the reduced temperature definition $T = k_B T_{real}/\epsilon_0$. Palermo *et al.* [74] estimated a value $\epsilon_0 \approx 1.22 \times 10^{-21}$J for the Gay-Berne parameters $\nu = 1$, $\mu = 2$, $\kappa = 3$ and $\kappa' = 5$. Allen and Warren [84] estimated a value $\epsilon_0 \approx 1.38 \times 10^{-21}$J for the Gay-Berne parameters $\nu = 3$, $\mu = 1$, $\kappa = 3$ and $\kappa' = 5$.

Taking the average of these to give $\epsilon_0 = 1.3 \times 10^{-21}$J, using $m = 4.839 \times 10^{-25}$kg as the approximate mass of a 5CB molecule, taking $\sigma_0 = 0.5 \times 10^{-9}$m and using the reduced simulation timestep $\delta t = 0.0015$ gives an approximate value for the timestep in seconds as $\delta t = 1.45 \times 10^{-14}$s. This gives an order-of-magnitude estimate for the timescale of the GB35 system of $10^6 \delta t \approx 15$ns. This contrasts with relaxation times in real cells of the order of microseconds.

Along with the estimate of the extremely high magnetic field strengths needed to align the GB35 system, this further suggests that the relaxation processes observed in these simulations may not correspond to the macroscopic processes observed experimentally.

In a real cell, on relaxation from the splay geometry, the flow induced in the bulk by regions near the surfaces is in opposite directions for each surface. It seems reasonable to assume, therefore, that to simulate the backflow pattern expected in a splay cell, the surface regions must be separated by a bulk region large enough to support regions of flow near the surfaces with zero velocity at the centre of the film.

In the molecular systems studied here, attempting to create this large field-aligned bulk region by increasing the applied field strength reduced the order parameter in the surface regions. The results suggest that a transition region of around $30\sigma_0$ would be needed to avoid reducing the order significantly. Attempt-

ing to accommodate transition regions of this size by increasing the system size appears to reduce the direct influence of the aligning surfaces on the bulk region, leading to long timescale variations in the director profile.

There are numerous differences between the systems simulated here and the continuum theory approximations to these systems. With no surface structure, the simulated systems will possess some degree of slip at the boundaries whereas theoretical treatments assume non-slip boundary conditions. Theoretical approaches assume an effectively infinite field strength, producing normal alignment of the director everywhere except at the surface, no variation in order parameter and an instantaneous establishment of a velocity profile. Theoretical solutions consider only a two-dimensional system where the director always lies in a plane defined by the surface easy axis and the field direction, whereas some degree of twisting of the director profile was seen in many of the simulations here. For these reasons, no attempt was made to directly compare the relaxation results with the predictions of continuum theory.

Based on the results presented in this chapter, no further simulations to study the specific case of relaxation from the splay geometry were performed. Instead, the simulations which followed on from this work, presented in Chapter 5, explored a more general issue of whether the processes of induced flow and orientational kickback could be seen in a molecular system.

Chapter 5

Relaxation of Hybrid Aligned Systems

5.1 Hybrid Aligned Systems

As a compromise between system size constraints and the need for a transition region of a certain size, a series of simulations were performed using hybrid aligned nematic (HAN) systems, where the surface induced tilt angle is different for each surface. The HAN systems studied here promote normal alignment at the lower surface and either planar or tilted alignment at the upper surface. When a field is applied normal to the surfaces, the normal alignment at the lower surface extends into the bulk region. This allows an extended 'saturated' field aligned region, whilst only requiring a single transition region at the upper surface. Whilst these systems did not correspond to any of the standard Fréedericksz geometries, the aim of these HAN studies was to determine whether the macroscopic processes of backflow and orientational kickback could be observed in a molecular system.

5.2 Particle-Substrate System

A preliminary study of relaxation in a HAN system with normal and planar aligned surfaces was performed. The required surface alignment was forced on the system by using particles fixed in position at the surfaces. A system of 3008 GB35 particles was created with surface separation $L_z = 64.273506\sigma_0$ and simulation box sides of $L_x = L_y = 12\sigma_0$ giving a number density of $\rho = 0.325$.

The surfaces were modelled by the continuum surface potential with no azimuthal alignment used in Section 4.2, together with a rectangular array of regularly spaced particles. On the lower surface at $z = 0$, there were 12×12 particles with orientation vectors $\mathbf{u} = (0, 0, 1)$, and on the upper surface at $z = L_z$, 4 rows of 12 particles with orientation vectors $\mathbf{u} = (1, 0, 0)$. The interaction potential between surface and bulk particles was identical to that between the bulk particles.

The system was created at a temperature T=1.3 using the method described in Section 4.1.4 and equilibrated for 480,000 timesteps in the NVT ensemble. A run of 240,000 timesteps on 32 nodes took around 315 minutes. The system was not cooled. This gave a system with a lower elastic constant than that of the previous field-aligned GB35 system studied in Section 4.4. As a consequence of this, it was thought that this system would be able to accommodate distortions in the director field, rather than forming dislocations.

The field model used was the same as in Section 4.4, although the critical field equation is not valid for this geometry. The field was increased until a satisfactory director profile was achieved, at the expense of reduced orientational order in the system. Values of $h^2 k_{11}/\rho$ of 8, 16 and 32 were used, each equilibrated for 240,000 timesteps. Each 240,000 step run took around 310 minutes on 32 nodes. The

$h^2k_{11}/\rho = 32$ system was then equilibrated for a further 240,000 timesteps. A snapshot of this system is shown in Fig. 5.1. Configurations were saved every 500 timesteps. Static profiles were block averaged over 240,000 timesteps.

The director profile in Fig. 5.2 shows the saturated lower region. There was no twist of the director in this lower region but some twisting occurred in the transition region. The order profile in Fig. 5.3 shows that the system developed high order at the surfaces, a large reduction in order in the transition region and some structure at lower surface. The normalised density profile in Fig. 5.4 shows the structure was due to smectic-like layering in the lower surface region, to a distance of around $20\sigma_0$.

Figure 5.1: Snapshot of the field-aligned fixed-particle substrate HAN system: Lower surface on left, upper surface on right, fixed particles shown in blue.

As with the relaxation runs in Chapter 4, relaxation on removal of the field was performed in the NVE ensemble. The simulation box was divided into 15 slices, with $i = 1$ the lowest. Director tilt angles θ, measured relative to the surfaces, and velocities in the x direction were calculated for each slice in each saved configuration, then smoothed with smoothing parameter $w = 0.02$ to produce time-resolved plots. The timescale of these plots is in units of $10^6\delta t$ where δt is the timestep. The time of field removal is used to set $t = 0$.

The tilt angle for each slice is shown in Fig. 5.5. The velocity v_x in the surface

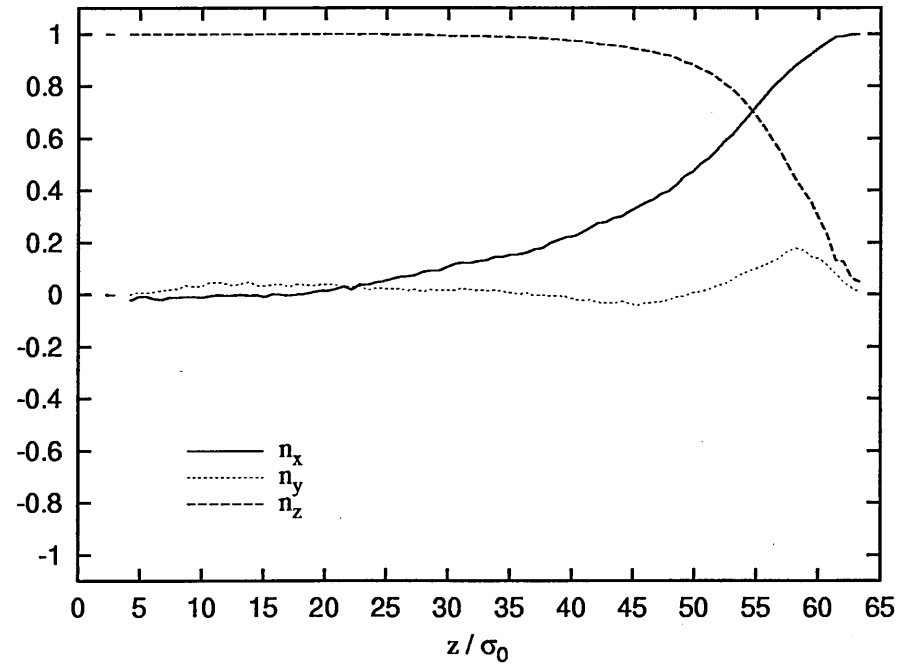

Figure 5.2: Field on director profile of the fixed-particle substrate HAN system.

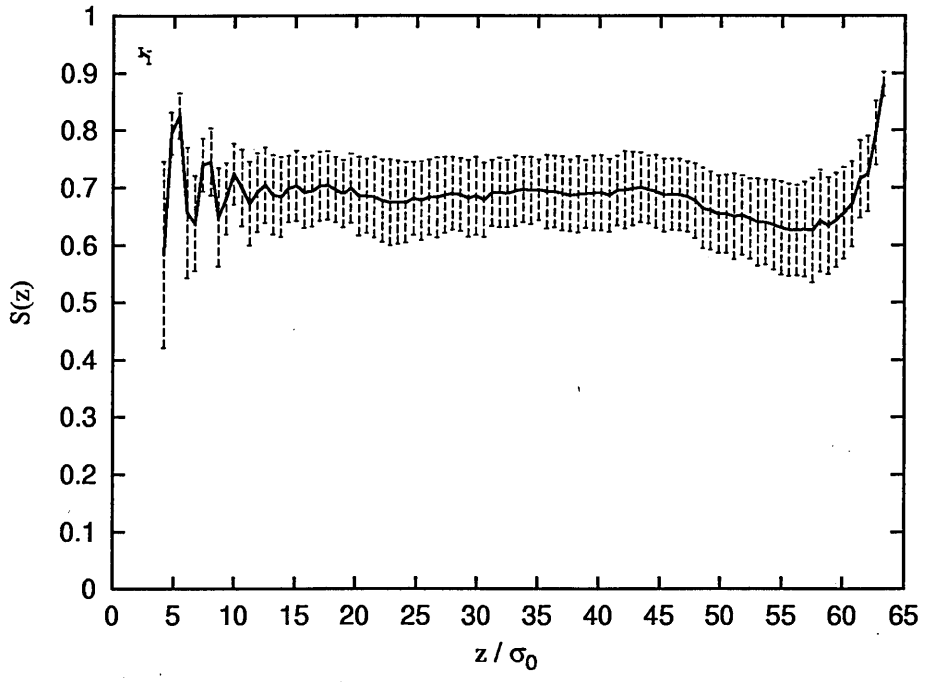

Figure 5.3: Field on orientational order profile of the fixed-particle substrate HAN system.

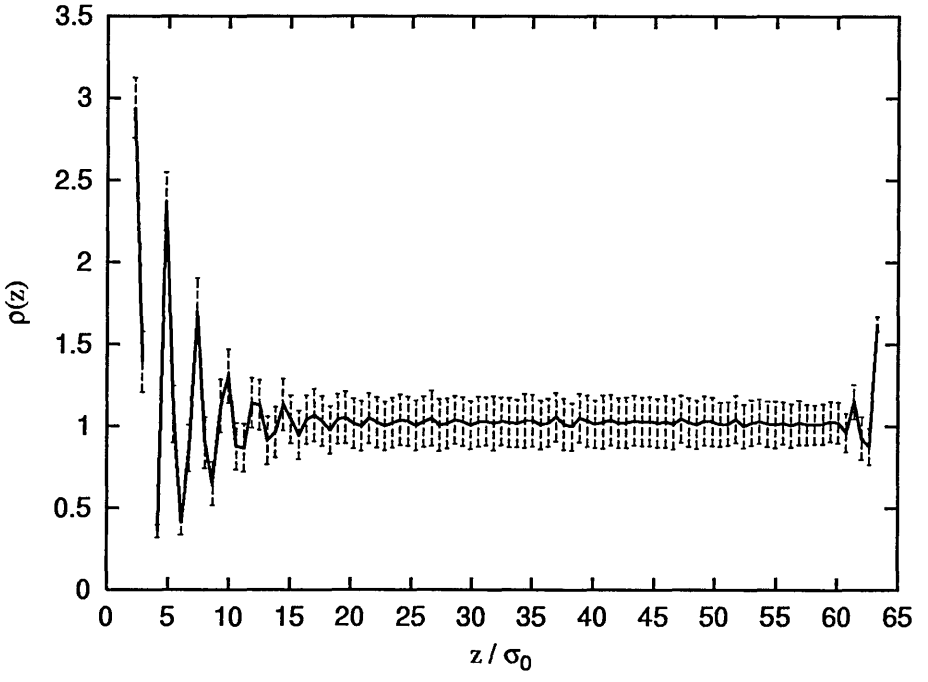

Figure 5.4: Field on normalised density profile of the fixed-particle substrate HAN system.

regions and alternate bulk regions are shown in Fig. 5.6, with each region offset by 0.05. These show that the relaxation, unlike that of the systems in Chapter 4, was not smooth.

The tilt angles in the central region, which were initially aligned normal to the surfaces, relaxed back to their equilibrium values with what appears to be an oscillatory motion. Oscillatory behaviour can also be seen for the velocity in the central regions.

A clearer representation of the overall relaxation can be gained by visualising the director and velocity profiles over time as shown in Fig. 5.7 and Fig. 5.8. Profiles are taken from the data in Fig. 5.5 and Fig. 5.6 at intervals of $60\times10^3\delta t$ with $t = 0$ leftmost. The directors are coloured blue for $\theta = 0°$, through yellow at $\theta = 45°$ and back to blue at $\theta = 90°$. The velocities are coloured red for $v_x > 0$ and green for $v_x < 0$.

These visualisations show that an initial relaxation of the director occurred in the upper half of the box followed, at around $0.3 \times 10^6 \delta t$, by a large positive flow in the upper half of the box. This was followed by a rotation of the director in the lower half of the box. This rotation then reversed after $0.6 \times 10^6 \delta t$, and was followed by a negative flow. From then on, the tilt and flow showed damped oscillatory behaviour as the system relaxed.

The geometry of this system could be compared to the upper half of a splay geometry cell where backflow and kickback can be observed, as illustrated in Fig. 2.2. If the dynamics were comparable, then, in this system, the large magnitude initial flow ought to have been negative, thus causing the director in the lower region to tilt to an angle greater than 90°.

In contrast, the behaviour of this system appears to be dominated by the relaxation of orientational elastic stresses, subject to strong pinning at the bottom surface. The elastic wave appears to have been reflected at the boundaries, and gradually dissipated by viscous damping associated with the observed velocity profile.

The flow in the system was concentrated in the upper regions, with no flow present at the surfaces. The bulk flow pattern indicates that the larger velocities are developed in regions with approximately planar alignment. This is consistent with studies [66, 67] of the Gay-Berne nematic showing that, of the Miesowicz viscosity coefficients, the coefficient η_2, corresponding to a director parallel to the flow velocity gradient, is the largest. Another factor which could influence the flow profile is an effective increase in viscosity caused by interdigitation of the smectic-like layers in the lower surface region. The absence of flow at the surfaces indicates strong coupling between the bulk and surface particles.

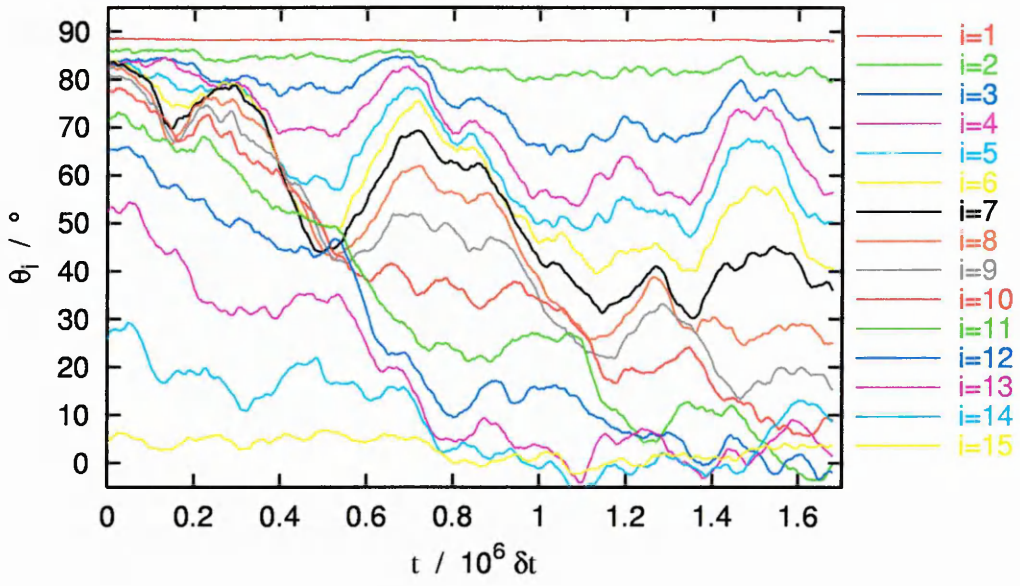

Figure 5.5: Director tilt angle on relaxation of the fixed-particle substrate HAN system. The simulation box is divided into 15 slices with index i, where $i = 1$ is the lower surface.

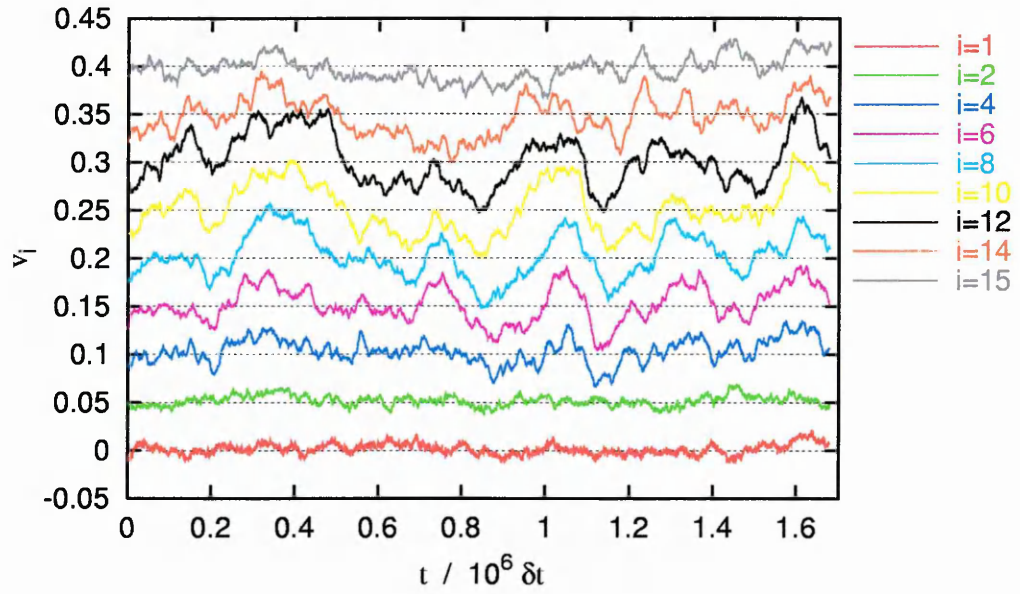

Figure 5.6: Velocity on relaxation of the fixed-particle substrate HAN system. The simulation box is divided into 15 slices with index i, where $i = 1$ is the lower surface and the lowest line on the plot. Each slice is plotted with a 0.05 offset from the previous slice.

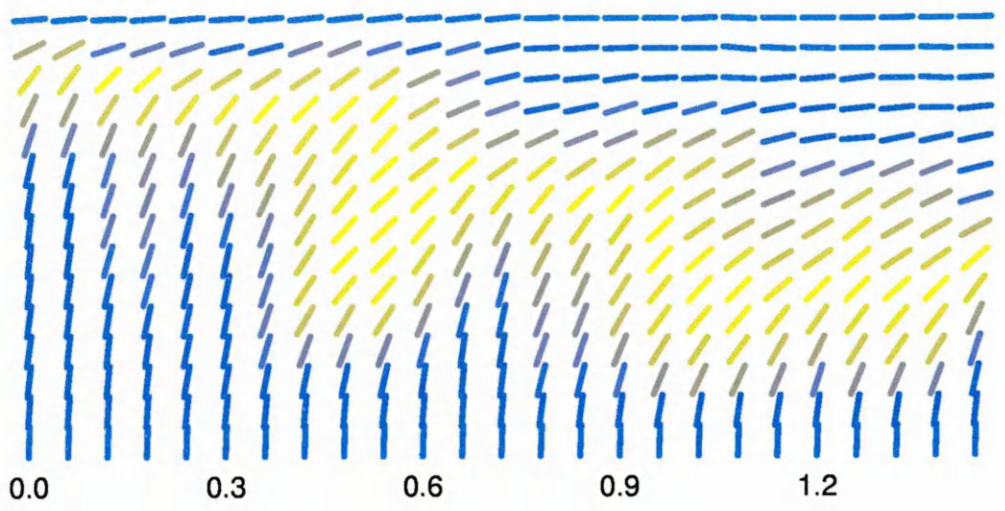

Figure 5.7: Visualisation of the director at intervals of $60\times10^3\delta t$ during relaxation of the fixed-particle substrate HAN system shown in Fig. 5.5. Directors are coloured blue for $\theta = 0°$, through yellow at $\theta = 45°$ and back to blue at $\theta = 90°$.

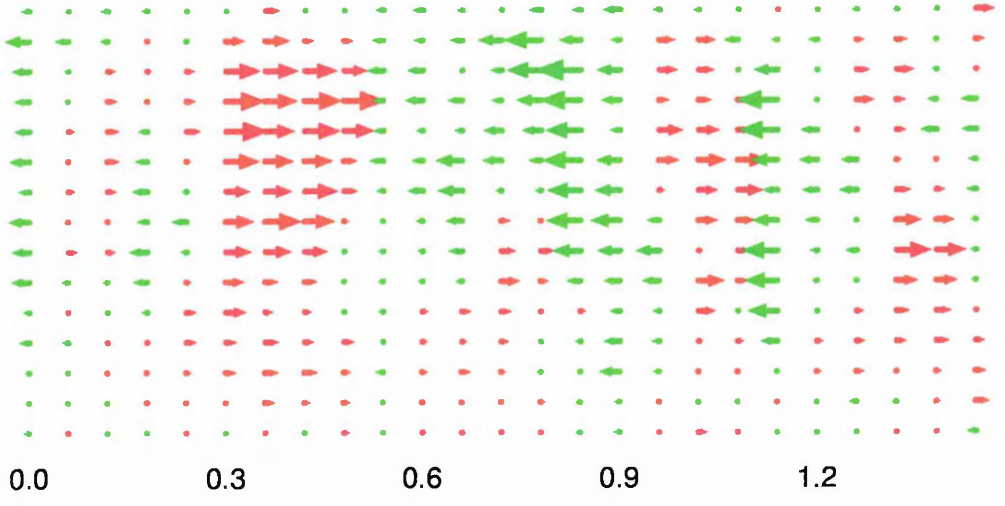

Figure 5.8: Visualisation of the velocity at intervals of $60\times10^3\delta t$ during relaxation of the fixed-particle substrate HAN system shown in Fig. 5.6. Velocities are coloured red for $v_x > 0$ and green for $v_x < 0$.

5.3 Planar Upper Surface System

To study a HAN system with less imposed structure at the surfaces, a system was created with continuum surfaces, giving normal alignment at the lower surface and planar alignment at the upper surface. The well-depth function was modulated across the surface to model the effects of surface structure and reduce slip across the surface.

The surface potential used was the 9-3 continuum surface used in Section 4.2, with modifications made to the shape and well-depth functions to create the required surface alignments. To create normal alignment at the lower surface, a sphere-sphere shape function was used, which reduces the function to a constant thus,

$$\sigma_{sp} = \sigma_0. \tag{5.1}$$

This allows penetration of the surface, leading to alignment normal to the surface as shown in Fig.5.9.a. A similar orientation-independent well-depth function was used,

$$\epsilon_{sp} = \epsilon_0 \left[1 + A(1 + \sin(Br_x))\right], \tag{5.2}$$

in which surface friction is modelled by modulating the well-depth ϵ_0 by a frequency ω where $2A$ is the amplitude and $B = \frac{2\pi\omega}{L_x}$ and L_x is the size of the simulation box in the x direction. The aim of this modulation was to restrict movement across the surface, without pinning particles or introducing smectic ordering.

To create planar alignment at the upper surface, a particle-plane shape function was derived by integrating the particle-sphere function in the xy plane giving

$$\sigma_{sp} = \sigma_0 \sqrt{\frac{1 - \chi \sin^2\theta}{1 - \chi}}, \tag{5.3}$$

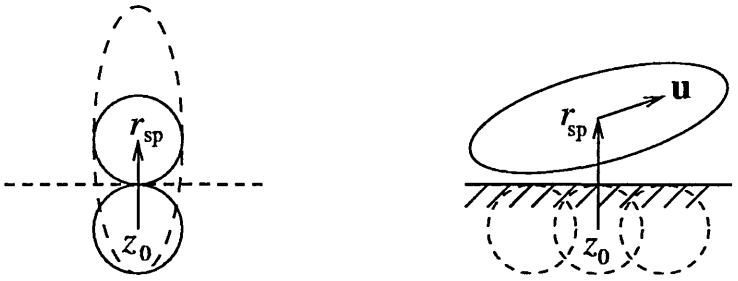

a b

Figure 5.9: Particle-surface shape functions: (a) Sphere-sphere, (b) Particle-plane.

where θ is the angle between the particle long axis and the surface normal **Z**. With this shape function, the particle is repelled if it penetrates the plane of the surface, leading to planar surface layer alignment, as shown in Fig.5.9.b. A similar change was made to the well-depth function,

$$\epsilon_{sp} = \epsilon_0 \left[\left(\frac{1-\chi'}{1-\chi' \sin^2 \psi} \right)^{\mu} + \chi'' \cos^2 \phi (1 - \cos^2 \theta) + A(1 + \sin(Br_x)) \right], \quad (5.4)$$

which also included the azimuthal alignment terms used in Chapter 4 and the well-depth modulation terms.

A system of 3520 GB35 particles was created using the method described in Section 4.1.4. The simulation box dimensions were $L_x = 15$, $L_y = 12$ and $L_z = 60.17094$ giving a number density $\rho = 0.325$.

The surface parameters used were $\chi'' = 0.2$, $\delta = 5°$ and $\alpha = 2\sqrt{10(1-\chi^2)^{\nu}/9}$. The pretilt was included here to bias the direction of any small tilt occurring at the surface.

Two independent runs were performed. The initial configurations were created by re-randomising the velocities of existing systems with temperature T=1.2, which had been used to explore suitable temperatures and field strengths. The

first of these runs was an equilibration of a system with no applied field and surface alignment but no surface structure. The second was a relaxation run of a field-aligned system, with roughening of the surfaces.

The field off system was equilibrated at T=1.2 for 1,320,000 timesteps. A run of 220,000 steps on 32 nodes took around 335 minutes. Configurations were saved every 500 steps. Static profiles were block averaged over 220,000 timesteps.

The director profile in Fig. 5.10 shows that the system developed regions near each surface where the surface alignment was projected into the bulk region. There is also a large twist in the central region.

The orientational order profile in Fig. 5.11 shows that while high order developed at the surfaces, the order reduced in the surface regions; the greatest reduction being near the upper surface. This suggests that the surface separation was too small to allow a change in the tilt from one surface to the other without a reduction in order in some part of the box.

The density profile in Fig. 5.12 shows that similar smectic-like layering occurred in the lower surface regions to that in the fixed-particle HAN system in Section 5.2.

For the field-aligned system, the surface structure was modelled by setting the well-depth modulation amplitude $A = 0.5$. The modulation parameter B was set to give 17 undulations across the surface in the x direction. This was found to promote hexagonal packing of particles on the lower surface, with rows of particles aligned with the x sides of the simulation box.

The applied field strength was $h^2 k_{11}/\rho = 16$. This system was equilibrated for 1,760,000 timesteps at T=1.2. A snapshot of this system is shown in Fig. 5.13.

The director profile in Fig. 5.14 reveals a saturated region in the lower half of

the box and a transition region in the upper half. A twisting of the director is apparent in the transition region.

The order profile in Fig. 5.15 shows a reduced order in the transition region. A comparison of the order profiles for the field off and field on systems shown in Fig. 5.16 reveals that the applied field had the effect of enhancing the order in the lower surface region and reducing the order in the upper surface region. The order in the central region does not show a significant change.

Compared with the profiles for the fixed particle field-aligned system in Fig. 5.2 and Fig. 5.3, where the director rotated smoothly through the transition region and the lowest order in the transition region was near the surface, the profiles here show a series of regions where the director changes alternately slowly, then quickly and the lowest order in the transition region is away from the surface.

The same plots of the relaxation of this system as those shown for the fixed-particle system in Section 5.2 are shown in Fig. 5.17 and Fig. 5.18, with $t = 0$ set at the time of field removal. For the visualisation of this motion, in Fig. 5.19 and Fig. 5.20 profiles are shown at intervals of $48 \times 10^3 \delta t$.

The overall relaxation was similar to, but smoother than, that of Section 5.2. Again, the director profile displayed damped oscillatory motion on relaxation. The initial reorientation extended down near to the lower surface at around $0.24 \times 10^6 \delta t$. The lower regions then rotated back up before relaxing to their equilibrium orientations.

Various factors could be responsible for the difference in the overall character of the relaxation between this system and the particle surface system: the field strength here was weaker than that in the particle surface system, the initial tilt profile in this system would lead to the initial reorientation occurring further into

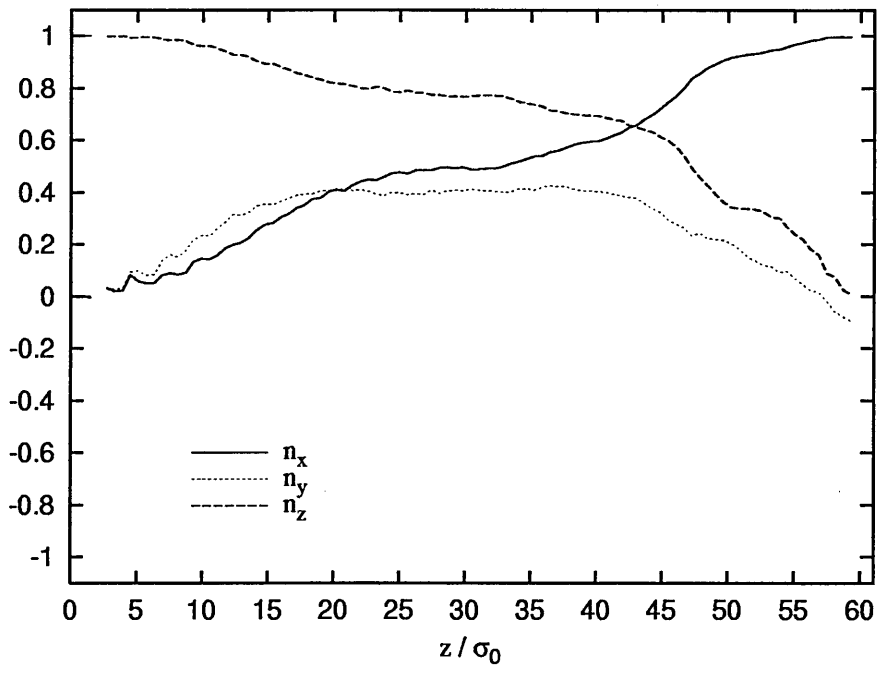

Figure 5.10: Field off director profile of the planar upper surface HAN system.

the bulk region than in the particle surface system, the splay region developed a larger twist here than in the particle surface system and weaker pinning of the surface layer here than in the particle surface system could have provided an extra damping mechanism through near surface diffusion.

The region of positive flow, which occurred just before the tilting of the director in the lower regions in the system in Section 5.2, here seems to have occurred just after the director motion. This suggests that the tilt and the flow are coupled and influence each other, but that the flow did not necessarily cause the tilt in the lower regions in the system in Section 5.2.

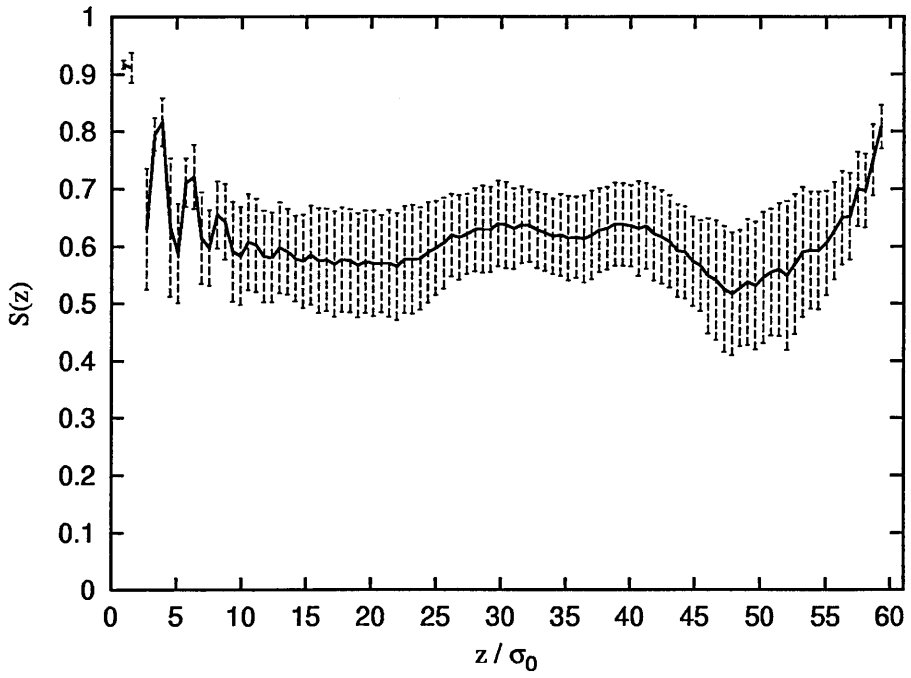

Figure 5.11: Field off orientational order profile of the planar upper surface HAN system.

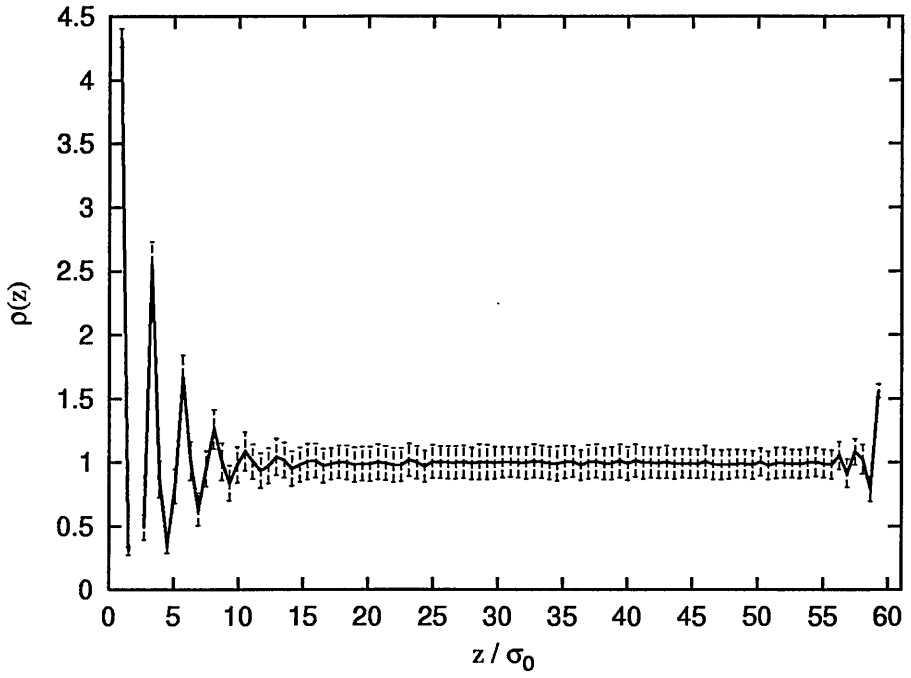

Figure 5.12: Field off normalised density profile of the planar upper surface HAN system.

Figure 5.13: Snapshot of the field-aligned planar upper surface HAN system: Lower surface on left, upper surface on right.

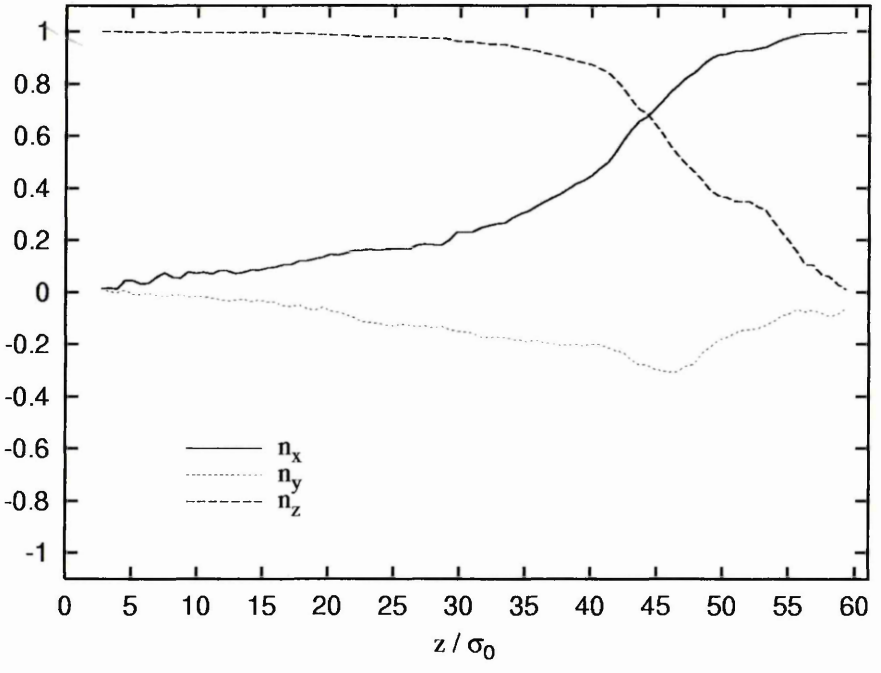

Figure 5.14: Field on director profile of the planar upper surface HAN system.

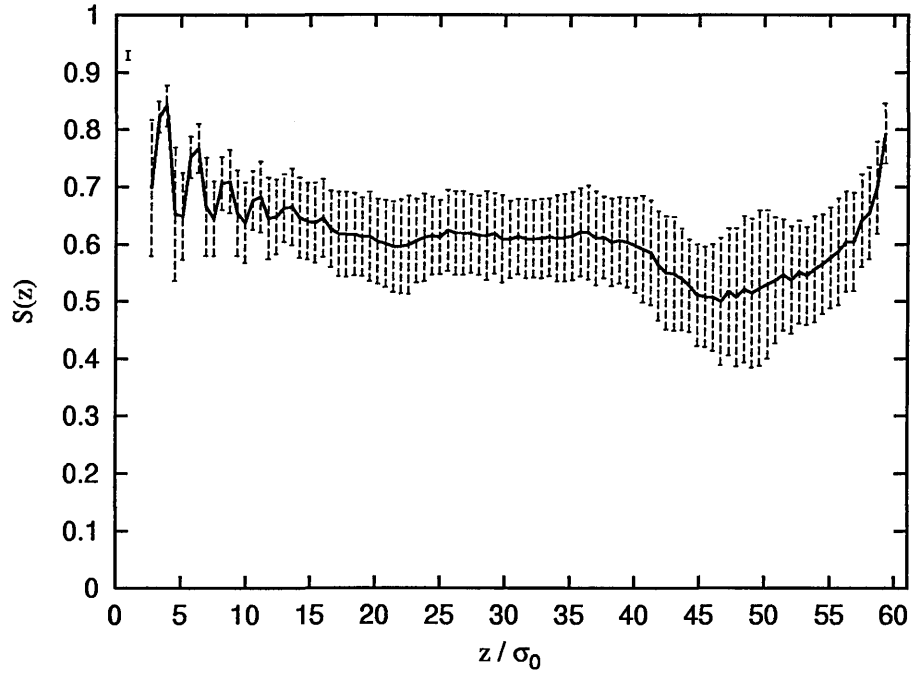

Figure 5.15: Field on orientational order profile of the planar upper surface HAN system.

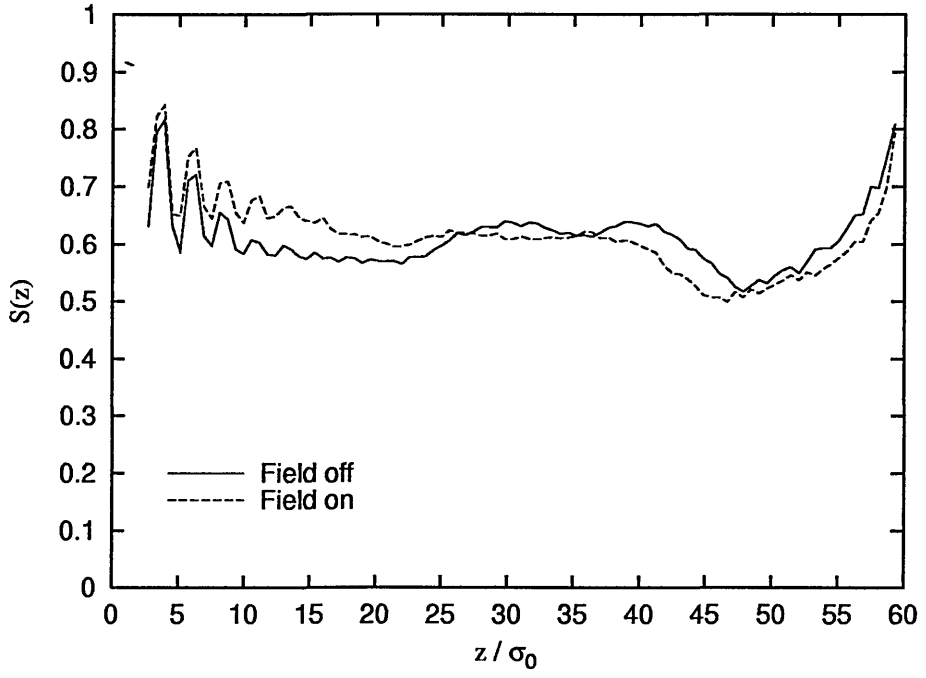

Figure 5.16: Orientational order profiles of the field off and field on planar upper surface HAN systems.

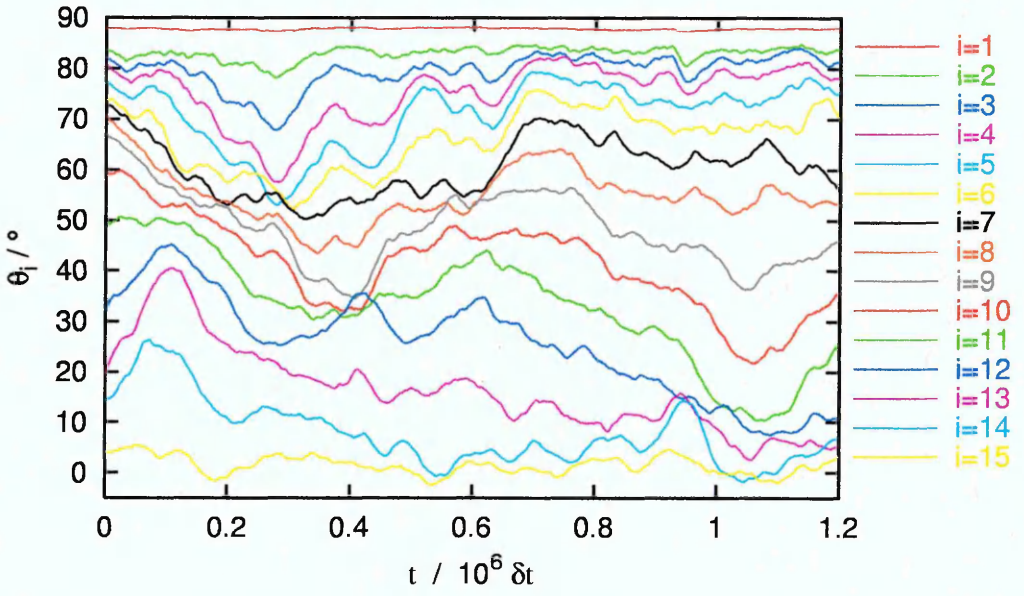

Figure 5.17: Director tilt angle on relaxation of the planar upper surface HAN system. The simulation box is divided into 15 slices with index i, where $i = 1$ is the lower surface.

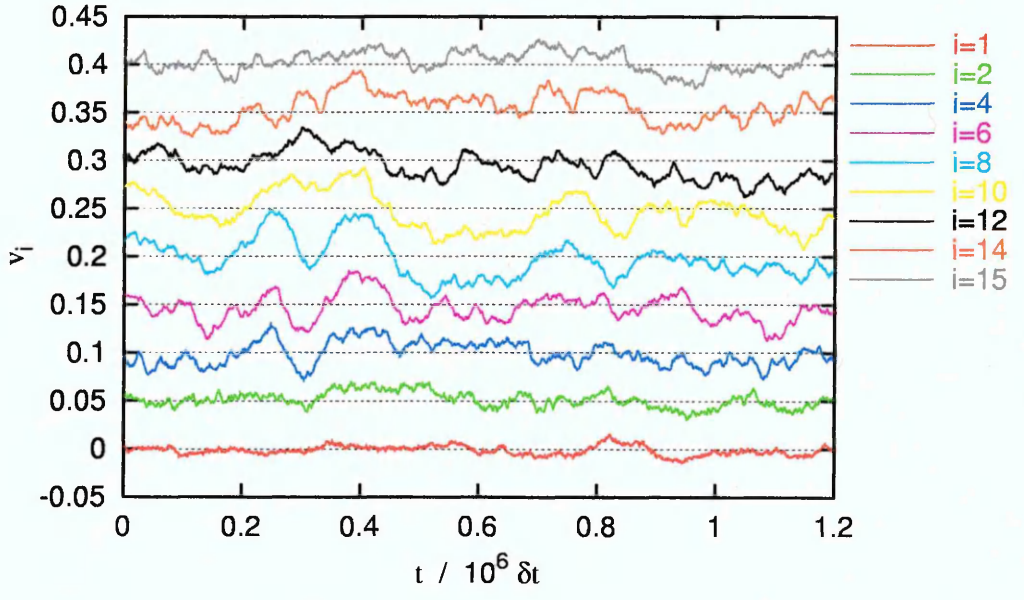

Figure 5.18: Velocity on relaxation of the planar upper surface HAN system. The simulation box is divided into 15 slices with index i, where $i = 1$ is the lower surface and the lowest line on the plot. Each slice is plotted with a 0.05 offset from the previous slice.

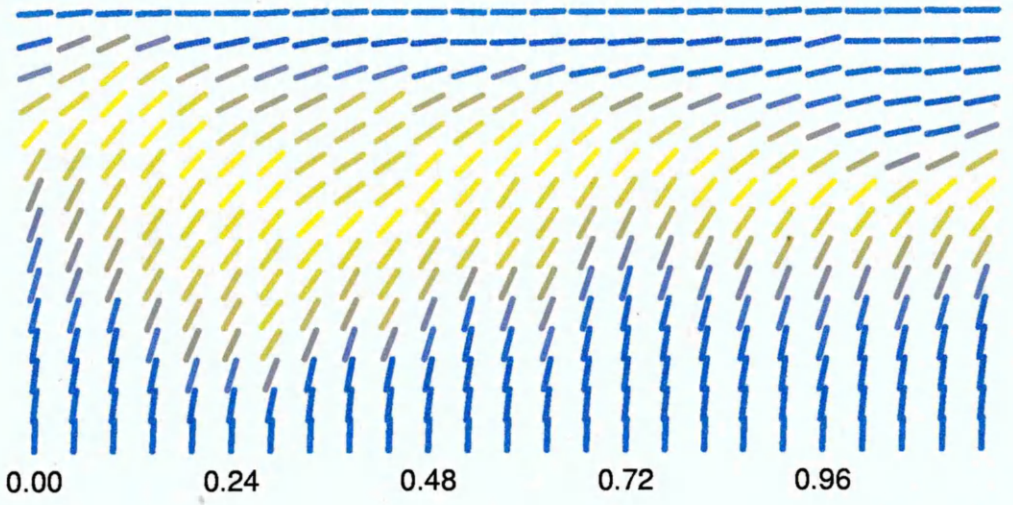

Figure 5.19: Visualisation of the director at intervals of $48\times10^3\delta t$ during relaxation of the planar upper surface HAN system shown in Fig. 5.17. Directors are coloured blue for $\theta = 0°$, through yellow at $\theta = 45°$ and back to blue at $\theta = 90°$.

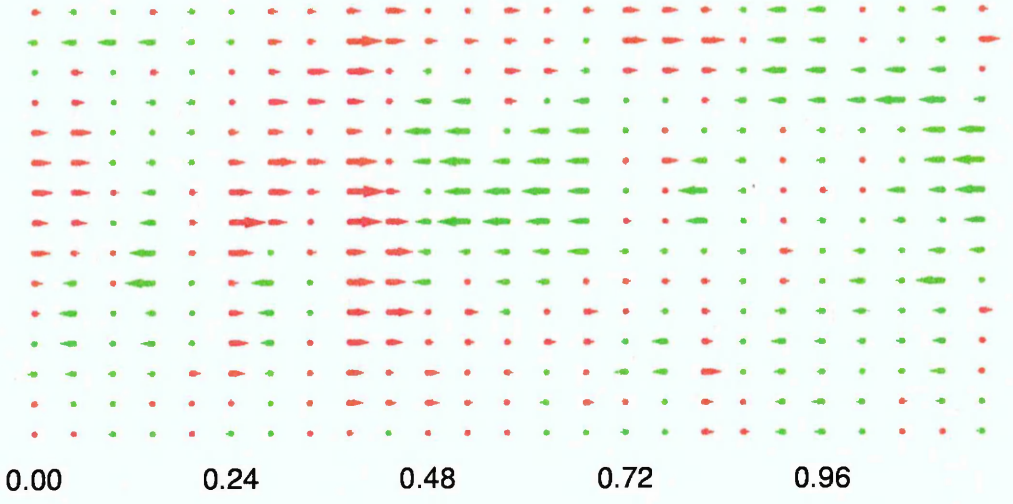

Figure 5.20: Visualisation of the velocity at intervals of $48\times10^3\delta t$ during relaxation of the planar upper surface HAN system shown in Fig. 5.18. Velocities are coloured red for $v_x > 0$ and green for $v_x < 0$.

5.4 Tilted Upper Surface System

In order to further reduce the director distortion needed to create a large saturated bulk region, a simulation of HAN system with a tilted upper surface was performed.

For the lower surface, the same sphere-sphere potential was used as that used for the lower surface of the HAN system in Section 5.3. For the upper surface, the same particle-sphere surface potential was used as that used in the GB35 system in Section 4.4, with the addition of the well-depth modulation term to give

$$\sigma_{sp} = \sigma_0 \left[\frac{1}{1 - \chi \cos^2 \theta} \right]^{\frac{1}{2}} \tag{5.5}$$

and

$$\epsilon_{sp} = \epsilon_0 \left[(1 - \chi' \cos^2 \psi)^{\mu} + \chi'' \cos^2 \phi (1 - \cos^2 \theta) + A(1 + \sin(Br_x)) \right]. \tag{5.6}$$

The field strength, surface potential parameters, system size and preparation and equilibration of the initial configuration were identical to those of the HAN system in Section 5.3.

For the field off system, the director profile in Fig. 5.21 shows that the two surface regions had the surface orientation projecting into the bulk, and that in the central bulk region the director rotates from its normal to its tilted orientation.

The order profile in Fig. 5.22 reveals a dip in the order above the lower surface region, and a near surface order profile at the upper surface similar to the particle substrate HAN system in Section 5.2. This suggests that the change in director orientation from one surface to the other was localised in small regions near both surfaces rather than being concentrated in the upper surface as in the HAN system in Section 5.3. The reduced density profile in Fig. 5.23 again shows smectic-like layering at the lower surface.

A snapshot of the field-aligned system is shown in Fig. 5.24. For this system, the director profile shown in Fig. 5.25 reveals a twisting of the director in the splay region, which was also observed in the field-aligned profiles of the HAN systems in Section 5.2 and Section 5.3.

A comparison of the order profiles for the field off and field on system in Fig. 5.26 shows that the applied field enhanced the order in the bulk and reduced the order in the distorted upper surface region. Even though for the field off case, this system had higher order in the tilted upper surface region than that in the planar upper surface region of the HAN system in Section 5.3, with the field on, a similar reduction in order occurred as that in Section 5.3, with the lowest order again occurring away from the surface.

The same plots of the relaxation on removal of the field were created as those for the relaxation of the HAN system in Section 5.3. These are shown in Fig. 5.27 to Fig. 5.30, with $t = 0$ set at the time of field removal.

The overall relaxation behaviour again shows that the region of reorientation moved down to rotate the director in the lower surface region. This rotation then reversed. The flow pattern was less distinct and of lower magnitude than in the previous HAN systems. No large initial flow associated with the reorientation of the director in the lower surface regions is apparent and the damped oscillatory behaviour established itself earlier.

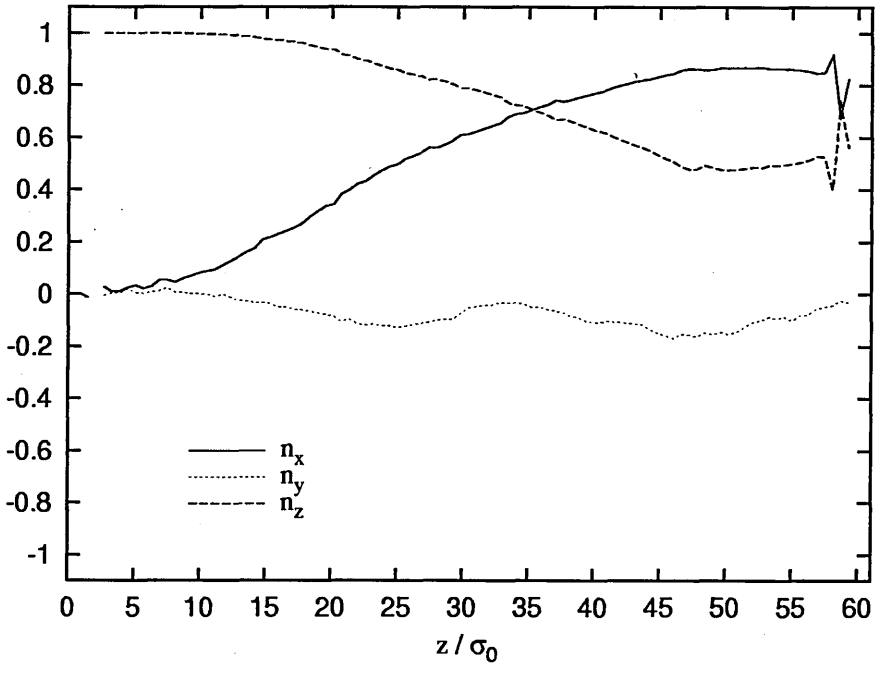

Figure 5.21: Field off director profile of the tilted upper surface HAN system.

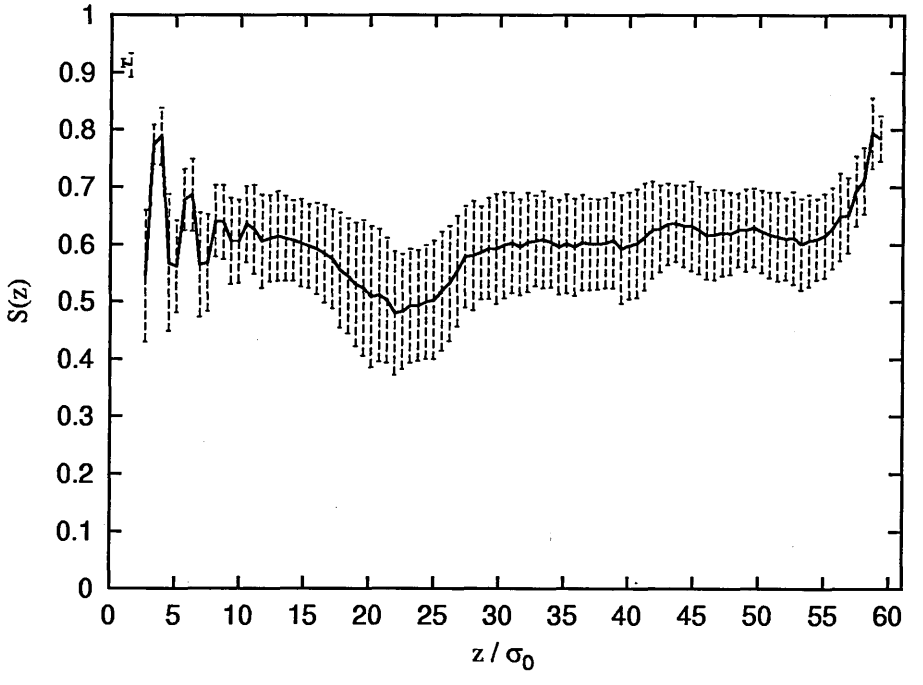

Figure 5.22: Field off orientational order profile of the tilted upper surface HAN system.

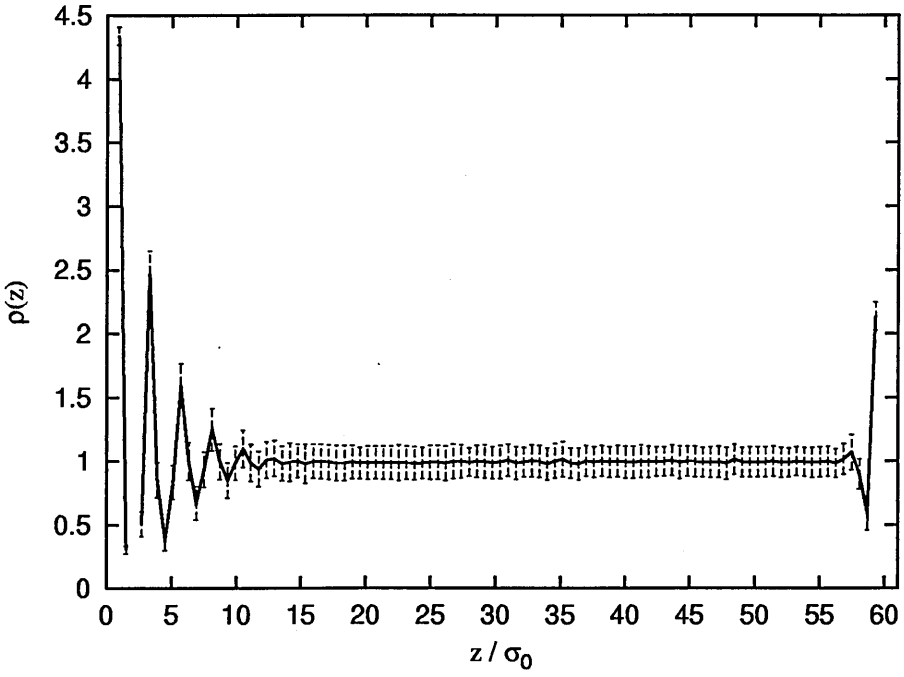

Figure 5.23: Field off normalised density profile of the tilted upper surface HAN system.

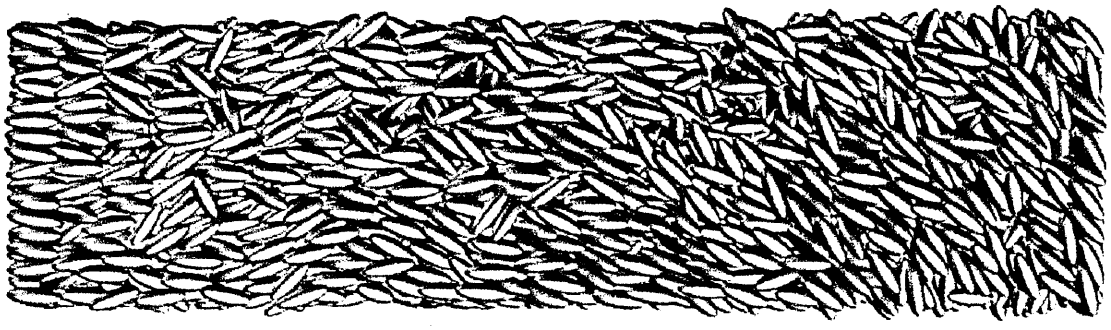

Figure 5.24: Snapshot of the field-aligned tilted upper surface HAN system: Lower surface on left, upper surface on right.

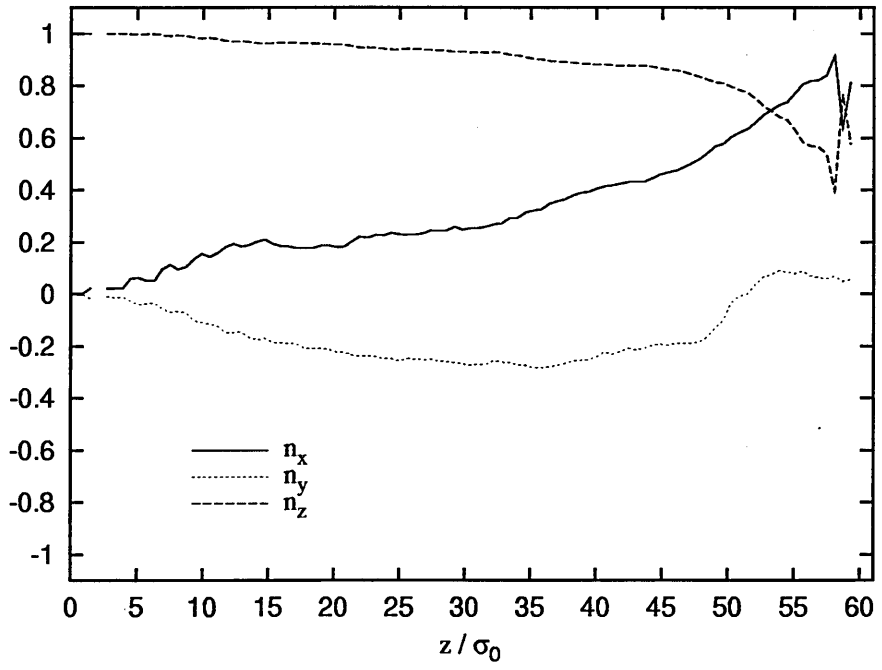

Figure 5.25: Field on director profile of the tilted upper surface HAN system.

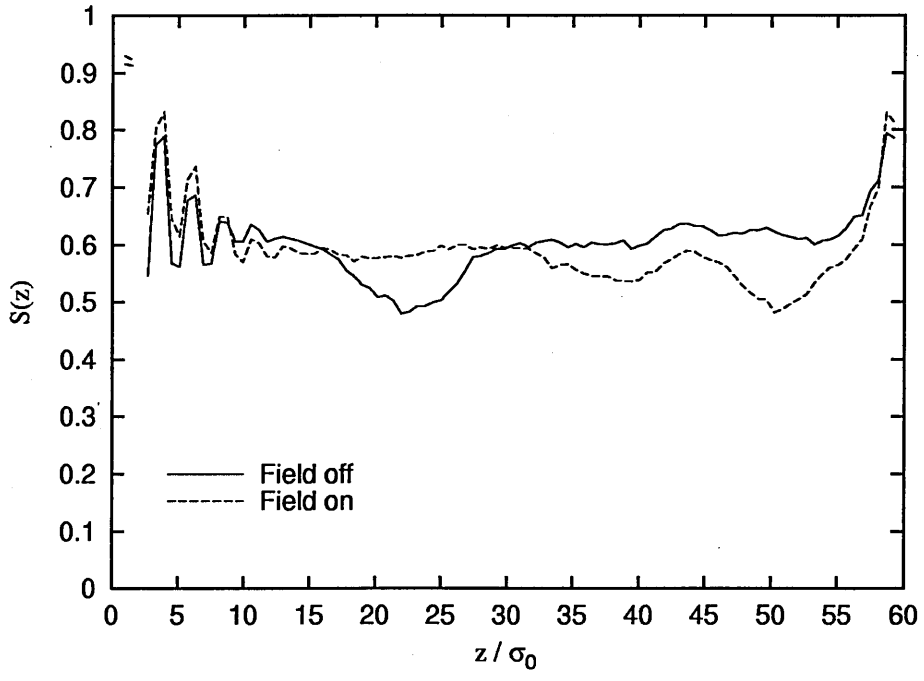

Figure 5.26: Order profiles of the field off and field on tilted upper surface HAN systems.

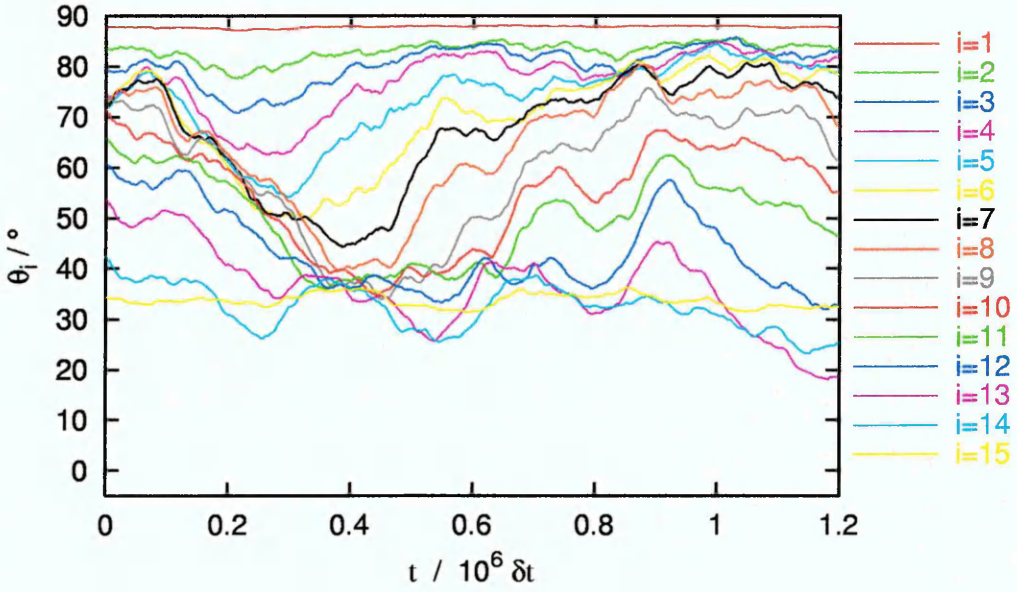

Figure 5.27: Director tilt angle on relaxation of the tilted upper surface HAN system. The simulation box is divided into 15 slices with index i, where $i = 1$ is the lower surface.

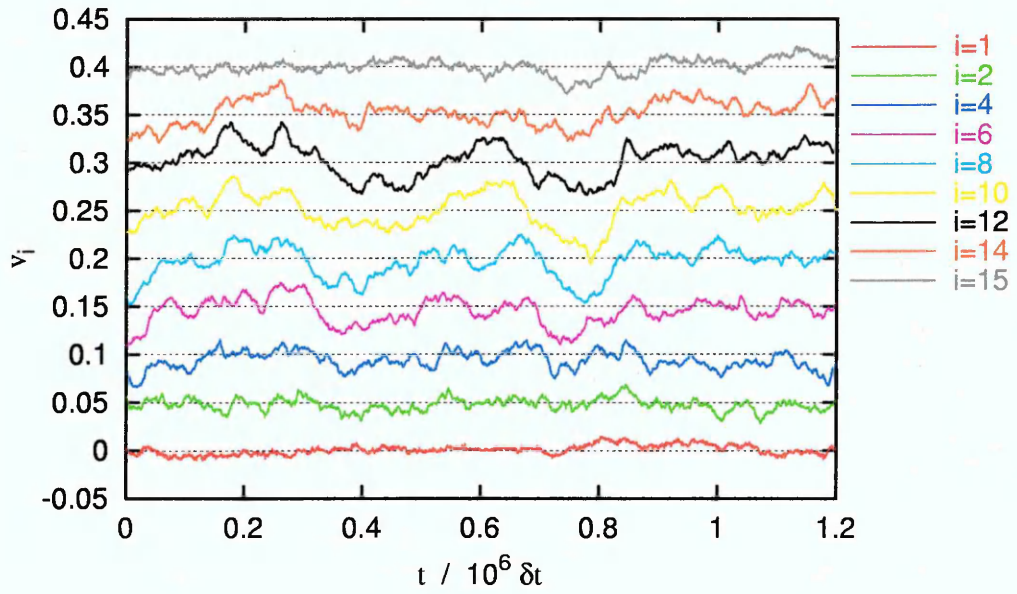

Figure 5.28: Velocity on relaxation of the tilted upper surface HAN system. The simulation box is divided into 15 slices with index i, where $i = 1$ is the lower surface and the lowest line on the plot. Each slice is plotted with a 0.05 offset from the previous slice.

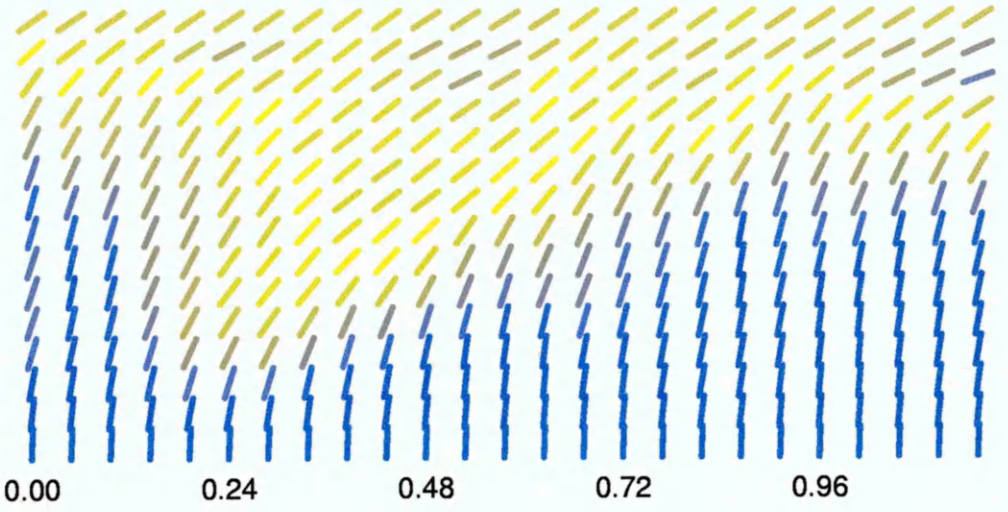

Figure 5.29: Visualisation of the director at intervals of $48{\times}10^3\delta t$ during relaxation of the tilted upper surface HAN system shown in Fig. 5.27. Directors are coloured blue for $\theta = 0°$, through yellow at $\theta = 45°$ and back to blue at $\theta = 90°$.

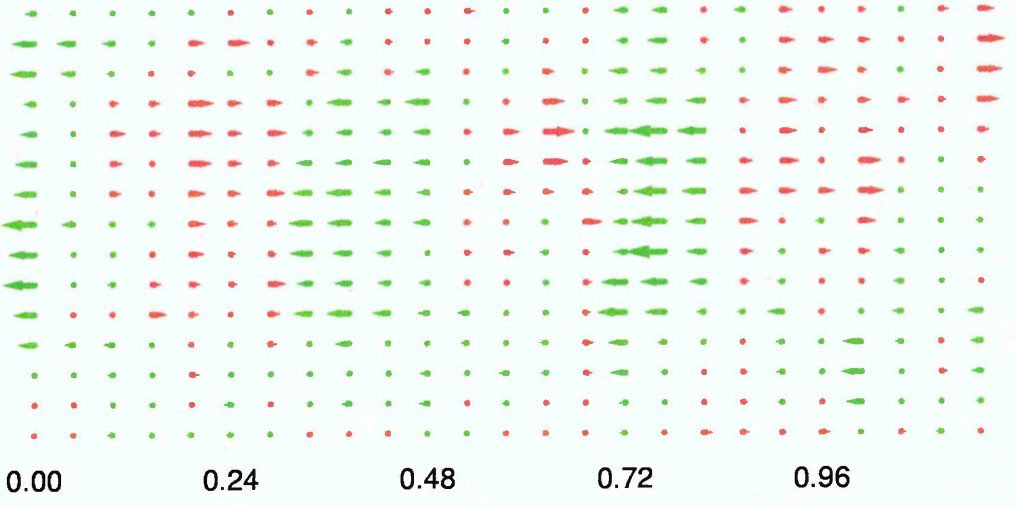

Figure 5.30: Visualisation of the velocity at intervals of $48{\times}10^3\delta t$ during relaxation of the tilted upper surface HAN system shown in Fig. 5.28. Velocities are coloured red for $v_x > 0$ and green for $v_x < 0$.

5.5 Summary

The aim of the simulations of the HAN systems presented in this chapter was to determine whether the macroscopic processes of backflow and orientational kick-back could be observed in a confined molecular system on removal of an aligning field. The geometry of these systems required only one transition region at the upper surface, and so allowed a large field aligned bulk region, thought necessary for induced flow phenomena, without excessive distortion of the transition region.

The field off director and order profiles for the continuum wall systems suggest that the surface separation of $\approx 60\sigma_0$ may not have been sufficient to allow the director to rotate from its lower to its upper surface orientation without a reduction in order somewhere in the system. This appears to have happened at arbitrary points between the surfaces, rather than across the box as a whole. The points where the director changes suddenly seem to correspond to regions of low order in the system.

All the field-aligned systems showed a reduction in order and some degree of localised twisting of the director throughout the distorted near-surface transition regions.

On relaxation, all systems displayed the same overall behaviour. The initial rotation of the director occurred near the upper surface and then this region of reorientation moved down to the lower surface. The rotation of the lower surface region then reversed, with the director motion and flow showing damped oscillatory behaviour as the system relaxed.

The overall flow pattern showed an absence of flow at the surfaces, indicating coupling between the bulk particles and the surfaces. The flow was concentrated in the upper regions, which is consistent with the estimated Gay-Berne nematic

viscosities $\eta_2 > \eta_1$ and could also be due to the influence of interdigitation of the smectic-like layers induced by the lower surface.

The magnitude of the initial flow, associated with movement of the initial reorientation region down to the lower surface, compared with the flow magnitude in the later stages of the relaxation was greatest for the particle substrate system, less for the planar continuum surface system and least for the tilted continuum surface system. The main reason for the large magnitude of the flow in the particle substrate system was probably the higher field strength and thus higher initial distortion in the upper surface region. The lack of an initial large magnitude flow in the tilted continuum surface system was probably due to the lower director distortion needed to rotate the director from the field-aligned bulk orientation to the tilted surface orientation. Another factor responsible for the difference in overall behaviour could be weaker pinning of particles in the continuum surface systems creating an extra damping mechanism for the oscillating flow patterns in these system.

The estimate made in Section 4.7 of the real value of the simulation timescale in these systems gives a value of $10^6 \delta t \approx 15$ns. This contrasts with relaxation timescales of real cells of the order of microseconds. This estimate of the relaxation timescale, and the oscillatory nature of the relaxation in these systems, suggests that their behaviour was dominated by elastic forces and that the director motion and flow observed here do not correspond to the macroscopic processes of backflow and kickback observed in real cells.

Chapter 6

Chevron Formation and Stability

6.1 Introduction

This chapter presents results of an attempt to study a surface-stabilised chevron structure. The mechanism thought to be responsible for chevron formation is the need to resolve the mismatch between changing bulk layer spacing and frozen surface layer spacing which develops on cooling a system. Although the transition from a S_A or S_B phase to a S_C phase would produce a change in the layer spacing, the S_C phase has only been observed in the single-site Gay-Berne model by the addition of quadrupoles, as in [63], which is beyond the scope of this work.

Layer thinning due to increased interdigitation on cooling has been observed in Gay-Berne smectic systems. Simulations of a Gay-Berne S_B phase by Hashim *et al.* [59] showed values of the layer spacing d_s ranging from $2.64\sigma_0$ to $2.57\sigma_0$ for particles of length $3\sigma_0$. Simulations of a Gay-Berne S_A phase by Bates and Luckhurst [62] showed values of d_s ranging from $3.9\sigma_0$ to $3.85\sigma_0$ for particles of length $4.4\sigma_0$.

The layer tilt θ given by the layer thinning mechanism for a bulk layer spacing

d_s and a surface layer spacing s_s is

$$\theta = \arccos(d_s/s_s). \tag{6.1}$$

This would give tilt angles for the systems in [59] and [62] of $\theta \approx 13.2°$ and $\theta \approx 9.2°$ respectively. These compare with a tilt of $\theta = 8.5°$ measured experimentally by Morse and Gleeson [23] in a S_A chevron.

The mechanism of chevron formation could perhaps be studied with some form of frozen-particle surface with a structure matched to the layer spacing of a high temperature smectic phase, but the effect of periodic boundary conditions could invalidate analysis of any tilt produced on cooling. In a simulation, smectic layers can tilt in order to resolve a mismatch between the periodicity imposed by the layer spacing and the periodicity imposed by periodic boundaries. In a simulation, it would be difficult to determine whether any tilt seen was due to interaction between bulk layers and surface layers or due to interaction between bulk layers and the periodic boundary conditions. For these reasons the following simulations were limited to determining whether a surface stabilised chevron structure could exist in a molecular thin film and if so, the possible effects of surface anchoring on the stability of the structure.

Periodic boundary conditions will also affect the fine detail of the chevron tip structure. If the periodicity of the tilted layers in a chevron structure is matched to the size of the simulation box, at the chevron tip, where the tilt approaches zero, this match will break down. This mismatch could be resolved at the tip by melting or by the layers twisting to an angle equivalent to the tilt angle.

6.2 Simulation Details

In the simulations for a small system of 256 particles performed in Section 4.2 the smectic phase obtained consisted of three tilted layers. The tilt was probably influenced by both the surface pre-tilt and the interaction between the layer spacing and the periodic boundaries. The method used here to attempt to create a chevron structure was to use two surfaces having equal and opposite pre-tilts which would impose equal and opposite tilts on the smectic layers in each half of the simulation box.

Rather than slowly cooling a system into the smectic region, the method of formation used was to quench a nematic into a S_B phase. To induce the system to form a symmetric chevron the system was quenched from a point close to the N-S_B transition line, with the intention that the tilted layers would grow out from each surface and meet in the middle to form a chevron tip.

The parameters used for the intermolecular potential were $\nu = 1$, $\mu = 2$, $\kappa = 3$ and $\kappa' = 5$. The conditions for the simulation were chosen from the phase diagram for this parameterisation in [54] to be a system with density $\rho = 0.33$ quenched from T=0.95 to T=0.85 as shown in Fig. 6.1.

The surface model used was the particle-sphere model with pre-tilt and well-depth modulation described in Section 5.4 with parameters $\alpha = 2\sqrt{\frac{10}{9}(1-\chi^2)^\nu}$, $\chi'' = 0.2$ and $\delta = \pm 5°$.

Well-depth modulation amplitudes of $A = 0.0$, $A = 0.2$ and $A = 0.5$ were used, all with $B = 32\pi/L_x$ where L_x is the length of the simulation box in the x-direction. This gave a width of σ_0 for each oscillation. This size corresponds to the particle width rather than to the smectic layer spacing as used in the surface energy modulation term of Ul Islam *et al.* [33]. This was chosen because the tilt

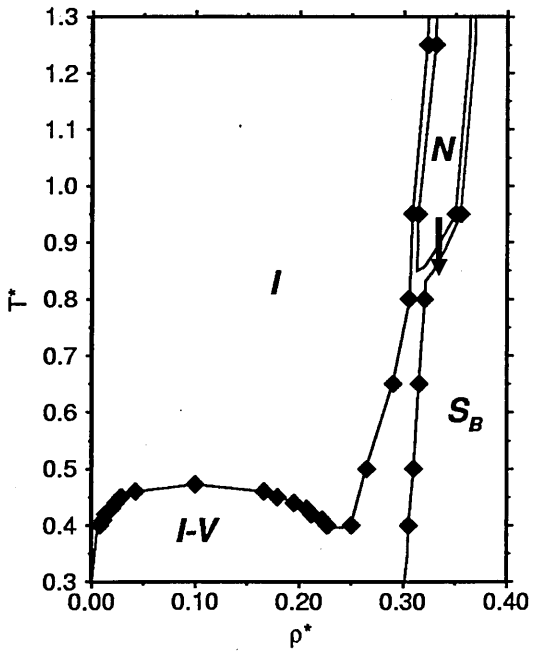

Figure 6.1: Quenching a system from the nematic region at T=0.95 into the Smectic-B region at T=0.85.

of the smectic layers observed in Section 4.2 did not match the tilt of the surface particles and the orientational order dropped near the surface suggesting that the layers did not extend directly onto the surfaces.

The density $\rho = 0.33$ is higher than that of the 256 particle system of $\rho = 0.3$ which gave 3 tilted layers in a box with sides $x = y = 8.101915\sigma_0$. The box sides used here were, therefore, set for six layers with a slight reduction in spacing due to higher density giving $x = y = 16\sigma_0$. The number of particles was 3520, which represents a compromise between system size and simulation time, and the separation between the surfaces was that required for $\rho = 0.33$ giving $z = 41\frac{2}{3}$.

The initial configuration was created in the nematic phase using the method described in Section 4.1.4, at a temperature T=1.2. The first run was performed

in the NVE ensemble to test the code for energy conservation. Then the system was cooled in the NVT ensemble from T=1.2 to T=0.95 in steps of 0.05. Each run consisted of 210,000 steps with a time-step $\delta t = 0.0015$ and took approximately 6 hours on 32 nodes. The T=0.95 system was then equilibrated for a further 630,000 steps when pre-transitional ordering was observed.

6.3 Analysis

To examine the order profile of the structures formed in this system a translational order parameter S_k was used in addition to the orientational order parameter S. This parameter is more significant in distorted smectic systems than the orientational order parameter. The method used to determine S_k is described in Section 3.6.2. This requires the director and the smectic layer spacing to be known.

These were determined by maximizing S_k with respect to the layer spacing by a method similar to that used in [62]. To do this, firstly a suitable part of a run where stable smectic layers had formed was selected. For each saved configuration in this part of the run, the director of the smectic region was found and then used to calculate S_k for a range of trial layer spacings from $2.5\sigma_0$ to $2.6\sigma_0$ in steps of 0.001. The layer spacing for that configuration was taken as that which gave the maximum S_k value. These values were then averaged over the selected part of the run to give the final layer spacing. Finally, this layer spacing was used, together with the local director in each slice, to calculate S_k profiles of the system at all points in the run.

The orientational profiles are shown as a director tilt angle θ measured relative to the xy-plane and the director azimuthal angle ϕ measured in the xy-plane

relative to the positive x-axis. In the S_B system, the director tilt angle also represents the layer tilt angle away from the substrate normal.

To calculate block average profiles the box was divided into 120 slices. Values were taken from the director for each slice in each saved configuration and these were then averaged over the configurations to find the mean and error values for each slice. This was done on the assumption that if the range of angles was small then a simple mean could be used to find the average angle.

This assumption fails in certain cases because an angle is a periodic parameter. For example, the mean of 170° and −170° is 0° whereas the correct value ought to be 180°. The angles were therefore clipped to lie in the range −90° to 90° so that positive and negative angles summed to the correct value. This could be done because the director has no sign, so that angles of θ and $\theta \pm \pi$ are equivalent.

This method still fails if the difference between two angles is greater than 90° because the correct mean angle can only be found by choosing one of the angles to lie outside the range −90° to 90°. To guard against this, a check was made during the analysis to ensure that the range of angles used to calculate the mean within any slice did not exceed 90°.

The position of the chevron tip between the surfaces is taken to be at $\theta = 0$ because even in a melted tip region the nematic director is still defined. To locate this point, starting from a slice above the lower surface region, each slice is checked in turn until the sign of θ changes. The z position for a slice is taken as the z coordinate at the centre of that slice.

The radial distribution function $g(r)$ gives information about the internal structure in a system. It represents the probability of finding two particles at a separation r relative to the expected probability if the distribution of particles

were continuous. In a simulation, $g(r)$ is calculated by forming a histogram of separations to some maximum radius.

For this study, $g_\perp(r_\perp)$ was used to examine the structure within the layers. This takes the separation $r_\perp$ perpendicular to the director between particle centres projected onto the plane of the smectic layers and only considers separations between particles which are in the same layer. Particles are considered to be in the same layer if the separation $r_\parallel$ parallel to the director satisfies $|r_\parallel| < \frac{1}{2}d_s$, where d_s is the layer spacing.

6.4 Quenching

6.4.1 Quenching on Smooth Surfaces

Two quenches of this system were undertaken, the second after a further 110,000 steps. A snapshot of the nematic system at T=0.95 close to the N-S_B transition is shown in Fig. 6.2. Some layering is visible in the upper half of the system.

Profiles of this system were created over 50,000 steps prior to the first quenching. The S profile (Fig. 6.3.a) shows a slight difference in order between the lower and upper halves of the box, and a slight drop in the centre. The S_k profile (Fig. 6.3.b) shows weak positional order ≈ 0.2 throughout the whole box. The tilt angle θ profile (Fig. 6.4.a) shows the desired chevron-like character: rather than a continuous change in tilt between the surfaces, it shows surface regions where the tilt was influenced by the surface pre-tilt, and a central region where the tilt changed quickly. The twist angle ϕ profile (Fig. 6.4.b) shows two domains, each with a different twist at the surface, separated by a region with an oscillating twist profile.

These twists could be due to coupling between the weak positional ordering and the periodic boundaries. To match the period of the box, the weak layers may have twisted rather than tilted in the central region, the oscillations being caused by neighbouring regions twisting in opposite directions.

The normalised density profile (Fig. 6.5) does not show any structure in the bulk.

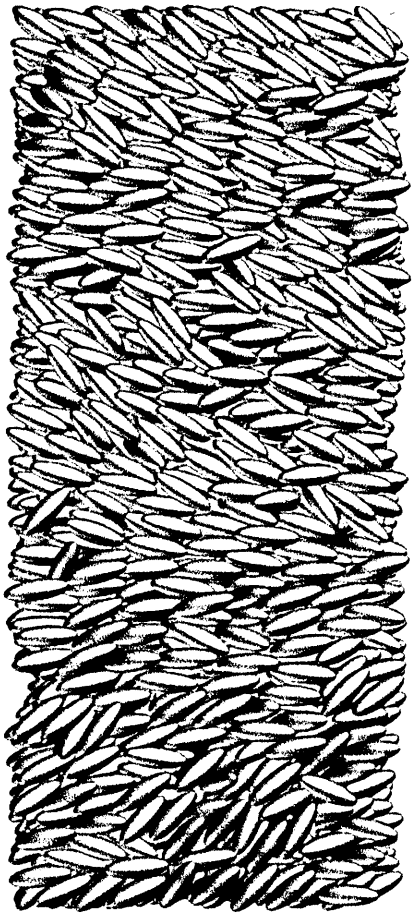

Figure 6.2: Snapshot of the nematic system close to the nematic-S_B transition. The lower surface is at the bottom of the picture.

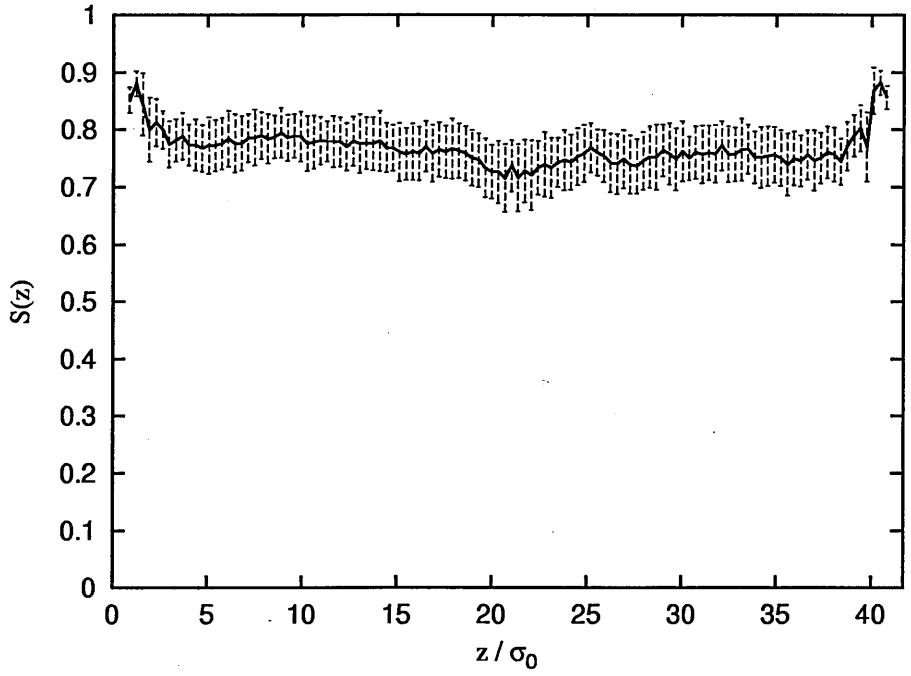

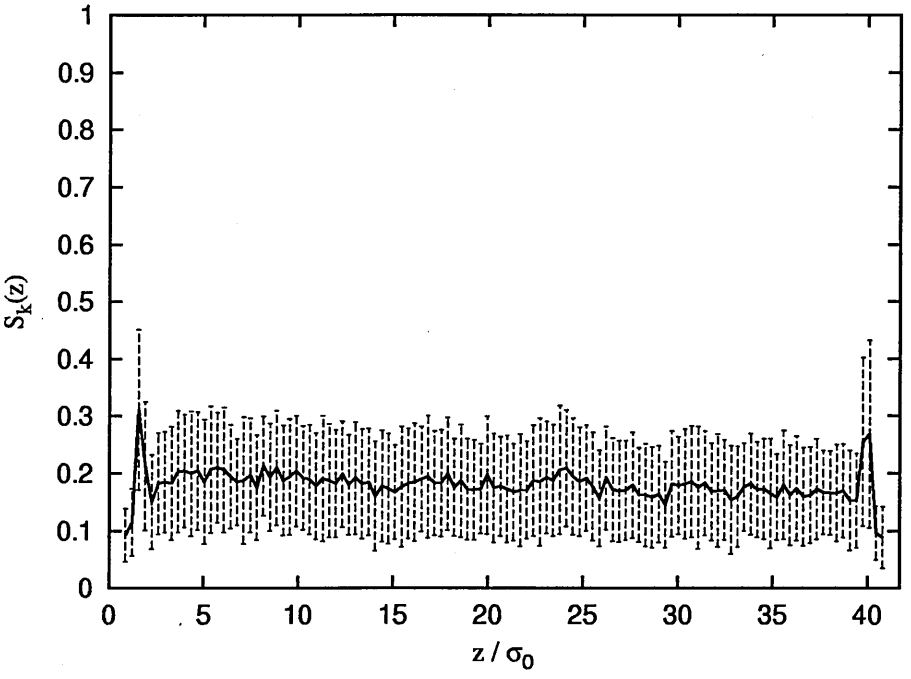

Figure 6.3: Order profiles of the nematic system: (a) orientational order, (b) positional order.

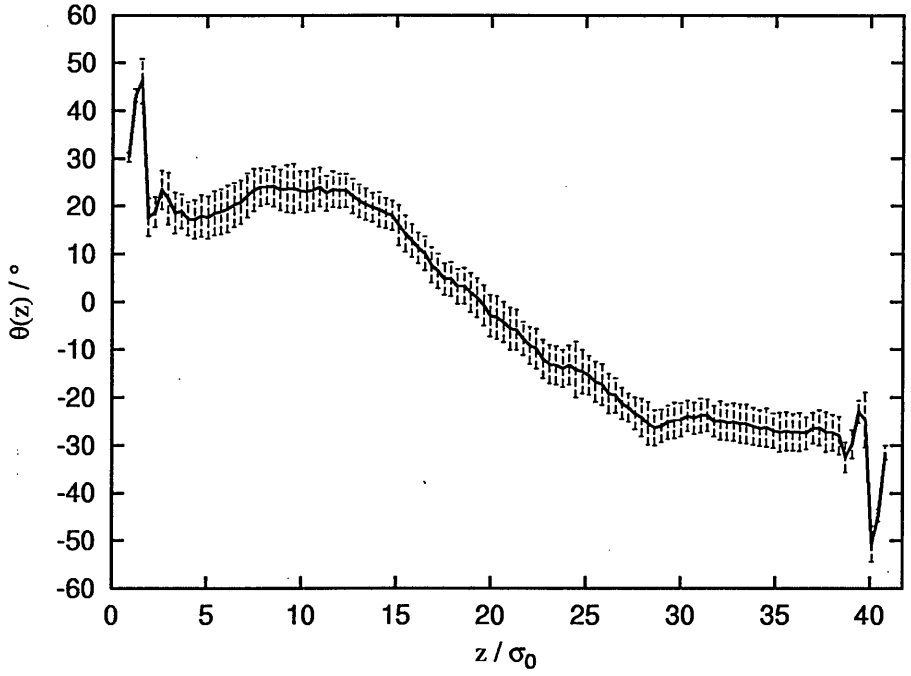

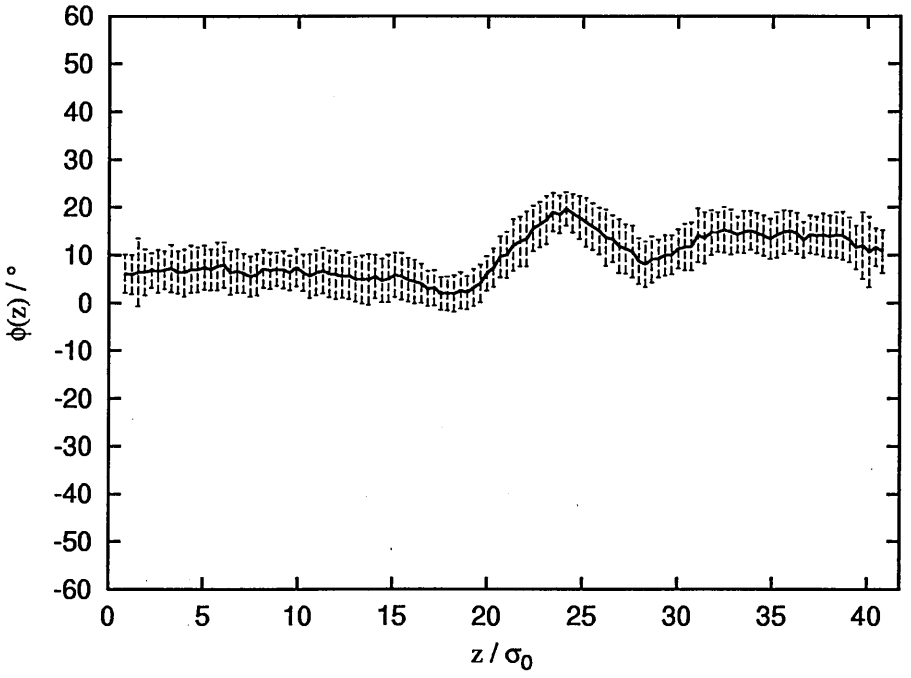

Figure 6.4: Tilt (a) and twist (b) profiles of the nematic system.

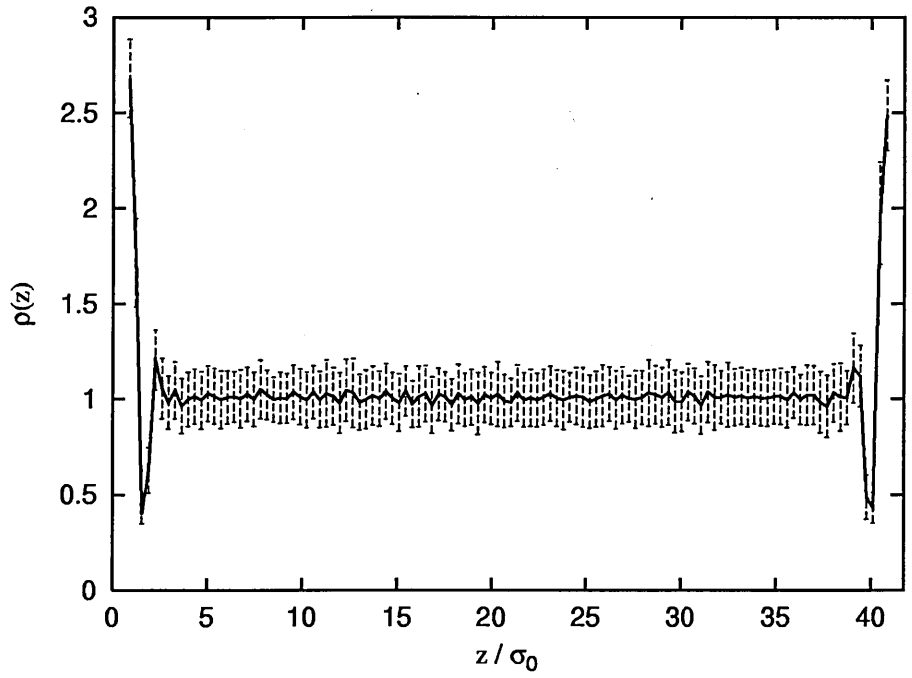

Figure 6.5: Normalised density profile of the nematic system.

The time-resolved position of the tip on quenching is shown in Fig. 6.6. The tip position was found for a series of timepoints by taking small block averages of 5,000 steps. The timescale used is the block number, with t=0 set at the start of the final equilibration run of the nematic system at T=0.95. The first quench was performed at t=20 and the second at t=42. In both quenches, the tip moved down towards the lower surface at a similar rate.

The structure which formed in the box can be seen from time-resolved profiles of the quench at initiated t=20. The evolution of the order profiles (Fig. 6.7) shows rapid onset of orientational and positional order in two domains, one in each half of the box. The order at the surfaces did not change. At each timepoint, the lower domain was smaller and of lower order than the upper domain. The movement of the tip towards the lower surface appears to have been driven by growth of the stronger upper domain at the expense of the weaker lower domain.

The evolution of the tilt angle profile (Fig. 6.8.a) shows that as the smectic layers formed, the tilt of the surface regions changed from its surface-induced value to a value which allowed the periodicity of the layers to match the box dimensions. These profiles confirm that, at short times, this system formed two domains of approximately equal and opposite tilt, with a relatively sharp interface between them. The twist angle (Fig. 6.8.b) which initially showed a kink in the centre, quickly developed a twist of around 10° throughout the box.

The first quench was run for 10^6 steps to equilibrate the resulting structure. A snapshot of this tilted layer structure is shown in Fig. 6.9. The order profiles are shown in Fig. 6.10 and reveal that the orientational and positional order at the upper surface did not change from those of the nematic system. The lower surface region showed lower order due to the director rotating in a small region in order to connect to the lower surface, shown in the tilt profile Fig. 6.11.a. The twist profile in Fig. 6.11.b shows that twist of the bulk smectic layers reduced in the lower surface region. The nematic nature of the lower surface region presumably reduced the need for the system to twist in order to match the smectic layer spacing with the box dimensions.

A comparison of the normalised density profiles of the nematic system and the tilted layer system is shown in Fig. 6.12. A slight reduction in density can be seen in the lower surface region.

The structure of the S_B layers is shown in Fig. 6.13. Fig. 6.13.a shows particle positions projected onto the plane of the layers, viewed along a direction normal to the layers. Two layers are shown, which demonstrate the ABC packing structure of the layers. The large grey dots show particles from a layer i and the black dots show particles from a layer $i + 3$. The hexagonal structure seems to

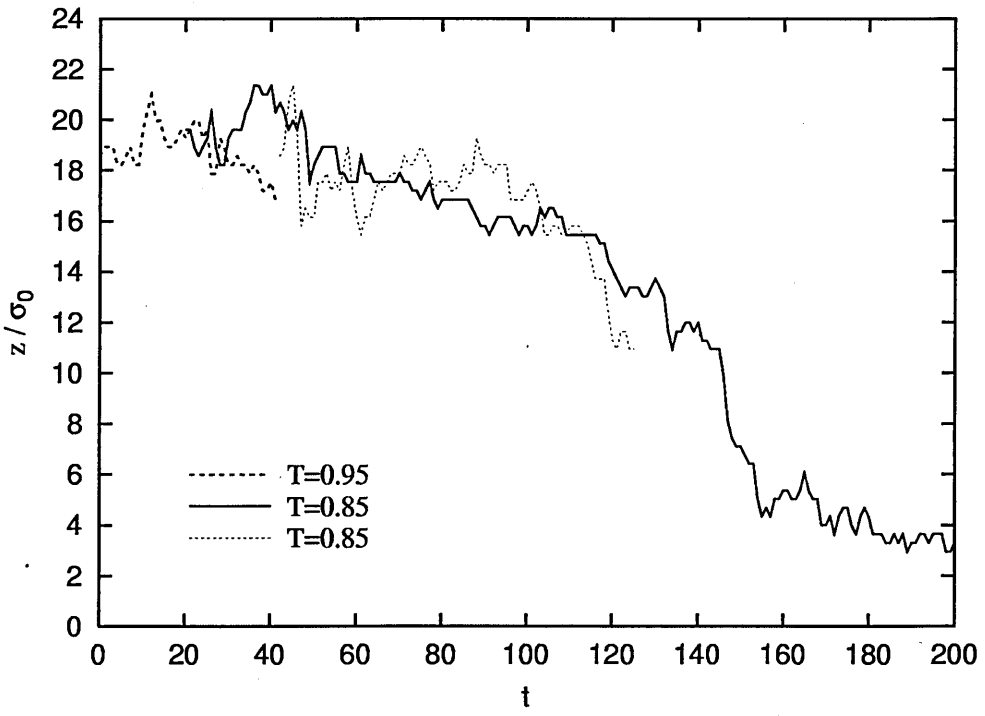

Figure 6.6: Time-resolved tip position after quenching on smooth surfaces: dashed line shows nematic system at T=0.95, solid line shows quench at t=20 and dotted line shows quench at t=42.

have an arbitrary orientation relative to the surface, further suggesting that the smectic domains formed in the bulk rather than growing out from the surfaces. Fig. 6.13.b shows the positions of particles within a slice parallel to the xy-plane of the surfaces, viewed looking down through the upper surface. The black dots show the positions of particles within the simulation box and the grey dots their periodic images. This reveals the reason for the twist angle of the layers. Rather than forming 6 independent layers in the box, the system effectively formed as a single layer which was wrapped around on itself by the periodic boundaries.

Taking angles from the director for the upper region of the tilted layer gives a tilt angle $\theta \approx 14.11°$ and a twist angle $\phi \approx 11.13°$. The layer spacing is $d_s \approx 2.553\sigma_0$. These angles represent a solution to the problem of matching the layer spacing with the box dimensions.

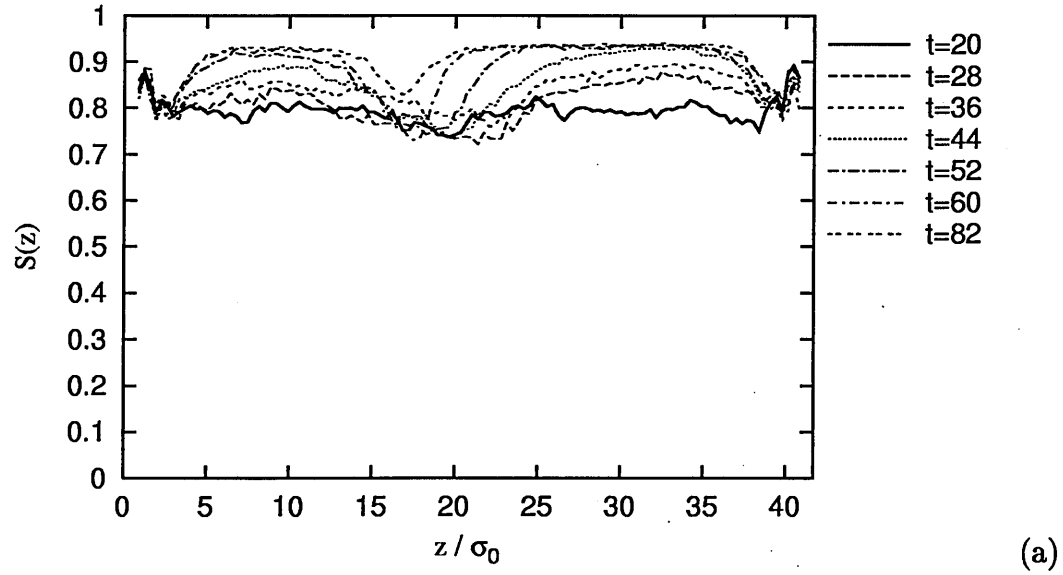

(a)

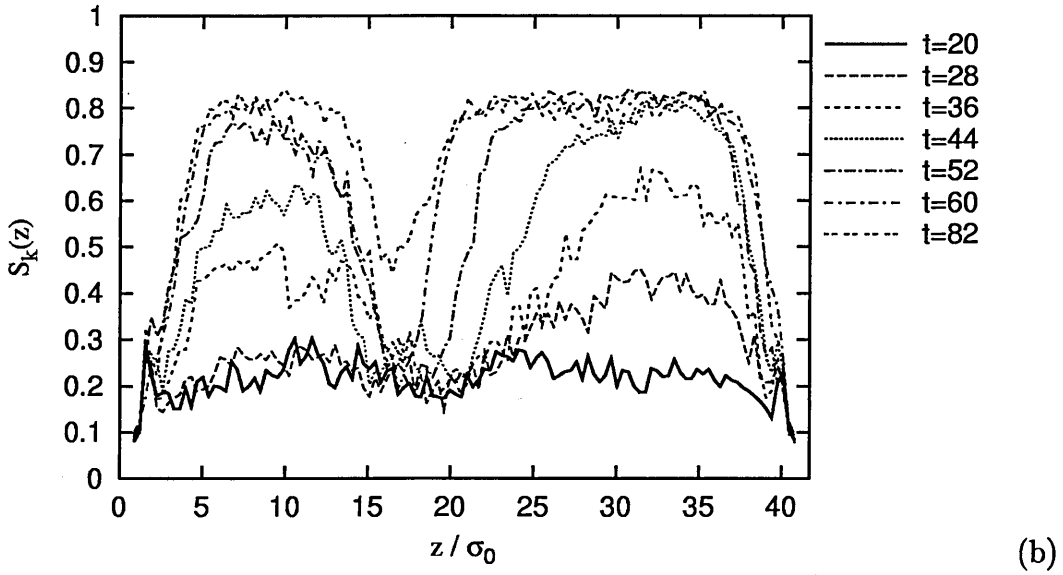

(b)

Figure 6.7: Time-resolved orientational (a) and positional (b) order profiles for the smooth surface system quenched at t=20.

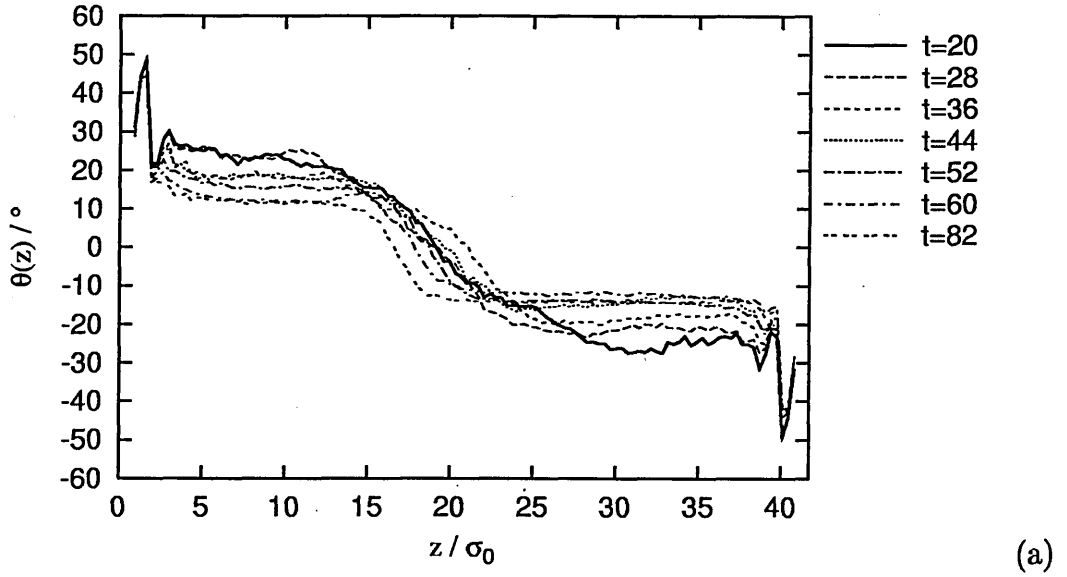

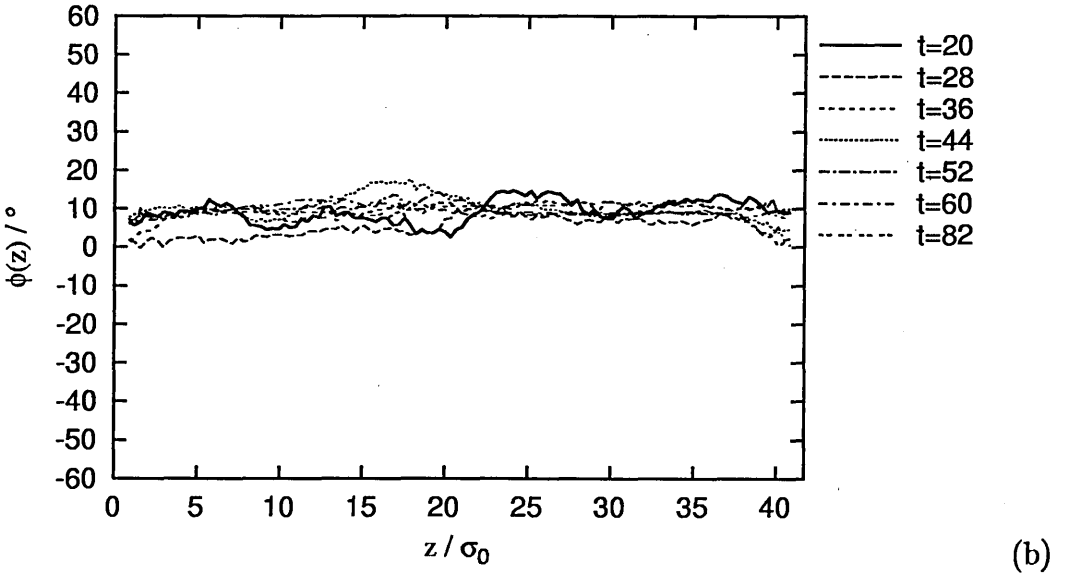

Figure 6.8: Time-resolved tilt (a) and twist (b) profiles for the smooth surface system quenched at t=20.

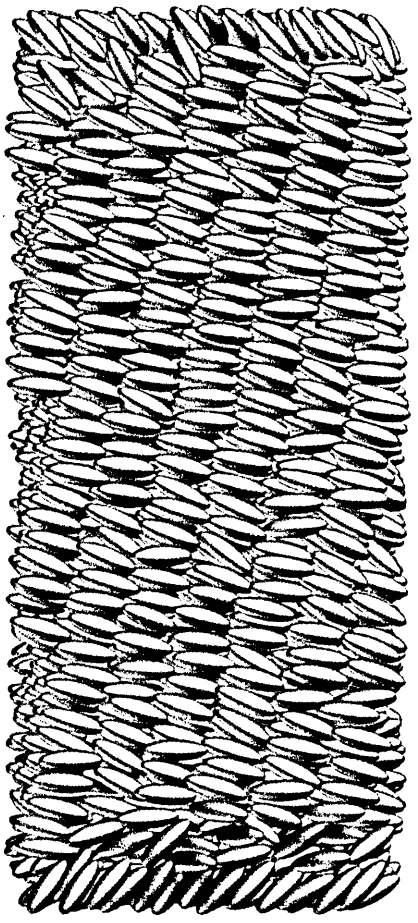

Figure 6.9: Snapshot of the tilted layer structure formed by the system quenched at t=20.

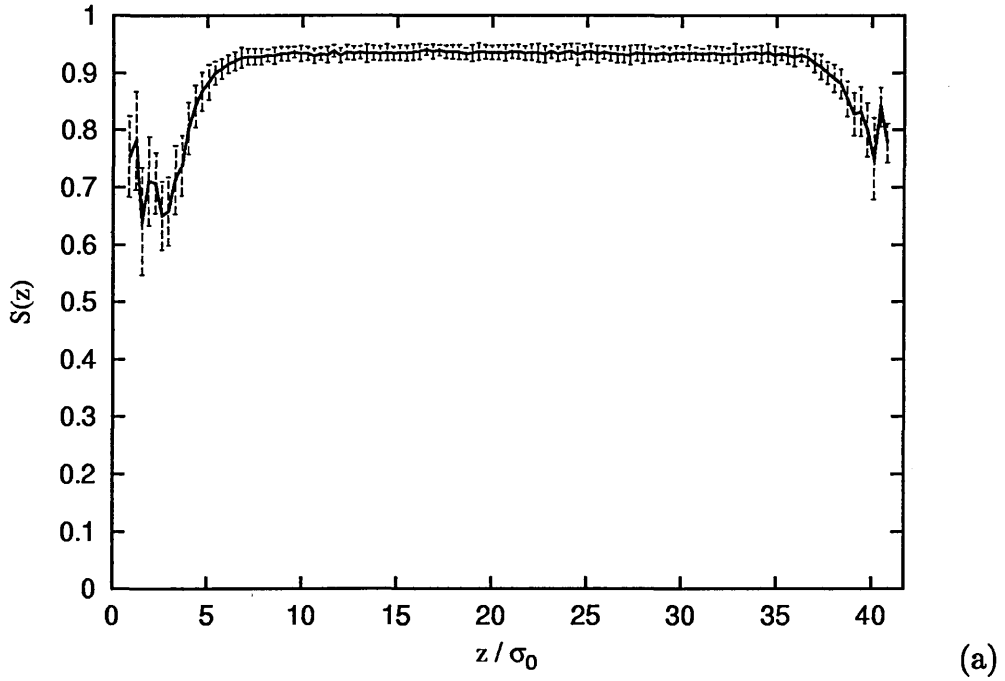

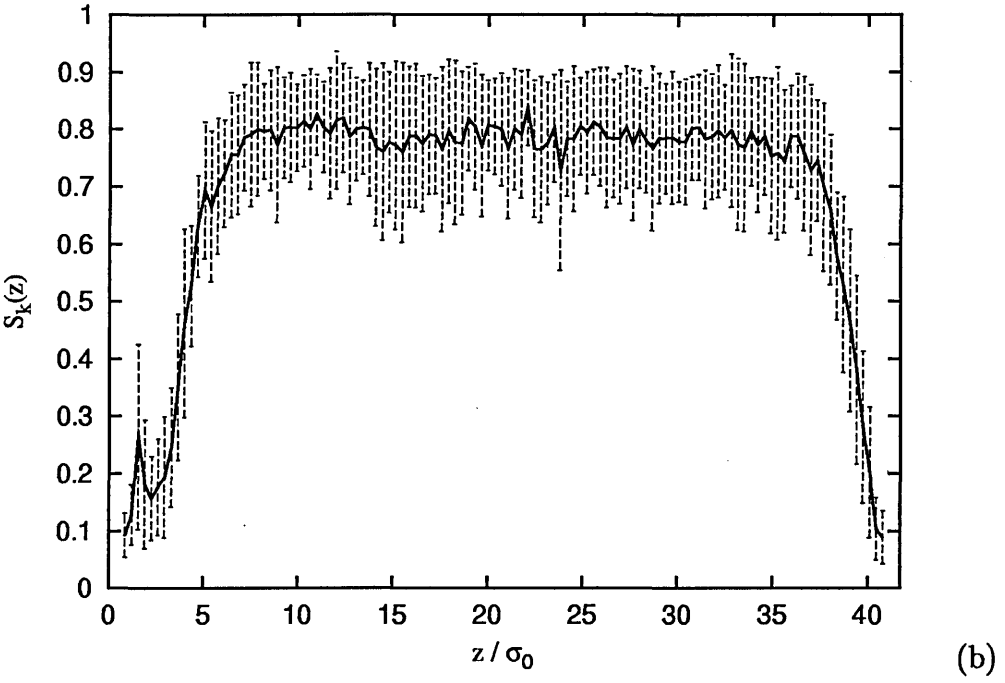

Figure 6.10: Tilted layer structure orientational (a) and positional (b) order profiles.

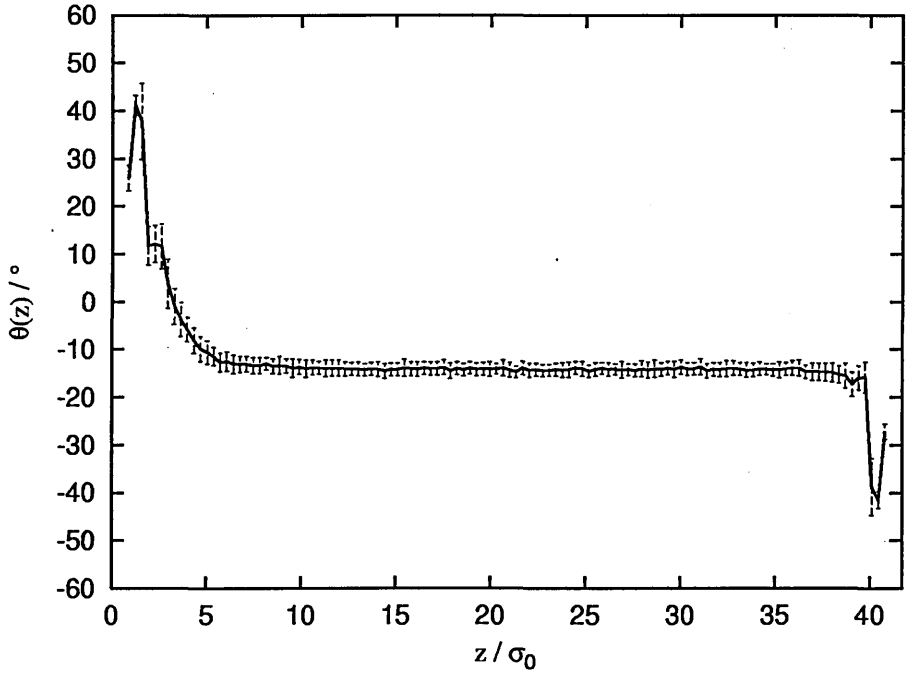

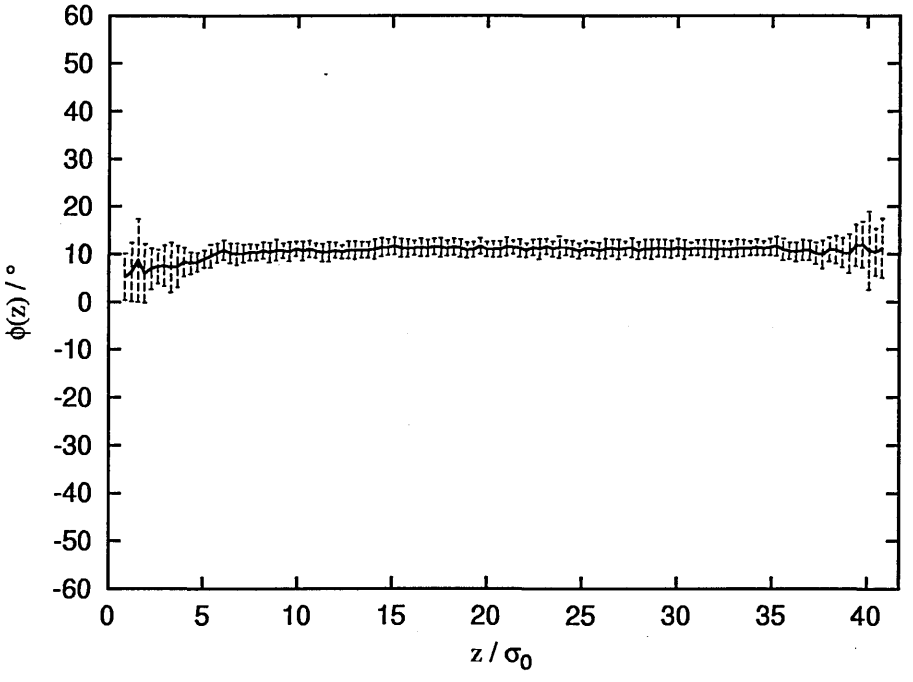

Figure 6.11: Tilted layer structure tilt (a) and twist (b) profiles.

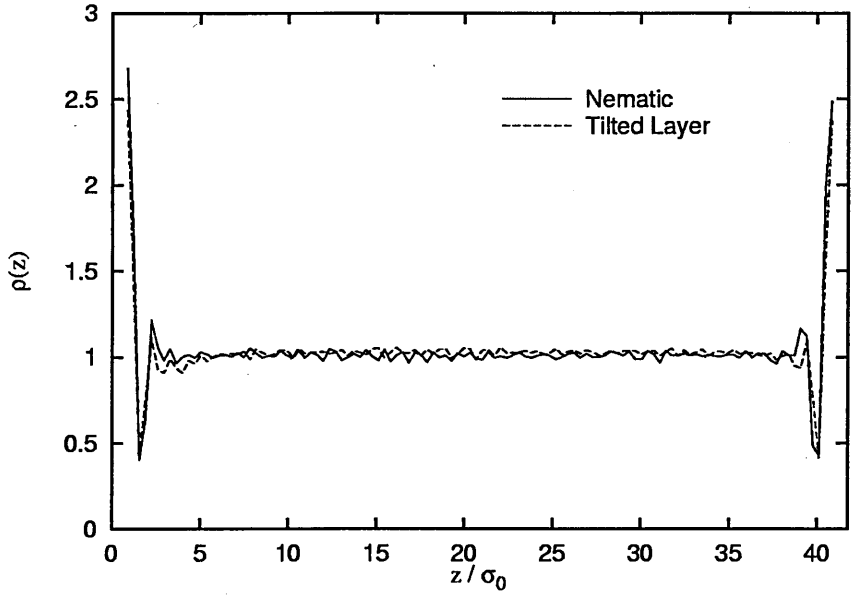

Figure 6.12: Nematic and tilted layer structure normalised density profiles.

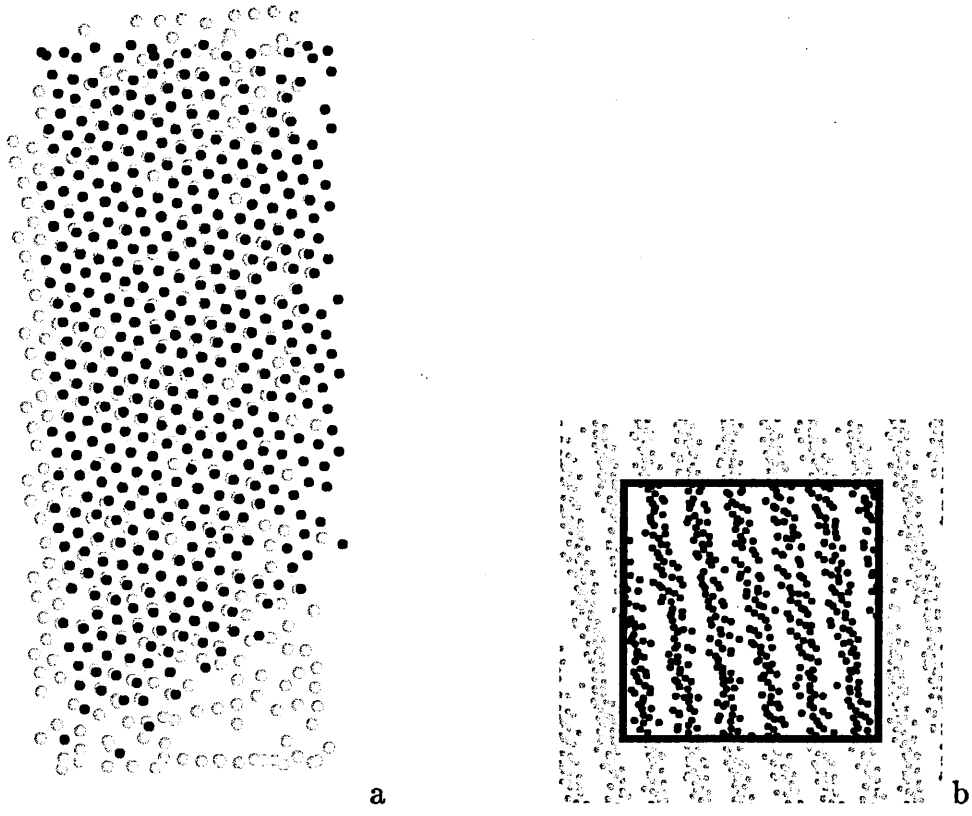

Figure 6.13: Tilted layer structure S_B packing arrangements: (a) particle positions projected onto the layer plane for a layer i (grey dots) and a layer $i+3$ (black dots), (b) positions of particles within a slice of the simulation box (black dots) and their periodic images (grey dots) viewed through the upper surface.

6.4.2 Quenching on Rough Surfaces

To try to stabilise the chevron-like structure formed in the early stages of quenching a system with smooth surfaces, the process was repeated on rough surfaces, created by setting the well-depth modulation parameter A=0.5. These surfaces were imposed on the configuration taken from the start of the smooth surface nematic run at t=0 in Fig. 6.6. This system was then equilibrated for 420,000 steps prior to being quenched.

Unlike the systems shown in Fig. 6.6, this system formed a bookshelf structure. As with the previous quenches, time-resolved profiles were created by taking small block averages of 5,000 steps. The time t represents the block number, with t=0 here set at the time of quenching. The order profiles in Fig. 6.14 show that the orientational order in the lower surface region dropped as the bookshelf structure formed. The initial positional order was higher in the centre of the box. A single smectic domain formed in the bulk and then grew towards the surfaces.

The orientational profiles in Fig. 6.15 show that while the initial tilt profile was similar to the previous cases, on quenching, a single domain of zero tilt formed. The initial twist profile shows a smooth rather than a kinked arrangement. The twist was zero at the surfaces and rose to around 30° in the lower third of the box. As the bookshelf structure formed, the lower surface twisted round to 75° and the bulk twisted to around 20°. The lack of a kink in the twist profile and the higher initial positional order in the centre suggests that the roughness of the surface was not the reason for the formation of the bookshelf structure in this system. Rather the system may have been biased to form a bookshelf structure by the initial twist and order profiles.

The system was equilibrated for 840,000 steps from the time of the quench. A

snapshot of the resulting structure is shown in Fig. 6.16. Block averaged profiles were created for this structure over 50,000 steps. The order profiles (Fig. 6.17) show a large disordered region at the lower surface where the director twists 75° but also a region of disorder at the upper surface larger than that for the tilted layer structure. The twist profile (Fig. 6.18.b) shows the lower surface twisted round at 75° with a linear change in the surface region to the bulk twist angle 19°. The normalised density shown compared with the nematic profiles in Fig. 6.19 is slightly reduced in the surface regions and slightly increased in the bulk. This could be due to the increased density of the bulk smectic layers leading to reduced density of the surface regions.

Projections of particle centres for a layer i and a layer $i+3$ onto the plane of the layers, shown in Fig. 6.20.a, again reveal the ABC packing of the layers. The orientation of the hexagonal packing relative to the surfaces is different from that of the tilted layer case and again appears to be arbitrary. Fig. 6.20.b shows the particle centres in the simulation box, surrounded by its periodic images, viewed looking down through the upper surface. The reason for the twist in the bulk can be seen to be the periodic boundaries wrapping each layer i round onto a layer $i+2$. Thus, the system effectively formed two interleaved layers.

Overall, the bookshelf structure had $\theta = 0°$, $\phi = 19°$ and $d_s \approx 2.53\sigma_0$. This represents another solution which satisfies the tilt/twist/layer spacing constraints in the system.

There is a small difference between d_s here and the tilted layer value $d_s \approx 2.553\sigma_0$. This could be an indication that the layer spacing is also being influenced by the periodic boundaries.

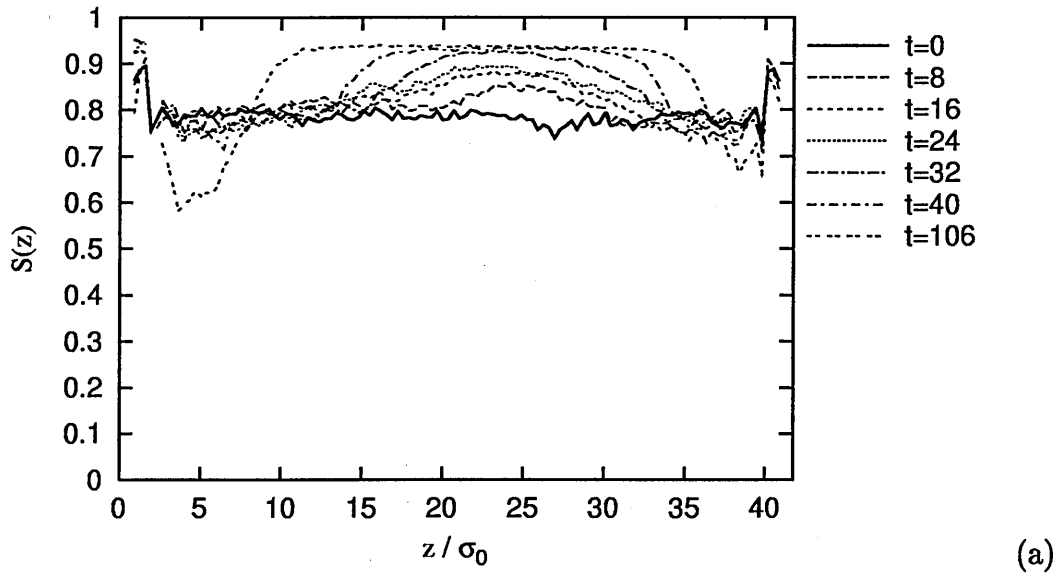

(a)

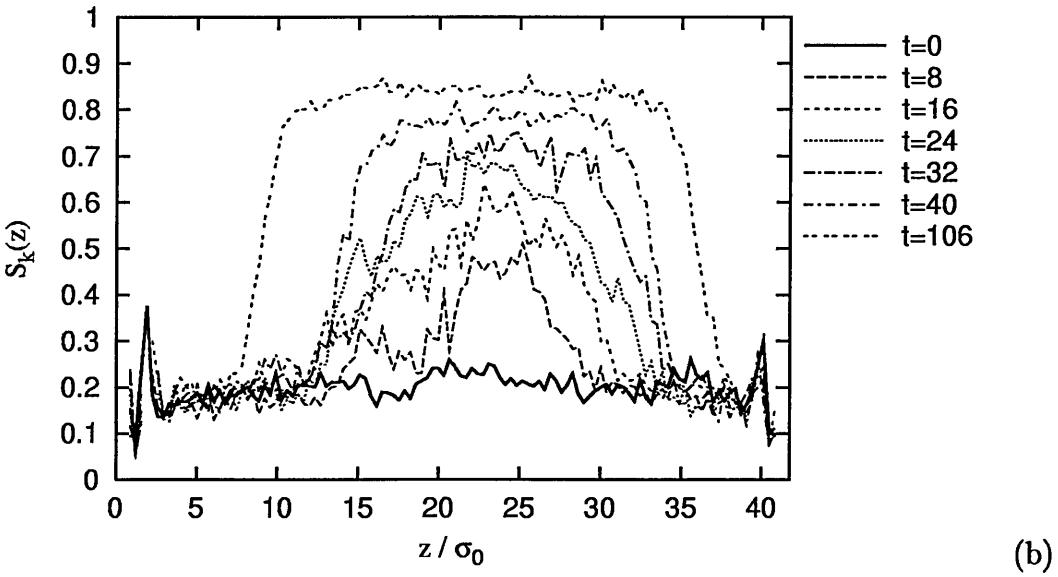

(b)

Figure 6.14: Time-resolved orientational (a) and positional (b) order profiles for the rough surface A=0.5 system quenched at t=0.

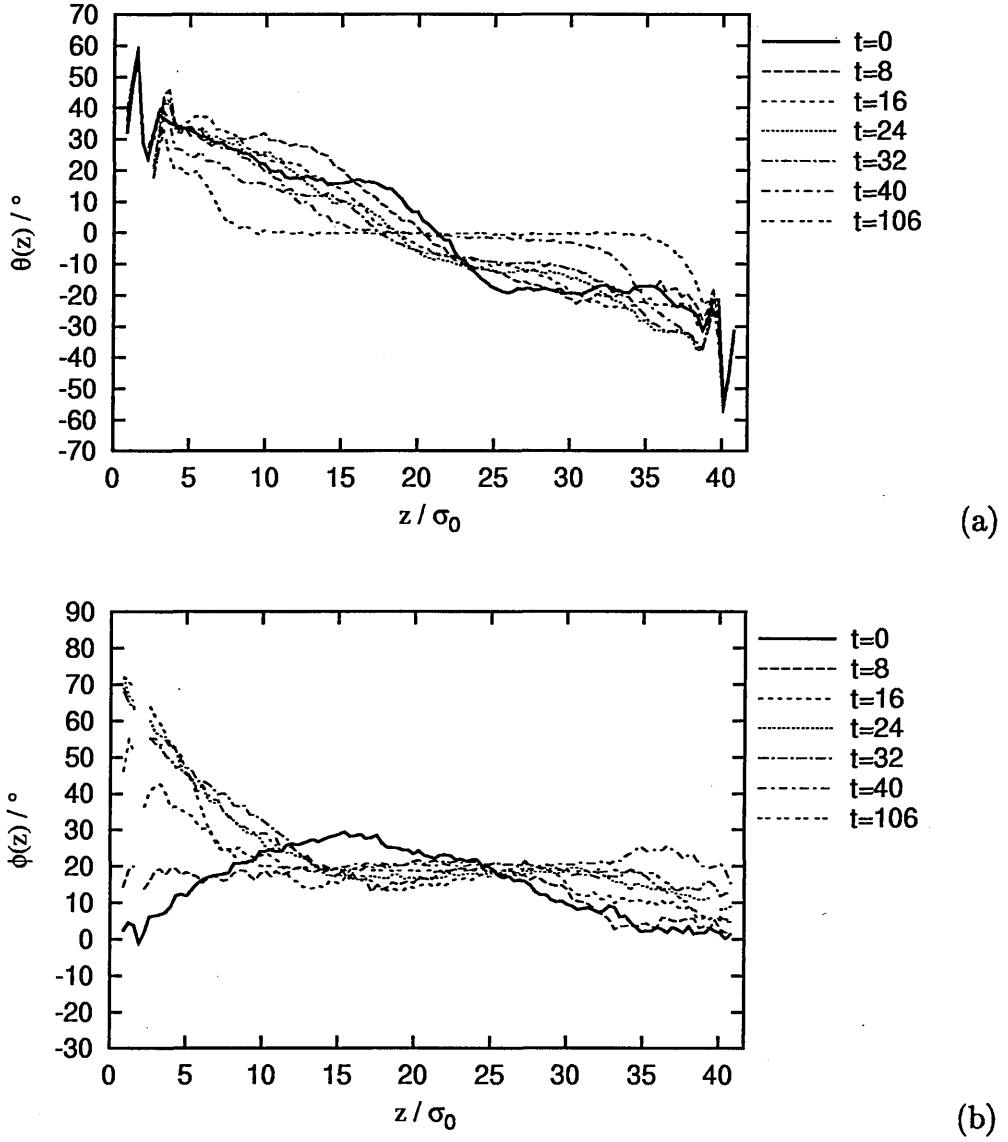

Figure 6.15: Time-resolved tilt (a) and twist (b) profiles for the rough surface A=0.5 system quenched at t=0.

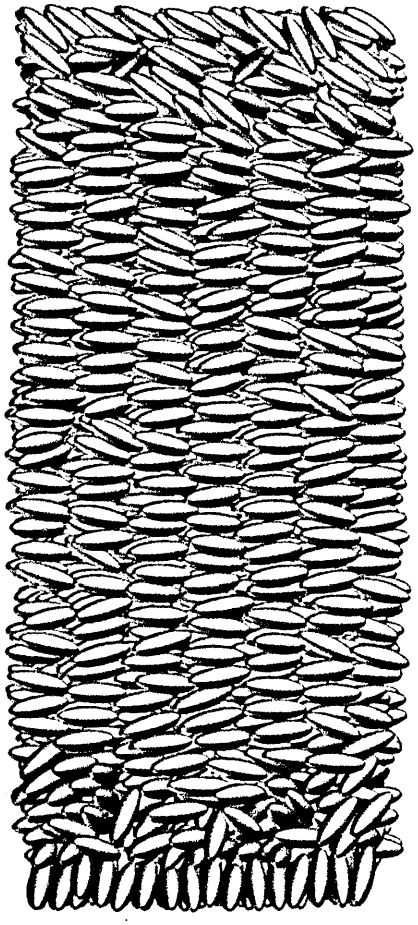

Figure 6.16: Snapshot of the bookshelf structure formed on quenching the rough surface A=0.5 system.

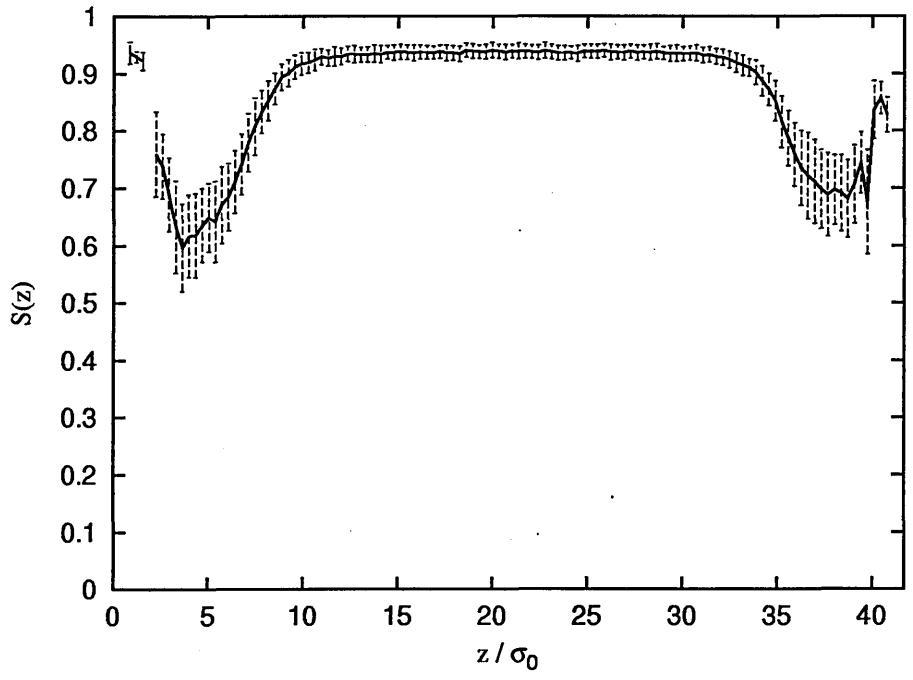

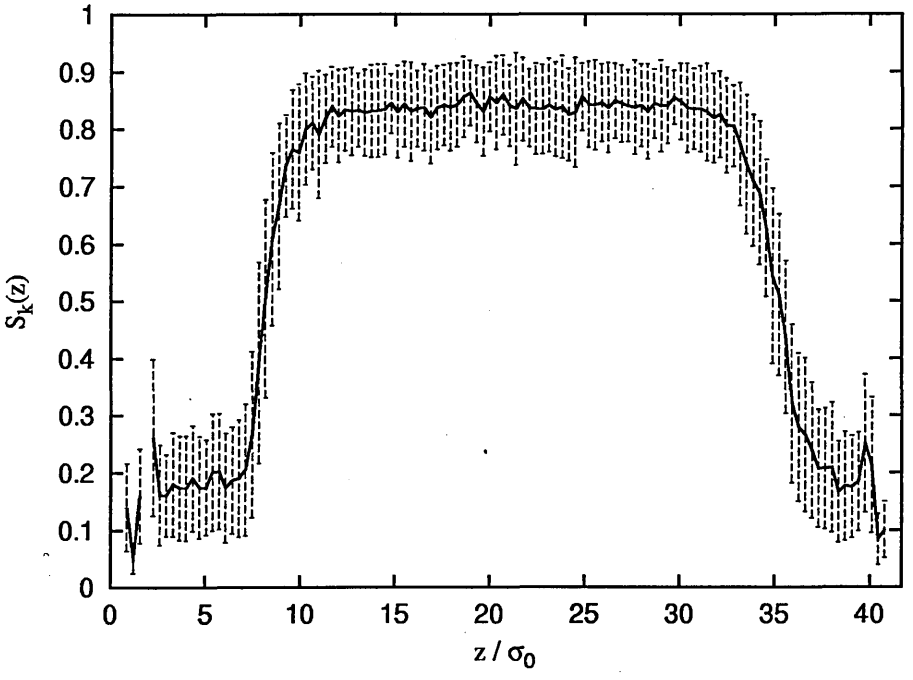

Figure 6.17: Bookshelf structure orientational (a) and positional (b) order profiles.

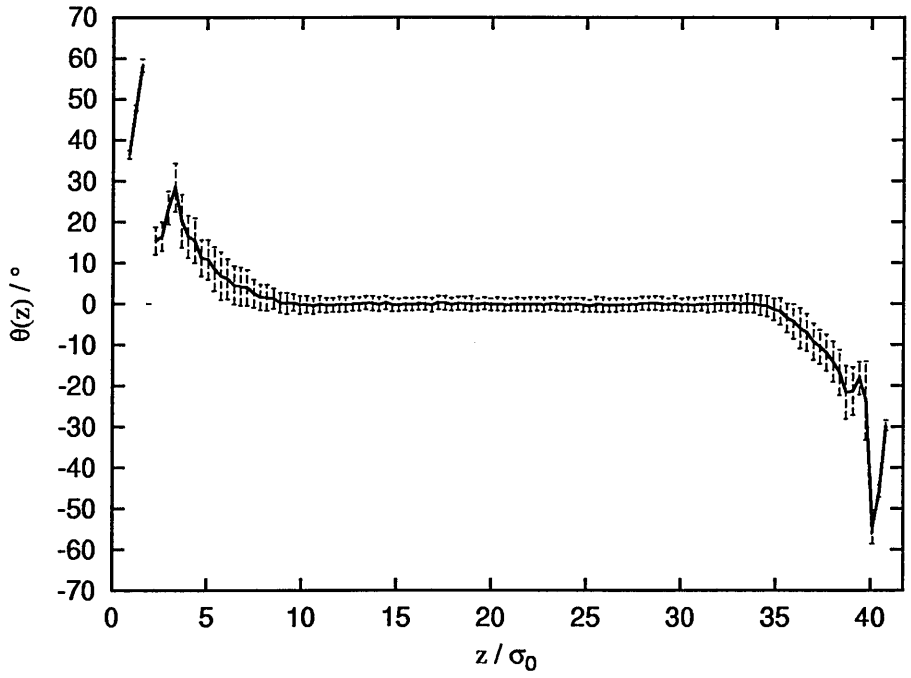

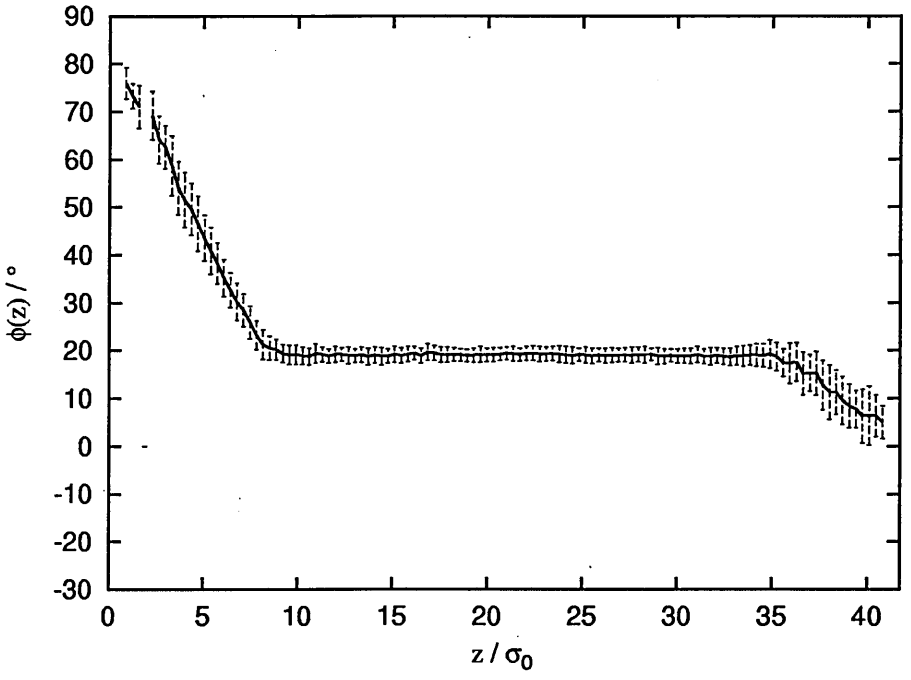

Figure 6.18: Bookshelf structure tilt (a) and twist (b) profiles.

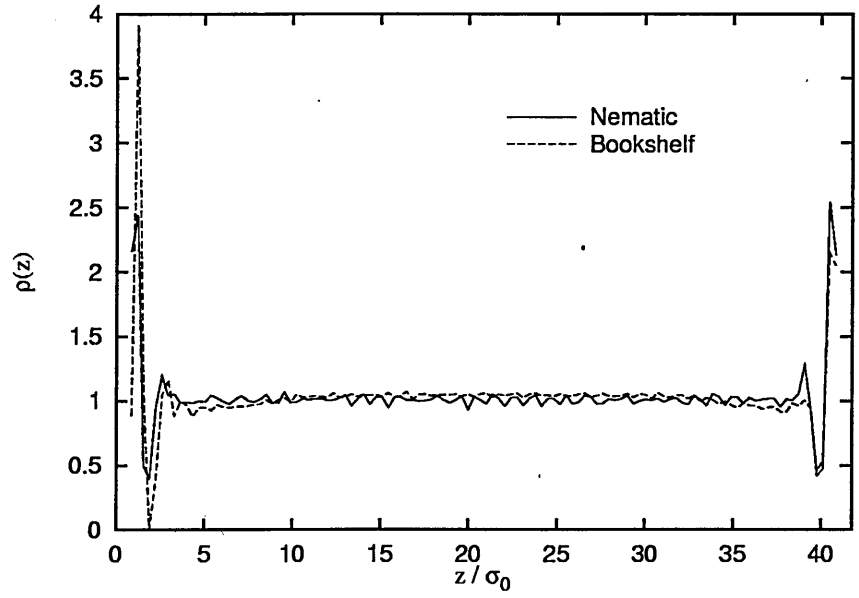

Figure 6.19: Nematic and bookshelf structure normalised density profiles.

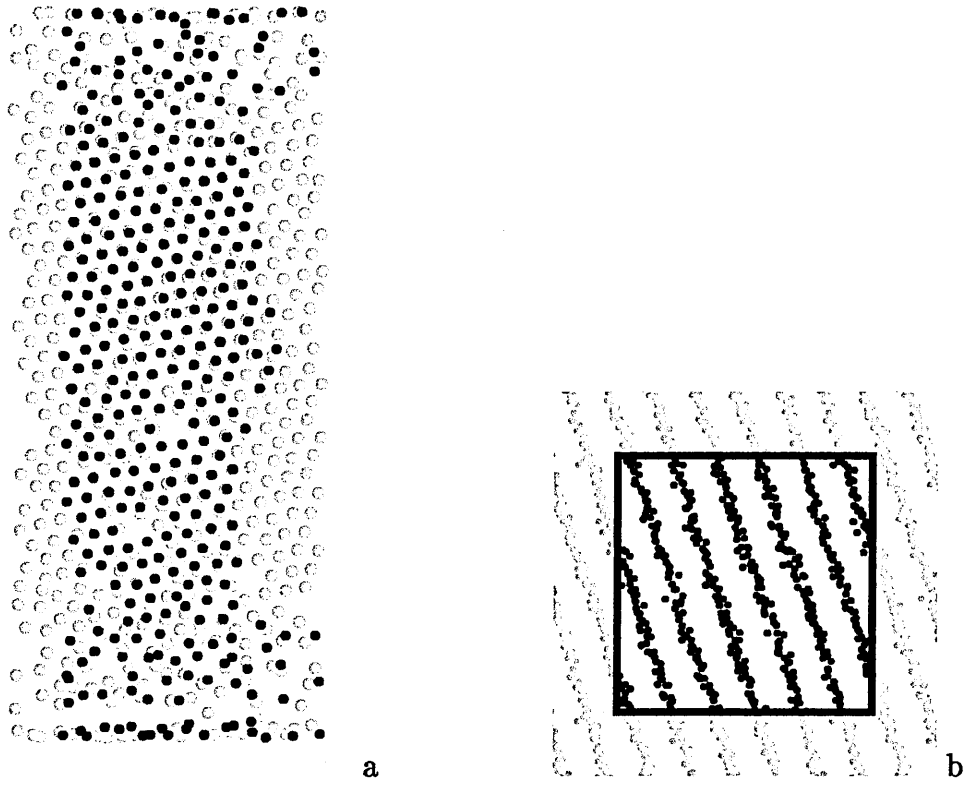

Figure 6.20: Bookshelf structure S_B packing arrangements: (a) particle positions projected onto the layer plane for a layer i (grey dots) and a layer $i+3$ (black dots), (b) positions of particles within a slice of the simulation box (black dots) and their periodic images (grey dots) viewed through the upper surface.

6.5 Formation

6.5.1 Introducing Rough Surfaces

Since the early stages of quenching on smooth surfaces had produced a chevron-like structure, attempts were made to stabilise this structure by introducing rough surfaces mid-quench. To do this, various levels of surface roughness were introduced onto the smooth surface A=0.0 system which had been quenched at time t=20 (recall Fig. 6.6).

Fig. 6.21 shows the time-resolved tip positions for these systems. A=0.0 is the original smooth surface system. A surface with A=0.2 was introduced at t=60, and surfaces with A=0.2 and A=0.4 at t=106. For the last two systems, the tip moved towards the lower surface as with the smooth surface system, although this movement appears to have been delayed by a small amount. For the first A=0.2 system, the tip moved steadily to the centre of the box.

A snapshot of this chevron structure is shown in Fig. 6.22. Block averaged profiles were created for this structure over 50,000 steps. The orientational and positional order, as shown in Fig. 6.23, was less for the lower half of the chevron than the upper half. Also, the lower order in the surface regions extended further into the bulk for the lower surface. The tip structure shows a larger reduction in positional order than orientational order.

The director profiles in Fig. 6.24 show that the two domains formed with slightly different tilt and twist angles, giving the tip an asymmetrical structure. From the tilt profile, the lower portion of the tip occupies a z-range of around $4\sigma_0$ whereas the upper portion occupies around $5\sigma_0$.

The normalised density profile shown in Fig. 6.25 reveals a regular structure

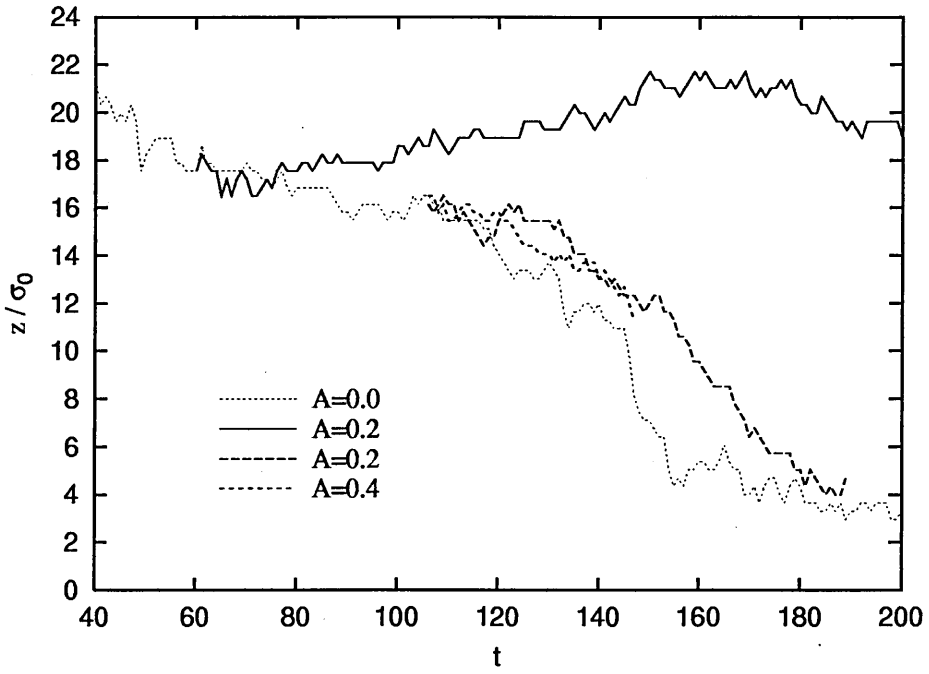

Figure 6.21: Time-resolved tip position after introducing rough surfaces onto the system quenched on smooth surfaces: dotted line shows the smooth surface system which was quenched at time t=20 in Fig. 6.6, solid line shows the system with rough surfaces A=0.2 introduced at time t=60, dashed lines show systems with rough surfaces A=0.2 (long dashes) and A=0.4 (short dashes) introduced at time t=106.

in the lower half of the chevron. To check for possible crystallisation, the in-plane pair distribution function $g_{\perp}(r_{\perp})$ was calculated for the smectic region of the lower half of the chevron. This is shown in Fig. 6.26. The plot is characteristic of a S_B liquid crystal phase with broad peaks, rather than sharp peaks, as would be the case for a crystal phase.

The reason for the structure in the density profile can be seen from a plot of the particle positions in one layer running from the lower to the upper surface, viewed along the direction of the director at the tip, shown in Fig. 6.27.a The orientation of the hexagonal packing of particles relative to the simulation box allows the thin slices parallel to the surface used in the profiles to resolve the internal structure in the lower half. In the upper half, the angle of the hexagonal structure relative to

the slices creates an effectively continuous density profile. This packing geometry is also likely to influence the coupling of the smectic layers to the surface.

Projections of particle positions for a layer i and a layer $i+3$ onto the plane of the layers for the upper (Fig. 6.27.b) and lower (Fig. 6.27.c) halves of the chevron illustrate the ABC layer packing structure of both halves.

Results for the whole smectic region of the lower half give $\theta = 12.407°$, $\phi = 7.278°$, $S_k = 0.770$, $S = 0.931$ and $d_s = 2.565$. For the smectic region of the upper half, the equivalent results are $\theta = -14.110°$, $\phi = 11.129°$, $S_k = 0.824$, $S = 0.935$ and $d_s = 2.553$.

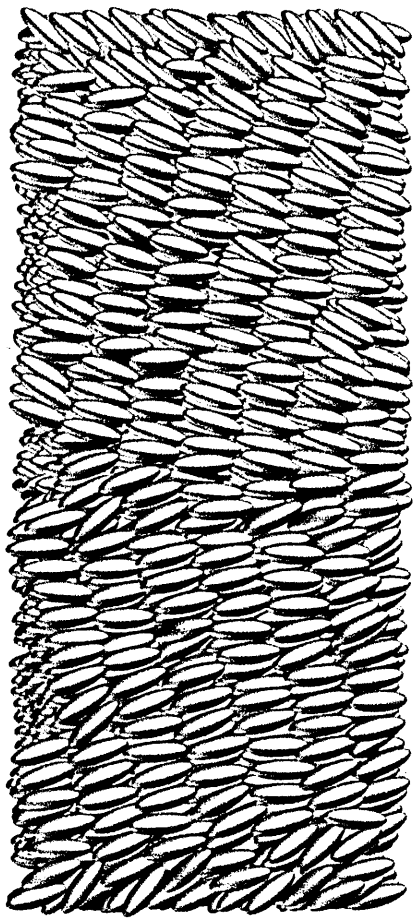

Figure 6.22: Snapshot of the chevron structure formed by introducing rough surfaces A=0.2 onto the system quenched on smooth surfaces.

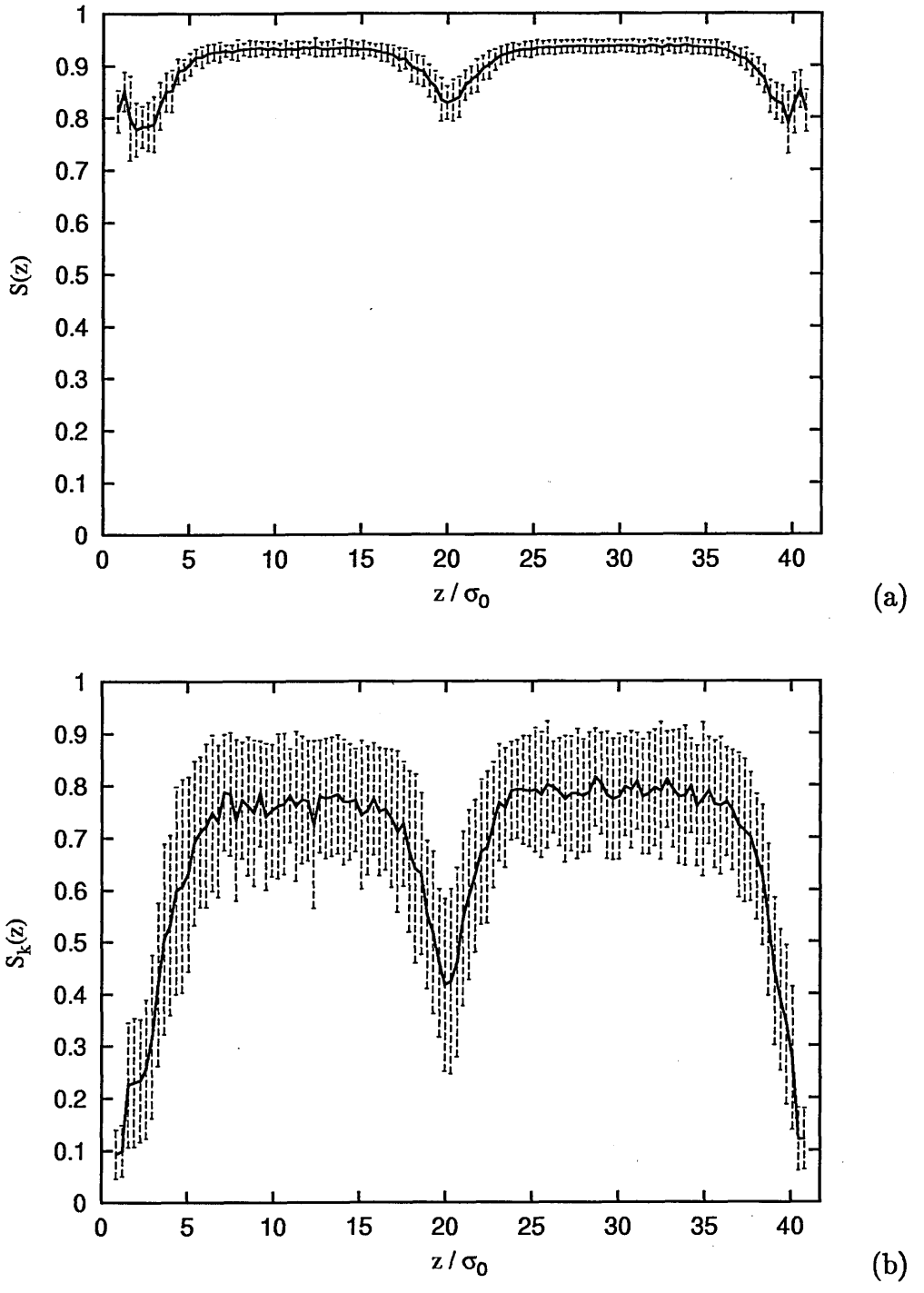

Figure 6.23: Chevron structure orientational (a) and positional (b) order profiles.

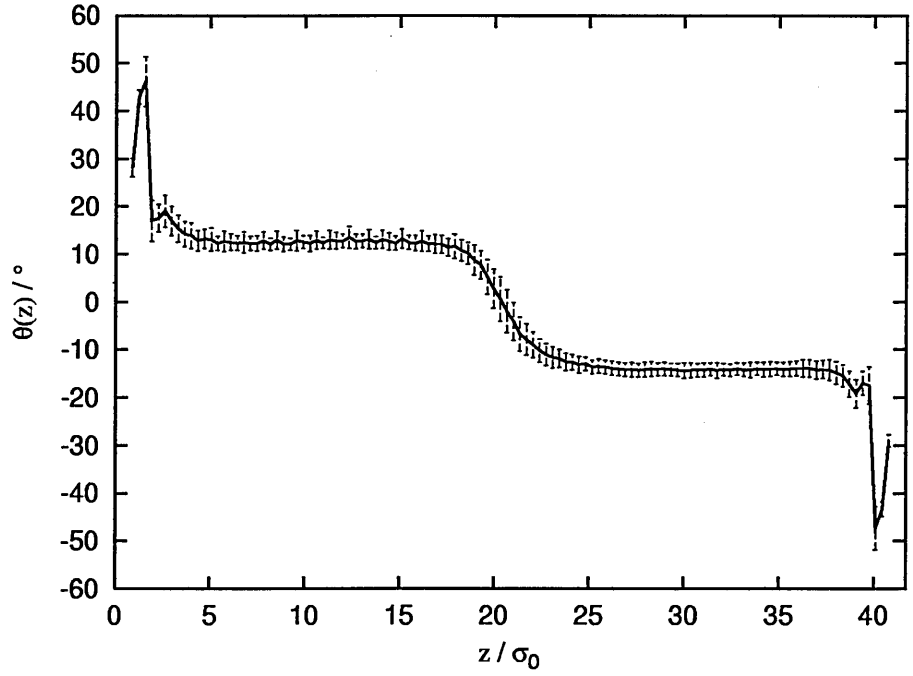

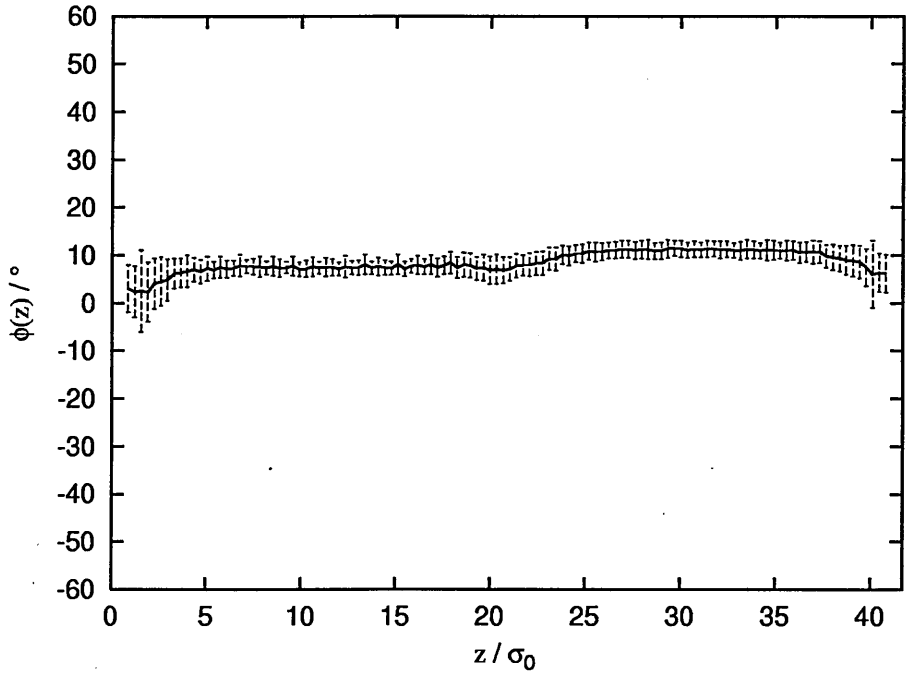

Figure 6.24: Chevron structure tilt (a) and twist (b) profiles.

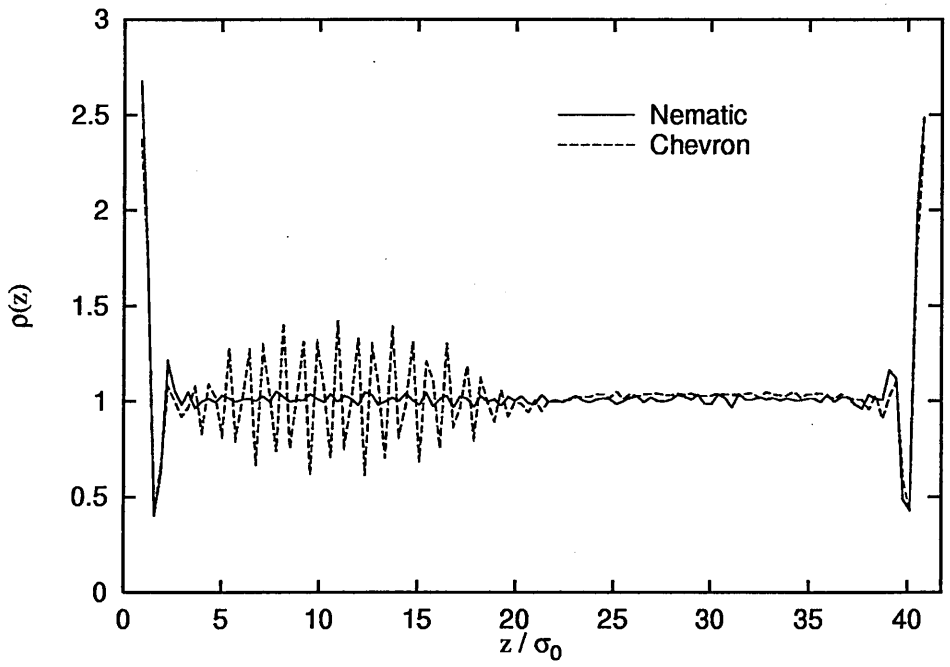

Figure 6.25: Nematic and chevron structure normalised density profiles.

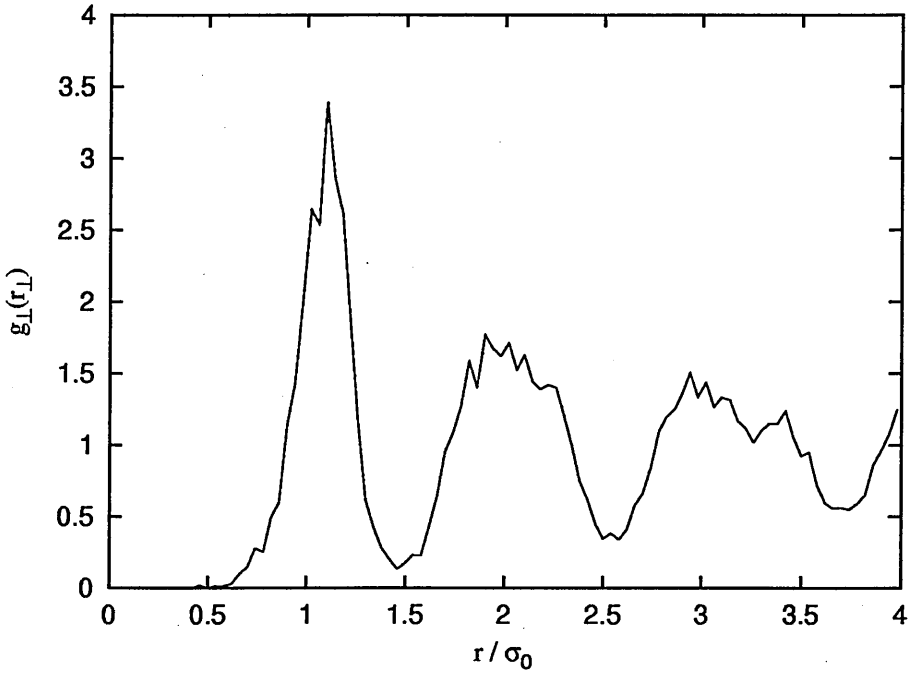

Figure 6.26: Chevron structure lower domain $g_{\perp}(r_{\perp})$.

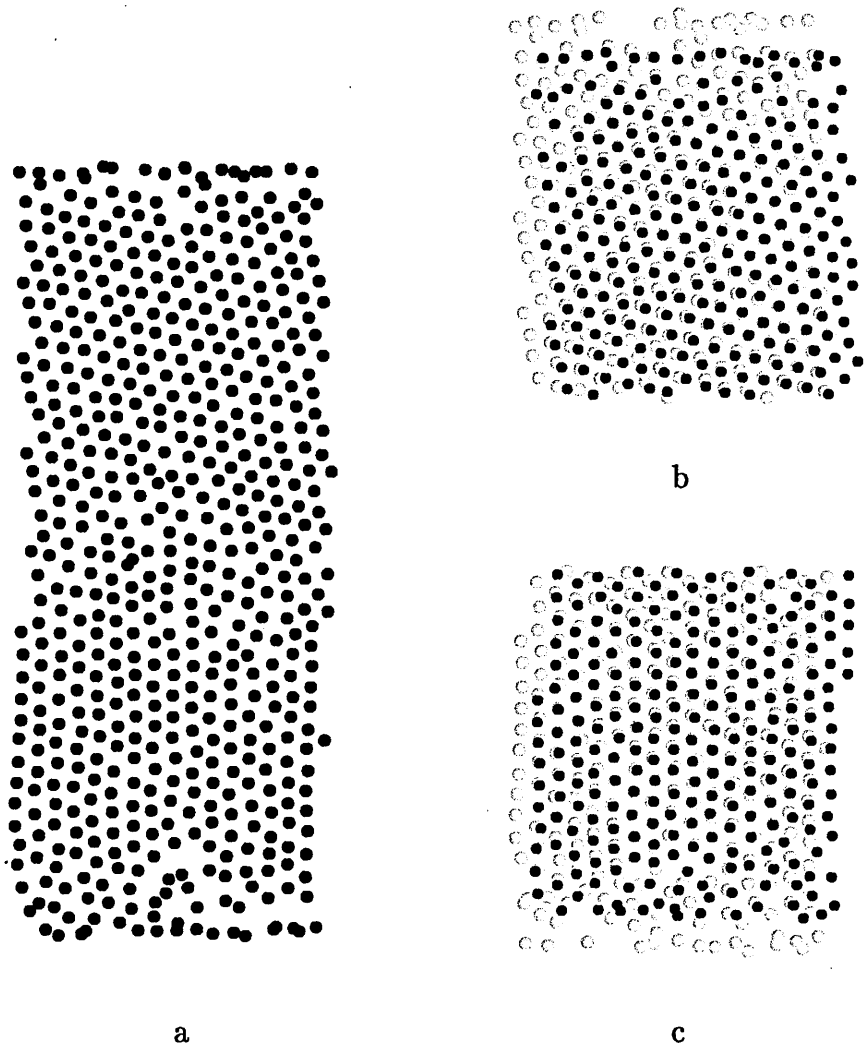

Figure 6.27: Chevron structure S_B packing arrangements: (a) positions of particles in one layer running from the lower to the upper surface, viewed along the direction of the director at the tip, (b,c) particle positions projected onto the layer plane for a layer i (grey dots) and a layer $i + 3$ (black dots) for the upper domain (b) and the lower domain (c).

6.6 Relaxation to Tilted Layer Structure

Although the introduction of rough surfaces appeared to stabilise the chevron structure, extended runs indicated that it was not fully stabilised.

Rather, the system relaxed to a tilted layer structure via an asymmetric chevron as the tip moved towards the lower surface. Further changes were, therefore, made to the surface roughness to explore its effects on this relaxation.

Fig. 6.28 shows the time-resolved tip position for the relaxation of the chevron structure. The beginning of this plot overlaps the end of Fig. 6.21. The system with A=0.2 is the relaxation of the chevron structure formed in Fig. 6.21. The system with A=0.5 is the relaxation of that system with rougher surfaces introduced at time t=102. This further roughening of the surface slowed, but did not prevent, the relaxation process.

Fig. 6.29 again shows the relaxation of the A=0.2 chevron system, together with that of a system where the roughness was removed at time t=186, and another system created from this A=0.0 system by reintroducing the A=0.2 surface at time t=240 in an attempt to recreate the original formation of the chevron structure. The smooth surface does not appear to have changed the relaxation time as the original chevron and the smooth surface chevron follow similar paths. The reintroduced rough surfaces did not recreate the original chevron formation but did seem to delay the relaxation slightly.

These results suggest that the rough surfaces introduced soon after quenching stabilised the formation of the chevron structure but were not sufficient to fully stabilise the structure once it had formed.

The nature of the relaxation process can be determined from plots showing the histories of particles originally from a single layer of the original chevron structure.

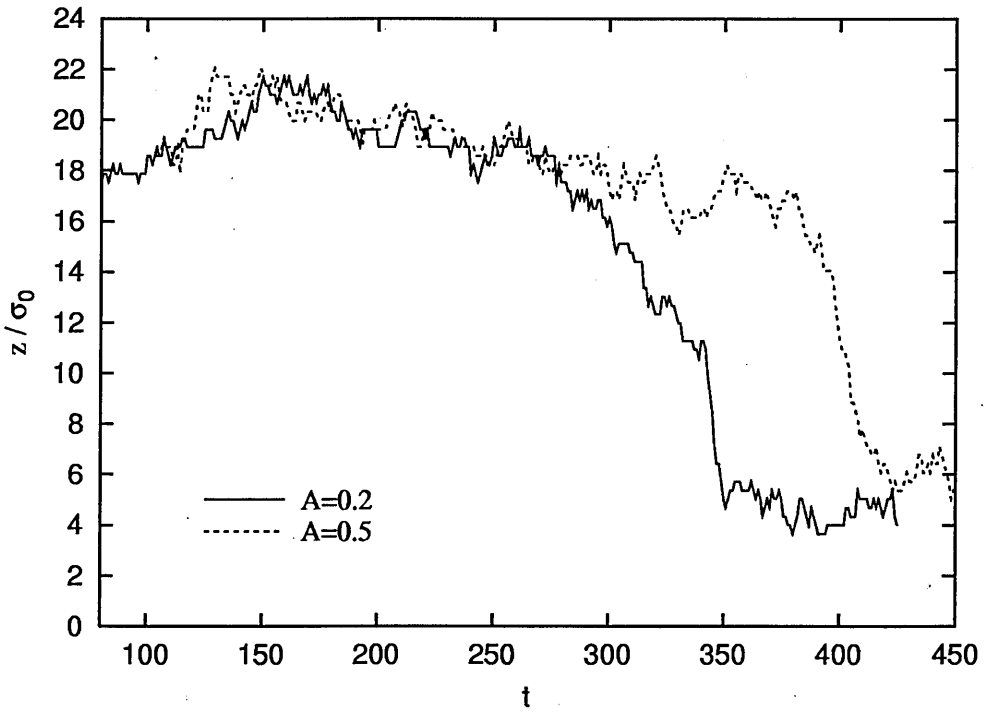

Figure 6.28: Time-resolved tip position for the relaxation of the chevron structure, following on from Fig. 6.21: solid line shows the relaxation of the A=0.2 surface chevron system, dashed line shows the relaxation after the introduction of rougher surfaces A=0.5 at time t=102.

Fig. 6.30 shows three stages in the relaxation of the A=0.2 stabilised chevron system. Fig. 6.30.a shows, at time t=182, the positions of the chosen particles as black dots and the positions of the remaining particles as grey dots. Fig. 6.30.b shows the same system at time t=286 where the asymmetric chevron structure is apparent. By this stage, some diffusion of particles had occurred in the surface region and at the tip, but the layers in the lower and upper portions were still in registry. The tilted layer structure at time t=350 is shown in Fig. 6.30.c and reveals that the layers maintained registry throughout the relaxation. Although not shown here, registry between lower and upper layers was found to be maintained in all of the other systems which showed relaxation from the chevron to the tilted layer structure.

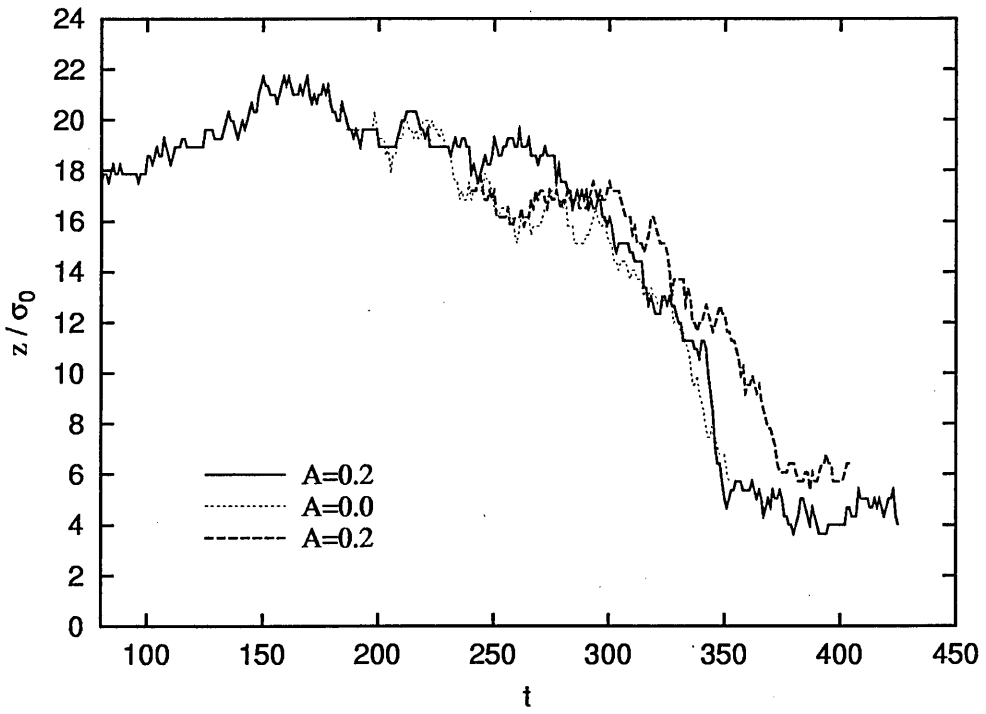

Figure 6.29: Time-resolved tip position for the relaxation of the chevron structure, following on from Fig. 6.21: solid line shows the relaxation of the A=0.2 surfaces chevron system, dotted line shows the system with roughness removed at time t=186, dashed line shows a system created from this A=0.0 system by reintroducing the A=0.2 surfaces at time t=240.

Since the layers maintain registry during the relaxation, the process must involve slip across the surface to allow relative motion of the lower and upper halves of the chevron structure. This relative motion can be seen by making a snapshot of a system which shows the true diffusion taking place (i.e. which has had the effects of the periodic boundary conditions undone) over a short part of the relaxation. Fig. 6.31 shows such a snapshot of the asymmetric chevron structure. The particle positions shown are the true positions at time t=268 given by using the positions within the simulation box at time t=226 as the starting positions. Again, the diffusion at the surfaces and at the tip can be seen, together with a shift of the particles in the lower domain.

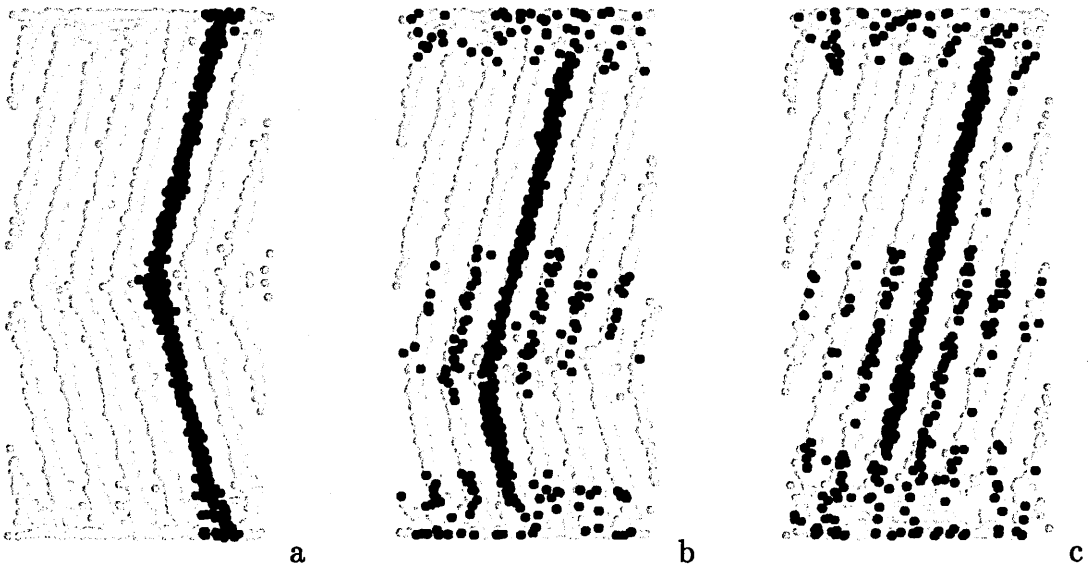

Figure 6.30: Relaxation of the A=0.2 chevron system with black dots showing positions of particles originally in one layer and grey dots showing the remaining particles: (a) chevron structure at time t=182, (b) asymmetric chevron structure at time t=286, (c) tilted layer structure at time t=350.

Figure 6.31: Snapshot showing the true diffusion which occurred during the relaxation of the A=0.2 chevron system from time t=226 to time t=268, created by undoing the effects of the periodic boundaries.

6.7 Fixed Particle Substrate System

To try to fully stabilise the chevron structure through surface pinning a substrate was created which combined the continuum surface model with a layer of particles, each having a fixed position and orientation. The interaction between surface and bulk particles used the same parameterisation as the intermolecular potential. The structure of the surface was designed to match that of the bulk layers

The continuum surface potential used was the particle-sphere interaction with no tilt or well-depth modulation (δ=0 and A=0). So that the surface particles could pin the bulk particles, the centres of the surface particles were set to stand out from the surface at a z position of $z_0+0.5\sigma_0$ for the lower surface and $z_0-0.5\sigma_0$ for the upper surface. The tilt of the surface particles was $\pm 13.923°$ and particles were arranged in 6 layers in the x-direction and 17 particles in the y-direction. Alternate layers were offset in the y-direction by $0.5\delta y$, where δy was the y-spacing, to give the hexagonal-type packing necessary for the required x-spacing.

The simulation box size was calculated assuming that the surface particles were inside the box and contributed to the number density, effectively increasing the total number of particles from 3520 to 3724. This gave box dimensions of $x = 15.782303$, $y = 17.160763$ and $z = 41.666664$, with $\rho = 0.33$, $\delta y = 1.0094566$ and smectic layer spacing $\delta x \cos(13.923) = 2.5531044$.

An initial test of the influence of the substrates on the system was carried out. The initial configuration was taken from the T=0.95 nematic system used for the quenches in Section 6.4. This was slowly resized to the required box dimensions over a 200,000 step run at T=0.95. The z coordinates were then rescaled to move the particles away from the surfaces and the particle substrate was introduced. This system was equilibrated for 1,000,000 timesteps at T=0.95, then quenched

to T=0.85 and equilibrated for a further 1,200,000 timesteps.

Although this system did form a stable chevron-like structure, it possessed many undesirable characteristics. A snapshot of the system, shown in Fig. 6.32, reveals tilted surface layers in registry with the surface particles, but separated by a large central disordered region.

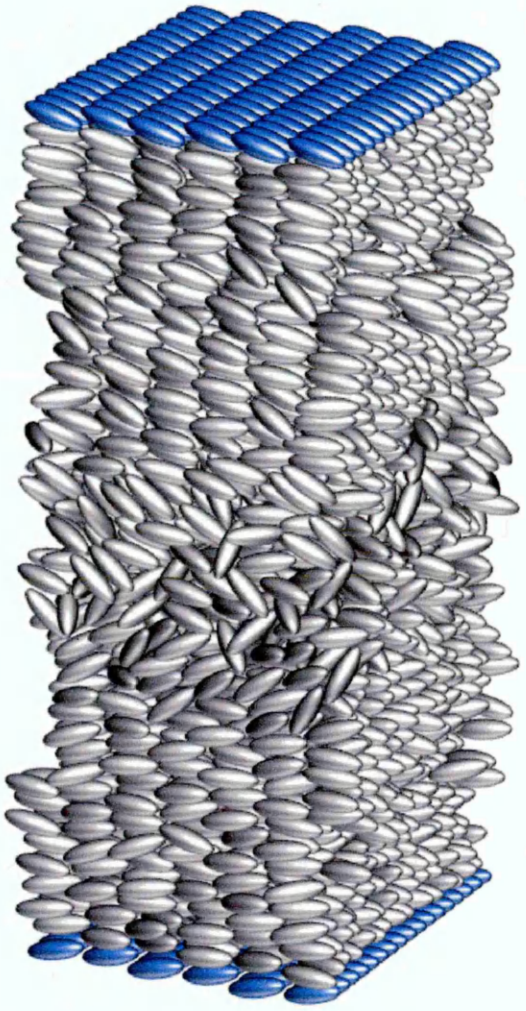

Figure 6.32: Chevron-like structure stabilised by fixed hexagonally-packed tilted surface particles, shown in blue.

Block averaged profiles of this structure were created with 120 slices over 200,000 steps with configurations saved every 500 steps. All these profiles contain

voids, especially in the surface regions. The order profiles in Fig. 6.33 show a large nematic central region. The tilt and twist profiles in Fig. 6.34 both show kinked structures within this region. If this system were sheared, by moving the surfaces, the layers are likely to move over each other, separated by the disordered central region.

The normalised density profile in Fig. 6.35 shows voids due to the structure of the smectic layers. The sinusoidal variation in the layered regions represents the beat frequency between the slices used to make the profiles and the periodicity of the internal structure of the layers.

A block average of the number density in a central region of z dimension $2\sigma_0$ gave a value $\rho = 0.307$, which at T=0.85, from the phase diagram in Fig. 6.1, is on the edge of the stable nematic region. The voids in the structure of the layered regions make determination of their density difficult, but the low density of central region suggests that the highly ordered layered regions drew particles out from the central region, thus reducing the local density, and that the layered regions could represent a crystal phase induced by the highly ordered substrates.

The particle substrate in this system effectively dictates the tilt, twist, layer spacing and near-surface structure. The structure which formed probably does not represent a natural structure, rather the result of too many constraints imposed on the system, and so this system was not studied further.

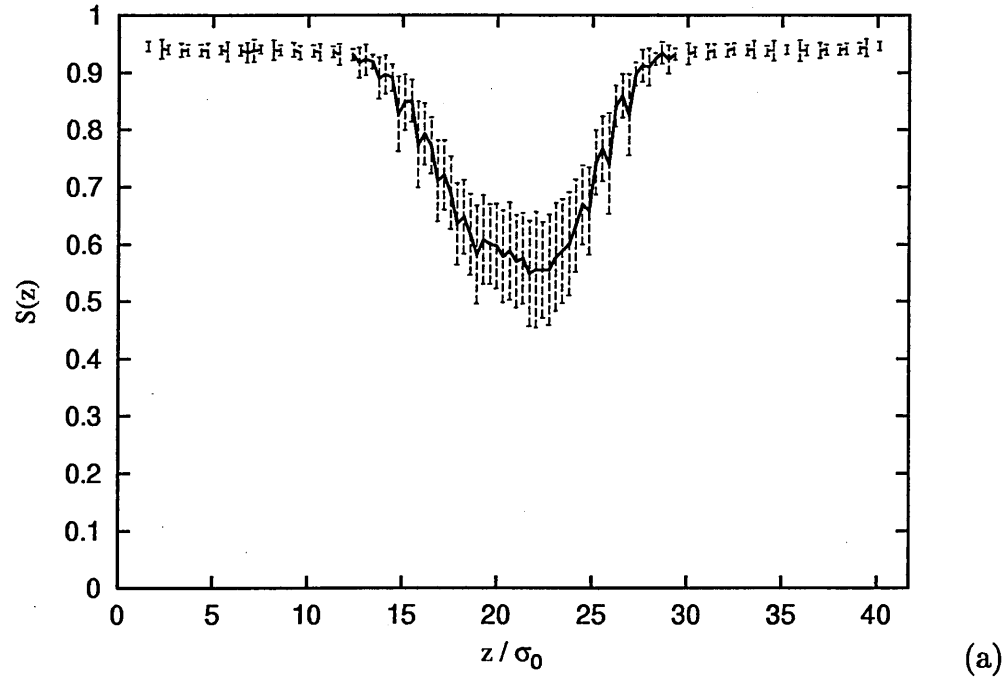

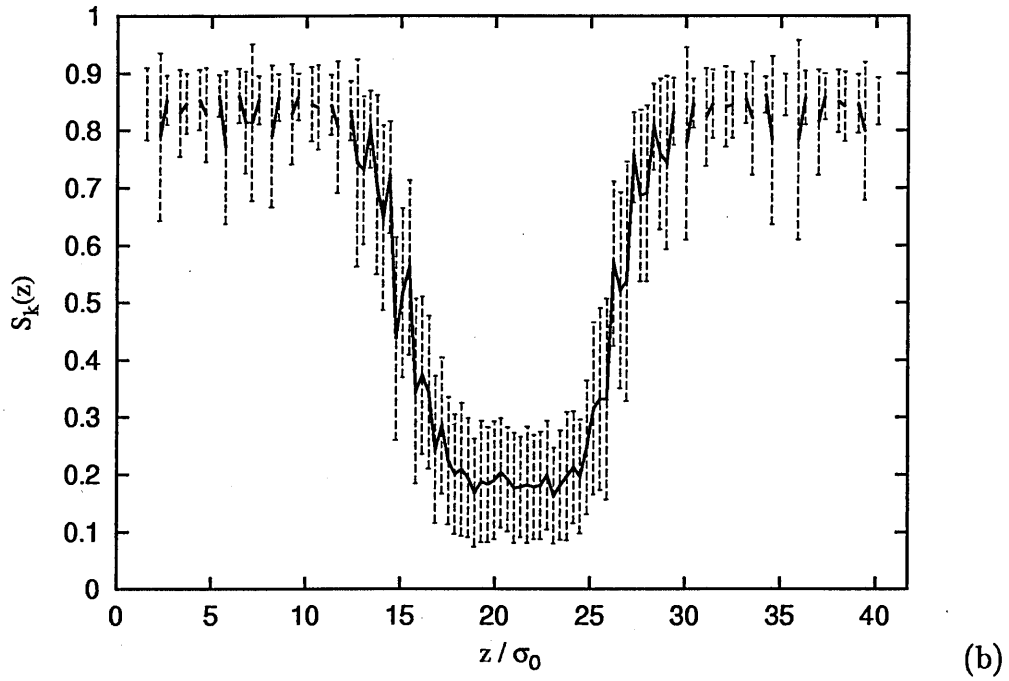

Figure 6.33: Orientational (a) and positional (b) order parameter profiles of the particle substrate stabilised structure.

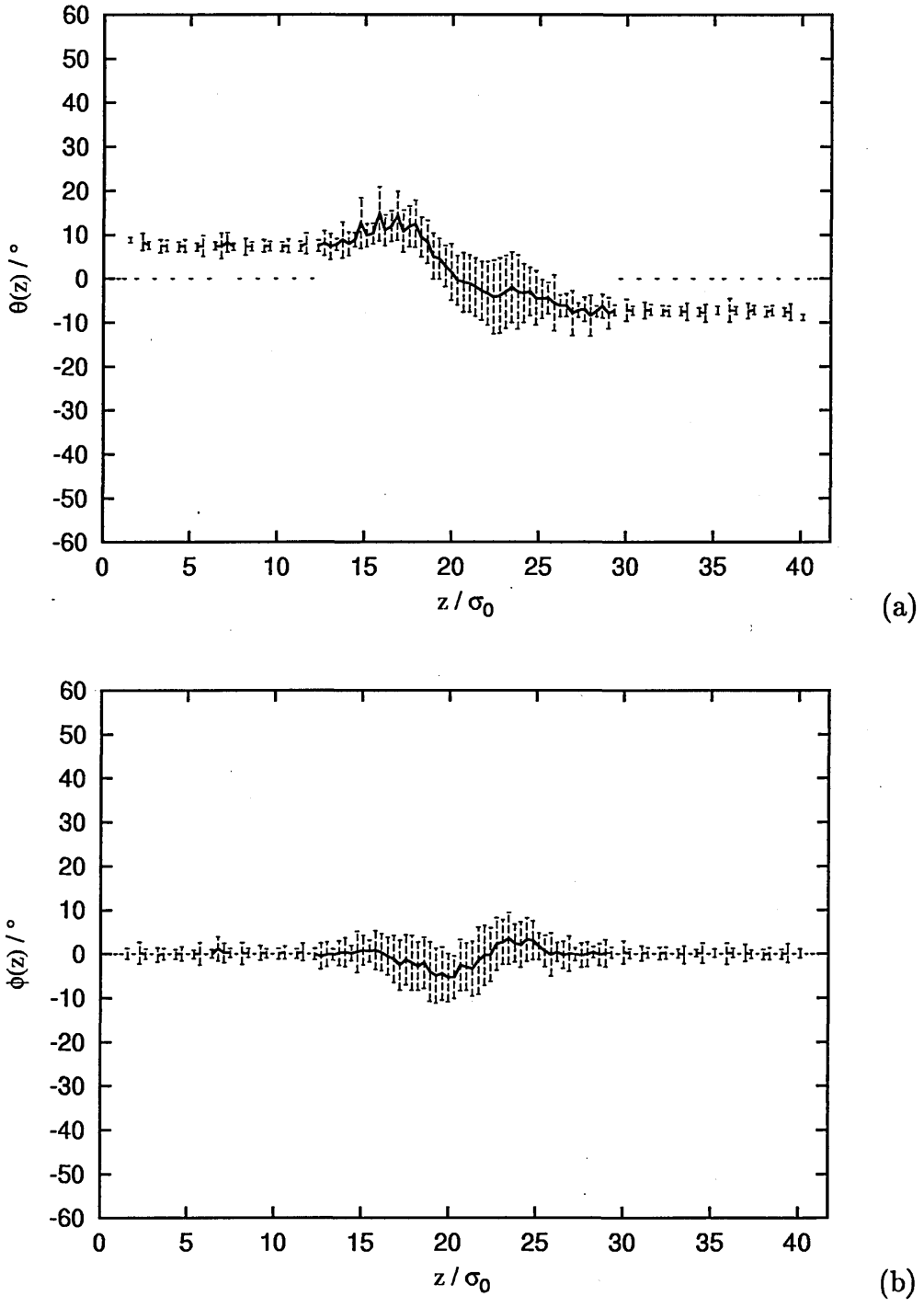

Figure 6.34: Tilt (a) and twist (b) profiles of the particle substrate stabilised structure.

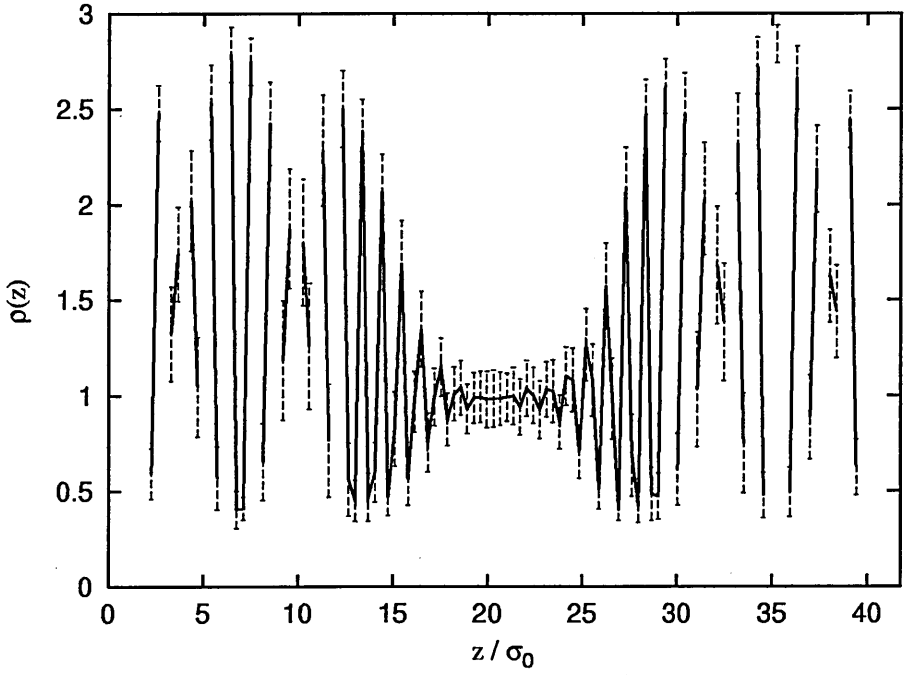

Figure 6.35: Normalised density profile of the particle substrate stabilised structure. The sinusoidal variation in the layered regions represents the beat frequency between the slices used to make the profiles and the periodicity of the internal structure of the layers.

6.8 Summary

The aim of the simulations presented in this chapter was to determine whether a surface stabilised chevron structure could be observed in a molecular system and to study the possible effects on its stability of surface slip.

The results demonstrate that the method of quenching a nematic system confined by surfaces with equal and opposite pretilts into the smectic phase can produce tilted layer, chevron and bookshelf structures, without requiring detailed modelling of the layer thinning mechanism thought to be responsible for chevron formation in device scale smectic cells.

The system which formed a chevron/tilted layer structure on quenching had smooth surfaces with no well-depth modulation, whereas the system which formed a bookshelf structure on quenching had rough surfaces. The director profiles of these systems prior to quenching suggest that the differences in the structures formed were due not to the different surfaces but to the initial twist profiles biasing the systems to form the resulting structures. The chevron/tilted layer system had two domains with a low twist angle, divided by a small central region of large twist variation. This would have suppressed formation of smectic layers in the central region, allowing the two initial smectic domains to form. The bookshelf system had a smooth twist profile between the surfaces, with a large twist angle in the lower half of the box. This would have allowed a single central smectic domain to form; the large twist angle allowing the period of the smectic layers to match the periodicity imposed by the boundary conditions.

The smectic layers in both these system did not form 6 independent layers but formed layers which were effectively wrapped around onto each other by the periodic boundaries. However, the order due to the hexagonal packing of particles

within the layers of the S_B phase is not long-ranged, and the ABC arrangement of the layers in both systems is a natural arrangement for 6 layers able to move independently within the layer plane. This could indicate that the system was of sufficient size for the layers to act as 6 independent layers.

In both cases the smectic domains formed in the bulk region rather than growing out from the surfaces. This, together with the arbitrary orientation relative to the surfaces of the hexagonal packing structures within the smectic layers, suggests only weak coupling between the smectic layers and the surfaces.

The initial chevron-like structure which formed on quenching the smooth surface system quickly formed a tilted layer structure through the upper domain growing at the expense of the lower domain; presumably due to the higher orientational and positional order of the upper domain.

Imposing various levels of surface roughness on this system appeared to influence its stability. Rough surfaces introduced soon after the quench appeared to stabilise the structure, leading to the tip moving to the central region. Rough surfaces introduced a short time later did not stabilise the structure but did appear to slow the growth of the upper domain.

The profile of the stabilised chevron structure showed a small melted tip region and small disordered regions near the surfaces. The effect of the periodic boundary conditions on the local tip structure is likely to have been a melting of the tip region, as the director orientation at the tip would mean the periodicity of the smectic layers would not match the periodicity imposed by the periodic boundaries. Therefore the chevron tip in this system was probably larger than that which would be observed in an ideal system.

The two domains of the chevron structure formed with slightly different values

of tilt, twist, orientational order and positional order. The lower order of the lower domain could have been due to the interplay between the periodic boundary conditions and the orientation of the layers; the orientation becoming trapped by the lower surface and the upper domain.

The orientation, relative to the surfaces, of the hexagonal packing within the layers was different in each domain of the chevron structure, again suggesting that the two domains formed in the bulk with only weak surface coupling and no direct influence of the surfaces on the internal structure within the layers.

In the long term this chevron structure relaxed to a tilted layer structure via an asymmetric chevron. Increasing the roughness of the surfaces slowed this relaxation. This can be explained by the fact that the layers in the upper and lower domains maintained registry as the chevron tip moved down to the lower surface and thus the motion of the tip involved relative motion of the two domains across the surfaces. The low order and diffusion at the surfaces would always allow some slip, so it is possible that this system could not be fully stabilised by any degree of pinning of the surface particles. Removing the surface roughness did not reduce the relaxation time, which suggests that although the surface slip was an influence on the stability of the chevron structure, the structure possessed enough stability for the overall relaxation process to be relatively slow.

For the fixed-particle substrate chevron system, the forcing of the layer spacing, layer tilt and surface structure lead to high density, possibly crystal layers growing out from the surface and a low density nematic central region. This was probably due to the number of constraints on the system preventing it from finding a natural way to match the layer tilt angle and layer spacing with the periodic boundary conditions in the simulation box.

Overall, the results presented in this chapter suggest that, due to the small size of the low order surface and chevron tip regions, chevron structures can be observed in a Gay-Berne system of the size simulated here. The surface roughness does appear to have influenced the stability of the chevron structure, whilst not fully stabilising it. The probable mechanism for this influence is a restriction of the movement of the domains across the surfaces during the movement of the tip between the surfaces, the movement of the domains being necessary due to the registry between the layers in the upper and lower domains.

Chapter 7

Conclusions

7.1 Introduction

This chapter summarises the main results of this thesis and suggests directions for future work. Due to the different nature of the systems studied, the main points from the nematic and smectic systems are considered separately. The results from relaxation studies of field aligned nematics are considered in Section 7.2 and the results from the studies of confined smectic structures are considered in Section 7.3. Overall conclusions from the work are presented in Section 7.4.

7.2 Relaxation of Field Aligned Systems

The results presented in Chapter 4 of the relaxation of GB35 and GB25 systems of around 3000 particles show that relaxation timescales of these systems are accessible.

The tilted surface of the GB35 system lead to a near surface region with a complicated relationship between density, director and orientational order profiles.

In the field off case for the GB35 system, the bulk tilt was lower than the tilt in the surface regions. The tilt angle of the bulk could represent a compromise between the tilt imposed by the tilted surface layer and an overall planar aligning influence due to the presence of the surfaces.

For the field aligned systems, it would seem that a small transition region of less than around $30\sigma_0$ cannot be created without lowering the order parameter significantly, destabilising the nematic in the surface region and placing the system outside the scope of continuum theory treatments.

Relaxation on field removal shows a slight movement of particles across the surfaces, rather than in the bulk as would be the case with induced backflow. The lack of surface structure in these systems effectively creates slip boundary conditions at the surfaces. Theoretical predictions of backflow and kickback assume non-slip boundary conditions. The flow profile on relaxation may have been different with strong surface pinning of particles. However, the lack of a large field aligned bulk region separating the regions of initial director reorientation was probably the main reason why no backflow was seen. Any flows induced would be cancelled out due to the proximity of the reorientation regions.

The estimate made in Section 4.7 of the real value of the GB35 parameterisation timestep of $10^6\delta t \approx 15$ns gives timescales for the relaxation of these systems of the order of tens of nanoseconds, as opposed to microseconds for a real nematic cell. This suggests that the relaxation processes observed here are not equivalent to the macroscopic processes observed in real cells.

Increasing the surface separation in order to allow a large field aligned bulk region would seem to reduce the direct influence of the aligning surfaces on the central bulk region, leading to long timescale variations in the director in this

region. An attempt to align this bulk region by tilting the field caused the planar surface regions to grow into the bulk, thus reducing the effective surface separation.

The results of the simulations of HAN systems presented in Chapter 5 demonstrate that flow patterns associated with director reorientation can be seen in the molecular systems studied here.

For the field off continuum surface systems, the director and order profiles suggest that even the surface separation of $60\sigma_0$ used here was not enough to allow the rotation of the director between the surfaces without a reduction in order. This appears to have happened at arbitrary points between the surfaces, rather than across the box as a whole, allowing sudden changes in the director at the points of low order. The smectic-like layered structure induced in the lower surface region would also project the normal alignment of the lower surface out some distance into the bulk, effectively reducing the size of the bulk region available to accommodate the change in director orientation.

In the field aligned HAN systems, the order was enhanced in the bulk and reduced in the transition regions, again a feature not considered in continuum treatments.

All of the HAN systems displayed the same overall relaxation behaviour. The initial rotation of the director moved down to the lower surface, then reversed in the lower surface region, the director motion and flow pattern subsequently showing damped oscillatory behaviour. This behaviour suggests that the relaxation in these systems was dominated by elastic forces and that the director motion and flow do not correspond to the relaxation processes of backflow and kickback observed in real cells.

The lack of flow in the lower regions could be due to the relationship of the

Gay-Berne viscosities $\eta_2 > \eta_1$, but since the flow is probably not a macroscopic flow, the mechanism of suppression of translational motion through interdigitation of the smectic-like layers at the lower surface may be more likely.

The difference in the overall magnitude of the relaxation behaviour between the three HAN systems is probably due to a combination of factors. The stronger oscillatory behaviour in the particle substrate system could be a product of the higher field strength and stronger surface pinning. The weaker oscillatory behaviour of the tilted upper surface system could be due to the lower director distortion in the upper surface region.

A feature exhibited by the field aligned systems in Chapter 4 and especially those in Chapter 5 is some degree of twisting of the director throughout the distorted near-surface transition regions. Theoretical treatments of the splay geometry cell make the assumption that the director rotates in a plane defined by the field and the surface easy-axis and, therefore, that the system can be considered to be two dimensional. The assumption is also made that the length scale of any director distortion is large compared with molecular lengths and so the local order parameter does not change. In the systems simulated here, the length scale of the director distortions was only an order of magnitude greater than the particle lengths and the order was reduced in the distorted regions. These systems can, therefore, be said to have been distorted on a molecular scale. This could provide a driver for the local twisting of the director through packing effects, whereby adjacent particles twist relative to each other to satisfy the constraints of a locally splayed configuration and the ellipsoidal particle shape.

The nature of the relaxation mechanisms observed in these simulations suggests that much larger system sizes would be needed to simulate relaxation pro-

cesses corresponding to macroscopic backflow and kickback processes. Whatever the exact nature of the flow in these systems, the effects on the overall damping of reducing surface roughness, and hence reducing the degree of pinning, could be investigated in a more systematic way.

A more tractable possibility for future study based on the results presented here would be static studies of the detail of the surface region of a system with a tilted surface layer, with the aim of determining the interaction between the density, tilt and order profiles.

The mechanism for the twisting seen in the director within the transition regions of the field aligned systems could be studied further. If the packing of ellipsoidal particles subject to a molecular scale director distortion were responsible for the twist, then presumably the degree of twisting would be some function of the degree of splay distortion imposed. This could be studied by making small changes in the strength of the applied field.

7.3 Confined Smectic Systems

The results presented in Chapter 6 demonstrate that bookshelf, chevron and tilted layer structures can be observed in a confined smectic Gay-Berne system.

The method of quenching a nematic into the smectic phase allows chevron and tilted layer structures to form without requiring detailed modelling of the layer thinning mechanism thought to be responsible for experimentally observed layer tilting in smectic cells on cooling.

The initial profiles of the nematic systems prior to quenching corresponded to the structures formed in each system on quenching. This suggests that, even though the chevron/tilted layer system was quenched on smooth surfaces and the

bookshelf system was quenched on rough surfaces, the different structures formed were the result of the initial profiles, rather than the influence of the surfaces.

In both the bookshelf and the chevron/tilted layer systems, the smectic domains formed in the bulk rather than growing out from the surfaces as desired. This suggests weak coupling between the smectic layers and the surface. This could account for the arbitrary orientation relative to the surfaces of the hexagonal packing structure within the S_B layers, and the slight differences in tilt, twist, and order parameters in the two domains formed in the chevron/tilted layer system.

These differences between the order parameters in the upper and lower domains of the chevron/tilted layer system account for the movement of the chevron tip towards the lower surface rather than towards the upper surface. The higher order of the upper domain favoured its growth at the expense of the weaker lower domain.

Introducing rough surfaces into this system soon after quenching caused the tip to move to the centre of the box. This suggests that even as the smectic layers were forming, there was some connection between the layers in the upper and lower domains which required some degree of relative movement of the domains across the surfaces in order for the tip position to change. Rough surfaces introduced a short time later slowed the growth of the upper domain but did not cause the tip to move to the central region. This suggests that the more asymmetric the structure, the greater the surface pinning is required to be in order to stabilise it.

The profile of the stabilised chevron structure showed a small melted tip region and small disordered regions near the surfaces. This suggests that a simulation of this size is large enough to support the two smectic-surface interfaces and the

central smectic-smectic interface formed by a confined chevron structure.

In the long term the chevron structure was not fully stable and relaxed to a tilted layer structure, the layers in the upper and lower domains maintaining registry throughout the relaxation. Increasing the surface roughness slowed this relaxation. Due to the registry between the upper and lower domains, relative movement of the domains across the surfaces was needed for the chevron tip to move. This provided the mechanism for the surface roughness to influence the stability of the chevron structure.

Removing the surface roughness from the chevron structure did not shorten the relaxation time, demonstrating that this relaxation is a relatively slow process. The effect of the periodic boundary conditions dictating the layer tilt could play a role in stabilising the system, preventing further tilting of the layers in an asymmetric chevron structure.

Re-introducing the rough surfaces did not recreate the original formation of the centred chevron structure. This could be due to the weak layers which formed on quenching being influenced more by the surfaces than the stronger layers which developed in the chevron structure; the stronger layers appeared more able to dominate the behaviour of the system due to the weak surface coupling.

If, during the initial quench, the two domains of the chevron system had formed with the same internal structure and order, the system may have been fully stabilised by the rough surfaces. However, the long term stability of such a system might be difficult to determine as the relaxation timescale of a chevron structure with domains of equal order may be unaccessible in this system.

It is difficult to predict what might happen in such a surface stabilised system on shearing. The registry between the domains would suggest that the tip would

move towards one surface, forming an asymmetric chevron. However, the reduced nematic order in the melted tip region could allow the system to focus the shear at the tip, particularly at high shear rates.

The particle substrate system did not form a satisfactory structure, probably due to the imposition of too many constraints, but the structure did appear to be stable. This suggests a possible direction for further study. Using the method of chevron formation via imposed surface pretilt, a stabilised chevron structure could perhaps be produced in a system using particle substrates in which each particle is allowed to move by some small amount from its set position and orientation so as to avoid imposing a rigid structure on the near surface region. Such particles could be held in position by spring-like intramolecular potentials used to model bonds in hybrid Gay-Berne–atomistic molecular models.

7.4 Summary

The aim of this work was to determine whether simulations relevant to dynamic phenomena observed in device-scale liquid crystal cells could be performed using parallel molecular dynamics of the Gay-Berne model.

Relaxation timescales of confined field aligned nematic systems have been shown to be accessible. Flow phenomena associated with director reorientation have been observed in hybrid aligned nematic systems. The damped oscillatory nature of the flow and director reorientation suggests that the behaviour of these systems is dominated by elastic forces and that the processes observed do not correspond to the macroscopic processes of backflow and orientational kickback. This suggests that molecular dynamics of the Gay-Berne model is not an effective method for studying backflow and orientational kickback in nematic cells.

Bookshelf, chevron and tilted layer structures have been simulated in confined smectic systems. Surface slip has been shown to influence the formation and stability of the chevron structure. The chevron structure was not fully stabilised and relaxed to a tilted layer structure via an asymmetric chevron. The simulation of a stable chevron-like structure in a fixed-particle substrate system suggests that surface stabilised chevron structures can be simulated in Gay-Berne systems of the size studied here given development of a suitable substrate model.

A theme occurring throughout this work has been the search for a substrate model appropriate for the system being studied. Although the simulation of bulk liquid crystal phases using the Gay-Berne model is well established, there is obviously much scope for development in the area of Gay-Berne molecule-substrate interaction models.

Bibliography

[1] P.G. de Gennes and J. Prost. *The Physics of Liquid Crystals.* Oxford University Press, 1993.

[2] P.J. Collings and M. Hird. *Introduction to Liquid Crystals Chemistry and Physics.* Taylor & Francis, 1997.

[3] B. Jérôme. Surface effects and anchoring in liquid crystals. *Rep. Prog. Phys.*, 54:391–451, 1991.

[4] J. Israelachvili. *Intermolecular & Surface Forces.* Academic Press, 2nd edition, 1991.

[5] P.J. Collings. *Liquid Crystals.* IOP Publishing Ltd, 1990.

[6] D.P.E. Smith, H. Horber, C. Gerber, and G. Binnig. Smectic liquid crystal monolayers on graphite observed by scanning tunneling microscopy. *Science*, 245:43–45, 1989.

[7] D.P.E. Smith, J.K.H. Horber, G. Binnig, and H. Nejoh. Structure, registry and imaging mechanism of alkylcyanobiphenyl molecules by tunneling microscopy. *Nature*, 344(6267):641–644, 1990.

[8] T.J. McMaster, H. Carr, M.J. Miles, P. Cairns, and V.J. Morris. Scanning tunneling microscopic images of the surface ordering of the liquid-crystal 4-n-octyl-4'-cyanobiphenyl. *Liq. Cryst.*, 9(1):11–18, 1991.

[9] M. Hara, Y. Iwakabe, K. Tochigi, H. Sasabe, A.F. Garito, and A. Yamada. Anchoring structure of smectic liquid-crystal layers on MoS_2 observed by scanning tunneling microscopy. *Nature*, 344(6263):228–230, 1990.

[10] S. Chandrasekhar. *Liquid Crystals.* Cambridge University Press, 1992.

[11] J. Cheng and G.D. Boyd. The liquid-crystal alignment properties of photolithographic gratings. *Appl. Phys. Lett.*, 35(6):444–446, 1979.

[12] M.F. Toney, T.P. Russell, J.A. Logan, H. Kikuchi, J.M. Sands, and S.K. Kumar. Near-surface alignment of polymers in rubbed films. *Nature*, 374:709–711, 1995.

[13] J.K. Moscicki. Measurements of viscosities in nematics. in [85].

[14] P. Pieranski, F. Brochard, and E. Guyon. Static and dynamic behavior of a nematic liquid crystal in a magnetic field. *J. Phys. (Paris)*, 34:35–48, 1973.

[15] T. Fukazawa, T. Tadokoro, H. Toriumi, T. Akahane, and M. Kimura. Application of time-resolved spectroellipsometry to the study of liquid crystal reorientation dynamics. *Thin Solid Films*, 313:799–802, 1998.

[16] F. Yang, J.R. Sambles, and G.W. Bradberry. Guided modes and related optical techniques in liquid crystal alignment studies. in [86].

[17] M. Mitsuishi, S. Ito, M. Yamamoto, T. Fischer, and W. Knoll. Time-resolved optical waveguide study of the reorientation in a nematic liquid crystal under applied electric field. *J. Appl. Phys.*, 81(3):1135–1142, 1997.

[18] S.J. Elston. The alignment of a liquid crystal in the smectic a phase in a high surface tilt cell. *Liq. Cryst.*, 16(1):151–157, 1994.

[19] T.P. Rieker, N.A. Clark, G.S. Smith, D.S. Parmar, E.B. Sirota, and C.R. Safinya. "Chevron" local layer structure in surface-stabilized ferroelectric smectic–C cells. *Phys. Rev. Lett.*, 59(23):2658–2661, 1987.

[20] S.J. Elston and J.R. Sambles. Characterization of reorientation of a thin layer of ferroelectric liquid-crystal material under an applied electric field by excitation of optical modes. *Appl. Phys. Lett.*, 55(16):1621–1623, 1989.

[21] M. Cagnon and G Durand. Positional anchoring of smectic liquid crystals. *Phys. Rev. Lett.*, 70(18):2742–2745, 1993.

[22] G. Srajer, R. Pindak, and J.S. Patel. Electric-field-induced layer reorientation in ferroelectric liquid crystals: An x-ray study. *Phys. Rev. A*, 43(10):5744–5747, 1991.

[23] A.S. Morse and H.F. Gleeson. Observation of a chevron hybrid structure in the smectic a phase of a liquid crystal device. *Liq. Cryst.*, 23(4):531–535, 1997.

[24] N.A. Clark and S.T. Lagerwall. Submicrosecond bistable electro-optic switching in liquid crystals. *Appl. Phys. Lett.*, 36(11):899–901, 1980.

[25] F. Brochard, P. Pieranksi, and E. Guyon. Dynamics of the orientation of a nematic-liquid-crystal film in a variable magnetic field. *Phys. Rev. Lett.*, 28(26):1681–1683, 1972.

[26] C.Z. Van Doorn. Dynamic behavior of twisted nematic liquid-crystal layers in switched fields. *J. appl. Phys.*, 46:3738, 1975.

[27] D. Berreman. Liquid-crystal twist cell dynamics with backflow. *J. Appl. Phys.*, 46(9):3746–3751, 1975.

[28] M.G. Clark and F.M. Leslie. A calculation of orientational relaxation in nematic liquid crystals. *Proc. R. Soc. Lond.*, A(361):463–485, 1978.

[29] L. Limat and J. Prost. A model for the chevron structure obtained by cooling a smectic A liquid crystal in a cell of finite thickness. *Liq. Cryst.*, 13(1):101–113, 1993.

[30] A. de Meyere, H. Pauwels, and E. de Ley. Calculation of chevron profiles in ferroelectric liquid crystal cells. *Liq. Cryst.*, 14(5):1269–1282, 1993.

[31] S. Kralj and T.J. Sluckin. Landau-de Gennes theory of the chevron structure in a smectic-A liquid crystal. *Phys. Rev. E*, 50(4):2940–2951, 1994.

[32] N. Vaupotič, S. Kralj, M. Čopič, and T.J. Sluckin. Landau-de Gennes theory of the chevron structure in a smectic liquid crystal. *Phys. Rev. E*, 54(4):3783–3792, 96.

[33] N. Ul Islam, N.J. Mottram, and S.J. Elston. Stability of the formation of the chevron structure. *Liq. Cryst.*, 26(7):1059–1065, 1999.

[34] N.J. Mottram and S.J. Elston. Shearing of planar smectic C chevrons. *Eur. Phys. J. B*, 12:277–284, 1999.

[35] M.P. Allen and D.J. Tildesley. *Computer Simulation of Liquids.* Oxford University Press, 1989.

[36] H. Goldstein. *Classical Mechanics.* Addison Wesley, 1966.

[37] A.J. Stone. *The Theory of Intermolecular Forces.* Oxford University Press, 1996.

[38] J.M. Illnytsyi and M.R. Wilson. Molecular models in computer simulation of liquid crystals. *J. Mol. Liq.*, 92(1-2):21–28, 2001.

[39] M.R. Wilson. Atomistic simulations of liquid crystals. in *Structure and Bonding*, 94, 41–64, Springer Verlag, 1999.

[40] D.J. Cleaver and D.J. Tildesely. Computer modelling of the structure of 4-n-octyl-4'-cyanobiphenyl adsorbed on graphite. *Molec. Phys.*, 81(4):781–799, 1994.

[41] M. Yoneya and Y. Iwakabe. Molecular dynamics simulations of liquid crystal molecules adsorbed on graphite. *Liq. Cryst.*, 18(1):45–49, 1995.

[42] D.J. Cleaver, M.J. Callaway, T. Forester, W. Smith, and D.J. Tildesley. Computer modeling of the 4-n-octyl-4'-cyanobiphenyls adsorbed on graphite - energy minimizations and molecular-dynamics of periodic-systems. *Molec. Phys.*, 86(4):613, 1995.

[43] C. McBride, M.R. Wilson, and J.A.K. Howard. Molecular dynamics simulation of liquid crystal phases using atomistic potentials. *Molec. Phys.*, 93(6):955–964, 1998.

[44] D.R. Binger and S. Hanna. Computer simulation of interactions between liquid crystal molecules and polymer surfaces I. Alignment of nematic and smectic A phases. *Liq. Cryst.*, 26(8):1205–1224, 1999.

[45] D.R. Binger and S. Hanna. Computer simulations of interactions between liquid crystal molecules and polymer surfaces III. Use of pseudopotentials to represent the surface. *Liq. Cryst.*, 28(8):1215–1234, 2001.

[46] J. Corner. The second virial coefficient of a gas of non-spherical molecules. *Proc. R. Soc. Lond. A*, 192:275–292, 1948.

[47] B.J. Berne and P. Pechukas. Gaussian model potentials for molecular interactions. *J. Chem. Phys.*, 56(8):4213–4216, 1972.

[48] J. Kushick and B.J. Berne. Computer simulation of anisotropic molecular fluids. *J. Chem. Phys.*, 64(4):1362–1367, 1976.

[49] J.G. Gay and B.J. Berne. Modification of the overlap potential to mimic a linear site-site potential. *J. Chem. Phys.*, 74(6):3316–3319, 1981.

[50] D.J. Adams, G.R. Luckhurst, and R.W. Phippen. Computer simulation studies of anisotropic systems. XVII. The Gay-Berne model nematogen. *Molec. Phys.*, 61(6):1575–1580, 1987.

[51] G.R. Luckhurst, R.A. Stephens, and R.W. Phippen. Computer simulation studies of anisotropic systems. XIX. Mesophases formed by the Gay-Berne model mesogen. *Liq. Cryst.*, 8(4):451–464, 1990.

[52] E. de Miguel, L.F. Rull, M.K. Chalam, and K.E. Gubbins. Liquid-vapour coexistence of the Gay-Berne fluid by Gibbs-Ensemble simulation. *Molec. Phys.*, 71(6):1223–1231, 1990.

[53] E. de Miguel, L.F. Rull, M.K. Chalam, K.E. Gubbins, and F. van Swol. Location of the isotropic-nematic transition in the Gay-Berne model. *Molec. Phys.*, 72(3):593–605, 1991.

[54] E. de Miguel, L.F. Rull, M.K. Chalam, and K.E. Gubbins. Liquid crystal phase diagram of the Gay-Berne fluid. *Molec. Phys.*, 74(2):405–424, 1991.

[55] M.K. Chalam, K.E. Gubbins, E. de Miguel, and L.F. Rull. A molecular simulation of a liquid crystal model: Bulk and confined fluid. *Molecular Simulation*, 7:357–385, 1991.

[56] R. Berardi, A.P.J. Emerson, and C. Zannoni. Monte carlo investigations of a Gay-Berne liquid crystal. *J. Chem. Soc. Farady Trans.*, 89(22):4069–4078, 1993.

[57] E. de Miguel. System-size effects at the isotropic-nematic transition from computer simulation. *Phys. Rev. E*, 47(5):3334–3342, 1993.

[58] G.R. Luckhurst and P.S.J. Simmonds. Computer simulation studies of anisotropic systems. XXI. Parameterization of the Gay-Berne potential for model mesogens. *Molec. Phys.*, 80(2):233–252, 1993.

[59] R. Hashim, G.R. Luckhurst, and S. Romano. Computer-simulation studies of anisotropic systems. *J. Chem. Soc. Faraday Trans.*, 91(14):2141–2148, 1995.

[60] E. de Miguel, E. Martin del Rio, J.T. Brown, and M.P. Allen. Effect of the attractive interactions on the phase behavior of the Gay-Berne liquid crystal model. *J. Chem. Phys.*, 105(10):4234–4249, 1996.

[61] J.T. Brown, M.P. Allen, E. Martin del Rio, and E. de Miguel. Effects of elongation on the phase behaviour of the Gay-Berne fluid. *Phys. Rev. E*, 57(6):6685–6699, 1998.

[62] M.A. Bates and G.R. Luckhurst. Computer simulation studies of anisotropic systems. XXX. The phase behaviour and structure of a Gay-Berne mesogen. *J. Chem. Phys.*, 110(14):7087–7108, 1999.

[63] M.P. Neal and A.J. Parker. Computer simulations using a longitudinal quadrupolar Gay-Berne model: Effect of the quadrupole magnitude on the formation of the smectic phase. *Chem. Phys. Lett.*, 294:277–284, 1998.

[64] J. Stelzer, L. Longa, and H.R. Trebin. Molecular dynamics simulations of a Gay-Berne nematic liquid crystal: Elastic properties from direct correlation functions. *J. Chem. Phys.*, 103(8):3098–3107, 1995.

[65] M.P. Allen, M.A. Warren, A. Sauron, and W. Smith. Molecular dynamics calculation of elastic constants in Gay-Berne nematic liquid crystals. *J. Chem. Phys.*, 105:2850–2858, 1996.

[66] A.M. Smondyrev, G.B. Loriot, and R.A. Pelcovits. Viscosities of the Gay-Berne nematic liquid-crystal. *Phys. Rev. Lett.*, 75(12):2340–2343, 1995.

[67] S. Cozzini, L.F. Rull, G. Ciccotti, and G.V. Paolini. Intrinsic frame transport for a model of nematic liquid crystal. *Physica A*, 240:173–187, 1997.

[68] D.J. Cleaver, C.M. Care, M.P. Allen, and M.P. Neal. Extension and generalization of the Gay-Berne potential. *Phys. Rev. E*, 54(1):559–567, 1996.

[69] M.R. Wilson. Molecular dynamics simulations of flexible liquid crystal molecules using a Gay-Berne/Lennard-Jones model. *J. Chem. Phys.*, 107(20):8654–8663, 1997.

[70] C. McBride and M.R. Wilson. Molecular dynamics simulations of a flexible liquid crystal. *Molec. Phys.*, 97(4):511–522, 1999.

[71] Z. Zhang, A. Chakrabarti, O.G. Mouritsen, and M.J. Zuckermann. Substrate-induced bulk alignment of liquid crystals. *Phys. Rev. E*, 53(3):2461–2465, 1996.

[72] J. Stelzer, P. Galatola, and G. Barbero. Molecular dynamics simulations of surface-induced ordering in a nematic liquid crystal. *Phys. Rev. E*, 55(1):477–480, 1997.

[73] G.D. Wall and D.J. Cleaver. Computer simulation studies of confined liquid crystal films. *Phys. Rev. E*, 56(4):4306–4316, 1997.

[74] V. Palermo, F. Biscarini, and C. Zannoni. Abrupt orientational changes for liquid crystals adsorbed on a graphite surface. *Phys. Rev. E*, 57(3):2519–2522, 1998.

[75] R. Latham and D.J. Cleaver. Substrate-induced demixing in a confined liquid crystal film. *Chem. Phys. Lett.*, 330(1–2):7–14, 2000.

[76] M.R. Wilson, M.P. Allen, M.A. Warren, A. Sauron, and W. Smith. Replicated data and domain decomposition molecular dynamics techniques for simulation of anisotropic potentials. *J. Comput. Chem.*, 18(4):478–488, 1997.

[77] P. Pasini and C. Zannoni, editors. *Advances in the Computer Simulations of Liquid Crystals.* Kluwer Academic Publishers, 1998.

[78] M. Kendall and J.K. Ord. *Time Series.* Edward Arnold, 3rd edition, 1990.

[79] M.J. Tuckerman, B.J. Berne, and G.J. Martyna. Reversible multiple time scale molecular-dynamics. *J. Chem. Phys.*, 97(3):1990–2001, 1992.

[80] R. Latham. A computer simulation of confined liquid crystal mixtures. MPhil. to PhD. transfer report, Sheffield Hallam University, 1998.

[81] W.H. Press, S.A. Teukolsky, W.T. Vetterling, and B.P. Flannery. *Numerical Recipes in C.* Cambridge University Press, 1990.

[82] D.J. Evans and G.P. Morriss. *Statistical Mechanics of Nonequilibrium Liquids.* Academic Press, 1990.

[83] G.D. Wall and D.J. Cleaver. To be published.

[84] M.P. Allen and M.A. Warren. Simulation of structure and dynamics near the isotropic-nematic transition. *Phys. Rev. Lett.*, 78(7):1291–1294, 1997.

[85] D. Dunmur, A. Fukuda, and G. Luckhurst, editors. *Physical Properties of Liquid Crystals: Nematics.* The Institute of Electrical Engineers, 2001.

[86] S. Elston and R. Sambles, editors. *The Optics of Thermotropic Liquid Crystals.* Taylor and Francis, 1998.

[87] S.L. Price, A.J. Stone, and M. Alderton. Explicit formulas for the electrostatic energy, forces and torques between a pair of molecules of arbitrary symmetry. *Mol. Phys.*, 52(4):987–1001, 1984.

[88] S. Wolfram. *Mathematica: A System for Doing Mathematics by Computer.* Addison Wesley, 2nd edition, 1991.

Appendix A

Calculating Forces due to Continuum Surface Potentials

Derivation

The molecular dynamics simulation method requires the calculation, on each timestep, of the forces responsible for translational and rotational motion. A method of deriving these forces and 'gorces' on a linear molecule from the intermolecular potential U has been developed [87].

The forces $\mathbf{F}$ responsible for the translational motion of the particle are given by

$$\mathbf{F} = -\sum \frac{\partial U}{\partial(\mathbf{s} \cdot \mathbf{R})}\mathbf{s}, \tag{A.1}$$

which is the negation of the sum of partial derivatives of the potential with respect to the dot products between space-fixed vectors $\mathbf{s}$ any vectors $\mathbf{R}$ which change with the position of the particle. The gorces $\mathbf{g}$ responsible for the rotational motion of the particle are given by

$$\mathbf{g} = -\sum \frac{\partial U}{\partial(\mathbf{s} \cdot \mathbf{t})}\mathbf{s} \tag{A.2}$$

which is the negation of the sum of partial derivatives of the potential with respect to the dot products between the space-fixed vector **s** and any vectors **t** which change with the orientation of the particle. To use this method, the potential needs to be written in terms of dot products between space-fixed vectors and vectors which change with the position and orientation of the particle.

For the aligning continuum surfaces used in this work, the space-fixed vectors are the surface easy-axis,

$$\mathbf{X} = (1, 0, 0), \tag{A.3}$$

the surface normal,

$$\mathbf{Z} = (0, 0, 1), \tag{A.4}$$

and the tilted surface normal,

$$\mathbf{P} = (\sin\delta, 0, \cos\delta) \tag{A.5}$$

where δ is the pre-tilt angle.

Re-writing the potential, the range function becomes,

$$r_{sp} = \mathbf{Z} \cdot \mathbf{r}_{sp} \tag{A.6}$$

where $\mathbf{r}_{sp} = \mathbf{r} - (0, 0, z_0)$, and the surface well-depth modulation term becomes

$$\sin(Br_x) = \sin(B(\mathbf{X} \cdot \mathbf{r})). \tag{A.7}$$

Terms involving the angle with the surface normal **Z** become, for the particle-sphere functions,

$$\cos^2\theta = (\mathbf{Z} \cdot \mathbf{u})^2 \tag{A.8}$$

and for the particle-plane functions,

$$\sin^2\theta = 1 - \cos^2\theta = 1 - (\mathbf{Z} \cdot \mathbf{u})^2. \tag{A.9}$$

Terms involving the angle with the tilted surface normal $\mathbf{P}$ become for the particle-sphere functions,

$$\cos^2\psi = (\mathbf{P}\cdot\mathbf{u})^2 \tag{A.10}$$

and for the particle-plane functions,

$$\sin^2\psi = 1-\cos^2\psi = 1-(\mathbf{P}\cdot\mathbf{u})^2. \tag{A.11}$$

For an easy axis $\mathbf{X} = (1,0,0)$, the azimuthal angle term $\cos\phi$ is the x-component of $\hat{\mathbf{u}}_{xy}$, where $\hat{\mathbf{u}}_{xy}$ is the unit vector of the projection of $\mathbf{u}$ onto the xy-plane. This gives,

$$\hat{\mathbf{u}}_{xy} = \left(\frac{u_x}{\sqrt{u_x^2+u_y^2}}, \frac{u_y}{\sqrt{u_x^2+u_y^2}}\right) \tag{A.12}$$

so

$$\cos^2\phi = \frac{u_x^2}{u_x^2+u_y^2}. \tag{A.13}$$

For the second half of the alignment term,

$$\begin{aligned} 1-\cos^2\theta &= 1-(\mathbf{Z}\cdot\mathbf{u})^2 \\ &= 1-u_z^2 \\ &= u_x^2+u_y^2 \end{aligned} \tag{A.14}$$

since $u_x^2+u_y^2+u_z^2 = 1$. This gives for the surface alignment term,

$$\begin{aligned} \cos^2\phi(1-\cos^2\theta) &= u_x^2 \\ &= (\mathbf{X}\cdot\mathbf{u})^2. \end{aligned} \tag{A.15}$$

Collecting these terms together gives an expression for the re-written potential as

$$U_{sp} = C\epsilon_{sp}\left[\frac{2}{15}\left(\frac{\sigma_0}{(\mathbf{Z}\cdot\mathbf{r}_{sp})+\sigma_0-\sigma_{sp}}\right)^9 - \left(\frac{\sigma_0}{(\mathbf{Z}\cdot\mathbf{r}_{sp})+\sigma_0-\sigma_{sp}}\right)^3\right] \tag{A.16}$$

where $C = \alpha \left[\frac{9}{10(1-\chi^2)^\nu}\right]^{\frac{1}{2}}$. For the sphere-sphere potential,

$$\sigma_{sp} = \sigma_0 \tag{A.17}$$

and

$$\epsilon_{sp} = \epsilon_0 \left[1 + A(1 + \sin(B(\mathbf{X} \cdot \mathbf{r})))\right]. \tag{A.18}$$

For the particle-sphere potential,

$$\sigma_{sp} = \sigma_0 \sqrt{\frac{1}{1 - \chi(\mathbf{Z} \cdot \mathbf{u})^2}} \tag{A.19}$$

and

$$\epsilon_{sp} = \epsilon_0 \left[(1 - \chi'(\mathbf{P} \cdot \mathbf{u})^2)^\mu + \chi''(\mathbf{X} \cdot \mathbf{u})^2 + A(1 + \sin(B(\mathbf{X} \cdot \mathbf{r})))\right]. \tag{A.20}$$

For the particle-plane potential,

$$\sigma_{sp} = \sigma_0 \sqrt{\frac{1 - \chi(1 - (\mathbf{Z} \cdot \mathbf{u})^2)}{1 - \chi}} \tag{A.21}$$

and

$$\epsilon_{sp} = \epsilon_0 \left[\left(\frac{1 - \chi'}{1 - \chi'(1 - (\mathbf{P} \cdot \mathbf{u})^2)}\right)^\mu + \chi''(\mathbf{X} \cdot \mathbf{u})^2 + A(1 + \sin(B(\mathbf{X} \cdot \mathbf{r})))\right]. \tag{A.22}$$

This gives for the forces,

$$\mathbf{F} = -\frac{\partial U}{\partial(\mathbf{Z} \cdot \mathbf{r}_{sp})}\mathbf{Z} - \frac{\partial U}{\partial(\mathbf{X} \cdot \mathbf{r})}\mathbf{X} \tag{A.23}$$

and for the gorces,

$$\mathbf{g} = -\frac{\partial U}{\partial(\mathbf{Z} \cdot \mathbf{u})}\mathbf{Z} - \frac{\partial U}{\partial(\mathbf{P} \cdot \mathbf{u})}\mathbf{P} - \frac{\partial U}{\partial(\mathbf{X} \cdot \mathbf{u})}\mathbf{X}. \tag{A.24}$$

Implementation

The following is an example of how efficient code was derived from the expressions for the forces and gorces. The software package Mathematica [88] was used to

differentiate the expressions and translate the derivatives into code. The Mathematica package uses braces () for parentheses, square brackets [] to denote arguments to functions and curly braces {} to denote vectors. Only the simplest case of the sphere-sphere potential is shown here.

Variable names were used to represent the dot products in the expressions giving $(\mathbf{Z} \cdot \mathbf{r}_{sp}) \longrightarrow$ `ZdotRsp` and $(\mathbf{X} \cdot \mathbf{r}) \longrightarrow$ `XdotR`. The expression for the potential U was built up as follows:

```
sigma0 = 1;
epsilon0 = 1;
sigma = sigma0;
epsilon = epsilon0 * (1 + A * (1 + Sin[B * XdotR]));
Usp = C * epsilon *
      ( 2/15 * (sigma0 / (ZdotRsp + sigma0 - sigma) )^9
        - (sigma0 / (ZdotRsp + sigma0 - sigma) )^3 );
```

The space-fixed vectors were defined as

```
Z = {0, 0, 1};
X = {1, 0, 0};
```

and the force vector $\mathbf{F}$ was defined as

```
{Fx, Fy, Fz} = -D[Usp, ZdotRsp] * Z - D[Usp, XdotR] * X;
```

where `D[U,x]` is a Mathematica function returning the partial derivative of `U` with respect to `x`. This gives for the potential and force,

```
Usp = C*(2/(15*ZdotRsp^9) - ZdotRsp^(-3))*
      (1 + A*(1 + Sin[B*XdotR]))
```

```
Fx = -(A*B*C*(2/(15*ZdotRsp^9) - ZdotRsp^(-3))*Cos[B*XdotR])

Fy = 0

Fz = -(C*(-6/(5*ZdotRsp^10) + 3/ZdotRsp^4)*
       (1 + A*(1 + Sin[B*XdotR])))
```

These expressions could have been translated directly into code, but to improve computational efficiency they were re-written in order to avoid the unnecessary recalculation of common terms. This was done by replacing common terms with variables, at each stage re-examining the expressions for further common terms. This sequence of substitutions and the resulting simplified expressions were then translated into the final code. The following sequence of substitutions was made, using the Mathematica function `ReplaceAll[ a, b -> c ]` which replaces in an expression a all occurrences of an expression b with an expression c.

```
exp = { Usp, Fx, Fz };

exp = ReplaceAll[ exp,  B*XdotR -> SP01 ];

exp = ReplaceAll[ exp,  1 + A*(1 + Sin[SP01]) -> SP02 ];

exp = ReplaceAll[ exp,  C * SP02 -> SP03 ];

exp = ReplaceAll[ exp,  ZdotRsp^(-3) -> SP04 ];

exp = ReplaceAll[ exp,  ZdotRsp^(-9) -> SP05 ];

exp = ReplaceAll[ exp,  ZdotRsp^(-4) -> SP06 ];

exp = ReplaceAll[ exp,  ZdotRsp^(-10) -> SP07 ];

exp = ReplaceAll[ exp,  2*SP05/15 -> SP08 ];

exp = ReplaceAll[ exp,  -SP04 + SP08 -> SP09 ];
```

This reduced the potential and force expressions to

```
Usp = SP03*SP09
```

```
Fx = -(A*B*C*SP09*Cos[SP01])

Fz = -(SP03*(3*SP06 - (6*SP07)/5))
```

Translating this into code gives expressions which are evaluated before the loop over the particles,

```
ABC = A * B * C

C215 = 2.0 / 15.0

C25 = 2.0 / 5.0
```

and expressions which are evaluated for each particle identified by the loop index I with position vector components RX(I), RY(I) and RZ(I),

```
XdotR = RX(I)

ZdotRsp = Z0 - RZ(I)

invZdotRSp = 1.0 / ZdotRsp

SP01 = B * XdotR

SP02 = 1.0 + A * (1.0 + sin(SP01))

SP03 = C * SP02

SP04 = invZdotRsp * invZdotRsp * invZdotRsp

SP05 = SP04 * SP04 * SP04

SP06 = SP04 * invZdotRsp

SP07 = SP05 * invZdotRsp

SP08 = C215 * SP05

SP09 = SP08 - SP04

Usp = SP03 * SP09

Fx = -ABC * SP09 * cos(SP01)

Fz = -SP03 * 3.0 * ( SP06 - C25 * SP07 )
```

This is not necessarily the most efficient coding which could be achieved and the original meaning of expressions tends to be lost, but this method enables reasonably efficient code to be quickly produced from complicated potential models.